UNIVERSITÀ
DI PAVIA

Multi-sensor analysis and machine learning classification approach for the diagnostics of electrical machines

DOCTORAL THESIS

UNIVERSITY OF PAVIA, ITALY

Department of Electrical, Computer and Biomedical Engineering

XXXIV PhD cycle in Electronics, Computer Science and Electrical Engineering

PhD candidate: Marcello Minervini

Supervisor: **Prof. Lucia Frosini**

Reviewers: **Prof. Daniel Moríñigo-Sotelo**

Prof. Sławomir Hausman

Pavia, May 2022

Dedicated to my mother

Summary

Abstract

The aim of this work is to expose the main research activities carried out by the author in his PhD course of study and to propose an accurate state of art in the field of diagnostics of electrical machines. This research matter has increased its diffusion exponentially in the last few years in both academic and industrial contexts. Many diagnostic techniques are exposed in this work. The author, through literature review, studied and implemented techniques for diagnosing induction machines, applying these methods mainly to analysing laboratory measurements of a 1.5 kW squirrel cage induction machine.

The measurements carried out include multi-signal acquisitions: stator current, axial and radial stray flux, and vibration from two different sensors are collected in various laboratory tests. Moreover, a detailed description of the laboratory equipment is presented to understand various aspects of the diagnostics of electrical machines.

The anomalies considered in the experiments presented in this work are: stator inter-turn short circuits, bearing faults of type "generalised roughness" or "localised fault", Low Frequency Torque Oscillations (LFTOs)– that can simulate a mechanical load anomaly or torque oscillation similar to that generated by broken rotor bars, and airgap eccentricity. The multisensor approach is used in most of the works of the author leading to enhanced performances; for example, the uncertainty of 1-2% on the calculated characteristics fault frequencies, due the slippage phenomenon in bearing, can be avoided in the study of electromagnetic signals spectra through the additional use of vibration signal. Moreover, comparisons between the signals analysed are carried out, showing pros and cons in various operating conditions of the machines. An analysis on the position of the fault in bearings is carried out since it can change the intensity of the characteristics harmonics.

Another important aspect to take into account when diagnosing a machine is the type of supply. The inverter supply of the machine can introduce additional difficulties in diagnosing the faults, since electromagnetic interferences will occur and speed transient or closed-loop control do not permit to use the same techniques as for mains-fed machines. Some insights and proposed methods on this point are presented in the work.

Artificial Neural Networks (ANNs) represent an important tool for automatic recognition of the faults in electrical machines. With the evolution of their algorithms and hardware in the last few years they can be used easier and can give more and more reliable results. Deep learning convolutional neural network (CNN) have been used by the author showing good results in classifying spectrograms of vibration or electromagnetic signals of an induction machine. The transfer learning technique has been used to train the CNNs: the networks used were already trained to classify an original task however they were retrained with spectrograms of vibration and electromagnetics signals from the machine using higher learning rate parameters in the final

classification layer of the network. With this technique the networks keep their feature extraction ability acquired with the first full training (to classify the original task) but can classify the new problem input (in this case for diagnostics purposes) using much less training images.

1 Introduction

Diagnostics of electrical machines leads to an improvement of the management of production equipment and facilities: foreseeing the faults in the machines can avoid unexpected and forced out-of-service of them and improves the maintenance program.

The main objective of this work is to show the potientality of the multi-sensor diagnostics for induction machines with and without the use of machine learning approach.

This thesis resumes the scientific works of the author during his PhD course of study. The work is organized as following:

- Firstly, an introduction and a state of the art of the main techniques used in the diagnostics of electrical machines is presented;
- In a subsequent chapter, the laboratory equipment used by the author in his research activities is described in details;
- The published scientific works of the author have been described in each of the following chapters of the thesis. Additional resources, as for example dedicated state of art paragraphs relative to the specific issue treated in the chapters, are added to the original published works. Moreover, a discussion about the results of every work is presented at the end of each chapter to have a wider view on the diagnostics of electrical machines: in fact, issues presented in the other chapters are often included and compared, for an amalgamation of the various arguments treated in the thesis;
- A final conclusion summarizes the issues and results reached in the various works of the author.

2 State of art in diagnostics of electrical machines

2.1 Introduction

2.1.1 Diffusion of electrical machines

Electrical machines have increased their population since the beginning of the twentieth century with a very high growing rate. The use of electric motors for industrial production purposes has expanded from slightly less than 5% of total mechanical power used in the USA manufacturing sector in 1899 to around 25% just ten years later. The ratio of electric motors power used in the industries continued to increase in the first half of the century to reach nearly 90% of total power in 1939 [1]. The diffusion of the electric motors use is of course related to the production of electricity which permits the delocalization of the industries from areas also far from rivers, primary source of the hydraulic-mechanical power, and from areas rich in coal mines, which was the major chemical-thermal energy source in the nineteenth century. The electricity of course gives rise to many other outstanding innovations in the industrial production such as automatic precision instruments for the monitoring, control and inspection of industrial operations; for example, the electrical automatic controls permitted the epochal transition from small scale batch production to continuous processing in the refining of petroleum products and in the paper industries [1].

The population of the electric motors and in particular Induction Motors (IMs) certainly does not decrease during the successive third industrial revolution and now is still growing with the advent of the industry 4.0. In fact, it is estimated that the population of the electrical machines has increased largely in recent years, with a number of operating machines of about 16.1 billion in 2011 and a growth of about 50% in the last five years [2,3].

With the advent of power electronic converters and control systems, that became more reliable and cheaper in the last few years, different kinds of machines can be found in industry, for example Permanent Magnets Synchronous Machines (PMSM) - that can be distinguished in brushless DC or Brushless AC - or Synchronous Reluctance Machines (SynRM). Though the diffusion of these kinds of machines is quick, it is still dependent on the market of rare earths (in case of PMSM) and the cost is not still competitive with the cost of induction motors. These kinds of machines are often used for applications in which the power to weight ratio and other constraints, such as very high efficiency or very high rotational speed, are required. To have a comparison, industrial electric motors used in heavy industry produce less than 1 kW per kilogram of machine's weight, motors for Electric Vehicles (EVs) produce around 2 kW/kg and special machines designed for aircraft application can reach 10 kW/kg [4].

For all the other “classical” industrial applications, the induction motor is still the most diffused [5]. In fact, the induction machines have the advantages to be more rugged, cheaper and need very little maintenance in comparison with the other kinds of machines. Moreover, they are self-starting machines also in mains-fed operations. According to the study [7], in which three different machines for drive-trains application are compared, the specific cost for the induction machines is about 7.2 $/kW while it is 10.1 $/kW for a DC machine and 16.3 $/kW for a DC-brushless. To the cost of the machine itself should be added the cost of the electronic converter if used, as discussed in [6]. Since in many industrial applications is not necessary a variable rotational frequency, the advantage of the choice of the IMs is evident as the cost is much lower than a synchronous machine with electronic converter.

Some changes are coming with the application of the directive 2009/125/EC, through the commission regulation (EU) 2019/1781, in which most of the electrical machines in the European Union must meet certain standards in terms of energy efficiency. The regulation is oriented mainly on squirrel cage induction machines (SCIM) of rated power range from 0.12 kW to 1000 kW, with some notes about the efficiency of the Variable Speed Drives also. All the new IMs installed in Europe, after 1st July 2021, from 2 to 8 poles in the power range from 0.75 kW and equal to or below 1000 kW, should have an efficiency level of at least IE3. Moreover, from 1st July 2023 the IMs in the range 75-200 kW must have IE4 efficiency level.

The efficiency level classes are defined in the IEC 60034-30-1:2014 standard, where the designation “IE” (International Energy-Efficiency), is directly followed by a number representing the classification (the higher the number, the higher the efficiency). The efficiency values for classes of four poles motors in the complete power range under the standard are visible in Figure 1.

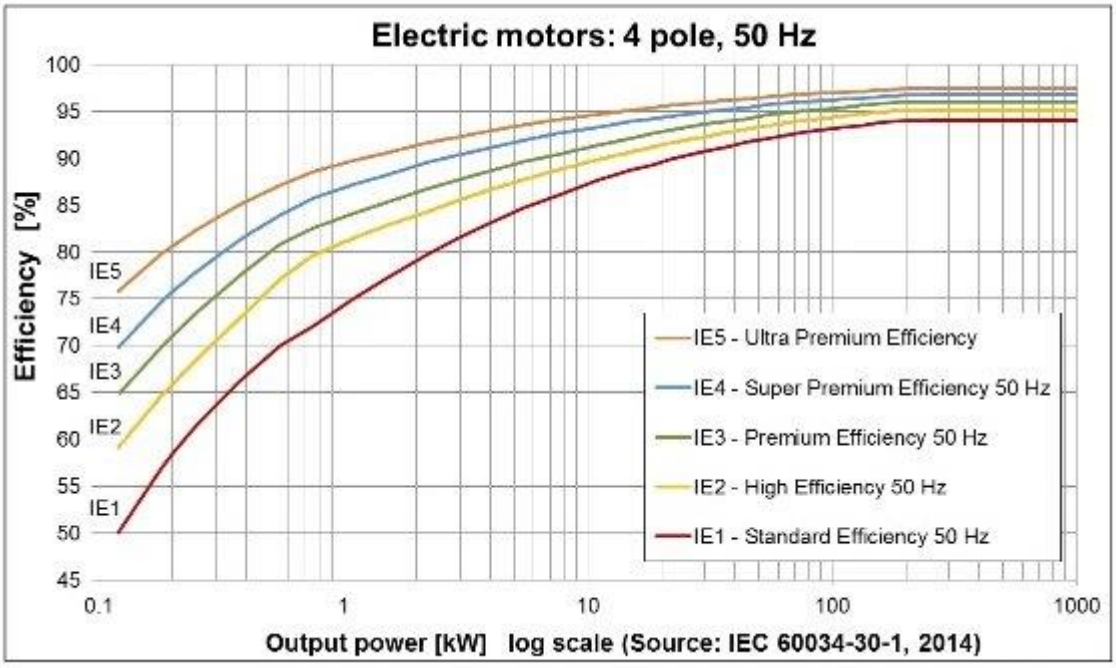

Figure 1: Efficiency levels according to IEC 60034-30-1:2014 standard

The requirement of more efficient machines induces the producers to use high quality iron materials and different technologies from standard productions, such as copper die-cast rotors. Moreover, the machines with higher values of efficiency level, namely IE3, IE4, IE5, are heavier and have more inertia momentum [8]. These machines are more expensive, and to reach these high efficiency levels different type of machines are appearing with more prominence on the market: the PMSM and the SynRM. These kinds of synchronous machines virtually eliminate any rotor losses (expecially the SynRM), because no current is induced in the rotor, and so a 25% reduction in the overall losses with respect to IE3-class SCIMs can be assumed [8]. Despite this and other advantages of synchronous machines, The IE4-class SCIMs are present in the market since almost ten years, and on average, they cost only about 15% more than IE3-class SCIMs. These kinds of machines are still an excellent option for small–medium power ranges, particularly in fixed-speed applications, in which they are still competitive and cheaper than synchronous machines [8].

2.1.2 Diagnostics of electrical machines

Diagnostics and protection from faults has an ancient hystory that can be considered as archaic as the history of electrical machines themselves. Initially the users and manufacturers of the machines relied on the simple protections such over-current, over-voltage, earth-fault, etc. to ensure reliable and safe operation conditions. With the increasing of the tasks performed by these machines, improvements were also sought in the field of fault diagnosis [9]. The diagnostics of

electrical machine is a concept stricly correlated to condition monitoring and various kinds of maintenance.

The condition monitoring of a machine is the process of monitoring a parameter in the machine e.g. vibration, line current, etc., in order to identify a significant change that is indicative of a developing of a fault. The condition monitoring is a major component of predictive maintenance. In fact, the use of condition monitoring allows maintenance to be scheduled, or other actions to be taken to prevent damages and avoid their consequences. Condition monitoring has the unique benefit in that conditions that would shorten normal lifespan can be individuated and fixed before they develop into a major failure. The definitions of these three concepts are resumed in the following:

- ***Condition monitoring***. It is composed by the actions carried out for having a monitored status of the machines. It can be subdivided into data acquisition and data pre-processing of some of the parameters and variables of the machine. The last step of the process, that is the decision taking, is not generally included into the condition monitoring process but it is reserved to the diagnostics issue. Condition monitoring could be "*online*" when the acquisition of the data is continuous in time, during the normal operation of the machine and generally is visualized and elaborated in remote, often in "live" mode, or "*offline*" when the measurements are periodic or intermittent, when the machine is not working and often elaborated at a later time.
- ***Diagnostics of electrical machines***. It is the general issue related to the detection, localization and identification of various kinds of fault (electrical, mechanical or thermal faults) in the machine. The concept includes also the decision-making process on what actions should be carried out after the identification of the fault. This decision process could be made by trained personnel or by algorithms (often bonded to machine learning techniques).
- ***Predictive maintenance***. It is the kind of maintenance strictly related to the condition monitoring and the diagnostic concepts. Predictive maintenance lets one to estimate the time-to-failure of a machine. Knowing this time, often called Remaining Useful Life (RUL), it is possible to find the optimum time to schedule the maintenance for the system. Predictive maintenance is opposed to reactive and preventive maintenance: the former is when the machine is used until its failure and substitution and repair are executed only after the failure has occurred, while the latter is performed by regular checks on the equipment and the maintenance is planned over regular intervals. It is clear that predictive maintenance can give better results especially in costly and safety-critical equipment because it reduces the run-off time of the machine (as opposed to reactive maintenance) and optimize the exploitation of the various parts of the machines to their real life term (in contrast

with preventive maintenance) [10]. This kind of maintenance is similar to the concept of prognostics of the machines, introduced for example in [11].

A schematic representation of the differences between the various kinds of maintenance descripted above is visible in Figure 2, [10].

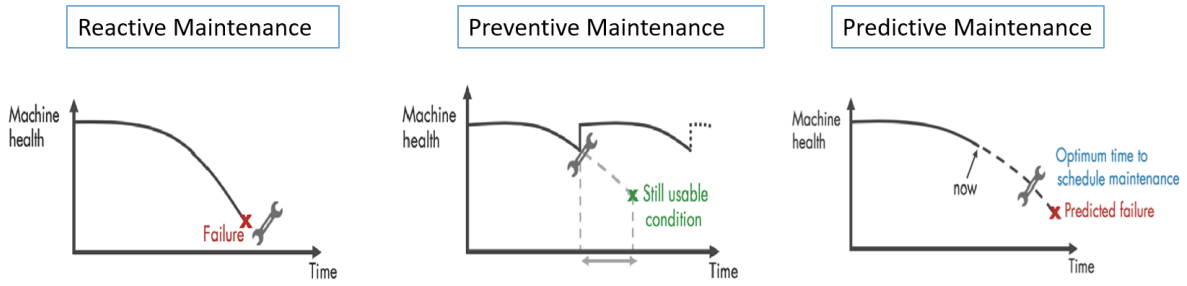

Figure 2: different kinds of maintenance. In the case of predictive maintenance, the maintenance is scheduled only when it is necessary, by forecasts obtained by condition monitoring information [10].

The diagnostics of the rotating electrical machines has reached a high diffusion and development, recently. It can be observed, in fact, that numerous scientific papers have been published in these recent years on this theme as stated in [12]. The growth of the diagnostics happened for several reasons. First of all, the predictive maintenance has increasingly spread in the industrial sector and in other fields, such as, for example, electric traction. As stated above, the predictive maintenance is the type of maintenance in which the RUL of the machine (or other devices) is calculated with algorithms and requires the use of advanced diagnostic techniques. The fault in the machine should be individuated as soon as possible –in the incipient state – to have more time to predict the RUL and schedule a maintenance operation in the future with more precision.

With the evolving of some techniques, such as Machine Learning and its branch Deep Learning, and with the lowering of the cost of the sensors and computational devices, the diagnostic techniques became more effective and this contributes to greater diffusion of the diagnostics in the industrial context. Moreover, with the increase of the cost of the machines, due to the new efficiency rules discussed in the previous paragraph, the tendency of the diffusion of the diagnostics can increase; in fact, for the monitoring of these machines, that need to be always in a very good healthy condition to have a good efficiency, condition monitoring and diagnostic techniques are likely to be more widely implemented in the future to check if the efficiency of these machines is always at its maximum value.

Some of the techniques used in the diagnostics of electrical machines will be reported in the following part, with some description of their main characteristics, advantages and disadvantages.

2.2 Major techniques used in diagnostics

The parameters to be monitored in a machine could be different and any parameter could be more appropriate for a different kind of fault. The main faults in a rotating electrical machine, with particular reference to the induction machine, are located in the stator windings, rotor bars, bearings, air gap eccentricities. Other anomalies can occur with a wrong mechanical coupling (shaft misalignment), mechanical imbalance, or can occur in the transmission mechanism (gears, bell and pulleys, etc.) or in the mechanical load itself.

The various types of fault will be discussed in the next paragraphs, here a presentation of the main quantities monitored will be given.

The main physical quantities measured in an electrical machine are:

- line current
- vibration
- magnetic stray fluxes
- temperature
- mechanical displacement (laser measurements)
- chemical analysis
- acoustic emission
- sound pressure
- radio frequency spectra analysis

Many of these signals are presented in [13], with particular reference to the bearing fault detection. The main characteristics for some of these signals are reported in the following sub-paragraphs. In particular, the study of the most used signals by the candidate in his research project will be reported: motor current signature analysis (MCSA), vibration analysis and stray flux analysis. In fact, the candidate has focused his research work in particular on induction machine of small size, with mains or inverter supply, and not all the techniques presented above are suitable for diagnostics of this type of machine.

The faults detectable with the techniques outlined above are electrical, mechanical or thermal; the most important of them are reported in the following list (see for example [14] for a literature reference):

- Rotor faults – broken rotor bars or end connection-rings
- Air-gap eccentricity
    - Static eccentricity
    - Dynamic and mixed eccentricity
- Permanent magnet demagnetization
- Stator winding partial short circuits
- Stator partial discharges
- Bearing faults
- Shaft misalignment
- Load anomalies
- Gear faults

Some of these faults will be discussed in more details in the following of this chapter. In particular, the fault characteristic frequencies available in literature will be reported, with which one can individuate some of the faults listed above checking these harmonics in current or other signal frequency spectra.

2.2.1 Motor Current Signature Analysis

The Motor Current Signature Analysis (MCSA) is the acquisition and elaboration of the stator phase current signal of a machine for diagnostic purposes. The current signal is generally taken by current transformers already installed for protection purposes (overload protection) or directly by installing permanent or temporary sensors, for a continuous or a periodic condition monitoring. Continuous monitoring is also referred as online condition monitoring, in which the sensors and signal conditioners are permanently installed and acquire data with continuous regularity. In contrast to online condition monitoring, offline condition monitoring is referred to periodic acquisitions, that can be scheduled with a certain regularity (for example once a year, etc.).

Usually MCSA is referred to the analysis of a single phase current; only one current sensor is used and it is placed on any of the three mains phases. The main reason is that the rotating flux waves produced by the different failures in the machine cut all the three stator phase windings; so corresponding currents are induced in each of the three phases [15].

MCSA started its development during the late 1970s to the mid-1980s decades in USA and Europe [16]. As reported in [16], many researchers collaborate to lay the foundation of this new approach for diagnosis. Some of them are reported in: Filippetti et al. [19], Vas [20], Kliman et al. [21] and Cameron et al. [22]; a more accurate information list is included in [16]; moreover, most

of them are reviewed in the important work of Benbouzid [23], though generally it includes also more recent works.

In more detail, the MCSA technique could be summarized with the following steps:

- acquisitions of the data with appropriate sampling frequency and number of samples
- filtering of the signal (antialiasing or others)
- windowing of the signal
- frequency domain transformation - Fast Fourier Transform (FFT) or other algorithms
- other digital filtering techniques
- individuation of the fault characteristic harmonics in the spectra

The acquisition should be made with appropriate sampling frequency and number of samples acquired. The former influences the bandwidth of the signal: the maximum bandwidth of a digital signal is the half of the sampling frequency, applying the Shannon-Nyquist theorem. However, a high sampling frequency with a not high number of samples acquired in the acquisition brings to a low frequency resolution in the FFT-transformed signal. The resolution of a FFT is defined as the frequency distance between two adjacent discrete points in the transformed signal. It is measured in hertz and the formula to calculate it is:

$$res_{FFT} = \frac{N_{samples}}{f_{sampling}} = \frac{1}{T_{acquisition}} \tag{2.1}$$

where:

- $N_{samples}$ is the number of samples acquired in the acquisition;
- $f_{sampling}$ is the sampling frequency;
- $T_{acquisition}$ is the time elapsed during the acquisition.

It is interesting to notice that the resolution is practically dependent only on the acquisition time (it is inversely proportional to the acquisition time). So, to have a good frequency resolution (small in value) in the frequency domain signal it is necessary to have a high acquisition time. Having a good frequency resolution means that it is possible to see very adjacent peaks in the spectra as separated peaks, while having low frequency resolution means that the peaks close to each other will be identified as a single peak. Conversely, a very long acquisition time can hide transient behaviour in the machine. It will be explained later in this work that FFT, and in general frequency-transformation, is not appropriate to study transient signal; however, very long transients, for example the thermal transient of the machine, could have different harmonic spectra

signatures, and with an appropriate acquisition time differences between a cold motor and a hot motor may be detected.

The antialiasing filters are analog low pass filters and they are used at the input of analogue-to-digital converters. They are used to reduce the aliasing phenomenon that is the effect that causes distinct signals to become indistinguishable (aliases of each other) when sampled. The specific details and explanation of the phenomenon will be omitted in this work, but in general an antialiasing filter will be low-pass with a cut-off frequency lower than the Nyquist frequency of the sampling process: an ideal filter (with an infinite slope at the cut-off limit) could be with a cut off frequency equal to the Nyquist frequency, but a real filter does not have an infinite slope and so its cut-off frequency has to be chosen lower than the Nyquist frequency. Higher order filters are preferable, though in some cases it could be convenient to use passive single-order filters.

Before performing the frequency transformation, a windowing function is generally used to pre-process the signal: the shape of the current in the time domain is multiplied by a window function that reduces the ends of the signal as shown in the left side of Figure 3. This reduces the disturbance known as 'leakage' due to a non-integer number of periods of the fundamental harmonic included in the acquisition time. This is visible on the right side of the Figure 3.

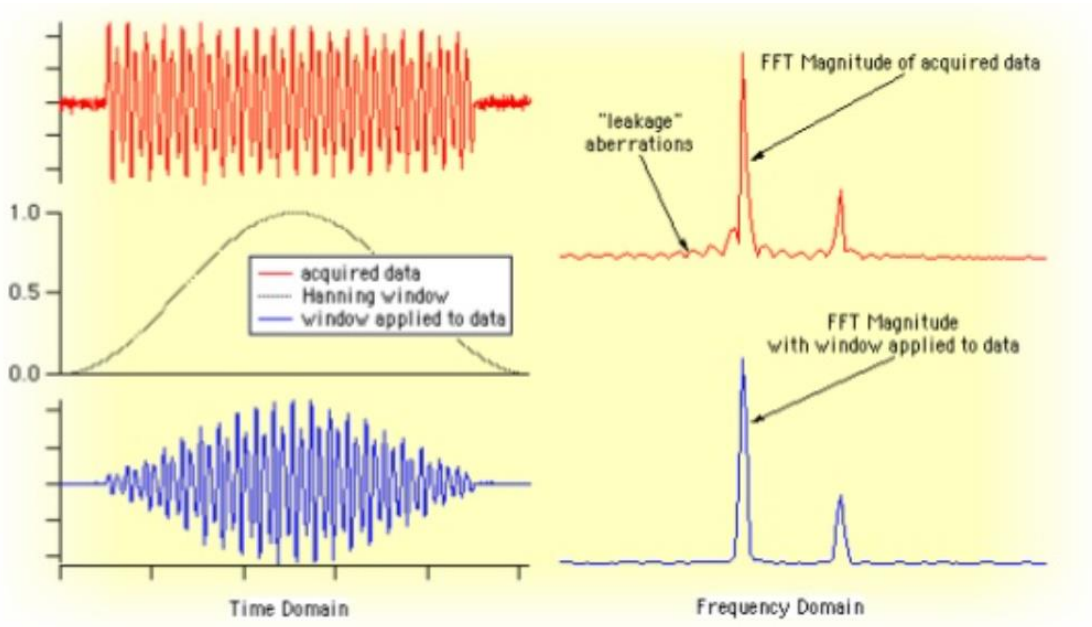

Figure 3: Signal windowing and frequency transforms with or without windowing [24]

The application of windowing is often included in frequency transformation functions such as MATLAB's “pspectrum” function. There are various functions for windowing, although the difference in results is very small; Hann's function is the most widely used.

For the frequency transformation a FFT algorithm or others algorithms can be used. FFT is one of the most efficient algorithms for effectuating the Discrete Fourier Transform (DFT) of a signal. It reduces the number of operations from $O(N^2)$ of a DFT algorithm to $O(N \cdot \log(N))$

operations with a FFT (Cooley-Tuckey algorithm). This means that, with a number of samples N=100, the direct DFT calculation needs $100^2 = 10000$ operations while with a Cooley-Tuckey FFT $100 \cdot \log(100) = 200$ operations will be needed, with an evident computational cost saving. Often, in practical use, pre-set functions could be used in computational software instead of the FFT function. For example, in MATLAB environment the function *pspectrum* could be used. This function calculates the power spectrum of the signal that is substantially proportional to the squared signal. The function permits to do the calculation with a selectable frequency resolution to save computational time in case of a first study of the signal, and a full frequency resolution in case of fine study of the signal (the maximum resolution achievable is anyway given by the formula (2.1)). Moreover, the function *pspectrum* permits other options to be changed. For example, the extrapolation of the spectrograms, that represent a form of time-frequency domain representation, could be done using the *pspectrum* function. This kind of transformation will be discussed in the next chapters of this work.

Once the signal is digitalized, many other filters and pre-processing techniques could be used more conveniently than with analogue signals. Examples of digital processing could be band-pass filtering, notch filtering, etc. Moreover, especially in the last decades more and more machine learning techniques are implemented to make automatic recognition or classification task for the healthy and faulty signals.

The last step of the MCSA technique is generally the identification of the fault characteristic harmonics in the spectra. The fault characteristic frequencies are calculated with formulas available in literature, obtained over the years by various researchers. Some of the formulas will be presented in the paragraph 2.3.

As anticipated before, more often in recent times machine learning techniques for the classification of the fault are used. In fact, the individuation of the characteristic harmonics is not easy. Signal to Noise Ratio is not very high; in fact, the fault harmonic could have very low amplitude compared to the fundamental frequency of the stator current. This is true especially for faults like bearings faults, in which the first diagnostic effect is visible on the vibration signals. The vibration of the bearings brings to a variation of the airgap of the machine and to a cyclic variation of the torque (in case of localized or “cyclic” bearings faults) in the machine and this brings to the visualization of characteristics harmonics also on current and electromagnetics signals [25]. A more in-depth discussion about the various specific faults will be presented in section 2.3 together with the harmonic characteristic frequencies of the faults.

2.2.2 Vibration Analysis

Vibrations are one of the major wear factors in complex mechanical systems. They can have various causes, such as mechanical, fluid-dynamic or electromagnetic.

Vibrations are mechanical oscillations around a reference position and are characterised by values of displacement, velocity and acceleration. In large mechanical systems, vibrations are generated at low frequencies (< 1 Hz), in this case the displacement relative to a reference position of the mechanical part under examination has to be measured. In the frequency range between 1 and 1000 Hz it is common to measure the speed of motion. Above 1000 Hz, acceleration is measured [26]. The sensitivity of the measure function (displacement, velocity, acceleration) is showed in the next Figure 4.

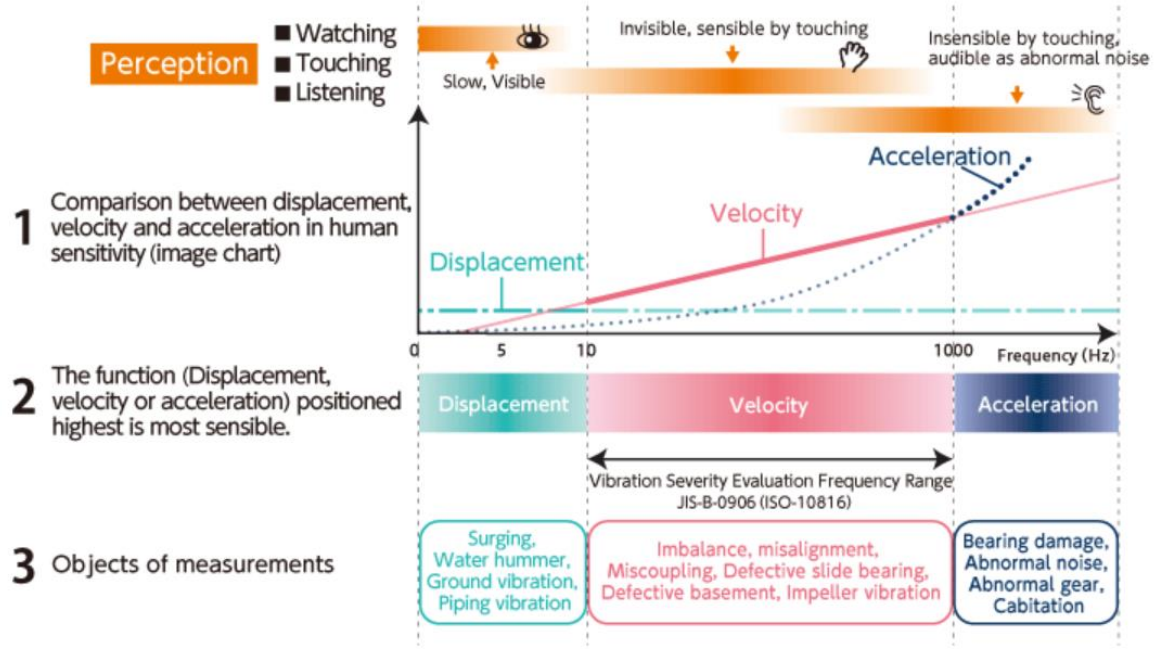

Figure 4: sensitivity of the measure function [26]

The quantities are related to each other by derivation and integration operations, so if you have a velocity measurement, you simply perform a derivation to obtain an acceleration.

In reality, a differentiation process accentuates the small non-linearity, measurement errors and noise present in the source signal, and while this may produce an acceptable degree of accuracy for the first derivative, further differentiation would result in an unacceptable error.

In measurements taken on electrical machines, acceleration is usually used, even for values below 1000 Hz.

The vibration analysis can be easily carried out by positioning one or more accelerometers on the mechanical part to be measured. Models of simple mechanical parts could be implemented and analytically solved; for example, systems with a low number of degrees of freedom such as single or double pendulum, or spring-mass systems, etc. The study of real objects is much more difficult as it involves the study of the body itself as an infinite degrees of freedom object (with continuous elastic members) [27]. In fact, most structural and machine systems have deformable or elastic members and so have an infinite number of degrees of freedom. Systems with a number of degrees of freedom finite are called *discrete* or *lumped* parameter systems, and those with an infinite number of degrees of freedom are called *distributed* or *continuous* systems. Usually, continuous systems are approximated as discrete systems and the solutions are often calculated through computational calculation. In fact, though analytical methods to resolve continuous systems give exact results, they are available only for a few selection of problems, such as uniform beams, slender rods, and thin plates. Often most of the practical systems are so treated as finite lumped masses, springs, and dampers. The increasing in the number of the degrees of freedom gives more accurate results at the cost of greater complexity of the system and calculation effort [27].

Systems and mechanical parts can have one or more vibrating modes that correspond to different natural or resonant frequencies. The Frequency Response Function (FRF) is a frequency based measurement function used to identify the resonant frequencies, damping and mode shapes of the structure. It can be considered as a transfer function between the input (force solicitation) and the output (acceleration measurement) of the mechanical system [28].

The natural frequencies of the system can enhance the characteristic fault frequencies of bearings as described for example in [29]. To do so, it is important to filter the FRF with a band pass filter around the resonant frequency of the system. This can enhance the characteristic harmonics of the fault (for example the bearing) that otherwise will be covered by other harmonics and noise in the spectra. The low-frequency fault harmonics cause an amplitude modulation of the resonant harmonics. Band-pass filtering, wave rectification (envelope transformation) and frequency transform of the spectrum (envelope spectrum) can make more visible the characteristic fault harmonics as they are enhanced by the resonance phenomenon. This technique is called "envelope analysis" and can be much more effective than a raw analysis of the frequency spectrum of the vibration. In fact, though characteristic fault frequencies could be visible in raw spectra, usually, and especially in case of incipient fault of the bearing, they are small in amplitude, compared to other low frequency harmonics and noise and so they can be easily hidden by these other harmonics [29-30]. The essential procedures of the envelope analysis are resumed in Figure 5.

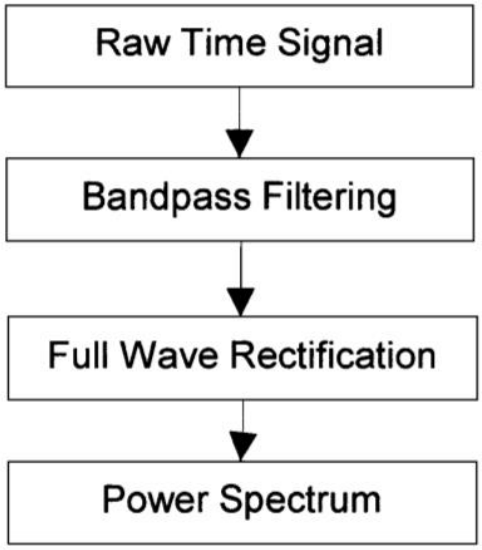

Figure 5: Data processing procedures used in envelope analysis [30]

Vibration analysis proved to be the most effective diagnostic technique for mechanical faults such as bearing faults [16]. Anyway in some occasions vibration analysis could be costly and difficult to perform (it needs the direct access to the machine for the installation of the accelerometers, and the vibration signal could be corrupted by vibration of other machines in the nearing space); so other techniques may be used (such as MCSA) with some advanced signal processing techniques or machine learning based classification algorithms.

In an electrical machine, the main sources of vibration are:

- aerodynamic: air pressure variation caused by fans, air agitators and salient poles;
- mechanical: manufacturing defects, mechanical unbalance of the rotor, defects in couplings, bearing failures;
- electromagnetic: magnetostriction, unbalanced mains power supply, inverter power supply, Lorentz and Maxwell forces.

The harmonics generated by mechanical causes appear in the spectrum at the rotational frequency f_r (in Hertz), and its harmonics $k \cdot f_r$ (with k integer).

Harmonics of electromagnetic nature depend on the frequency and shape of the electrical voltage at the machine's input. The forces of an electromagnetic nature that generate vibrations and acoustic noise are, as already mentioned, the magnetostriction, Lorentz and Maxwell forces.

Magnetostriction is the phenomenon whereby the material crossed by the magnetic flux changes its shape or size during the magnetisation process. The force is applied to the entire

volume of the iron-magnetic core. However, in electrical machines, materials with a low magnetostriction coefficient are generally used, so these forces are usually negligible.

Lorentz forces are applied to a current carrying wire in a magnetic field. The Lorentz force, applied to the rotor bars (immersed in the magnetic flux at the air gap), generates the motor's useful driving torque.

For a straight conductor, the following formula applies:

$$\overline{\boldsymbol{F}}_{tang} = I \cdot \bar{\boldsymbol{l}}_{\boldsymbol{s}} \times \overline{\boldsymbol{B}} \tag{2.2}$$

Where I is the current flowing through the conductor, $\bar{\boldsymbol{l}}_{\boldsymbol{s}}$ is a vector indicating the direction of the conductor (in which I flows longitudinally), $\overline{\boldsymbol{B}}$ is the magnetic flux density in which the conductor is immersed and the symbol × denotes the vector product. The direction of the force is given by the left-hand rule.

Although these forces are tangential to the rotor, and therefore able to generate the machine's useful torque, when produced by current harmonics they generate torque oscillations (or torsional vibrations).

Furthermore, the Lorentz forces act on the stator and rotor windings in a radial direction when considering the stray flux in which they are immersed rather than the stator-rotor coupling flux.

In this case the fundamental frequency of the vibrations will be twice the machine supply frequency (for stator windings) or twice the slip frequency (for rotor windings). For rotor windings the physical situation is shown in Figure 6. The force is proportional to the square of the current and therefore the heaviest effect will be on the starting rotor, with high currents and equally high slip frequencies. If the rotor bars are not tightly clamped in the slots, the vibrations will eventually damage the iron core and cause friction between the bars and core, which can lead to discharges and further losses, especially for large motors [16].

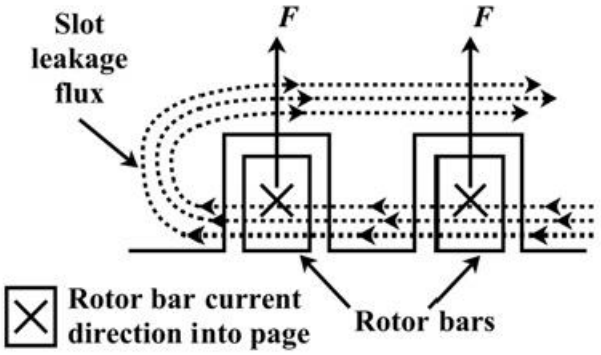

Figure 6: Radial force at frequency 2sf (generating vibrations) due to the interaction of the stray rotor flux with the rotor currents [16].

Maxwell forces develop on the surface of ferromagnetic cores where a strong change of magnetic reluctance occurs (i.e. on the surfaces of the rotor and stator cores facing the air gap). The forces are proportional to the square of the magnetic flux density B:

$$\sigma_n = \frac{F_n}{S} = \frac{B^2}{2\mu_0} \tag{2.3}$$

where σ_n is the mechanical stress measured in [N/m], F_n is the force normal to the surface S and μ_0 is the magnetic permeability in vacuum (or air).

Under ideal conditions (no eccentricity and smooth rotor and stator), these attractive forces would act symmetrically on the rotor, resulting in a null vector. However, vibrations occur due to the intrinsic eccentricity of the motor (due to construction and assembly tolerances). The fundamental frequency of these vibrations is $2f_s$, i.e. for a supply frequency of 50 Hz, the vibration fundamental frequency is 100 Hz.

It has been shown that in induction motors the vibrations at 100 Hz $(2f_s)$ and the vibrations at f_r and $2f_s \pm f_r$ increase rapidly for both static and dynamic eccentricity. Moreover, the effect is more pronounced at no-load than at load [31, 32].

In addition, again due to the Maxwell tensor, there are harmonics due to imperfect "isotropy" of the machine (even for isotropic machines):

- the "slotting" effect generates vibration harmonics as the reluctance of the airgap is affected by the presence of stator and rotor slots and changes depending on the relative positioning between the stator teeth and the rotor teeth. This generates a deformed flux density distribution with "steps" (see Figure 7) with respect to the ideal sinusoid. This produces a cogging torque in the motor and associated torsional vibrations.
- The saturation effect in the iron-core also introduces flux distribution dissymmetry and/or distortion of the flux fundamental, which in turn generates harmonics in the field and hence pulsating torque and vibration.

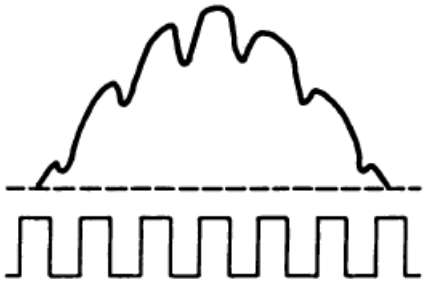

Figure 7: Deformation of the flux density fundamental waveform due to the slotting effect [17].

Important vibration-sensitive parts are the stator end-windings. Lorentz forces acting on the end-windings in the long term can loosen the fastening and bracing components of the windings and produce movement of the windings gaps that increase and accelerate vibration-related wear. This is especially true for large machines with rigid conductors ("form wound"), but it could also produce stresses on smaller machines with "hairpin" windings, especially when used in the automotive field, since they can be subjected to vibrations from both the motor itself and from the outside (stresses from the vehicle frame) [18].

It should also be remembered that the analysis of vibrations is correlated to that of acoustic noise generated by the phenomena discussed here. Of particular relevance is the study of vibrations and noise generated by modern machines (induction motors and others) used at variable frequency in the automotive field. This field of study is called NVH ("Noise Vibration & Harshness").

2.2.3 Stray flux Analysis

The use of the axial, radial and circumferential stray flux in the diagnostic process of an electrical machine has beginning and has been studied at least since the 1980s [33]. The main reason of using such signal is that it is low-cost, simple and has flexibility in the measurement. In fact, external flux coils can be retrofitted to motors already operating in the field (although it is necessary to have access to the machine, that it is not always possible) and they can easily be installed on the outer surface of the machines.

The sensors used to measure the stray flux are in the most cases simple circular coils of different diameters without any ferromagnetic core (air coils). One of the most used coil of this type is the Emerson CSi 343 flux coil sensor. This coil has a 22 cm average diameter and it is recommended for the application on the fan-end of the induction machine, centred with the machine shaft. This coil has been designed to be used for diagnosing machines with bigger outer diameter than the coil itself and has special thread mount or magnets mount systems to be attached on the rear frame of the motor. However, the candidate and his research group have reached satisfactory results with a machine slightly smaller in diameter than the coil as will be explained later in this thesis (the coil anyway has to be centred with the machine's shaft).

Figure 8: CSI Model 343 Flux coil (from product datasheet)

An extensive research activities on diagnostics of induction machines by means of stray flux was carried out and presented by Kokko in his doctoral thesis [34]. Kokko has performed measurements of the stray axial flux over a great number of machines. He has preliminarily analysed various types of sensors that can be used for the measurement of the industrial machines stray flux (the other sensors compared are fluxgate magnetometers and Hall effect sensors).

He has found that air-core coils are the best sensor for this kind of applications as the coil has practically no signal attenuation in frequencies below 20 kHz that are the most interesting frequencies for a diagnostic purpose. The disadvantage of the flux coil is that it is not possible to detect the dc or very low-frequency signal. In fact, the principle on which the coil works is based on Faraday-Lenz induction law: the induced voltage in the coil is directly proportional to the variation rate of the linked magnetic flux (at very low frequency the variation rate decreases). The Faraday-Lenz statement is reported in (2.4):

$$e = -N \cdot \frac{d\varphi}{dt} \tag{2.4}$$

in which e is the electromotive force generated on the coil, N is the number of turns in the coil and $\frac{d\varphi}{dt}$ is the variation of the magnetic flux φ linked orthogonally with one turn. Anyway the measurement of very low frequency signal is generally not considered useful in the diagnostic study of the machines.

Other methods to measure the magnetic field in the frequency range of 10 Hz to 3 kHz are presented in the standard IEEE 1308-1994 (currently inactive).

As stated by Kokko, the actual measurement of a machine's stray flux with a coil probe is not a magnetic flux but an electromotive force generated by the variation of the flux in time.

However, often it is not really necessary to calculate the value of the flux linked with the coil, because the variation (i.e. the time derivative) of it analysed in the frequency domain will highlight relative change in the harmonics at the same frequency of the flux itself.

It is possible anyway calculating the magnetic stray flux magnitude and frequency spectrum, inserting an integrator in the measurement cascade. The CSI 343 Flux coil can be supplied with a commercial Portable analyser (CSi Model 2120) that performs integration of the signal [34]. The measurement principle schemes are reported in Figure 9 and Figure 10; although they are not used in this thesis, these diagrams are useful to understand the principle of such measurement.

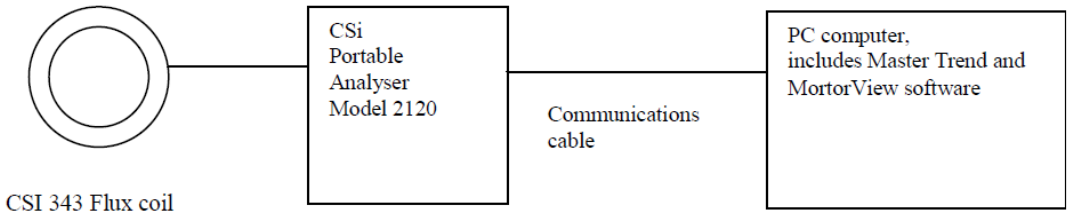

Figure 9: Measurement working principle for the system CSI Model 2120 [34]

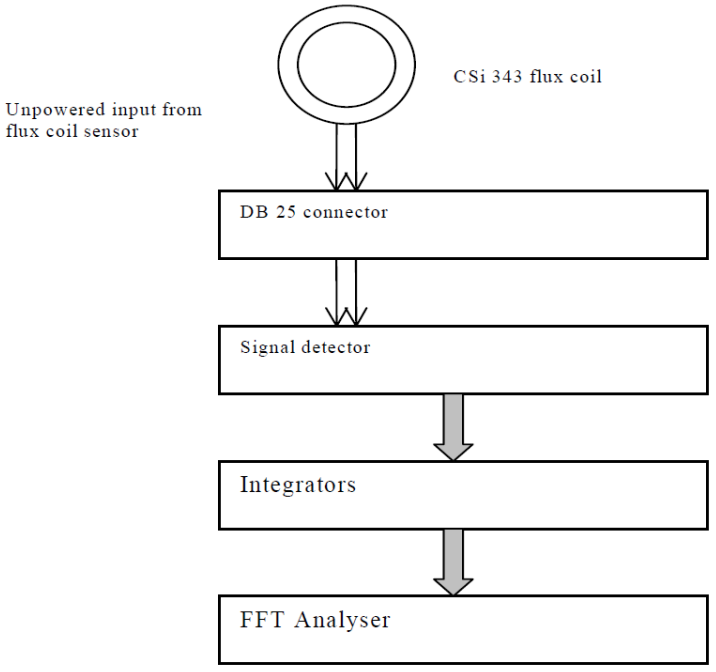

Figure 10: Principles of signal acquisition and processing cascade for the CSI 2120 Analyser [34]

The frequency resolution of the frequency-transformed spectrum is obviously as important as the frequency resolution used for a stator current spectrum of a MCSA analysis. The resolution can be calculated with (2.1). In the work [34], different resolutions are taken for each frequency range analysed. For example, in the range from 0 to 200 Hz, a frequency resolution of 0.06 Hz has

been chosen, while for 0 to 6000 Hz range, 0.93 Hz resolution has been chosen from the spectrum analyser CSI Model 2120. These resolution values are similar to that used and recommended for the MCSA analysis in the work [16].

Also the dynamic range of the amplifier/signal conditioner is a high important characteristic of the amplifier module. A dynamic range of 80-90 dB or more is recommended by both [16] and [34]. The dynamic range is the ratio between the maximum signal that can be acquired without distortion and the minimum signal that can be recognized by the amplifier or by the analog to digital converter. It is measured in decibel and an 80 dB dynamic range means that the maximum signal that can be received has amplitude 10000 times greater than the minimum distinguishable signal. As a remind, the dB value is calculated as ratio between measured signal and a reference signal, as reported in the next formula (2.5):

$$Value_{dB} = 20 \cdot \log_{10}\left(\frac{V}{V_{ref}}\right) \tag{2.5}$$

where the signals V and V_{ref} are in RMS values. In modern spectrum analysers the reference signal V_{ref} is set to 1 V [16]; this means that the 0 dB level will correspond to a signal with 1 V_{rms}, positive dB values refer to signals bigger than 1 V_{rms} and negative dB values are for signals with amplitude lower than 1 V_{rms}.

Usually the signal acquisition system has an analog to digital converter to convert continuous–time domain signals into discrete signals to be elaborated by a computer. The sampling acquisition frequency and the number of samples acquired give the x-axis resolution in the frequency spectra, calculated with formula (2.1); the y-axis resolution, i.e. the signal amplitude axis, depends on the number of bits available for the quantization of the signal and the maximum and minimum value that can be acquired (input voltage range). Possible values for the input range are for example from -10V to +10 V or from -5 V to +5 V. It is desirable to choice an adequate input range to reach the best possible y-axis resolution. For example, a resolution of a signal with peak values between ± 4 V is better with a selected input range of ± 5 V because the y-resolution achieves smaller values. In fact, the y-axis resolution is calculated with:

$$res_Y = \frac{voltage\ input\ range}{2^{Nbit}} \tag{2.6}$$

An A/D converter with 16 accuracy bits is generally advised for these type of measurements.

Different sensors may be used other than air-core flux probe. The most diffused are ferrite-core coil probes; for example, in [35] a C-shape magnetic-core flux coil is used for detection of radial stray flux. The magnetic-core probe is illustrated in Figure 11.

Figure 11: C-shape magnetic-core coil probe [35]

In the work [35] it is stated that the radial stray flux achieves similar diagnostic information with respect to current analysis about the healthy status of the rotor bar in an induction machine. In fact, depending on the winding configuration and on the probe size and location, the *e.m.f.* force induced in the coil is relative to one or two stator windings and so the analysis of the signal will give results similar to that of the stator current analysis. In the paper it is also stated that the radial stray flux intercepted by the probe is much more dependent on the stator field rather than the rotor magnetic field because this latter is shielded by the stator magnetic core of the machine. In the work the e.m.f. of the probe is directly frequency-transformed and analysed without any integration operation to obtain the real value of the magnetic flux. It is stated that in a narrow frequency range around the fundamental supply frequency of 50 Hz the increase in module of the higher-frequency harmonic (i.e. the right sideband harmonic) is not too big because of the small increase of frequency (smaller than 10-20 Hz).

As will explained later in this thesis, broken rotor bars of an induction machine generate sidebands around the supply frequency in the current or flux spectra. It is stated in [35] that the increase of the magnitude of the right sideband due to the increase of frequency is compensated by the slightly decrease of the amplitude of the left sideband due to the lower frequency. The spectra in fact is normalized in amplitude over the highest harmonic, i.e. usually the supply fundamental at 50 Hz; one method to diagnose the broken rotor bars is to compare the arithmetic average of the amplitude of the sidebands with respect to the supply frequency fundamental component. This method is still working if there is a slight decrease in the left sideband amplitude, because it is compensated by the slight increase of the right sideband amplitude. So it is not necessary in this case to integrate the e.m.f. signal to obtain the real value of the flux, and the

method remains as effective as MCSA [35]. The picture of radial stray flux spectrum around the supply frequency, with visible sidebands due to broken rotor bars, is shown in Figure 12.

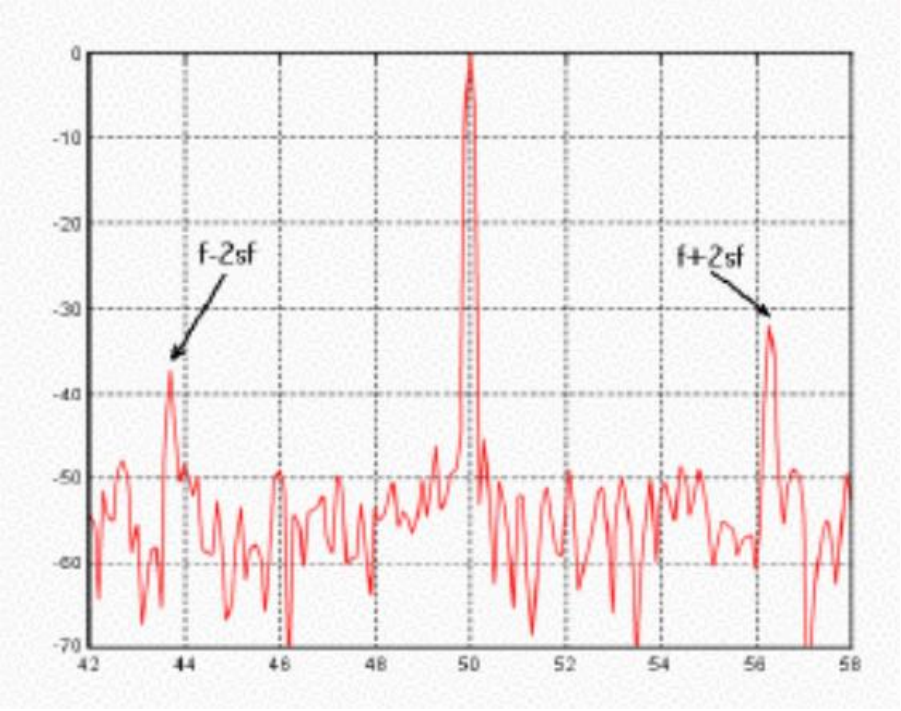

Figure 12: radial stray flux spectra in presence of broken rotor bars in induction machine [35].

In [36], a comparative study between MCSA and stray flux analysis has been performed concerning the diagnosis of partial short circuits in stator windings. The tests are carried out with the machine at standstill, at no-load condition and at rated-load condition. Moreover, tests are carried out with mains supply or Voltage Source Inverter (VSI) supply of the machine. According to the authors, the stray flux in the machine practically should not exist in a healthy machine ideally symmetrical. However, because of inherent dissymmetry in the machine, some residual stray flux is always present. According to the authors this stray flux is generated mainly by the stator and rotor end-windings/end-rings. So, a flux probe positioned near the end windings of the machine can intercept both the stator and rotor field.

The results of [36] show that the stray flux signal is much more sensitive to the recognition of the partial stator short circuits in almost all the conditions considered (with the different load conditions and with the different power supplies used). The rated-load condition is recognized as the most difficult to analyse because many harmonics arise in the spectra. This is actually a drawback because in field operation it is difficult to test a machine at no-load condition or at standstill (the mechanical load could be difficult to disconnect and in many cases the machine could not even be stopped for the test because installed in a continuous production plant). Anyway the stray flux analysis gave better results than MCSA, checking for the increasing of amplitude of different harmonics due to dissymmetry of the magnetic flux caused by the partial short circuit in one of the three phase windings.

A more recent work [37] presents a study similar to [36], i.e. a comparison between MCSA and stray flux analysis using an air-core flux probe located axially to the machine. Partial short circuits are executed and tested on one of the three phase windings in the same slot (turn-to-turn) or in different slots (coil-to-coil). According to results of the tests, axial magnetic stray flux analysis provides higher sensitivity in the case of turn-to-turn short circuit than current analysis, but lower in the case of coil-to-coil partial short circuit. In any case the authors, although highlighted both the advantages and disadvantages of stray flux analysis, claimed that the simplicity of the probe installation sometimes can turn in favour of stray flux analysis than MCSA (current clamps sometimes are difficult to install without the electrical disconnection of the machine).

In [38], two induction machines with a different rated power, the first of 3 kW and the second of 1.1 MW are modelled through specific Computer Software and a stray flux analysis is simulated via Finite Element Method (FEM) for detecting a broken rotor bar. Results show that characteristic fault harmonics arise in the spectra in a similar way as they could arise in a current spectrum. In fact, although some of the results do not exactly reflect what should have been expected, it turns out that the large motor has a higher harmonic sideband related to speed variation than the small motor; it is shown how the sidebands related to broken rotor bars increase in amplitude from the healthy case to the faulty case.

In [33] a study on Medium Voltage (MV) machines (rated voltage 6.6 kV) with ventilating axial ducts is carried out. Axial ducts are present in most medium-voltage machines to increase the heat dissipation through forced air ventilation and to decrease the quantity of construction material and the rotor inertia. When the number of axial ducts are equal to the number of poles of the machine, the reluctance of the rotor seen from the stator windings changes with the relative angular position between rotor and stator. The geometry of the machine with the axial ducts, with the magnetic flux paths in two different angular positions, is represented in Figure 13.

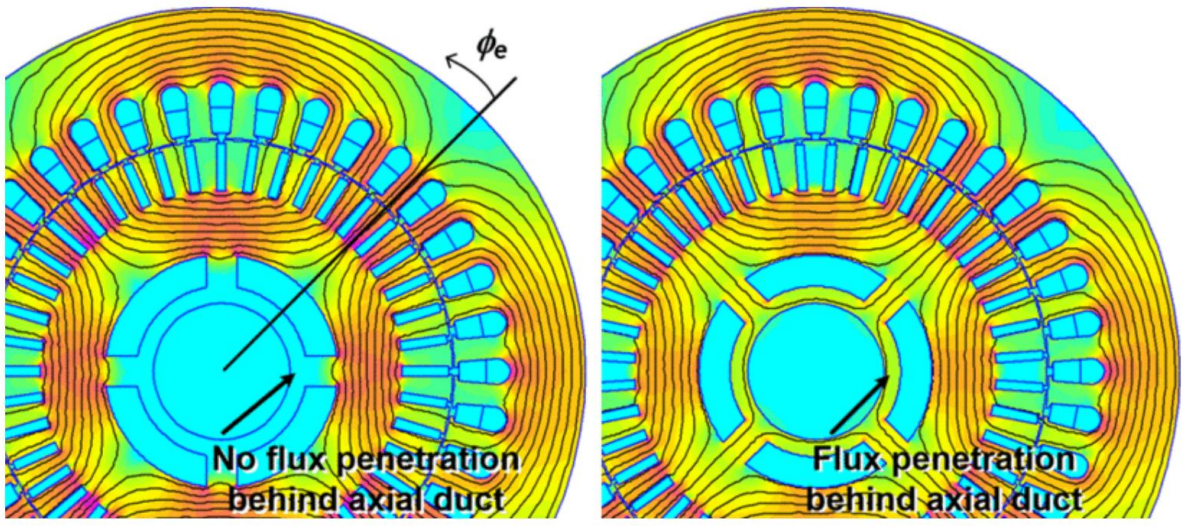

Figure 13: different flux paths for different positions in a four poles machine with four axial ducts [33].

As recognized also in [16], this condition ($2p = A_D$), where 2p is the number of machine poles and A_D is the number of axial ducts, can lead to false positives in detection of broken rotor bars with MCSA technique. This is true especially at low mechanical load because the magnetizing current is prevalent and the flux penetrates deeper in the core and in the bridges behind the ducts, than when the reaction rotor current due to the mechanical load (correlated to rotor slip) "shields" the rotor. Thomson in [16], states that if tests with variable load could be carried out, the false positive can be avoided (but changing the mechanical load is not always possible in industry measurements). Alternatively, more advanced techniques to avoid these false positives could be found in [39-40].

In [33], it is stated and proved with both laboratory and field measurements, that the radial flux signal is much more immune to the influence rotor axial ducts than the current signal. The authors state that deriving analytical equations or performing a 3-D FEM analysis with high precision is a really difficult task, as already known from literature. In fact, stray flux measurement is a complex phenomenon as the flux linked with the probe is a combination of axial, radial and circumferential leakage flux components. Moreover, stray flux is influenced by non-ideal asymmetries in the machine structure. A qualitative explanation is given by the authors based on the magneto-motive force (MMF) and magnetic reluctance variation. It is explained that the variation of the reluctance due to air ducts and their relative position with respect to the stator windings is smaller than the "effective" change in reluctance depending on rotor position due to a change in the armature reaction symmetry, if a broken rotor bar is present. To confirm the difficult prediction, the results are demonstrated with controlled laboratory tests and measurements on field machines as discussed before.

2.3 Analysis of the signals and characteristic frequencies for diagnostic purposes

The basic signal processing techniques for the acquisition and frequency transformation are exposed in the previous paragraph 2.2. The cases considered in this chapter are referred to stationary signals, i.e. when the machine is at a steady state with a constant supply frequency and with negligible speed variations. Under these hypothesis, a normal frequency spectrum transformation is enough to extrapolate diagnostic information. If the rotational speed is variable in a wide range (for example during a start-up) Fourier transform is not adequate because the signal is not under stationary conditions. The same situation could happen in case of a large oscillation of speed caused by load torque oscillation; anyway, the author has used simple frequency transformation to study machine's signal affected by torque oscillations, that generate speed oscillations in an uncontrolled machine, and extrapolate some diagnostic results, though with more difficulty than in case of constant speed operation.

Other techniques may be used to study transient or non-stationary signals, generally using time-frequency domain transformation. This could be obtained via the use of Short Time Fourier Transform (STFT), wavelet transform or other techniques. These more complicated techniques will be explained in the following chapters of this thesis.

In this paragraph, some considerations will be reported about the analysis of the stationary signals for electrical machine's diagnostic purposes. In particular, the fault characteristic frequencies will be exposed for the various faults that could happen in a machine.

Fault harmonics have been derived in various scientific works since at least the 1980s. There are numerous formulas for calculating these characteristic fault frequencies. The formulas often contain multiplication coefficients to account for the order of the harmonics since each harmonic may contain multiple harmonics (even or odd). An overview of the most commonly used characteristic frequencies for various faults can be taken from [14] and is shown in Figure 14.

In some cases, the detection of the characteristic frequencies is carried out according to a "deterministic" method: the harmonics are searched one by one, by looking at their amplitude and checking if there is a simultaneous presence at different harmonic orders given by formulas. In other cases, this detection becomes "probabilistic" by observing bands of the spectrum rather than harmonics at precise frequencies, as reported in [23] for the case of bearing faults.

FAULT (COMPONENT)	CHARACTERISTIC FAULT FREQUENCY
Static eccentricity	$\left[kR\left(\frac{1-s}{p}\right)\pm n\right]f_s$
Dynamic and mixed eccentricity	$\left[(kR\pm n_d)\left(\frac{1-s}{p}\right)\pm n\right]f_s$
Mixed eccentricity, PM demagnetization, SM open damper, and shorted field	$nf_s\pm kf_r=\left[n\pm k\frac{(1-s)}{p}\right]f_s$
IM broken rotor bars and end rings	$\left[\frac{k}{p}(1-s)\pm s\right]f_s$
Bearing outer race	$f_s\pm k\frac{N}{2}f_r\left(1-\frac{D_b}{D_c}\cos\beta\right)$
Bearing inner race	$f_s\pm k\frac{N}{2}f_r\left(1+\frac{D_b}{D_c}\cos\beta\right)$
Bearing ball element	$f_s\pm k\frac{D_c}{D_b}f_r\left[1-\left(\frac{D_b}{D_c}\cos\beta\right)^2\right]$

f_s: fundamental frequency, f_r: rotor rotational frequency, s: rotor slip, p: number of pole pairs, R: number of rotor slots, k: integer (= 1, 2, 3, ...), n: harmonic order (= 1, 3, 5, ...), n_d: dynamic eccentricity order, N: number of balls, D_b: ball diameter, D_c: ball pitch diameter, β: ball contact angle.

Figure 14:Characteristic fault frequency for harmonics produced in induction and synchronous machines [14]

It should be reminded that although diagnostic techniques such as MCSA [41]-[42] and stray flux analysis (sometimes called SFSA, stray flux signature analysis) are some of the most promising diagnostic techniques, they could have the following limitations (especially for the "deterministic" method described above and for some specific faults):

- they could require a precise estimation of the slip;
- the current and flux should be measured at steady state;
- unspecified harmonic orders lead to ambiguous diagnostics results.

In the following sections some of the most used formulas for the calculation of the fault characteristic frequencies are reported with more details and literature references.

2.3.1 Airgap eccentricity

Rotor eccentricity can be of two types, static and dynamic, depending on whether the centre of rotation of the rotor remains fixed with rotation or varies. Static eccentricity may be due to an ovalised internal stator circumference or incorrect rotor installation. The thickness of the air gap as seen from the stator reference in this case remains constant at any circumference angle. Dynamic eccentricity occurs when the geometric centre of the rotor does not coincide with its centre of rotation. In this case the length of the air gap depends on both the stator angle considered and the rotor rotation angle (that depends on its speed and so also from time) [42], since the minimum air gap (and the air gap profile in general) moves along the stator circumference with the rotor rotation. Since the magnetic flux density at the air gap depends on the magnetomotive force multiplied by the magnetic permeance, with rotor eccentricity the permeance is different due to the variable length of the air gap, which generates harmonics that deform the induction field [42]. Furthermore, with the variable air gap, the mutual and self-inductance of the windings varies [43].

When both types of eccentricity are present simultaneously in a machine, we speak of mixed eccentricity. A minimum eccentricity is always present in a machine, due to construction tolerances, but does not substantially influence its operation; on the contrary, an excessive eccentricity leads to excessive mechanical stresses due to mechanical unbalance and an unbalanced radial magnetic force due to the variation of the air gap (called UMP: Unbalanced Magnetic Pull). Radial mechanical stresses lead to overheating and accelerated bearing wear and for long flexible rotors (with a low number of poles) can lead to disastrous rub between the rotor and stator [15].

Schematic pictures of the two kinds of eccentricity are shown in Figure 15 and Figure 16.

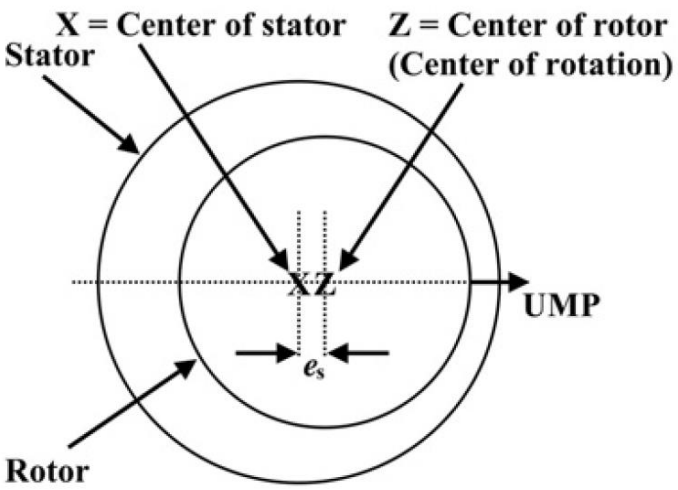

Figure 15: Static airgap eccentricity with direction of UMP [16].

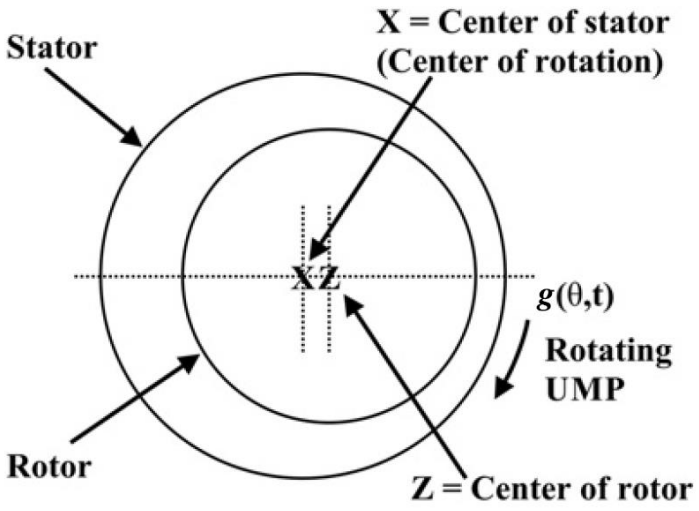

Figure 16: Dynamic airgap eccentricity with rotating UMP [16].

The air gap eccentricity can be identified by the lateral harmonics of the slot pass frequencies (localized at frequencies around 1000 Hz [44]):

$$f_{slot\_ecc} = f_s \cdot \left[(k \cdot R \pm n_d) \frac{(1-s)}{p} \pm n_\omega \right] \tag{2.7}$$

where:

- f_s is the supply frequency
- k =1, 2, 3...
- R is the number of rotor slots
- n_d is the order of eccentricity: 0 for static eccentricity, 1,2,3... for dynamic eccentricity
- *s* is the slip
- *p* number of pole pairs
- n_ω =1, 3, 5 ... order of time harmonic of magnetomotive force, due to the power supply waveform.

Alternatively, another formula that does not require knowledge of the number of rotor bars and shows harmonics below 100 Hz is [23]:

$$f_{ecc} = f_s \cdot \left[1 \pm m \cdot \frac{(1-s)}{p} \right] = f_s \pm m \cdot f_r \tag{2.8}$$

where:

m = 1,2,3 ... is an integer coefficient

$f_r = f_s \cdot \frac{(1-s)}{p}$ is the rotational speed of the rotor in Hz

Thought this simplified formula is very used in practice, Thomson [16] states that the primary cause that generates these harmonics is the axes misalignment. Since axes misalignment (especially horizontal or parallel misalignment) generates radial forces on the bearing and can lead also to an embowed shaft and rotor, a dynamic airgap eccentricity occurs. But Thomson states also that eccentricity can manifest itself from other causes, so he recommends to use formula (2.7) assuming that the number of rotor slots is known.

Another consideration by Thomson [16] and many other authors is that static and dynamic airgap eccentricity cannot be distinguished using MCSA. In practice, checking the amplitude of the characteristic harmonics, one can say that there is some level of eccentricity without discerning which type of eccentricity it is.

2.3.2 Broken rotor bars

For rotor bar failure the characteristic harmonics are searched at the following frequencies [14], [23]:

$$f_{brb} = f_s \cdot \left[\frac{k}{p}(1-s) \pm s\right] \tag{2.9}$$

where: $\frac{k}{p}$=1, 3, 5, …

In practical cases, fault harmonics are usually found at frequencies [15]:

$$f_{brb} = f_s(1 \pm 2 \cdot s) \tag{2.10}$$

where the frequency calculated with a $-$ sign is specifically due to the fault (counter-rotating magnetic field at $-s \cdot f_s$) and the frequency calculated with a + sign is due to the speed oscillation generated by the fault [15], [16].

The amplitude of the fault harmonic is proportional to the number of consecutive broken bars [45].

Furthermore, a threshold beyond which the rotor is considered to be faulty can be established: for example, if the harmonics detected have a difference in amplitude from the fundamental of at least 45 dB, the motor is considered healthy [15]; however, these thresholds may depend on the number of rotor bars and the number of poles in the machine.

The presence of several adjacent consecutive broken bars leads to an increase in the amplitude of the fault harmonics until the number of broken bars exceeds the ratio Nr/2p, where Nr is the number of rotor bars and 2p the number of poles of the machine [46].

For two non-adjacent broken bars placed at 90 electrical degrees between them on the rotor, the fault harmonics tend to cancel [47] at frequencies ±2·s, but in that case, other harmonics appear at:

$$f_{brb\_NA} = f_s(1 \pm 4 \cdot s) \tag{2.11}$$

In general, especially for machines with low inertia, where torque oscillations generate quite pronounced speed oscillations, and to cover all cases, the following formula can be used [47]:

$$f_{brb\_all} = f_s(1 \pm k \cdot s) \tag{2.12}$$

where k =2, 4, 6, …

It should be remembered that these harmonics are often present even in healthy machines and they should only be taken into account as an indicator of failure when they exceed a certain

threshold. An example of a current spectrum of a machine with broken bars (compared with a healthy case) is shown in Figure 17.

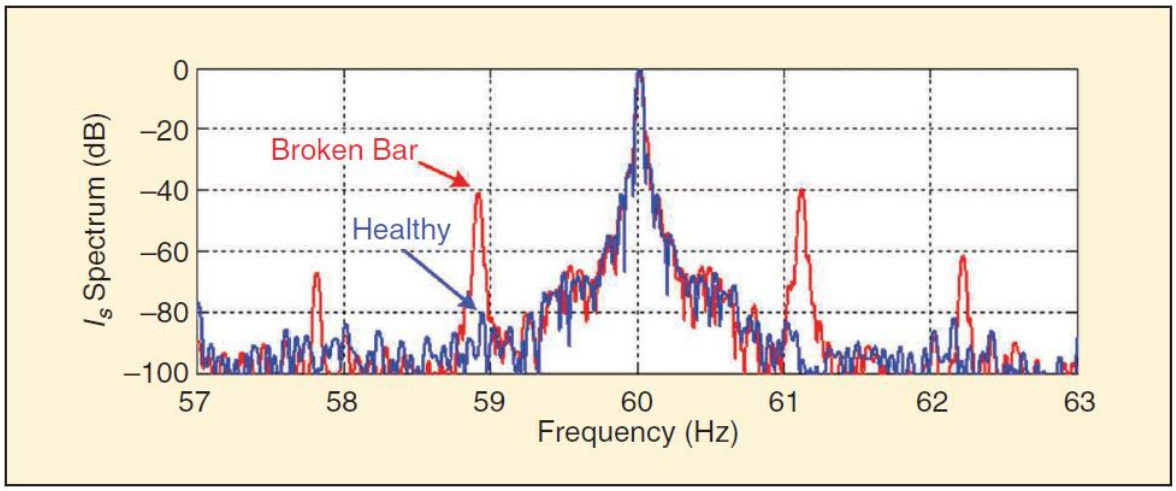

Figure 17: Example of current spectrum with broken rotor bars [14].

As reported in [48] and explained in depth in [49], only in flux signals (airgap or leakage fluxes), fault harmonics of broken rotor bars could be found at

$$f_{brb\_flux1} = s \cdot f_s, \qquad f_{brb\_flux2} = 3\,s \cdot f_s \tag{2.13}$$

These very low frequency harmonics are generated by the oscillation of the mechanical speed, due to the rotor bars, and are visible only in flux spectra and not in current ones. All the others characteristic harmonics are visible in both current and flux spectra since the flux signal is influenced by the stator current and so carries the same diagnostic information as already stated in the previous paragraph.

Vibrations in the axial direction can be generated when bars break and current flows between bars, i.e. in the rotor laminations between the broken bar and the two adjacent bars [35]. Various signals are analysed in the work: current, flux and radial and axial vibration. Although, according to Lorentz's law, axial vibrations should be generated in the case of a broken bar and transverse current between bars, the axial vibration component was absent in the work. This led the authors to state that the current between bars remains small, even in the case of a broken bar failure, for small motors.

However, the analysis of radial vibration led to the visualisation in the spectrum of side harmonics for fault cases at $f_{vib} = f_r \pm 2 \cdot sf_s$ (especially at full load) and side harmonics at $\pm 2 \cdot sf_s$ of the "principal rotor slot harmonic f_{RSH}" (harmonic frequency given by the number of rotor bars multiplied by the rotation speed). It is interesting to note that, according to the authors, intermodulation is generated in the vibration signal: harmonics at a frequency twice the power frequency will modulate harmonics at mechanical frequency, and vice versa.

Though these results on vibration analysis are recognized as important, MCSA remains a very reliable technique to diagnose broken rotor bars and it is generally preferable to use MCSA for this kind of faults as stated by Thomson [16].

2.3.3 Stator partial short circuits

In the case of low-voltage mains-powered motors (≤ 690 V), it is sometimes assumed that there are no symptoms indicating insulation degradation. In fact, partial discharges do not occur in such motors when powered from the mains. Without any type of condition monitoring of the machine, a short-circuit fault of a turn (or of a coil of the same phase) quickly evolves into a fault which completely compromises the operation of the machine, such as a phase-to-phase or phase-to-ground short-circuit.

It is emphasised that there is a big distinction between monitoring the condition of partial discharges in the windings of a high-voltage machine before a turn-to-turn failure and monitoring turn-to-turn short circuits in low-voltage machines. In the first case it is possible to monitor the degradation of the insulator before a discharge between conductors occurs, as the phenomenon is slowly progressive, whereas in the second case it is not possible to monitor the degradation of the insulator, but changes in the current spectrum are monitored when a turn-to-turn failure has already occurred [15].

Moreover, according to [15], a complete discharge fault pre-warning can be achieved if shorted coils within the same coil are promptly diagnosed by a continuous online diagnostic system.

Once the coil short-circuit occurs, the motor can still operate in near-optimal conditions, as there is only a slight increase in current and a slight magnetic field distortion at the air gap. However, there is a generation of heat and electrical discharge due to the current passing between the short-circuited coils, which accelerates the ageing of the thin insulating layer. The heat creates a chain effect whereby more and more turns are short-circuited until a complete phase-to-ground or phase-to-phase short circuit is achieved.

The degradation time of the insulator, once the first short circuit between turns happens, is short, and is difficult to calculate, since it varies from one machine to another; however, experience shows that in low-voltage machines this time may be sufficient to act and avoid a sudden failure [15].

The fact that the machine develops a fault that degrades quickly (and should in any case be repaired with machine downtime) discourages the use of expensive online diagnostic devices. However, in some strategic productions any advance in knowing the state of the machine can be

extremely advantageous to avoid unexpected downtime, and in some cases to avoid dangerous conditions.

The frequencies of the fault harmonics are:

$$f_{scc} = f_s \cdot \left[\frac{n}{p}(1-s) \pm k\right] \tag{2.14}$$

where, excluding the symbols already known, we have:

n=1,2,3,...

k=1,3,5,...

In [15], a 4-pole machine was diagnosed by observing the harmonics generated at around 125 and 175 Hz (slip was neglected), using the coefficients k=1 and n = 3 and 5 in formula (2.14). In fact, harmonics near 25 and 75 Hz for a 4-pole motor are often present due to construction tolerances (normal eccentricity values).

2.3.4 Bearings faults

Most small to medium-sized electrical machines have bearings with rolling elements (usually balls or rollers), while journal bearings are only used in large machines or for special applications. Rolling bearing failure is the most frequent failure in an electrical machine, occurring in up to 50% of cases.

Bearing faults are more difficult to diagnose by analysing the stator current and stray flux signals. In fact, this is a purely mechanical fault, the first effect of which is the occurrence of vibrations in the machine. It is usually easier to diagnose the fault using vibration analysis. However, a fault in the bearing also generates secondary effects such as eccentricity at the air gap [50] and torque oscillations [25], which can be detected by the MCSA and SFSA. The use of the MCSA can be advantageous as it does not require direct access to the machine, while SFSA needs the access to the machine but less effort is necessary to install the flux probe than installing accelerometers.

Bearing faults can be divided into two types: localised (or cyclic) faults and generalised roughness (or non-cyclic) faults. The former presents a point-type defect (which may be a crack, flaking, etc.) on one part of the bearing, while the latter occurs in a generalised manner through erosion, generally increasing internal mechanical clearances.

Localised or cyclic faults produce vibration harmonics at fairly precise characteristic frequencies due to the cyclical passage of balls over the defect. The characteristic fault frequencies are therefore vibration harmonics which then act as modulating waves in the spectrum of electromagnetic signals (current or stray fluxes).

Fault harmonics in the vibration spectra depend on the speed of rotation of the motor and the physical parameters of the bearing, such as the number of balls, the contact angle between the ball and raceway, and the dimensions (diameters) of the balls and the ball cage. The harmonics generated depend on the location of the fault. Faults can occur in the following parts of the bearing, generating harmonics at the frequencies indicated in (2.15) [29]:

- outer ring of the bearing (BPFO)
- inner bearing ring (BPFI)
- rolling element cage (FTF)
- rolling elements (BSF)

Ballpass frequency, outer race:

$$\mathrm{BPFO} = \frac{nf_r}{2}\left\{1-\frac{d}{D}\cos\phi\right\}$$

Ballpass frequency, inner race:

$$BPFI = \frac{nf_r}{2}\left\{1+\frac{d}{D}\cos\phi\right\}$$

Fundamental train frequency (cage speed):

$$FTF = \frac{f_r}{2}\left\{1-\frac{d}{D}\cos\phi\right\}$$

Ball (roller) spin frequency:

$$BSF(RSF) = \frac{D}{2d}\left\{1-\left(\frac{d}{D}\cos\phi\right)^2\right\}$$

(2.15)

where n is the number of rolling elements, d is the diameter of the rolling element, D is the average diameter of the ball cage and Φ is the contact angle between ball and raceway of the inner and outer rings (the contact angle is different from 0° for angular bearings, which also support axial loads). It is also considered here that the rotating ring is the inner ring while the outer ring is stationary and fixed to the stator.

Some pulses of the vibration waveform and the definition of some of the physical parameters of the bearings can be seen in Figure 18.

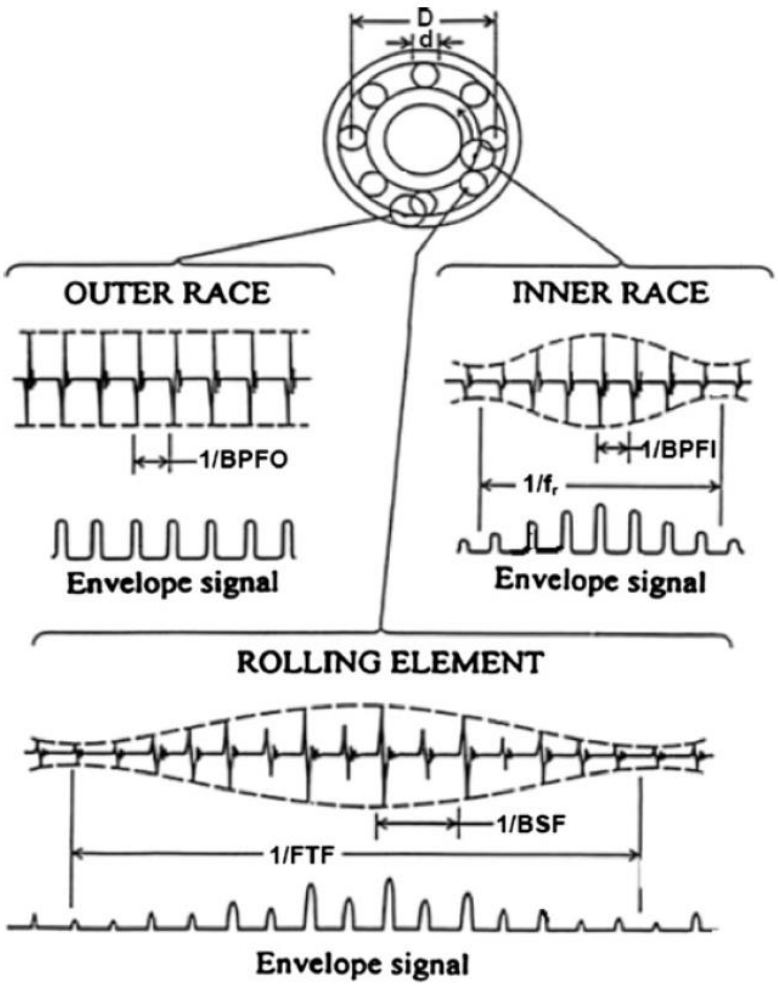

Figure 18: Pulses generated by localised faults in the bearings. Time–domain signals and envelope of the signal [29]

It can be seen in Figure 18 that the faults affect the vibration values differently depending on their location. In fact, they are influenced by the weight of the rotor, which acts radially on the bearing and gives more energy to the impulses when the localised fault is in the same direction of the weight force of the rotor.

In the spectra of the electromagnetic signals, the fault frequencies occur at the following values [50]:

$$f_{bear} = |f_s \pm k \cdot f_v| \tag{2.16}$$

where k = 1,2,3, ..., f_s is the power fundamental (in Europe 50 Hz) and f_v is one of the vibration characteristic harmonics defined in (2.15) excluding the characteristic frequency of cage rotation (FTF). These harmonics are generated by the change in the airgap due to the defect in the bearing (that produce a radial displacement of all the rotor).

According to a more recent study reported in [25], other frequencies can be considered as fault characteristics. These frequencies are summarised in (2.17) and are due to two causes: the airgap variations, as discussed before, and the torque variations. In fact, a little torque is required to overpass the defect by the balls and this can sometimes be visible in the current and flux spectra.

	Considering the airgap variations	Considering the torque variations	
Outer raceway	$f_s \pm k \cdot f_o$	$f_s \pm k \cdot f_o$	
Inner raceway	$f_s \pm f_r \pm k \cdot f_i$	$f_s \pm k \cdot f_i$	
Ball defect	$f_s \pm f_{cage} \pm k \cdot f_b$	$f_s \pm k \cdot f_b$	(2.17)

where f_o, f_i, f_b, f_{cage} correspond to *BPFO, BPFI, BSF* and *FTF* defined in (2.15), while f_r corresponds to the rotational frequency in Hz.

It should be pointed out that bearing harmonics have a limited amplitude in the spectra of electromagnetic signals, due to the fact, already mentioned, that this type of fault only generates a secondary effect on these physical quantities. An example of a current spectrum with fault harmonics produced by a bearing fault can be seen in Figure 19.

Other examples of measurements performed by the candidate will be presented in the next chapters. In particular, the author has used the vibration signal to exactly know the characteristic frequencies in vibration spectra of the fault in the outer race of the bearings (BPFO). Knowing the exact value of these frequencies, it was possible to observe the exact fault harmonics on the current and flux spectra. In fact, the formulas (2.15), (2.16) and (2.17) have an uncertainty factor of 1-2% due to the slippage phenomenon: the contact angle Φ assumes random values, also in radial bearings where it should be 0°, due to a different contribution of axial and radial load; due to this fact (and remembering that the balls are retained by the cage) some balls in the bearings do not rotate perfectly but have some slip on the ring [29]. This deviation of 1-2% of the real fault frequencies from the values calculated by the formulas makes difficult the recognition of the fault in Figure 19.

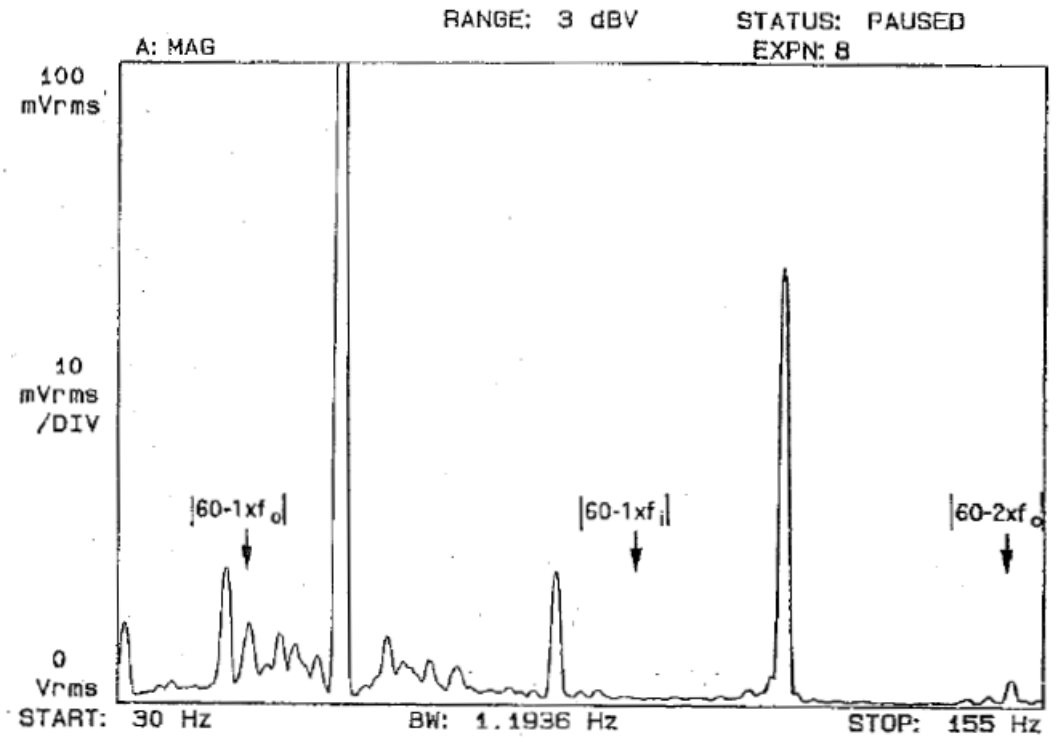

Figure 19: Stator current spectrum of loaded 4-pole induction machine with a hole in the outer race of the shaft-end bearing (frequency span: 30 - 155 Hz) [50].

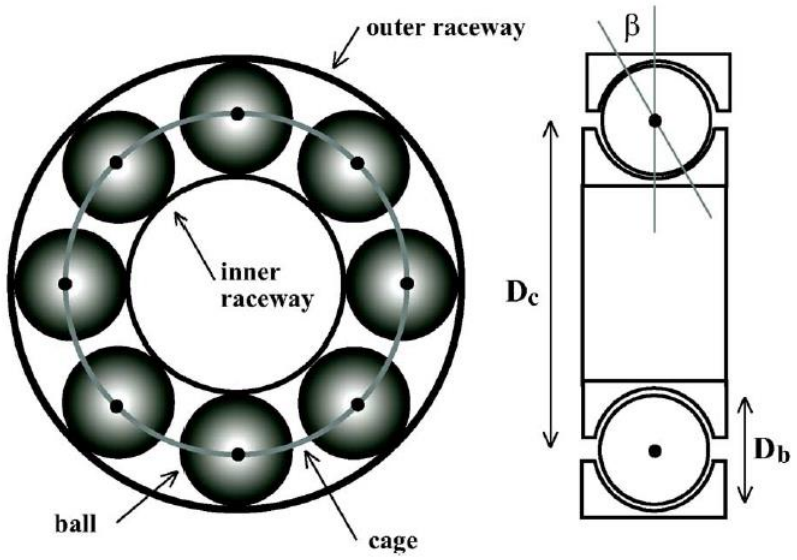

Figure 20: Geometry of a ball bearing, with indication of ball and pitch diameters and contact angle (here indicated with β)[25]

Numerous studies have been carried out to overcome these difficulties in diagnosing bearings with spectra of electromagnetic signals. The tendency is to approach machine learning or

deep learning techniques, as described in [51], often through the generation of diagrams in the time-frequency domain (that generates 2D images that can be used as inputs to train the neural network), or with other approaches of statistical type.

As regarding the generalised wear (roughness) faults (non-cyclic), the formulas described above would no longer be valid as there is no single fault that generates the cyclical pulses, but rather a distribution of wear over one or more parts of the bearing. Anyway, some works can prove that, even with generalized roughness, harmonics tends to increase around the characteristic frequencies [52], though this is rather a probabilistic method with a wider frequency range in which the fault harmonics are found.

According to Randall [29], in vibration spectra the generalized roughness can excite bands of the spectra rather than "discrete" harmonics. This could be possibly reflected also on electromagnetics' spectra.

The generalized defect, in any case, generates eccentricity in the motor as the clearance between the balls and the rings tend to increase; so excited eccentricity fault harmonics could arise also due to this defect.

Motors with inverter-fed supply are even more difficult to diagnose than the mains-fed ones, as the inverter introduces a large number of harmonics into the spectrum [53]. These new harmonics makes much more difficult to read the already low-amplitude bearing fault harmonics.

2.3.5 Low frequency torque oscillations

Torque oscillations due to mechanical loads are faults that can generate harmonics that cover other fault harmonics. Examples of load that generate oscillations are reciprocating compressors, which generate a torque dependent on the angle of rotation of the shaft. In this case, the load, by supplying a cyclic torque every revolution of the shaft, causes harmonics in the spectrum at the following frequencies:

$$f_{load1} = f_s \pm m \cdot f_r \tag{2.18}$$

which correspond exactly to the harmonics generated by the mixed eccentricity defect of the rotor air gap.

It is therefore evident that it is necessary to be able to separate the harmonics due to the load from the actual harmonics of the fault in order not to diagnose the machine as faulty (false positive); a quite complex technique for this purpose is presented in [54] while a review of the techniques in [55].

The same harmonic frequencies calculated with (2.18) can be generated with mechanical unbalance of the rotating masses of the motor and the load and misalignment between the

mechanical shafts. These factors introduce eccentricities in the motor and multiple torque oscillations of the rotational frequency f_r, although they are not in fact a specific malfunction of the motor but of the motor-load entire system.

Torque oscillations can also occur at frequencies not multiple of the rotational frequency. In this case, if the harmonics are at a low frequency relative to the power frequency and the oscillating torque has a small value relative to the average torque, a small-signal approach can be used. In this case the oscillations in the spectrum are given by:

$$f_{load2} = f_s \pm m \cdot f_0 \tag{2.19}$$

where f_0 is the frequency of oscillation of the load torque.

In these cases, the oscillating frequencies can cover the characteristic frequencies of broken rotor bars in the spectrum or a false positive of broken rotor bars fault can be diagnosed (if the frequency $\pm m \cdot f_0$ is very close to $\pm 2k \cdot sf_s$).

This situation can also occur when the motor is connected to a load via a speed reducer (e.g. a gear or a belt-pulley system). In this case the torque oscillations on the load may be at a fairly high frequency (e.g. f_s) but due to the gearbox they are seen at a lower frequency on the motor, possibly covering (or disturbing) the detection of harmonics of broken rotor bars.

Motor-load gear couplings can generate periodic torque drops if defects occur in the gear structure (tooth breakage). In this case too, the periodic torque variation is detected by the MCSA. Having as much data as possible about the structure of the load and the couplings helps to distinguish motor failure harmonics from those generated by load and coupling faults [55], [56].

As stated by Thomson [16], gearboxes are usually diagnosed by mechanical engineer using vibration analysis that is considered more reliable for this kind of fault. Randall [29], states that gear fault signal gives deterministic fault harmonics, in contrast with the bearing faults that has random slippage and so is not perfectly deterministic. This can be a way to distinguish the two fault harmonics in a vibration spectrum.

3 Test bench and equipment used for the diagnostics of electrical machines

In this chapter, the test bench and the equipment used for the scientific works carried out by the author will be described.

In fact, since same the test bench has been used for all the scientific works till now published by the author, the general considerations about the test bench will be reported in this chapter and not repeated in the successive chapters. In particular, all the information about the power equipment of this test bench will be described in the first paragraph 3.1.

In the second paragraph 3.2 the faults that can be simulated and studied with the equipment of the laboratory will be briefly presented.

In the third paragraph 3.3 the measurement equipment used in the scientific works will be presented.

In the fourth paragraph 3.4 of this chapter, some of the main characteristics of a second test bench will be exposed. In fact, thanks to a regional fund a new test bench for the "Laboratory of Diagnostics and Design of Electrical Machines" of the University of Pavia has been bought in the last few months. Though the author has not yet published any scientific work using this new test bench, general considerations about this new equipment will be reported.

3.1 Test bench used for the published works

The test bench used in the works presented in all the successive chapters of this thesis includes a magnetic powder brake and its relative control units. The magnetic powder brake is a "VIBRO-METER" model PB115 brake. Its main characteristics are reported in Table 1.

Table 1: main characteristics for VIBRO-METER PB115 brake

Maximum torque	100 Nm
Residual torque	2 Nm
Maximum rotational speed with excitation	3000 rpm
Maximum rotational speed without excitation	6000 rpm
Braking power	5 kW
Nominal excitation current at 20°C	5 A
Nominal excitation voltage at 20°C	30 V

This magnetic powder brake is mainly composed by:

- a stator on which an excitation winding is mounted;
- a drum rotor made up of four toothed rings separated by an air space. In order to contain the magnetic powder, a system of labyrinth seals is used;
- an electronic controlling unit "Dynamometer Control Unit" (DCU);
- an electronic unit for displaying the operating parameters "Dynatronic Unit Display" (DUD).

A schematic representation of the brake is presented in Figure 21, while the working principles will be exposed in the following.

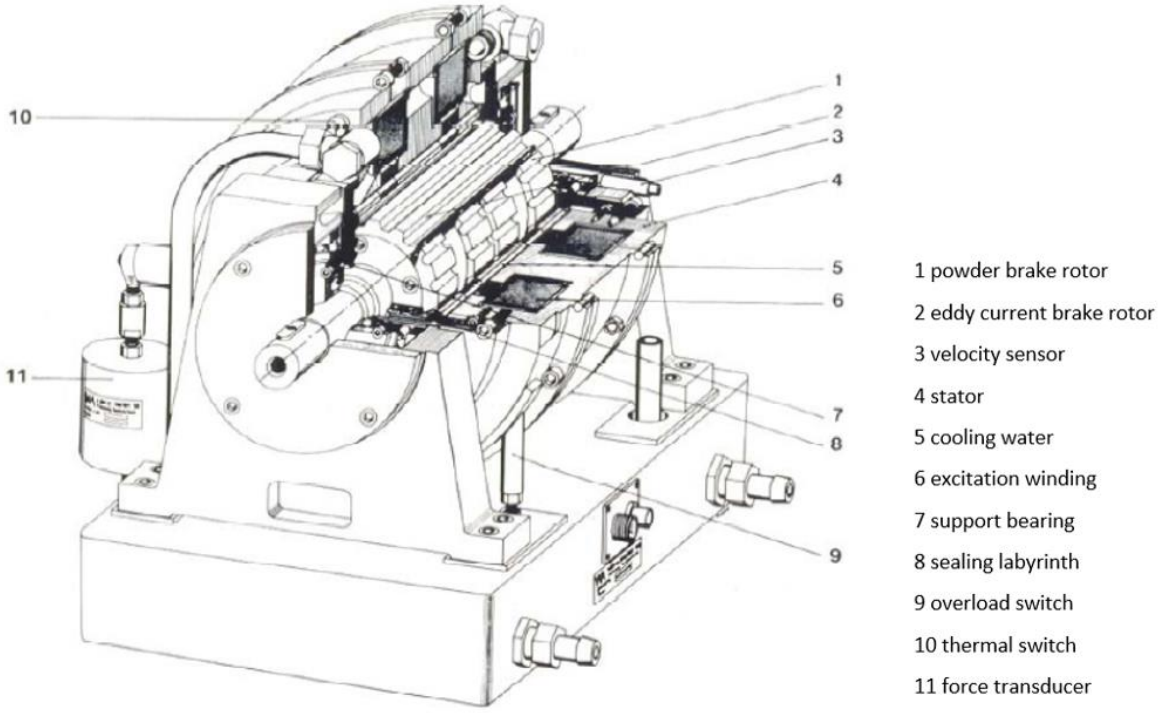

Figure 21: Schematic representation of the magnetic powder brake used.

The braking torque is generated electromechanically: when a current is flowing through the excitation winding, a magnetic field is created. This field interacts with the magnetic powder present in rotor air-gap. In fact, with the excitation field, the powder is attracted between the rotor's teeth and the stator, generating the resistant torque by friction.

The torque can therefore be adjusted by increasing or decreasing the intensity of the excitation current. It should be noted that the presence of labyrinth seals to contain the dust leads to a residual torque, which however does not influence the measurements as it is automatically balanced by the system by applying an excitation current to the brake that is proportional to the difference between the required torque and the residual torque. However, this residual torque can affect the no-load tests, especially for a small motor.

In order to control the torque supplied to the motor shaft, the stator rests on an oscillating support, called “cradle”, which transmits the torque values to a force transducer. The transducer is positioned in such a way as to transform the small movements of the stator, which occur during operation, into linear displacements. Using this dynamometer and knowing the geometry of the system, it is possible to calculate the torque that the stator transmits to the foundation; this torque is equal in value (but opposite in direction) to the value of torque transmitted by the motor to the brake.

A system based on a phonic wheel and a pulse detector, whose repetition frequency is proportional to the rotational speed, is used to measure the rotational speed. To ensure that the heat produced by the brake is dissipated, the brake is equipped with a forced-circulation water cooling circuit; in the event of a cooling-system malfunction, a relay is installed which, in the event of excessive heating of the components, interrupts the supply to the excitation circuit.

The brake is controlled through a power electronic circuit, the DCU. This unit consists of a module containing the electrical power circuit and the devices enabling regulation; it enables control of the magnetic powder brake, described above, in the following operating modes:

- at constant torque;
- at constant speed;
- at resistant torque proportional to the excitation current;
- at torque proportional to the square of the speed.

The front panel of the DCU includes potentiometers, which allow manual adjustment of torque and speed, and switches to set the operating mode and reset the device. At the rear, connectors for interfacing the unit to the brake and to the DUD display unit are present (the current level proportional to the desired braking is transmitted through these connections). Moreover, through the rear panel it is possible to connect analogical input signal (±10 V) for the control of the torque or speed through an external voltage generator. The latter functionality has been used in many scientific works of the author to generate low-frequency torque oscillations.

Data about the DUD display unit are omitted because considered irrelevant. The candidate wishes to point out that a magnetic powder brake has the advantage to provide an adjustable torque from standstill to a determined rotational velocity. This advantage allows to perform low speed tests (from 0 to 3000 rpm) with high braking torque. For higher speed, other kinds of brake are more suitable, e.g. the eddy current brakes. These brakes can reach higher speed but have a braking torque proportional to the square of the speed, so at low speed they cannot provide high braking torque. Combinations of these two brakes on the same shaft are provided by the brand of the equipment: at low speed the high-torque magnetic powder brake could be excited first, while when higher speeds are reached, the magnetic-powder brake is de-energised and the eddy-current is used. This arrangement combines the best qualities of both of the braking-machines.

To connect the induction motor under test with the brake, a flexible lamellar joint is used. This mechanical arrangement permits the coupling of the motor-dynamometer, even in conditions of imperfect alignment, without the use of precision instruments. Moreover, it helps to dampen vibrations and possible axial movements due to thermal effects that could alter the test results.

The device consists of four pins and, in order to make the coupling possible, is fitted with a flange with the same number of holes, offset by 90 degrees from each other. The lamellar coupling is represented in detail in Figure 22.

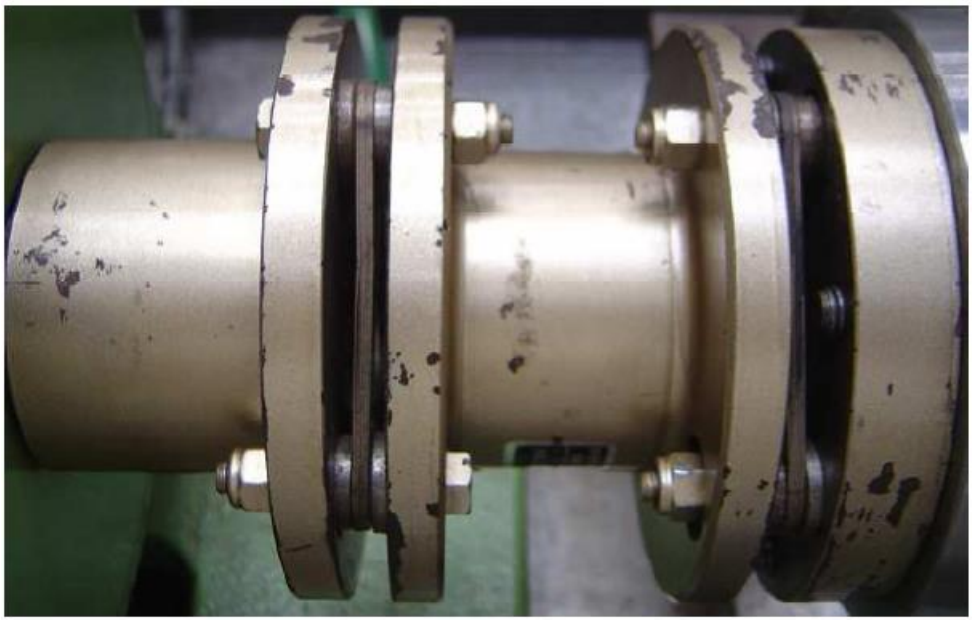

Figure 22: Lamellar coupling used for the mechanical connection between motor and dynamometer shafts.

The test bench is used in all of the scientific works carried out by the candidate with a 4-pole 1.5 kW explosive-proof induction motor.

The motor used is a three-phase induction motor, manufactured by RAEL (an Italian company), model RL 90L 4, with INERIS 05 ATEX 0025X certification, and is therefore able to

operate in environments with combustible or explosive gases (II 2G) with T4 temperature class according to standards IEC 60079.

The machine can operate at ambient temperatures between -20°C and +50°C and is air-cooled by an axial fan mounted on the shaft to remove the heat produced during operation. The machine is of type Totally Enclosed Fan Cooled (TEFC).

Table 2 shows the nameplate data and the main electrical and mechanical characteristics of the motor.

Table 2: Main electro-mechanical data of RAEL RL 90L 4 induction motor.

Rated power	1.5	[kW]
Rated voltage (Δ/Y)	230/400	[V]
Rated current (Δ/Y)	6.6/3.8	[A]
Rated frequency	50	[Hz]
Starting/nominal current ratio	5	-
Power factor	0.8	-
Poles	4	-
Nominal torque	10.4	[Nm]
Stator slots per pole per phase	3	-
Number of rotor slots	46	-
Axis height	90	[mm]
Service	S1	-
Insulation class	F	-
Protection grade	IP 55	-

The entire test bench with the RAEL induction motor is represented in Figure 23.

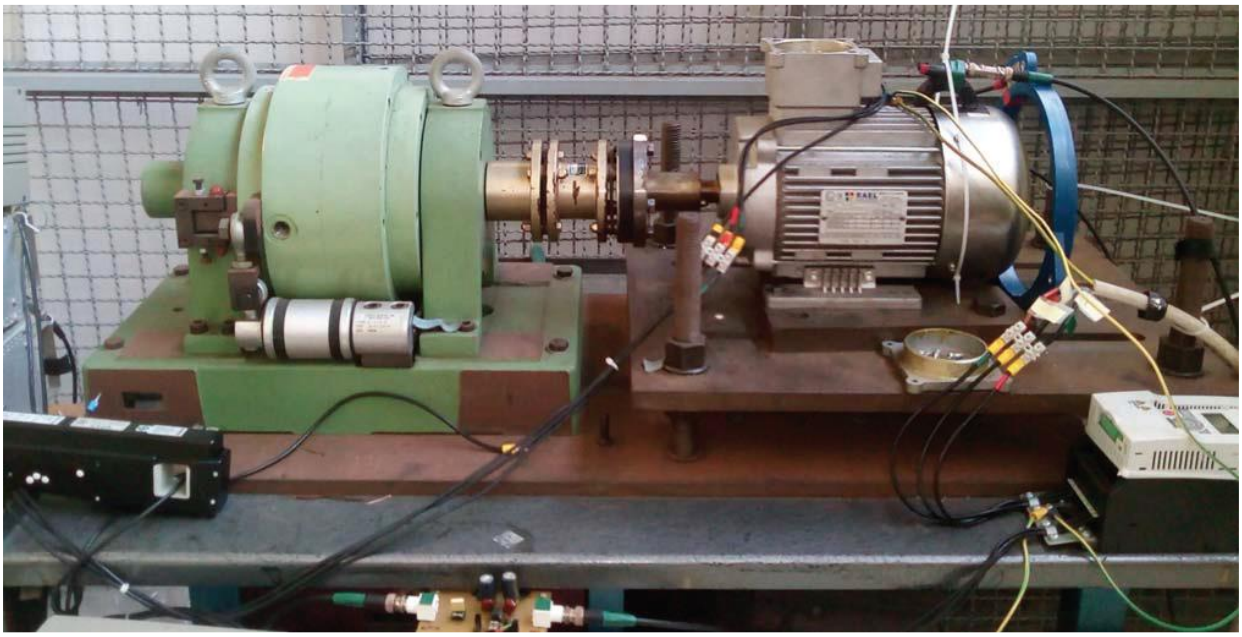

Figure 23: Test bench with motor RAEL "RL 90L 4"

The tests carried out in the laboratory are with the motor supplied from mains and from an electronic frequency converter.

This inverter is of EATON brand, model "MMX34AA5D6F0-0", open-loop type Space Vector Pulse Width Modulation (SVPWM). Its main characteristics are reported in Table 3.

Table 3: Main characteristics of the inverter used

BRAND AND MODEL	EATON MMX34AA5D6F0-0
INPUT	Three-phase; Uin = 380-480 V
	f = 50-60 Hz
	I_{phase} = 7.3 A
OUTPUT	Three-phase; voltage: (0 - Uin) V
	f = 0 – 320 Hz
	I_{phase} = 5.6 A
	Switching frequency = 6 kHz
POWER	2.2 kW at 440 V

The inverter is equipped with Insulated Gate Bipolar Transistors (IGBT). The schematic working principle with the main components of the electrical drive is shown in Figure 24.

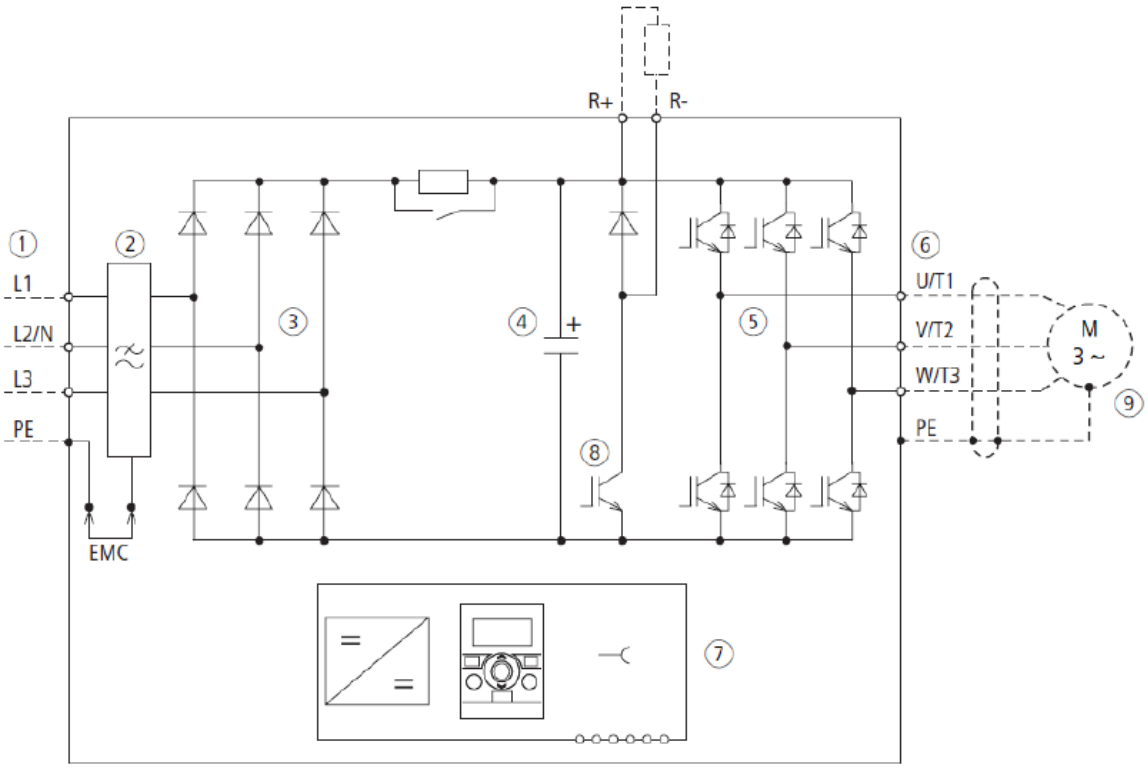

Figure 24: Main power components of the electrical drive.

This electrical drive contains the following blocks, visible in Figure 24 from left to right:

- input terminals;
- Electromagnetic Compatibility Filter (EMC), to reduce the harmonics injected by the inverter in the power grid;
- three-phase diode bridge rectifier, to convert the supply voltage from alternating to direct current;
- filter circuit, in which inductors and capacitors are used to filter out residual voltage fluctuations in the DC-link;
- braking circuit, with an external brake resistor; this part is optional and generally used for drives with high dynamic performance;
- three-phase Voltage Source Inverter (VSI) with SVPWM modulation. The switches are IGBTs that give to the motor a variable amplitude and frequency alternating voltage;
- output terminals and induction motor.

The inverter provides a scalar control (V/f= constant). This simple control allows to maintain the air-gap magnetic flux constant, in the range of frequency from zero to the rated frequency of the motor. In fact, the airgap flux is directly proportional to the V/f ratio. Keeping the rated airgap flux means to have the rated current and torque also at lower rotational frequencies.

Conversely, at frequencies higher than the rated one, it is necessary to keep the voltage equal to the rated one and, consequently, to reduce the airgap flux (flux-weakening region).

The works carried out by the author include only working points in the constant flux region, i.e. only supply frequencies lower than the rated one are used. For example, 30, 40, and 50 Hz are the inverter output frequencies used in [57], with V/f ratio maintained constant. A schematic exemplification of the scalar control technique with its main parameters is shown in Figure 25.

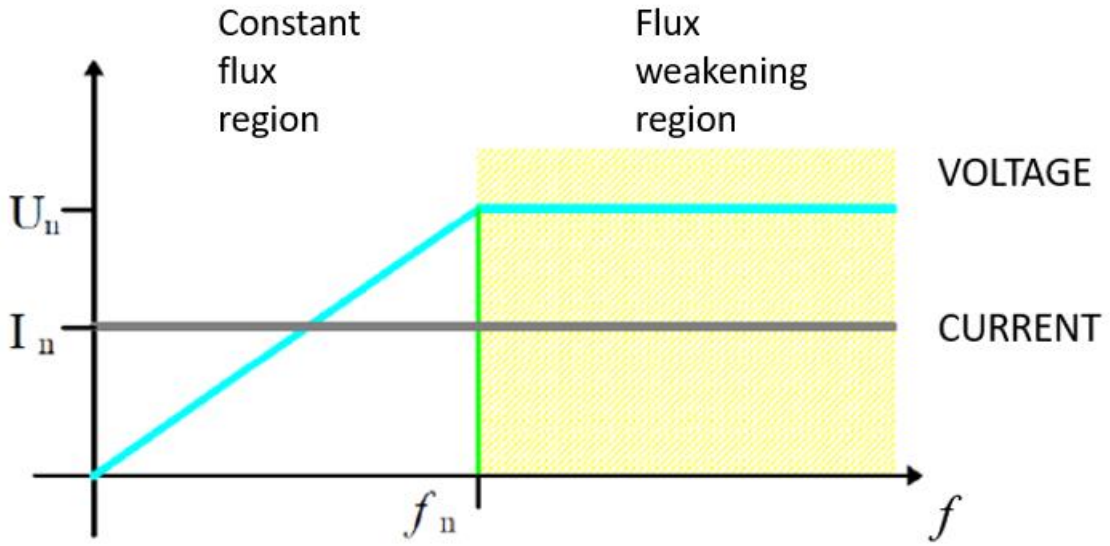

Figure 25: Scalar control of the inverter: constant flux and flux weakening region

The reason for testing the motor at different supply frequencies is to check whether the harmonic spectra, for example of the current or stray flux, provide different diagnostic information at different frequencies. In particular, a motivation is to check whether the harmonic spectrum of the stray flux provides different diagnostic information despite the airgap flux is kept constant by the power supply. In fact, changing the fundamental supply frequency can modify the ratio between the value of the stray flux and the constant airgap flux; this is because of the lower shielding, due to the motor housing, of the stray flux at lower frequencies.

3.2 Faults simulated in the laboratory

3.2.1 Bearings faults

The bearings of the RAEL motor can be quite easily substituted. In many works the author has changed the bearings (usually the drive end one) with faulty ones. The original bearings mounted on the motor are the 9-balls deep-groove NSK 6205Z. These bearing were substituted in

various works with defected ones, for example the 26-balls double-row SKF 1205ETN9 are used in some works. In particular, localized defects are considered in some works while generalized roughness defects in others.

3.2.2 Partial stator short-circuits

Another fault simulated in the motor is the stator winding partial short circuits. The RAEL motor was manufactured on purpose to partially supply one of the three phase windings in order to simulate a partial stator short circuit.

Three winding points, corresponding to 5%, 10% and 15% of the entire turns of one phase, were made accessible in the terminal box during the construction of the motor. The scheme of the modified winding is shown in Figure 26.

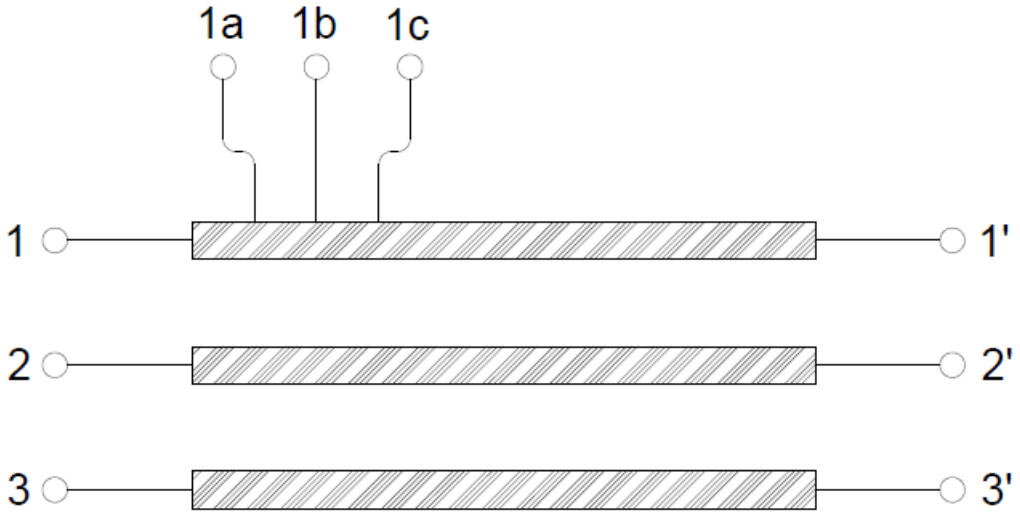

Figure 26: Circuital scheme for the realization of the partial stator short circuits.

When the first phase of the motor is supplied from terminals 1-1', 100% of the turns are supplied, as in the case of a healthy motor, and this condition corresponds to a resistance (measured at terminals 1-1') of 4.09 Ω. When power is supplied from points 1a-1', 5% of the winding turns are bypassed, while when power is supplied from point 1b or 1c, 10% or 15% of the turns are bypassed. The total number of turns in one phase of this motor is 294. So 15, 30 and 45 turns are excluded by feeding the winding from point 1a, 1b and 1c respectively. Table 4 resumes the main conditions of the simulated faults.

Table 4: characteristics of the partially bypassed stator winding

Connection	Number of turns excluded	Number of turns fed	% of the excluded turns	Resistance of the fed winding Ω
1-1’	0	294	0%	4.09
1a-1’	15	279	5%	3.9
1b-1’	30	264	10%	3.76
1c-1’	45	249	15%	3.58

Previous works carried out in the laboratory with these modifications of the winding can be found in [57, 59].

In particular in [59], it has been explained that, when a partial stator short circuit occurs, the current in the shorted turns can be very high and generates heat that degrades rapidly the insulation and leads to a phase to phase or phase to ground fault. In experimental tests, this current is normally limited through the use of external resistances, to not deteriorate the machine. Anyway, with the diagnostic results in [59], in the laboratory, it has been preferred to supply the “faulty” phase simply bypassing a certain percentage of turns (the short-circuit current in this way will not flow). This leads to similar diagnostic results as the rotating field will present in any case negative sequence components due to the imbalance in the magneto-motive force of one phase with respect to the other two.

Moreover, in the author’s opinion, this simulation of partial short-circuit increases the difficulty of detection of the fault. In fact, due to the Faraday-Lenz law, and considering that the shorted turns are a mainly inductive load (they have a resistance but the reactive power is more inductive than capacitive), the effect is to demagnetizing the phase-flux the machine. So, without considering current in the shorted turns, the detection of the fault should be harder; then, if a diagnostic system can diagnose this simulated fault, it diagnoses more easily the same fault considering the current in the shorted turns.

The two schemes considered in [59] are presented in Figure 27; the scheme b) is the one used by the author for the work that will be presented in chapter 4.

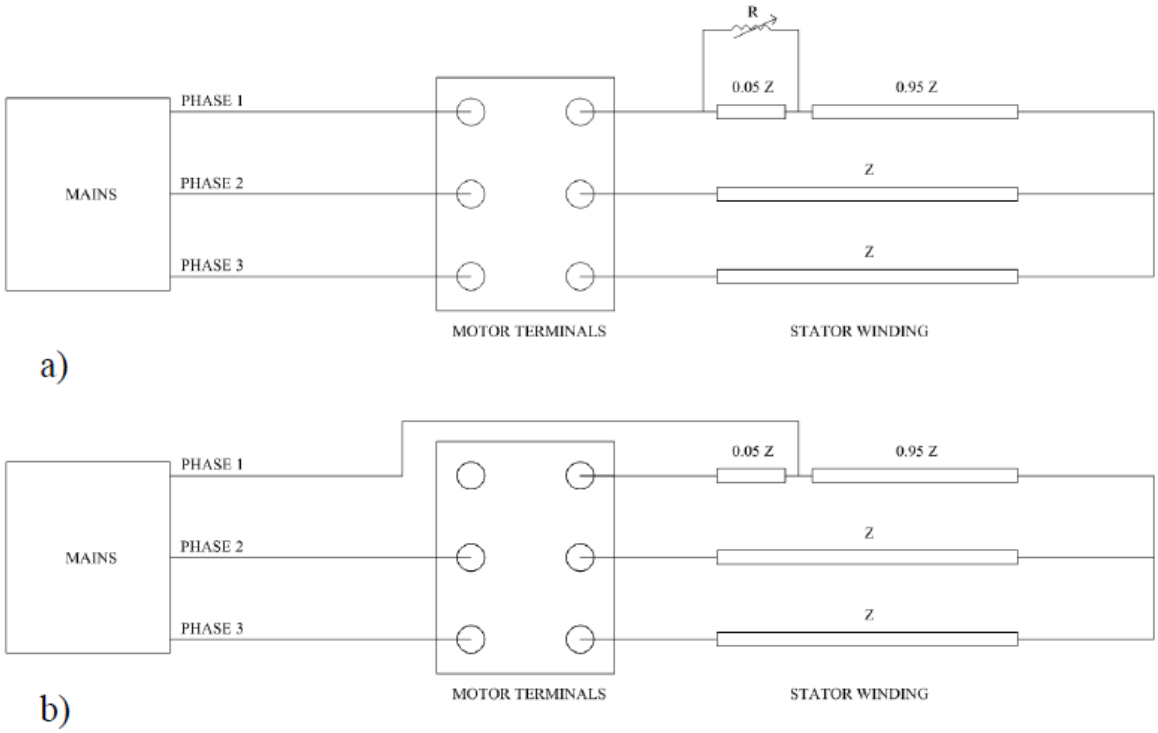

Figure 27: schemes for simulation of the partial stator short circuits. a) considering the current in the shorted turns and b) with no current in the shorted turns [59].

3.2.3 Low Frequency Torque Oscillations

Low Frequency Torque Oscillations (LFTOs) is a condition due to some characteristics of mechanical loads that introduces harmonics in the signal spectra that can lead to misclassification of the faults as described in 2.3.5. This anomaly is simulated in the test bench using a control signal of the brake (signal proportional to the excitation current) composed by a continuous component and a sinusoidal one. This signal is supplied to the DCU of the PB 115 brake through a Digital/Analog Converter (DAC) controlled by LabVIEW software, as it will be described in paragraph 3.3. An example of signal waveform for generating an LFTO, from an outline of the LabVIEW software, is presented in Figure 28; the signal has an amplitude that corresponds to a torque of 6 Nm as mean value, 1 Nm as peak value and a frequency of 4 Hz.

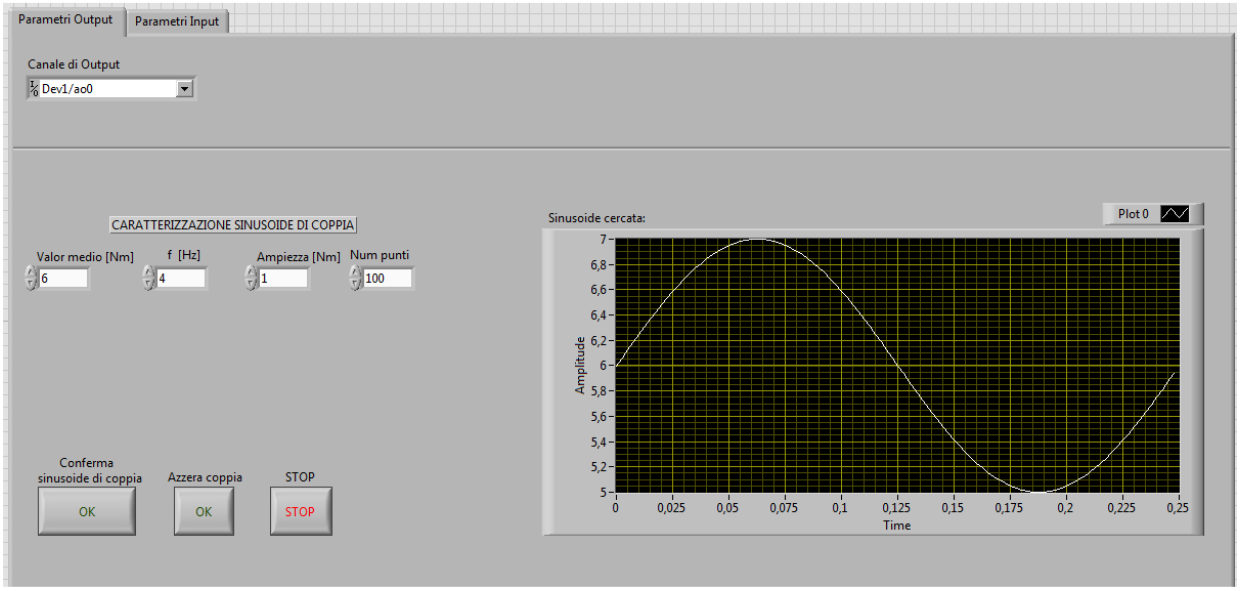

Figure 28: Example of signal waveform, from the LabVIEW software, for generating the LFTO.

3.2.4 Air-gap eccentricity and other mechanical faults

Another fault studied in laboratory is the air-gap eccentricity. Though with the available laboratory equipment is not possible to directly change the eccentricity, with a worn bearing the eccentricity increases and specific fault harmonics could be seen in spectra. Some results will be exposed in the following parts of the thesis.

Misalignment is another fault that can be studied with a few modifications of the test bench set-up. Specifically, by simply inserting shims between the basement of the motor and the foundation, the misalignment could be simulated, albeit in an approximate manner: in fact, the effect would be mitigated in comparison with a real situation, as the elastic joint would dampen the mechanical stresses on the shaft introduced by the fault.

Moreover, a diagnostic signature given by a motor with loosen anchor bolts on the foundation could be another easy-to-implement fault to study.

3.3 Measurement equipment

In this paragraph, the various sensors, measurement instruments and conditioners of the signals used in the works of the author will be presented. The main parts of the measurements equipment are reported in Figure 29.

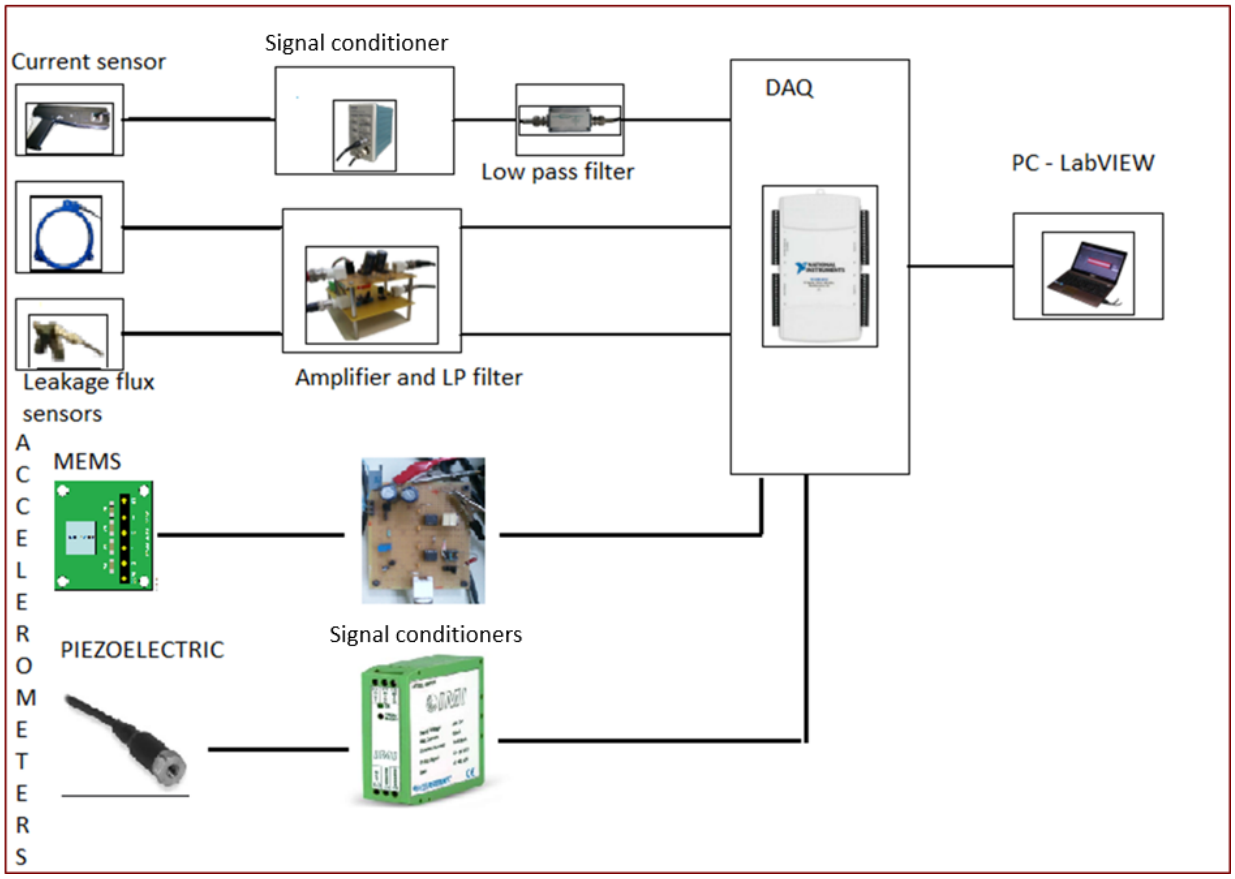

Figure 29: Measurement and acquisition equipment used in the laboratory.

The main components of the acquisition system, presented in Figure 29, are:

- Current and stray flux sensor (electromagnetic signal's sensors)
- MEMS and piezoelectric accelerometers
- Signal conditioners: for alimentation of the probes and filtering the signal
- Low-pass filters: used as antialiasing filters
- Data Acquisition (DAQ) board for the multichannel acquisition
- PC with LabVIEW, to store and elaborate the data.

Other devices are not reported in Figure 29, for example the digital wattmeter and the optical tachymeter. However, they will be described in the next subsections.

3.3.1 Digital wattmeter

A digital three-phase wattmeter is used in the laboratory test bench to monitor the main electrical parameters of the induction motor.

The digital wattmeter used in the tests is branded “Infratek” model “304B”. The wattmeter was used to measure the values of power, voltage, current and power factor, in real time during the tests, to check that the quantities did not exceed the values. Also balancing between phases has been checked during tests. The power equipment of the test bench and the schematic connection of the wattmeter during a test with inverter-fed machine is presented Figure 30.

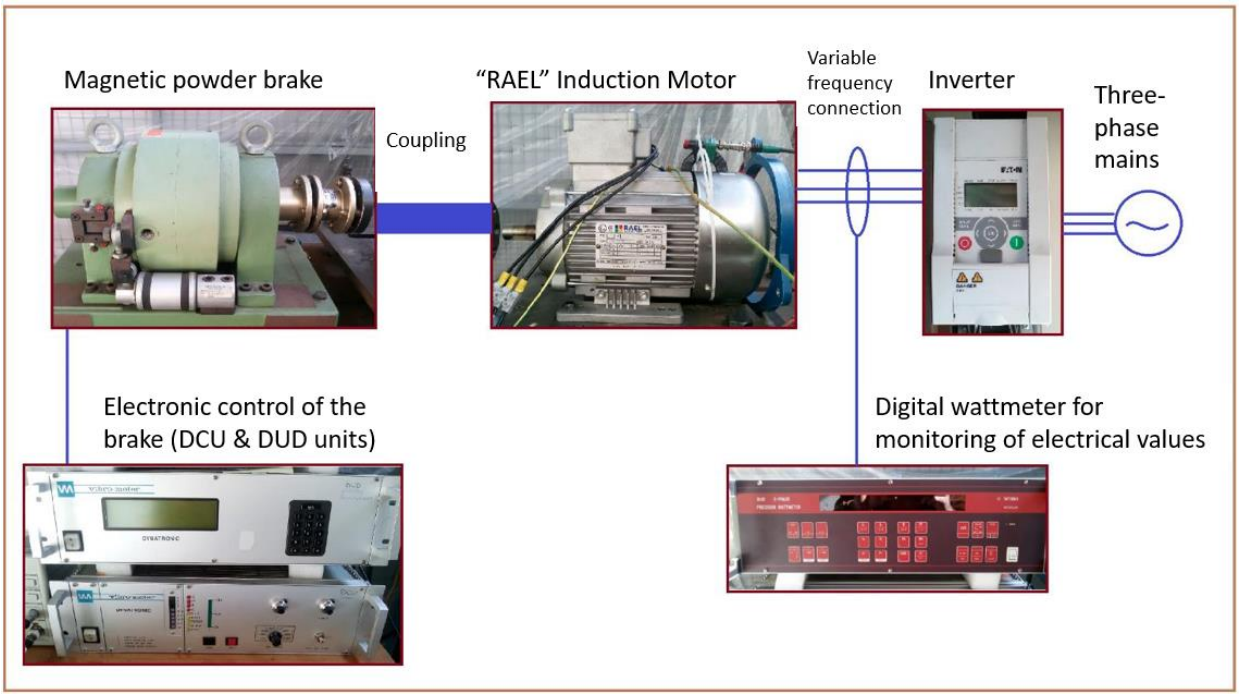

Figure 30: Power equipment of the test bench and schematic wattmeter insertion

The main characteristics of the wattmeter are resumed in Table 5.

Table 5: characteristics of the Infratek wattmeter

Input impedance	10 MΩ 20 pF
Current measurements	
Ranges [A]	0.2 / 0.6 / 2 / 6 / 20
Accuracy (rms value)	± (0.1% reading + 0.1% range)
Accuracy (average value)	± (0.1% reading + 0.2% range)
Voltage measurement	
Ranges [V]	2 / 6 / 20 / 60 / 200 / 600 / 1000
Accuracy (rms value)	± (0.1% reading + 0.1% range)
Accuracy (average value)	± (0.1% reading + 0.2% range)
Power measurement	
Ranges [W]	0.4 - 20000
Accuracy (rms value)	± (0.1% reading + 0.1% range)
Accuracy (average value)	± (0.1% reading + 0.2% range)

3.3.2 Current sensor

The current sensor used is a "Tektronix" brand, model "TCP303". The sensor has a Hall effect and is therefore equipped with a signal conditioning circuit, which amplifies the output signal. Table 6 below shows the main parameters of the Hall effect transducer used.

Table 6: main characteristics of the Hall effect sensor TCP303

Bandwidth (-3 dB)	0 – 50 MHz
Maximum current values (for the chosen conversion factor of 5 A/V)	25 A Direct Current
	17.7 A Alternating current (rms)
	50 A peak value
Typical accuracy	± 1% of reading
Sensitivity	5 mA

Hall effect sensors are able to detect and measure magnetic fields. In this case, the sensor is used to measure a current: it measures the magnetic field generated by a conductor carrying an electric current.

The sensor has the form of a current clamp, i.e. it wraps around the conductor. The sensor has a magnetic core to convoy the flux around the wire and address it on the Hall effect element. So, if this magnetic circuit is not-saturated the flux is proportional to the current wrapped by the sensor and so the reading from the Hall element can be converted into a current reading.

Hall effect sensors are very precise but also sensitive. They require a signal amplification circuit with a high input impedance, and they also need a current supply to operate (they are active sensors). An important advantage of these sensors is that they can be applied using a current clamp, i.e. without having to interrupt the circuit as with a traditional ammeter. Compared with a classic current clamp, which works with a Faraday principle, Hall effect transducers can also measure direct currents.

The amplification and conditioning circuit used for the probe is the "Tektronix" circuit model "TCP A300" specifically designed to work with "Tektronix" probes as the one used for the tests (TCP303).

The possible ranges conversion factors of the amplifier for converting the voltage signal into current values are 1, 5, 10 or 50 A/V. The range used for our test was 5 A/V: an output signal of 1 V peak-to-peak from the amplifier corresponds to a current of 5 A peak-to-peak.

A representation of the signal conditioner connection with two compatible probes is presented in Figure 31.

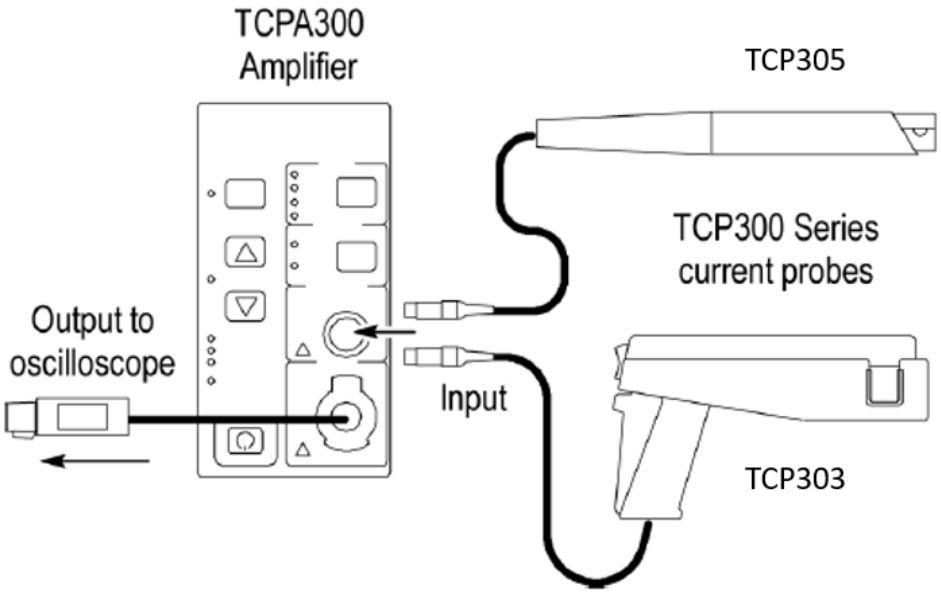

Figure 31: Probe and signal conditioner simplified scheme connection

3.3.3 Low-pass filter for current sensor

A passive single-order low pass filter has been added on the output of the current signal conditioner (as visible in Figure 29) to have a function of antialiasing filter. In fact, with the digital acquisition, alias phenomena can occur and harmonics whose frequency is higher than the Nyquist frequency have to be attenuated. A cut-off frequency of about 2000 Hz was chosen and considered suitable for the bandwidth used in diagnostics of electrical machines. The scheme of the simple passive single-order low pass filter is reported in Figure 32.

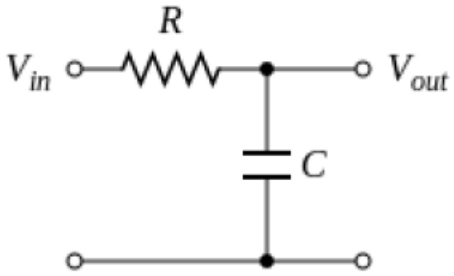

Figure 32: Single order low pass filter, used as antialiasing filter.

The cut-off frequency is given by the formula:

$$f_t = \frac{1}{2\pi RC} \tag{3.1}$$

The considerations for the choice of R and C are the following:

- Fixed the cut-off frequency f_t, too high values of R will correspond to very low values of C in which the parasitic parameters would be too preponderant;
- Alternatively, too low values of R would mean too high current from the power supply circuit upstream of the filter in the measurement chain. Integrated circuits have a maximum deliverable current that is not too high. It is necessary to consult the data-sheets for the choice of resistance and to avoid saturation of the device's output current.

The values chosen are R= 1 kΩ and C= 82 nF resulting in a cut-off frequency f_t of 1940.4 Hz. Ceramic type capacitors have been chosen as they limit the non-linear effect in frequency of the impedance, avoiding the formation of unfavourable current dividers when the capacitor has a grounded pin [62].

3.3.4 Magnetic flux probe Emerson

The magnetic flux is of the type “M 343 F – 1204”, of the brand “Emerson”. The probe consists of a coreless ferromagnetic coil with an internal radius of approximately 10 cm. This probe is the same used in [34], and described in 2.2.3 (Figure 8). The commercial name has been changed probably due to a company fusion/acquisition (from Csi became Emerson).

It is an air-core coil, so maximum linear behaviour is expected especially at not very high frequency. In [34], a frequency response of the probe is performed, showing a linear response at least at frequencies lower than 16 kHz. This range of frequency is considered wide enough to diagnose electrical machines.

The probe is connected to an instrumentation amplifier and a low-pass filter that will be explained in next subsections.

An image of the probe, located on the rear of the motor, is visible in Figure 33. In the figure is visible also the custom made flux-probe (in black) that will be exposed in subsection 3.3.5.

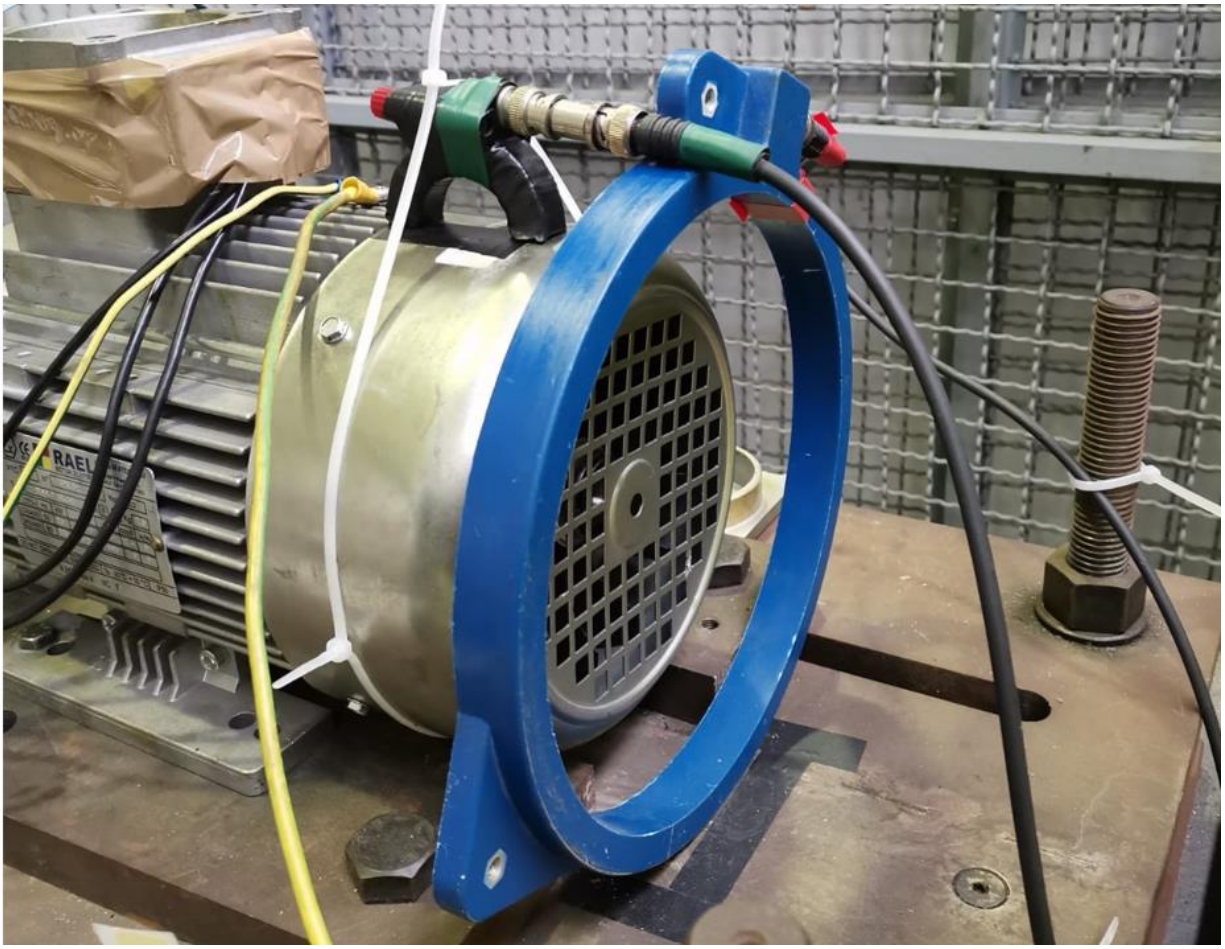

Figure 33: Emerson M 343 F – 1204, on the rear of the RAEL induction motor

3.3.5 Custom flux-probe

For the detection of radial stray flux, a custom flux probe with ferromagnetic ferrite core was constructed for conducting previous experimental works in the laboratory, e.g. [59]. The probe has a semi-circular shape with square cross section, as shown in Figure 34; the probe with its location used in the works described in this thesis is visible also in Figure 33.

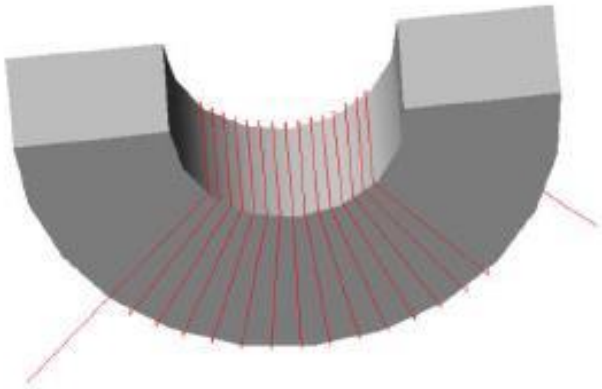

Figure 34: Construction rendering of the custom flux-probe.

The magnetic core is wound with approximately 300 turns of enamelled copper wire with a diameter of 0.112 mm. This custom probe, thanks to its magnetic core, is able to provide higher voltage values than the Emerson probe at the same density of linked magnetic flux [60]. A defect is the loss of linearity above a certain frequency level. However, it is shown in [60] that in the useful frequency band (50-1000 Hz) both probes behave linearly as illustrated in Figure 35.

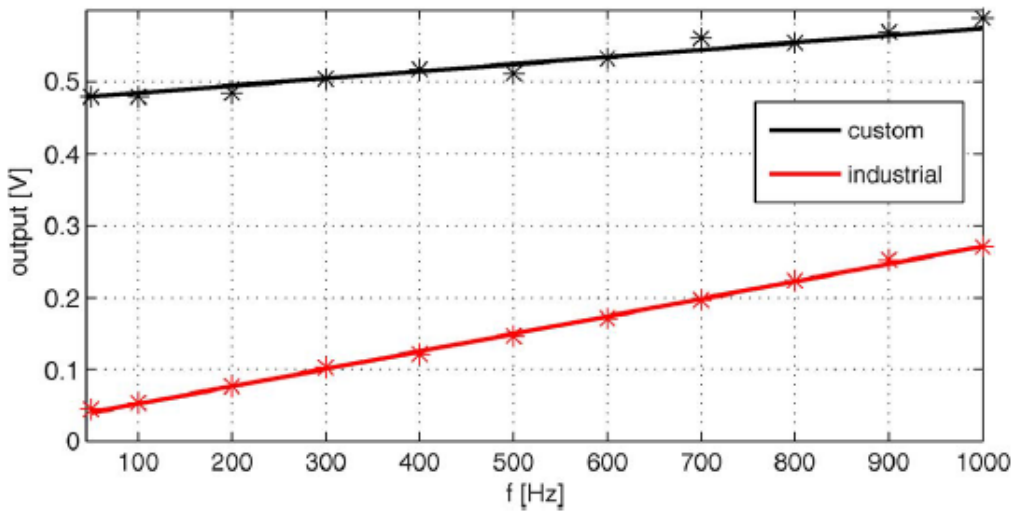

Figure 35: Frequency response of the Emerson (here called "industrial") and custom flux probes [60].

The custom flux sensor generates a signal with an intensity that is highly dependent on the position of the sensor in relation to the motor, on the load condition of the motor and also the type of motor (e.g. explosion-proof motors are better shielded from stray fluxes due to the greater thickness of the frame). Typical values range from 5 mV for a 300 W motor to 100 mV for the 1.5 kW motor under consideration [61]. The internal resistance of the probe is 30.2 Ω [62].

3.3.6 Signal conditioners for the flux probes

The signals from the flux probes are amplified with an instrumentation amplifier, and low-pass filtered with a filter identical to that presented in 3.3.3 subsection (one amplifier and one filter have been constructed for each of the flux signal).

The amplifier used is an OpAmp "INA128" configured as an instrumentation amplifier: it has a very high input impedance (10 GΩ), and a bandwidth of 100 kHz. The supply of this Integrated Circuit (IC) is given by two 9 V batteries, in order to lower the floor noise and making the instrument portable. The gain of the amplifier is adjustable changing an external resistance R_g, and it is given by the formula:

$$G = 1 + \frac{50\ k\Omega}{R_g} \tag{3.2}$$

In all the works carried out by the author the signal has been amplified with a chosen R_g of 1 kΩ, i.e. with a gain of 51. However, in other works performed in the laboratory, on different motors, the gain of the amplifier of the radial flux has been reduced because the signal reached the saturation.

The level of the signals downstream the amplifiers, and in input to the DAQ board are maintained approximately in the range of ± 10 V peak-to-peak.

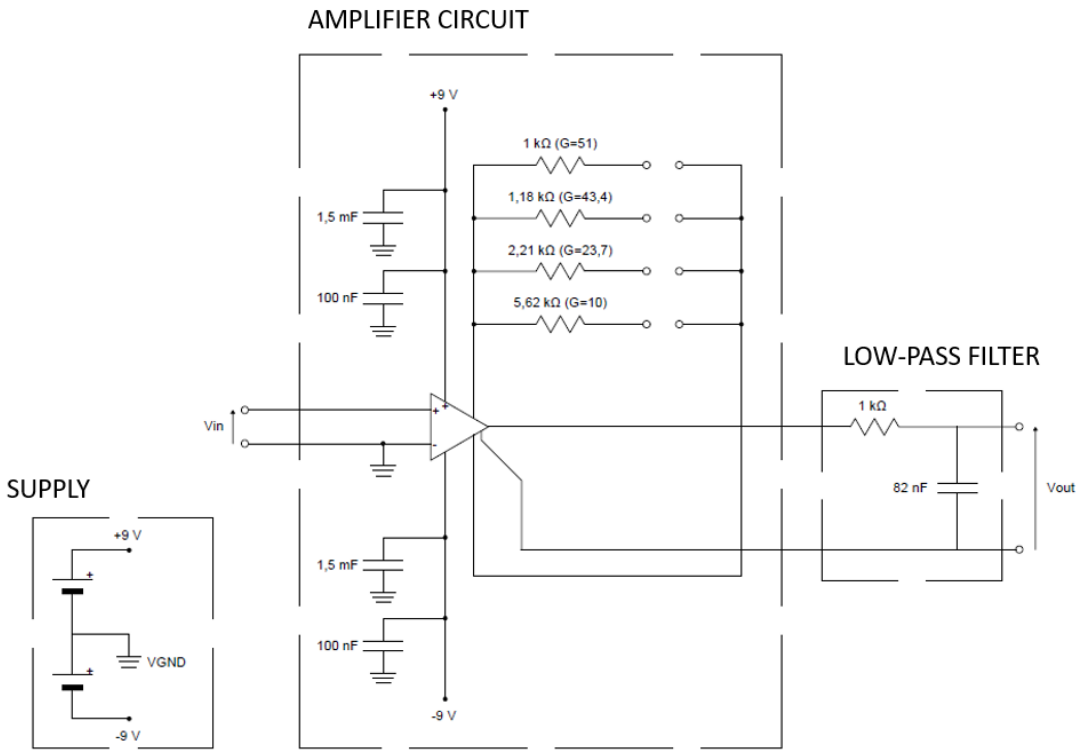

Figure 36: Amplification and filtering process for the axial and radial flux signals.

3.3.7 MEMS accelerometer with signal conditioner

One of the used accelerometers is the ADXL335 accelerometer from Analog Devices, which is very compact, capacitive MEMS, tri-axial with a voltage output. It measures accelerations with a minimum full scale range of ± 3 g. It can measure static gravity acceleration and dynamic acceleration such as motion, shock or vibration and continuous acceleration (it is used in smartphones as a "gravimeter").

The designer can select the bandwidth of the accelerometer channels choosing the values of the capacitors C_X, C_Y and C_Z at pins X_{OUT}, Y_{OUT} and Z_{OUT}, where the "X, Y, Z" nomenclature indicate the axis of the measurement.

The measurement bandwidth can be selected according to the application in the ranges of approximately 0 to 1600 Hz for the X and Y axis and approximately 0 to 550 Hz for the Z axis. Operating on a single 1.8÷3.6 V supply, the ADXL335 consumes 350 µA, and is available in a 16-pin package. Table 7 shows the main characteristics for typical parameters of Ta = 25°C, V_S = 3 V, $C_X = C_Y = C_Z$ = 0.1 µF, acceleration = 0 g, unless otherwise specified.

Table 7: Main characteristics of the ADXL335 accelerometer

Parameters	**Minimum**	**Maximum**	**Measurement unit**
Measurement range	-3	+3	g
Non linearity % of complete scale	-0.3	+0.3	%
Sensitivity of the 3 axes	270	330	mV/g
Noise axes X and Y	150		µg/Hz rms
Noise on axis Z	300		µg/Hz rms
Frequency response for X and Y	0.5	1600	Hz
Frequency response for Z	0.5	550	Hz
Resonance frequency	5.5		kHz
Supply voltage	1.8	3.6	V
Current absorption	350		µA
Working temperature	-40	+85	°C

The MEMS accelerometer was bought on a pre-soldered "EVAL-ADXL335Z" evaluation board. The standard C_X and C_Y capacitors were 100 nF but were changed to 3.3 nF to increase the system bandwidth from 50 Hz (factory setting of the test board) to about 1500 Hz, more useful for our purposes.

In fact, the bandwidth is calculated with the following formula:

$$f_{BW} = \frac{1}{2\pi(32k\Omega)C_{(X,Y,Z)}} \tag{3.3}$$

where 32 $k\Omega$ is the output resistance of the axis channel and $C_{(X,Y,Z)}$ is the external capacitor to be changed to reach the desired bandwidth. The working scheme of the accelerometer is reported in Figure 37, in which the location and connection of the external capacitors can be seen.

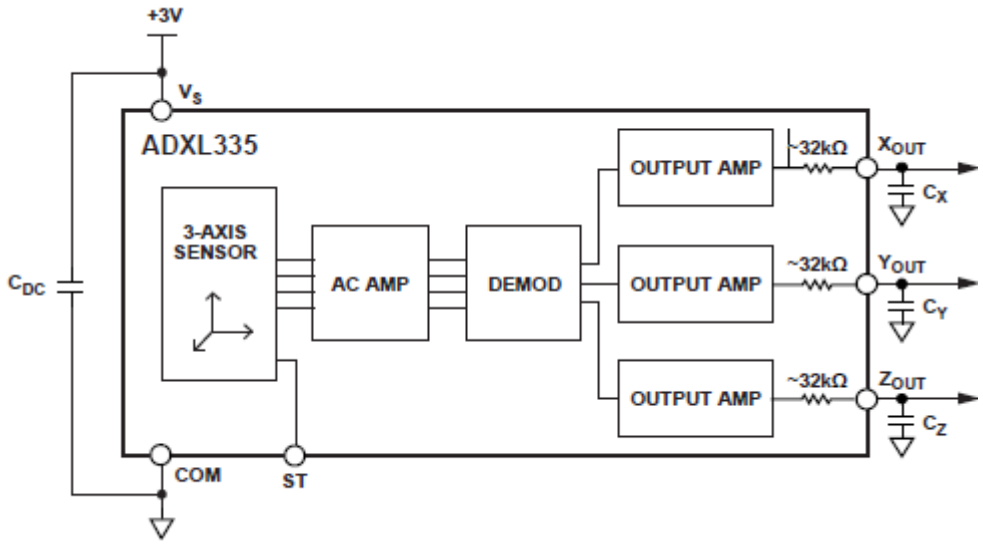

Figure 37: Working scheme of the ADXL 335 accelerometer

A custom signal conditioner has been constructed on a PCB board in previous works for conditioning the MEMS signal, in particular:

- An input buffer is used to increase the input impedance of the circuit;
- A high-pass filter is used to remove the continuous component of the signal, since the sensor is used to measure alternating signals (vibrations);
- An instrumentation amplifier is used to adapt the amplitude of the signal to a range similar with the other sensor used (almost all the other sensors used have an amplification stadium) to do better acquisition with the DAQ board;
- A regulated voltage supplier is included in the board to supply the MEMS element.

The scheme of the custom signal conditioner is reported in Figure 38.

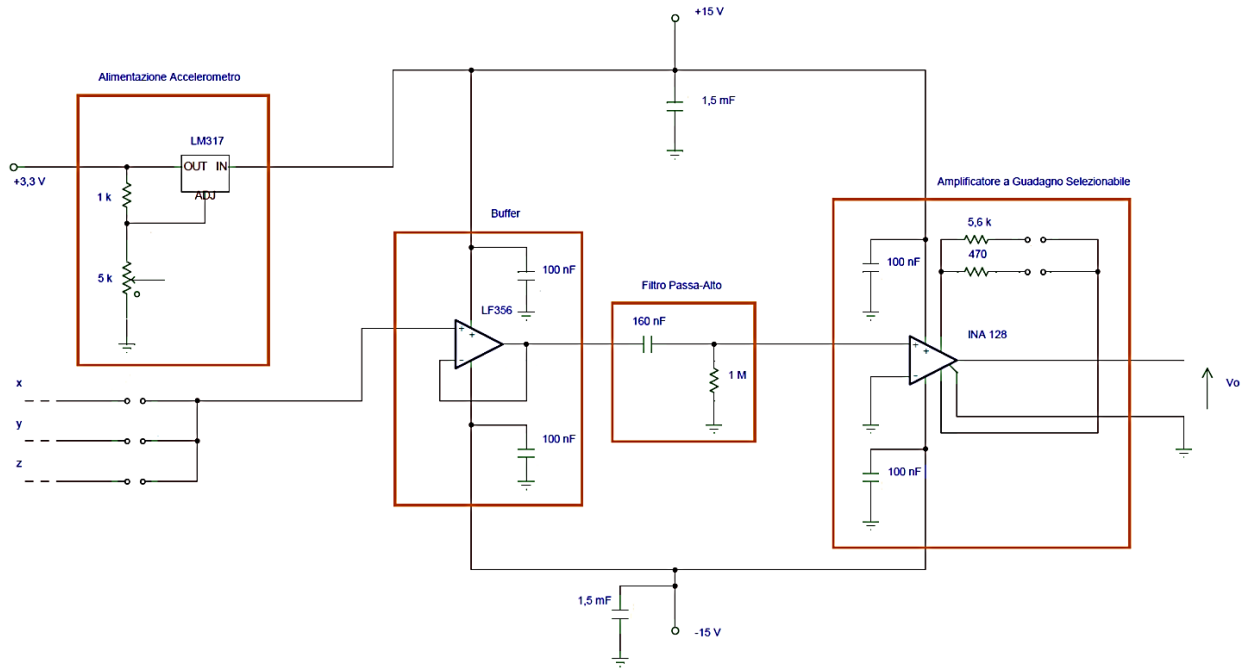

Figure 38: Custom signal conditioner for the MEMS accelerometer.

The instrumentation amplifier is the same used for the amplification of the flux signals described in 3.3.6. However, the selected R_g for the determination of the amplifier gain is in this case of 3.3 kΩ, giving a gain of the amplifier of 16.2.

The conversion factor between the acceleration values (measured in g) and the output signal from the amplifier can be found multiplying the sensitivity of the sensor (given in Table 7) by the amplification gain:

$$Conv_{factor} = Sens \cdot Gain \tag{3.4}$$

So, assuming a mean sensitivity of the sensor of 0.3 V/g and the gain of 16.2 of the amplifier, the conversion factor is 4.86 V/g.

This means that an amplified output-signal of 4.86 V peak-to-peak corresponds to an acceleration of 1 g peak-peak.

3.3.8 Piezoelectric accelerometer

An accelerometer branded PCB “PIEZOTRONICS” Model M608A11 single-axis, IEPE-type piezoelectric, has been used for some of the works carried out by the author. The choice of using a piezoelectric accelerometer is mainly due to its much wider measurement bandwidth with respect of the MEMS accelerometer (10 kHz versus 1.6 kHz).

An IEPE sensor (integrated Electronic Piezo-Electric) is a piezoelectric transducer with an integrated charge amplifier and impedance converter. The integration of the amplifier into the sensor itself greatly reduces the overall noise of the sensor. The supply current of the IEPE sensor is a constant current, while the output signal is an AC signal placed on the supply DC voltage or bias voltage. This configuration allows a two-wire cable to carry both the power and the sensor signal. Due to the presence of DC bias, the signal is typically AC-coupled to the interface circuit. To perform these operations on the signal (AC-coupling and constant current supply) it has been used a “PCB” model 682A02 signal conditioner, powered by two 9 V batteries in dual configuration. The signal conditioner performs also the amplification of the output signal with three different gains: 1X, 10X and 100X. However, the amplification has not been used in many measurements by the authors to not introduce noise in the signal and save batteries charge.

The accelerometer has been fixed through screw and stud mount. A representation of the sensor and its location on the machine is visible in Figure 39.

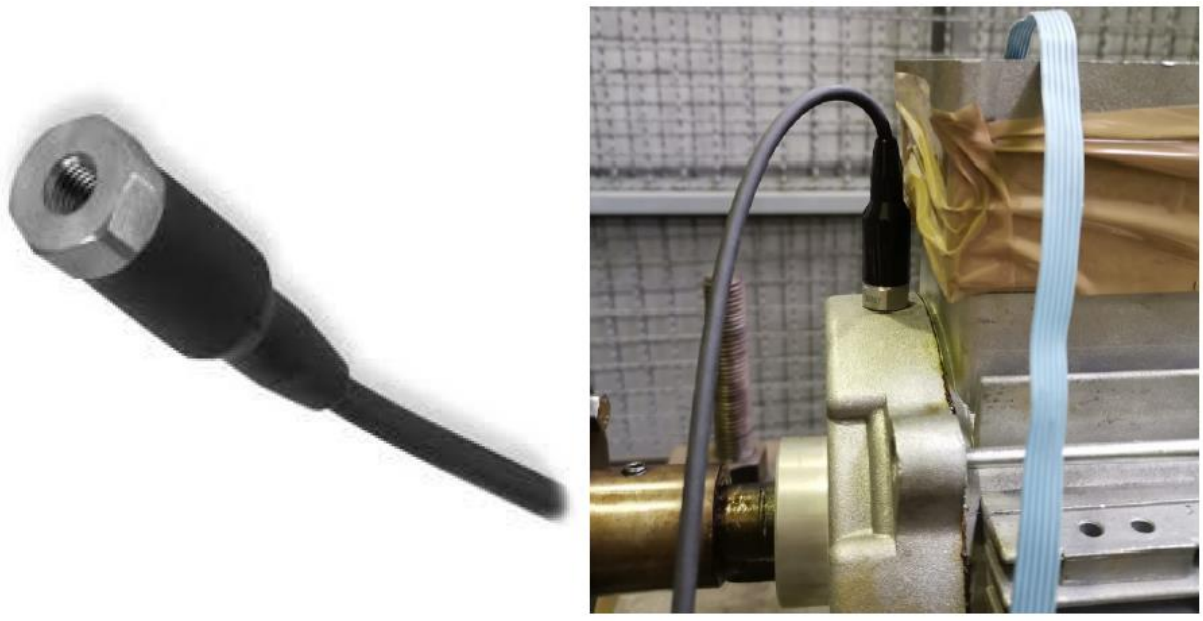

Figure 39: Accelerometer M608A11 and its position on the motor under test.

The main parameters of the accelerometer are reported in Table 8.

Table 8: Characteristics of the piezoelectric accelerometer PCB M608A11

Parameters	**Minimum**	**Maximum**	**Measurement unit**
Measuring range	-50	+50	g
Sensitivity (±15%)	100		mV/g
Frequency response (±3 dB)	0.5	10000	Hz
Resonance frequency	22		kHz
Bandwidth resolution (1 to 10000 Hz)	350		µg
Non-linearity % of the full scale	-1	+1	%
Temperature range	-54	+121	°C
Protection class	IP68		
Voltage supply	18	28	V
Current supply	2	20	mA
Output impedance	<150		Ω
Output voltage	8	12	V
Noise (10 Hz)	8		µg/Hz
Noise (100 Hz)	5		µg/Hz
Noise (1 kHz)	4		µg/Hz
Electrical insulation of the housing	>100000000		Ω

It can be noted that the sensitivity of the piezoelectric sensor is lower than the MEMS one (confronting Table 7 with Table 8); in fact, piezoelectric sensor's sensitivity is 0.1 V/g versus 0.3 V/g of the MEMS. However, the bandwidth is higher for the piezoelectric sensor and this is an indispensable feature to apply techniques such as envelope analysis explained for example in [29].

3.3.9 Data Acquisition Board (DAQ)

The DAQ board used in the laboratory is the "NI USB-6212" acquisition board from "National Instruments"; the board is visible in Figure 40, together with a plastic box used in the laboratory as mechanical protection. The board used allows easy interfacing with the PC, through the LabVIEW software, installed on the computer, also from "National Instruments" brand. The main task of a DAQ board is to convert an analogue signal into a digital one, to be acquired by a digital device, e.g. a personal computer. The DAQ can be called also Analogue-to-Digital

Converter (ADC), though sometimes it can give also an analogue output from a digital input, i.e. the reverse process (as in the case of the NI USB-6212, which includes two analogue outputs).

Figure 40: NI USB 6212 DAQ board and plastic case protection used.

The basic parameters that characterise the DAQ board are: resolution, measurement range, gain, sampling rate and filters.

- Acquisition resolution: this is defined as the greatest change that can be made to the input signal without giving rise to any variation in the output; it depends on the number of converter bits;
- measuring range: defined by the minimum and maximum voltage values allowed in input by the card; by modifying the input range, it is possible to adapt the range of the board to the range of the signal, thus guaranteeing the highest possible resolution;
- gain: it indicates an operation of amplification or attenuation of the signal before it is digitised; the aim is, as previously specified, to adapt the input signal levels to the input range of the board;
- sampling frequency: this is the fundamental parameter that characterises A/D conversion and is defined as the number of samples per second of an analogue signal stored in digital form (expressed in hertz). A high sampling frequency provides a better representation of the original signal than a lower one. All input values must be sampled at a sufficiently high frequency to adequately represent the analogue signal. Too low sampling frequency can result in a poor representation of the signal due to aliasing. According to Nyquist's Sampling

Theorem, in fact, to convert a signal without loss of information, it is necessary to sample uniformly (samples equidistant from each other) and with a frequency at least double the bandwidth of the signal of interest;

- filters: before being converted into a digital signal, the analogue signal in general is subject to degradation due to the presence of noise, the source of which can have the most varied origin. The antialiasing and other filters can sometimes be included in the DAQ board.

The main characteristics of the DAQ board are resumed in the next Table 9.

Table 9: Main characteristics of the NI USB 6212 DAQ board.

Number of Analogue Inputs	16 (configuration single ended) 8 (configuration differential)
Number of Analogue outputs	2
ADC Resolution	N=16 bits
Sampling rate	400 kS/s max
Input range	±10 V, ±5 V, ±1 V, ±0.1 V
Uncertainty at full scale (range = ±10 V)	2710 μV
Sensitivity (range = ±10 V)	118.0 μV
Resolution (range = ±10 V)	320 μV

It has to be noted that the declared resolution is very close but different from the value calculated with formula (2.6). This could be because of differences of definition (some free configurations of the converter are used for the auto-calibration process) or actual range values definitions (it is actually admitted to measure voltages between ±10.4 V). However, with formula (2.6) one can calculate at least a first approximation of the resolution of the ADC (305 μV calculated with (2.6) versus 320 μV declared).

The board is multichannel, so it is possible to acquire different channels simultaneously, thanks to a multiplexer included in the block chain. This component switches from one channel to another and take the instantaneous data, that will be amplified by the Programmable Gain Instrument Amplifier (PGIA) and converted by the Analogue-to-Digital converter. Data will be stored in memory registers of type First In First Out (FIFO) and then will be sent in the digital form to the computer. The working scheme of the DAQ is presented in Figure 41.

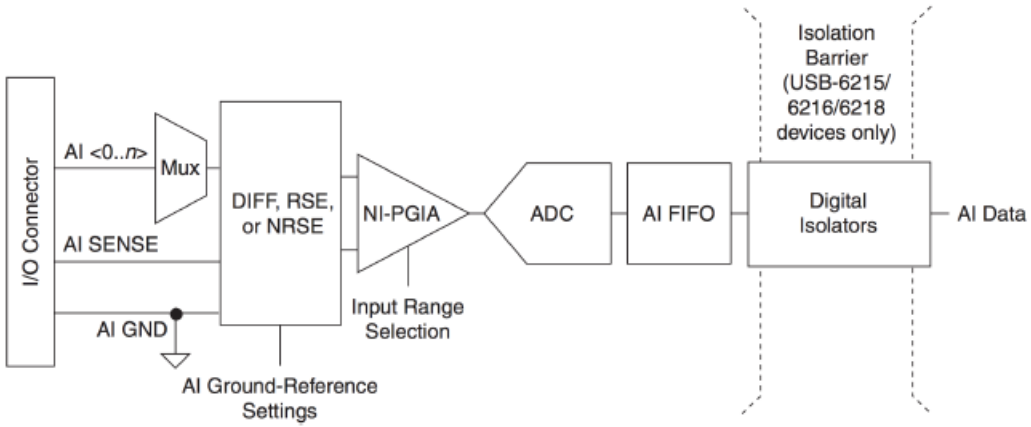

Figure 41: working scheme of the DAQ process in NI USB-6212.

Another important feature of the NI USB-6212 DAQ board is the input signal configuration. The signal connection can be single-ended when only the non-inverting input voltage of the signal is amplified and differential when the voltage difference between the two inputs is amplified. The differential configuration guarantees a better Common Mode Rejection Ratio (CMRR), i.e. it reduces the noise that is common in both the amplifier's inputs. The source of the signal can be of two types: floating or ground–referenced. The manual of NI USB-6212 recommends some types of connection according to the type of source. With a ground-referenced source more attention has to pay to prevent the ground-loop phenomenon: if both the source and one of the amplifier inputs are grounded, a loop is formed, and for the Faraday law a variation to the linked flux with the loop (e.g. magnetic flux generated in the ambient by others electric appliances) will generate a noise *e.m.f.* (often a 50Hz hum) that will be read by the device.

The signal configurations recommended by the DAQ manual are visible in the next Figure 42.

All the sources used in the laboratory are floating. The signal configuration used is the Non-Referenced Single Ended (NRSE) for all the probes (and related signal conditioners) except for the piezoelectric accelerometer. In the latter case, in fact, it has been chosen to not amplify the signal with signal conditioner and to use a differential input configuration to lower as possible the noise.

In fact, according to the DAQ manual, all the signals with voltage greater than 1 V and cable length lower than 3 m (as in the case of all the amplified signals in the laboratory) can be acquired with the NRSE configuration, while those with amplitude < 1 V (as the piezoelectric non-amplified signal) and cable length higher than 3 m have to be acquired with a differential configuration.

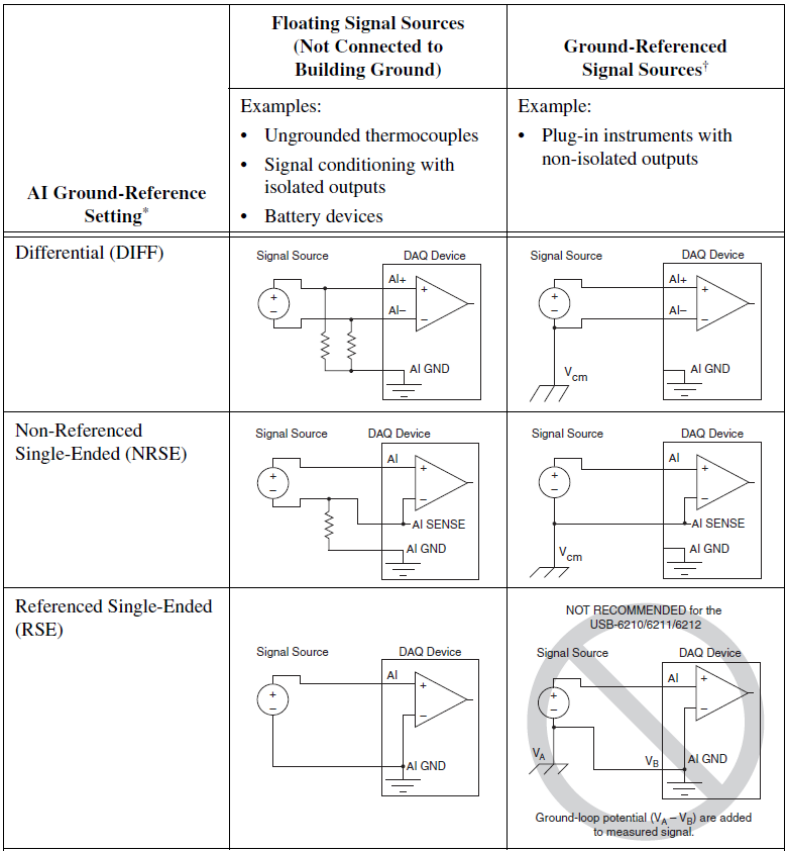

Figure 42: Analog Input Configurations for NI USB-6212

3.3.10 Optical tachometer

A digital laser tachometer (speedometer) marked Xinbaokeyi, model DT2236B, was used to measure the rotational speed of the machine. Moreover, to set the motor at the same load at each test, the tachometer has been used to measure speed as a reference value (because it is directly proportional to the slip and so to the load, in a non-controlled machine, in a stable working region).

The working principle of the tachometer is the following: it emits a laser which, reflected with a certain frequency by a reflecting element placed on the shaft, gives an indication of the motor's rotation speed. Figure 43 shows the tachometer used and Table 10 reports an extract from the datasheet.

Figure 43: Optical tachometer.

Table 10: Characteristics of the tachometer

Measurement range	5-99,999 [rpm]
Measuring distance	max 2[m]
Resolution (< 1000 rpm)	0.1[rpm]
Resolution (> 1000 rpm)	1 [rpm]
Accuracy	±0.05%+1dgt

3.3.11 Thermal imaging camera

Though no scientific work has been presented by the author using or including data from the thermal imaging camera, the camera can be a precious instrument to evaluate the health state of a machine. For example, it is known from literature [63] that a bearing fault can be detected using thermal data; however, it is not easy to know the temperature threshold beyond which the bearing can be considered faulty, because this can depend on ambient temperature and on the load of the machine and so on the heat generated by the machine.

Anyway, some temperature limits cannot be overcome because of the presence of the lubricant, that cannot reach very high temperatures. So a temperature measurement through thermal imaging camera can give at least a first "rough" diagnostics of the machine.

In the laboratory, a FLIR "E30" model thermal imaging camera was used to measure the temperature of certain parts of the electric motor. The main data of this thermal imaging camera are shown in Table 11.

Table 11: Data sheet of the "FLIR E30" thermal imaging camera.

Image resolution	19200 pixels (160x120)
Minimum focal length	0.4 m
Minimum sensitivity in the image	<0.1°C @ 30°C / 100 mK
Measurable temperature range	-20÷120°C
Measurement accuracy	±2°C or 2% reading
Degree of protection	IP 54

An example of thermal image of the RAEL motor, with a faulty bearing (localized fault: a crack in the outer ring) taken with the FLIR E30 is reported in Figure 44. As discussed previously, without any baseline reference it is difficult to determine whether the bearing is faulty or not. Anyway, in the case presented in Figure 44 the bearing zone reach the maximum temperature in the image range (about 46° C), so it can be assumed that the bearing is not working in its optimal conditions.

Figure 44: Thermal image of the RAEL motor with a faulty bearing in the drive-end side.

3.4 Magnetic hysteresis brake test bench

As briefly discussed in the introduction of this chapter, a new test bench has been bought and mounted in the laboratory in the last few months of the three-year doctorate of the candidate.

The candidate actively collaborated in the choice of the equipment, its installation and its commissioning.

The test bench has a magnetic hysteresis brake. The hysteresis machines can work both as motors and brakes/generators, basing their working principle on the magnetic hysteresis cycle to generate torque.

These machine generally have a rotor constructed with hard or semi-hard magnetic steel. Starting with a motor operation to give a principle explanation, a simple machine with cylindrical rotor and "classical" distributed stator winding can be considered. On the stator, a magnetic rotating field is generated through polyphase windings. The stator magneto-motive force (*m.m.f.*) magnetizes the hard magnetic steel of the rotor as the stator windings are energised. A magnetic field in the rotor is so produced. Due to hysteresis process, the revolution of the stator field is followed by the rotor magnetic axis with a lag angle δ dependent only on the hysteresis cycle of the material constituting the rotor. It can be demonstrated that in this acceleration phase (there is some slip, the rotor is rotating at lower speed than the stator field) the lag angle will keep a constant value. Because the torque is proportional to the stator *m.m.f* multiplied by the rotor flux and the sine of the angle between them (δ), it comes out that with a constant magnetizing flux (from the stator) the torque is constant in all the acceleration process [64].

The machine after reaching synchronism with the stator field, modified its working angle δ according to the mechanical load applied. So, with a constant torque characteristic over speed (also at standstill), the machine can be used for accelerating high inertia load till the synchronous rotational speed. The operation is very smooth as no slots are present on the rotor (small machines of this kind can be found in audio recorder-tape). The machine however does not have high efficiency and has a low power factor, so it can be used only in low-power applications. More information can be found in [64]. More recent interesting applications of hysteresis machines are presented for example in [65].

The brake bought for the laboratory, namely AHB-24 from "Magtrol" company, has a "cup" shaped rotor and a stator with a single and fixed excitation winding. When the winding is excited with a DC-current, a static field magnetizes the rotor material. Due to hysteresis process, with a constant excitation current, a constant torque characteristic is produced by the brake. The brake works in a reverse mode of an accelerating hysteresis motor (δ angle remains constant), because the synchronous operating mode in this case is not possible as in the stator is present only one fixed winding.

The heat generated by the hysteresis process in the brake (equal to the mechanical power input given by the motor under test) has to be removed to avoid high temperatures, that could demagnetize the brake. In the case of the AHB-24, compressed air is used as cooling mean. A scheme of the construction of the machine, from the Magtrol manual, available online, is visible in Figure 45.

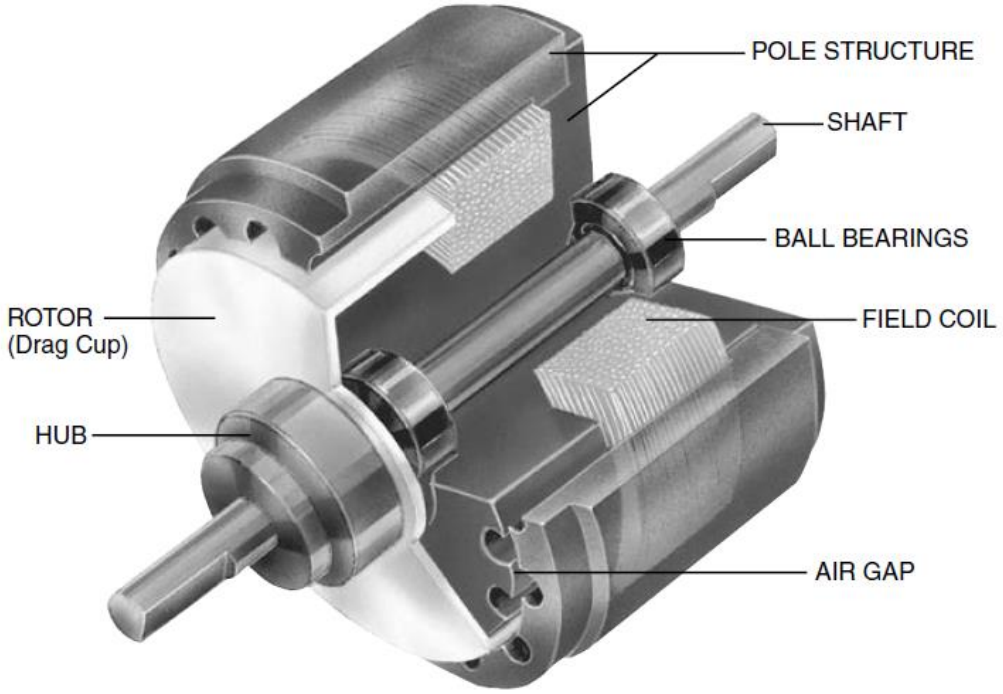

Figure 45: Construction components of the Magtrol AHB-24

The main characteristics of the AHB-24 are resumed in Table 12.

Table 12: Characteristics of the AHB-24

MINIMUM TORQUE AT RATED CURRENT (Nm)		24.0
RATED CURRENT (mA)		2400
RESISTANCE±10% @ 25°C (Ω)		10
VOLTAGE (Vdc)		24
EXCITATION POWER (W)		57.6
MAXIMUM SPEED (RPM)		12,000
AIR SUPPLY PRESSURE (kPa)		620±35
AIR CONSUMPTION (l/min)		567
KINETIC POWER RATINGS	5 MINUTE (W)	5,300
	CONTINUOUS (W)	3,000
DE-ENERGIZED DRAG TORQUE @ 1000 RPM (Nm)		$1.36 \cdot 10^{-1}$
EXTERNAL INERTIA (kg cm^2)		$1.12 \cdot 10^2$
TORQUE TO INERTIA RATIO (rad/s^2)		2,140

The excitation current is fed to the brake through a DC-power supply connected to a current-regulated supplier, to give constant current independent of the winding resistance that changes with the temperature. The current supplier can be controlled with an input signal (±10 V) that can be generated for example with the DAQ board.

With respect to the magnetic-powder brake presented in 3.1 (Table 1), the hysteresis brake has a very low de-energised drag torque, and higher maximum speed, though the maximum torque and power dissipated are lower.

Along with the hysteresis brake a torque transducer has been bought to be interposed between the motor and brake. The torque transducer, namely Magtrol TS 109, can measure a nominal torque of 20 Nm with a nominal speed of 8,000 rpm. The transducer has a digital output (USB) and an analogue one. The TS109 can be easily interconnected to a PC and data can be visualized and stored with a provided software with USB connection. With the analogue connection it is possible to acquire data at higher sampling frequency. Along with the torque signal, speed and power signals are measured with this transducer.

The test bench with some of the sensors previously introduced and the RAEL motor is visible in Figure 46.

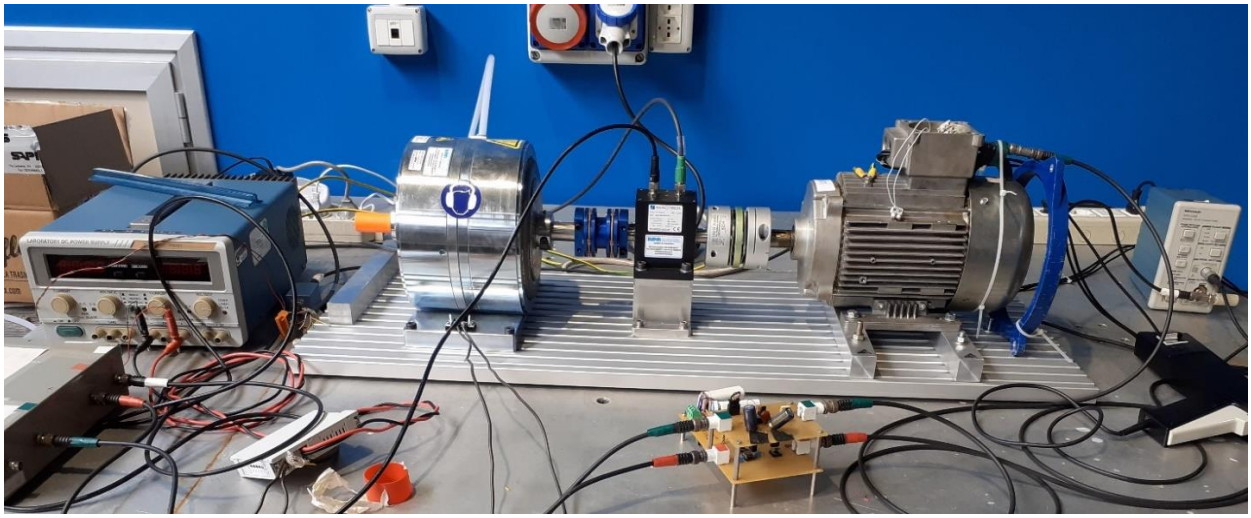

Figure 46: The new test bench with the AHB-24 brake and TS 109 torque transducer with the RAEL motor under test.

4 Multiple faults detection in electrical machines

4.1 Introduction

In this chapter, an evaluation of the multiple fault diagnostics techniques will be presented. In the first instance, a literature review regarding the issue will be exposed. Successively, a scientific work carried out by the candidate and his research group on this subject will be presented. The work has been published at SDEMPED conference, held in Toulouse, France, in 2019. The reference for this work is the [66].

The work has been carried out in the laboratory of "Diagnostics and Design of electrical machines" of the University of Pavia, with the main characteristics exposed in chapter 3. Results of the paper and perspectives for the future works on the topic of the multiple faults diagnostics in electrical machines will be exposed.

4.2 State of the art

As already described in chapter 2, the most prominent faults in induction machines are stator short circuits and bearing faults. However, the percentage incidence of the various faults changes with the size of the machines. In fact, bearing faults are the most prominent in small machines at low rated voltage (< 690 V), stator and bearing fault have more or less the same incidence on medium power/medium voltage machines, and stator faults are the most prominent in high power/high voltage machines [67]. The situation is represented in the next Figure 47.

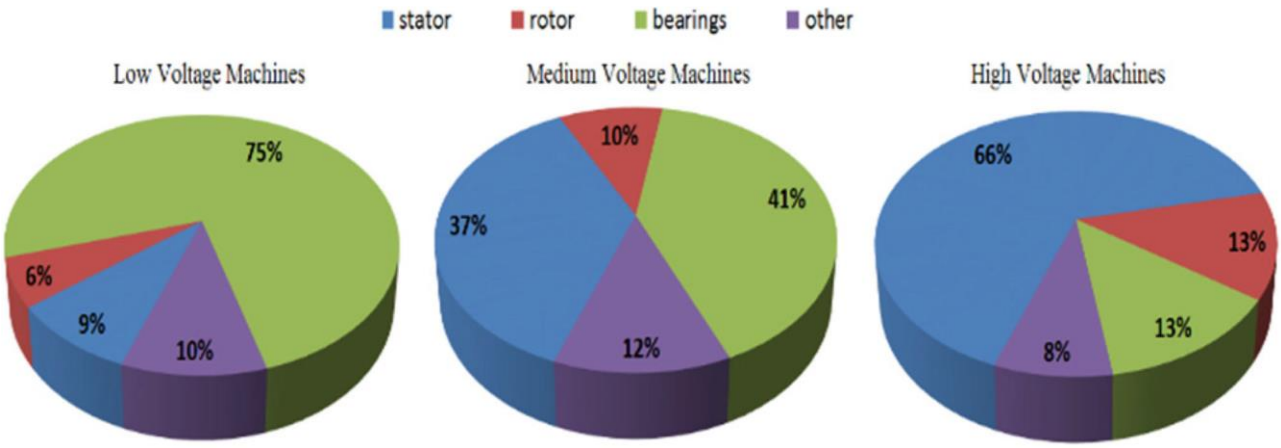

Figure 47: Distribution of machine faults depending on the machine voltage [67].

The main reason why the high power machines suffer less of bearing faults is because often they use sleeve bearings that reduce the mechanical wear present in rolling element bearings [67]. Always according to [67], [23], and many others papers, despite the more prominent faults are on stator and bearings components, the majority of papers concentrate on rotor defects such as broken rotor bars, rotor end-ring faults or eccentricity. In fact, consolidated techniques have been developed for detecting this kind of faults (especially with MCSA); conversely, for detecting stator incipient short circuits (inter-turn short circuits) or bearings faults, real consolidated techniques do not yet exist, and advanced signal processing or identifications through machine learning are often used [68]. The main reasons of this difficulty in detecting stator short circuits or bearing faults is exposed in the following.

Inter-turn stator short circuits (ITSC) or inter-coil short circuits (ICSC), in general denominated stator short circuits (SSC), are faults that quickly develop into a much more serious condition of phase to phase short circuit or phase to ground short circuit. This is true especially for mains-fed low-voltage machines. In fact, they need sensible condition monitoring systems, to quickly detect the defect in its early stage, and the monitoring systems have to be continuous (CCM, Continuous Condition Monitoring). Moreover, for FFT-based diagnostic systems, a high frequency resolution of the spectra can be required to recognize the fault. But, to have a high resolution, a high acquisition time is necessary, as resumed in (2.1). So a trade-off between resolution and acquisition time should be made because in a time comparable to the acquisition time the fault could be already developed in a more serious condition [69],[70]. Also in [67], the difficulties of the detection of these faults and the unreliability of many methods developed by researchers in real industrial applications are discussed. A method based on the Extended Park Vector Approach (EPVA) on current and stray flux signals is then proposed to detect these faults also in a low-severity level state.

So in general the detection of SSC is costly because of the reasons exposed and is used only on highly relevant or strategic machines, as insulation degradation monitoring through PDA (Partial Discharge Analysis) for medium or high voltage machines [69]. In fact, for medium or high voltage machines or even for low-voltage inverter-fed ones [71], not specifically the stator defects, but the insulation condition monitoring can be carried out through the PDA in the dielectric via different techniques. This gives an analysis of the degree of aging of the dielectric materials and can prevent the occurrence of stator short circuits. Anyway this topic is not treated in detail in this thesis.

Bearings faults are the most common fault in small machines reaching a percentage of 60-90% [69]. The bearing fault detection has been studied in deep especially through the vibration signature analysis (MVSA, Motor Vibration Signature Analysis). Many results are reported and branches of the MVSA such as envelope spectrum analysis demonstrated to be very effective [29]. Anyway, the MVSA requires sensors (accelerometers) to be installed permanently on the machine (for continuous condition monitoring) or requires the access to the machine for temporary

measurements (off-line monitoring). This fact is often undesirable, especially when current or voltage sensors are already installed for other purposes such as the control of the machine [69]. Anyway, diagnosing with the current signal can lead to some difficulties e.g. in case of variable-speed drives or when a supply unbalance occurs. This latter condition can be classified as double fault or double anomaly condition. The former condition has been studied by many authors but requires advanced digital signal processing techniques because of the number of harmonics induced in the spectra by the drive. Advanced techniques in bearing faults recognition with stator current signal are so necessary due to its low signal to noise ratio as already discussed in 2.3.4.

In this chapter multiple faults are considered as the main research interest. First of all, it has to be said that the topic of multiple faults is not wide covered in the literature. In fact, though many articles treat of multiple fault detection systems, these faults are often not diagnosed simultaneously. These systems are so able to identify different kinds of faults, but one by one. Anyway, sometimes the faults can appear simultaneously and the characteristic frequencies of one can hide those of a second fault; in fact, the characteristic frequencies can coincide as for example for Unbalanced Voltage Supply (UVS) and SSC [72]. This could lead to a stop of the machine for maintenance but without actually repair completely the machine since not all the faults were recognized but only one.

Some papers deal with the issue and present detection systems considered under simultaneous faults. For example, [73] considers SSC and bearing faults in the outer and inner ring simultaneously studying the vibration signal (MVSA). In particular, the severity levels of the SSC are of 1%, 2%, 3%, 4%, 5% for each phase, levels that are considered to be difficult to detect in the literature. The inner and the outer bearing faults are manufactured by drilling one hole in the respective rings. These two faults are tested one by one in simultaneous presence with the SSCs. Vibration signal is studied, with a particular signal processing: a Normalized Least Mean Square (NLMS) adaptive filter has been used to remove the noise signal. The signal is then band-pass filtered to focus on the fault characteristic frequencies. An envelope analysis is carried out and then Hilbert transform is used to demodulate the signal. Finally, FFT is applied to the envelope analysis to extrapolate the fault frequencies. In particular the presence of rotational frequency f_r and its multiples harmonics is checked in the spectra for the SSC while the BPFO and BPFI harmonics presence is checked for the bearing faults. SSC and one of the bearing faults can be detected simultaneously, though the fault harmonics of the bearing modify the amplitudes of the SSC harmonics. A scheme of the signal processing techniques used in [73] is reported Figure 48.

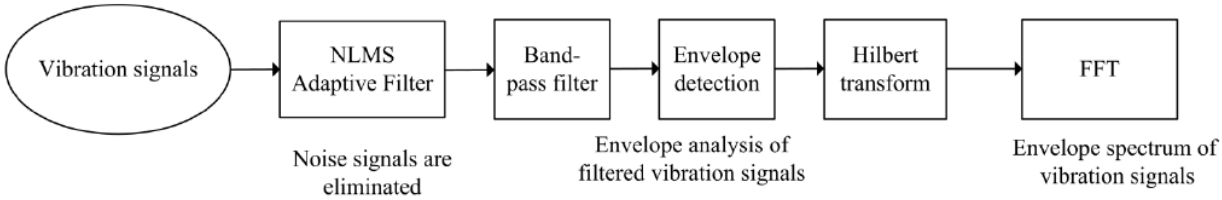

Figure 48: Flow diagram for signal processing used in [73].

In [74], a MCSA technique is used to detect multiple faults, load anomalies and mains supply abnormal conditions simultaneously present in the machine. In fact, for a three-phase induction motor the following conditions are considered: normal healthy operation, broken rotor bars, SSC, UVS, and the abnormal behaviour of the mechanical load (load torque fluctuations). In this case, bearing faults with their low Signal-to-Noise ratio are not considered. Moreover, the inverter-supply is not evaluated. Anyway, the implemented system diagnosed the faults in the conditions described also in a simultaneous presence, though results are better in a fully-loaded machine than in a slightly-loaded one.

In [75], multiple fault conditions, due to broken rotor bars, shaft misalignment and mechanical unbalance are considered. The work uses information entropy analysis as indicator of the multiple faults. Moreover, the machine is considered at three different rotational speeds: it has been fed by an Adjustable Speed Drive (ASD) to simulate a common practice in industry in which the motors are often inverter-fed. The electronic drive introduces harmonics into the current supply signal and this interferes with the detection of some faults. Information entropy has been used by the authors as single parameter for the fault detection by examining the information of steady current signal of one-phase of the machine. Moreover, the proposed algorithm is implemented into a Field Programmable Gate Array (FPGA) device to offer a portable low-cost solution, suitable for real-time online condition monitoring. In fact, the entropy definition used in the work is a simplified expression suitable for FPGA. The motor is fed at 30, 40 and 50 Hz; mean $\mu(H)$ and standard deviation $\sigma(H)$ are performed on 20 trials for each operating condition, identifying the detectability region into a $\pm 3\ \sigma$ region.

Faults in [75] are recognized, though results are better at low supply frequencies of 30 and 40 Hz since at 50 Hz the detectability of unbalance and misalignment decreases because a small overlapping of the $\pm 3\ \sigma$ region of the entropy measurements of the faults occurs. Some results are exposed in Figure 49. Anyway, also in this work the faults are not considered in a simultaneous presence.

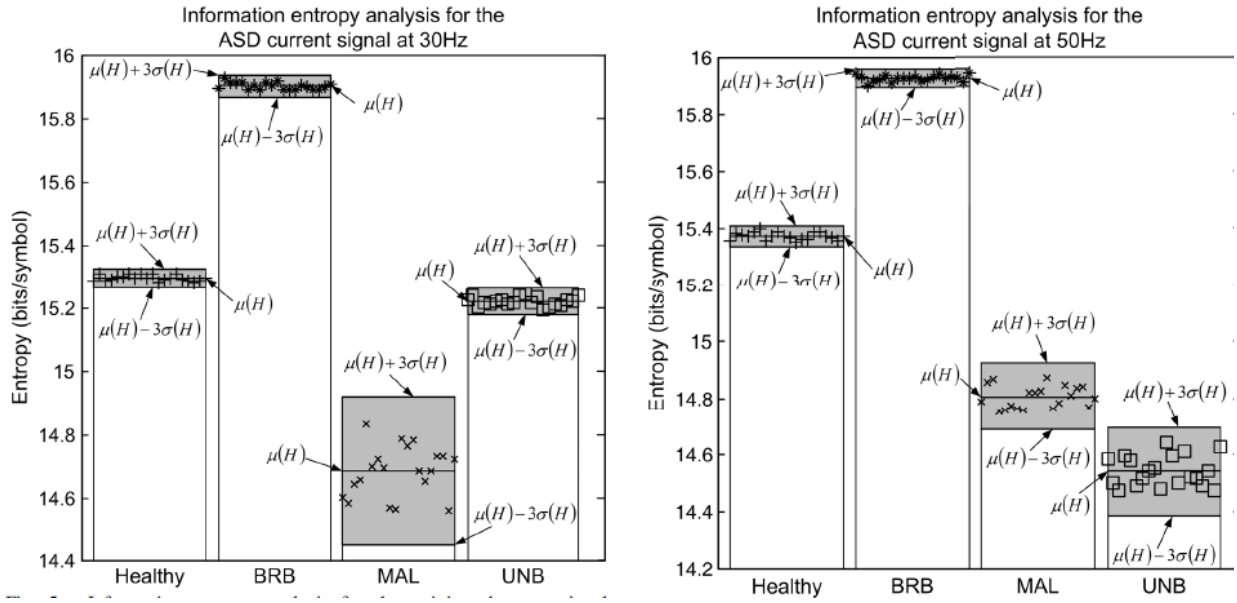

a) b)

Figure 49: Information entropy analysis for detecting the operational condition of an induction machine with: a) 30 Hz; b) 50 Hz supply frequency controlled by an ASD [75].

In many other works, decision process is carried out through the use of machine learning/artificial neural network techniques.

For example, in [76], an interesting study has been carried out on multiple faults detection also in simultaneous presence. SSC, outer-ring bearing defect and gearbox defect are diagnosed in a variable speed powertrain through a multi-sensor scheme with neural network classifiers. In fact, vibration signal and current signal are acquired to diagnose the faults. Thanks to the use of an encoder, a constant angle sampling technique is performed to treat the variable signals as stationary (also with a variable frequency the constant-angle sampled signal look like a constant frequency signal). The Park transform is applied on the three phase currents and the frequency of $2f_s$ of the Park's vector is tracked to detect the SSCs. Vibration characteristics frequencies BPFO and gear frequencies are checked on spectra, to diagnose these faults.

Three different classifiers are used, one for each fault. These classifiers are of type Convolutional Neural Network (CNN), usually used for image classification problems. The images in fact are generated by the pre-processing transformation through Short Time Fourier Transform (STFT) techniques, suitable to analyse transient signals. The images from vibration and Park's vector are merged and combined into lager images; this fact provides an enlargement in the feature space. CNN classifiers are then trained with these combined images. In particular, for the training process, only single fault signals are taken separately and fed to the network of interest; this means that Classifier 1 (C1) is trained for SSC, Classifier 2 (C2) for bearing faults and

Classifier 3 (C3) for gear faults. After the training process, anyway, the validation process is carried out on both single or simultaneous faults.

Results are very good for single fault classifications, but the efficiency decreases with multiple faults. This confirm the difficulties in diagnosing the condition of simultaneous faults. Anyway, results are still acceptable with classification accuracy always higher than 70%. The bearing defect remains the most difficult to classify. Moreover, in the opinion of the authors, more studies can be carried out implementing different severity of the faults and reducing the ratio of the SSC from 10% of the total winding impedance to lower values (that increase the difficulty for detection). A block diagram of the proposed fault diagnosis system is reported in Figure 50.

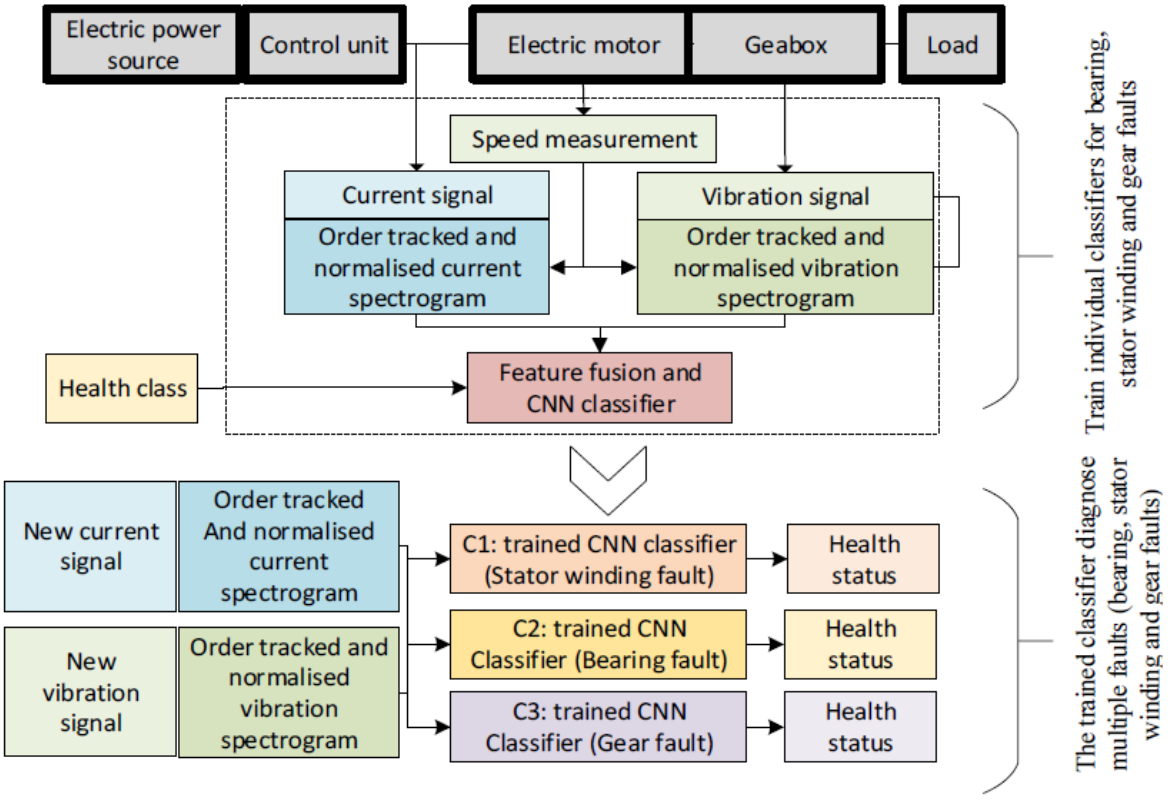

Figure 50. Block diagram of the fault diagnosis system proposed in [76].

Others works that treat of multiple fault, though in a non-simultaneous presence, and use machine learning based techniques for classification are [77], [78], [79].

In [77], five motor conditions are evaluated: healthy, faulty bearing, eccentricity, stator winding fault and broken rotor bar. These conditions have been tested on a motor at three different loads and at three rotational speeds, by measuring the stator current. A one class and a two class support vector machine (SVM) were trained and tested and their performances have been compared. Wavelets transforms are used as pre-processing of the training process. The aim of the work is to employ in industry a one class SVM using healthy data only. In fact, this could have important consequences as faulty data are difficult to collect for safety reasons and for the

difficulty to have data for each severity and type of fault. The data collected on field are mainly from healthy condition. Usually researchers use faulty data from laboratory tests (ad-hoc or accelerated wear introduced faults) that can be slightly different from the actual faults on the field. The results of [77] show that two-class classification SVM gives better results but this is because it has the double of the training data. While one-class SVM combined with wavelets gives lower classification Balanced Error Rate (BER) (a metrics used for measuring the performance of the classifiers), it gives in any case acceptable results, opening the way, according to the opinion of the candidate, for other interesting research works in this field.

In [78], a time domain diagnosis of multiple faults in a Three-phase Induction Motor (TIM) is presented. The approach used is to discretize the time-domain voltage and current signals into vectors to be fed into three different intelligent classifiers: artificial neural network of type multilayer perceptron (ANN/MLP), k-nearest neighbour algorithm (k-NN) and support vector machine with sequential minimal optimization (SVM/SMO).

The searched faults are: stator short-circuit, broken rotor bars and bearing defects. Moreover, the 750 W motor has been driven under varied load and unbalanced voltage conditions. Different statistical indices were used to evaluate the performances of the different classifiers: accuracy, Kappa, mean absolute error and relative absolute error. Classification accuracy above 89% are reached with MLP ad *k*-NN classifiers. While the MLP and SVM/SMO classifiers reach the best behaviour when the minimum number of input values was used.

In [79], four different motor health states (misalignment, unbalanced rotor, bearing damage and healthy status) at variable operating conditions (in terms of supply frequency and load torque) have been classified by means of a SVMs which uses information from radial vibration and stator current.

The work states that mixing vibration data with electrical data increases the detectability of the faults. Moreover, in the electrical variables, one-phase current signal is used for a MCSA representation and Clarke-vector from the transform of all the three current phases to increase the data features. A total of six distinctive features are extracted from the power spectra of these signals. Six different SVMs are implemented for each feature, to perform features fusion. Finally, a one-against-one procedure is used to distinguish the state of the machine.

In the work, the faults of unbalance and misalignment generated features that could not be separated in the features maps using only the Clarke vector and the phase current features; adding vibration feature it has been possible to distinguish these faults, justifying the increase of the cost of the measurement system.

The authors state that the proposed method could be implemented also for bigger machines (in the tests, authors have used a 2-pole, 375 W rated IM) as the diagnosis features did not depend on the power rating of the IM. As drawback, authors recognize the difficulty to extend the

algorithm to the classification of more faults, since in this case the number of the features and SVMs will have to increase.

4.3 Proposed method

A comparative method between diagnostic signatures in frequency domain has been used to diagnose different kinds of faults in a single or simultaneous presence. The faults considered are the partial Stator Short Circuits (SSCs), generalized roughness type bearing faults, and the inherent air-gap eccentricity of the induction machine. Moreover, the progression of the fault is considered for both the SSCs and the bearing faults. The inverter has been used to fed the machine. All the components used are those described in paragraph 3.1.

The approach to the problem consists of taking the acquisition of the electromagnetic signals and perform Fourier transform evaluating the presence of the fault characteristic harmonics in the spectra. The spectra are compared between them: many harmonics have been taken into account using the integer coefficients into the formula, checking for the presence of characteristic harmonics in the range from 0 to 2000 Hz, a quite wide frequency range for diagnostic purposes. Harmonics amplitudes are so checked, a statistical threshold has been used, and the harmonics that exceed this threshold has been counted for each case analysed.

To reduce as much as possible the harmonic distortion and the noise coming from the inverter, two main strategies have been adopted. First of all, the inverter introduces significant sideband harmonic components around multiples of its switching frequency (i.e. in this case 6 kHz), up to a multiple of ten. The sampling frequency of the electromagnetic signals has been chosen taking into account of this fact: since non-negligible amplitude harmonics could appear till 10 times the inverter switching frequency, it has been chosen to sampling the signals with a frequency 20 times bigger than the switching frequency. This lead to a sampling frequency of 120 kHz, that for Nyquist theorem can reconstruct a signal till 60 kHz that is exactly the frequency limit in which significant harmonics due to the electronic commutation could appear.

The second strategy used to remove the signal is the use of some signal processing techniques. A statiscally resonable number of acquisitions (40) with quite good resolution has been acquired and then mean of the spectra is performed. The threshold used to check harmonics takes into account that the actual amplitude is a mean of the single harmonics amplitude, and a t-student distribution is assumed. Frequency range windows are used to check the fault harmonics (that can slightly change their frequencies due to slight variation of load or supply frequency). Finally, an Infinite Impulse Response (IIR) Butterworth low-pass filter is used to better study the harmonics spectra in the 0-2000 Hz.

4.4 The experimental tests

The induction machine used is the RAEL induction motor, presented in paragraph 3.1, a 4 poles machine of 1.5 kW rated power, which has been fed with the MMX34AA5D6F0-0 voltage source inverter.

The stator short circuit faults have been simulated with 3 different severity levels by-passing 5%, 10% or 15% of the total turns of a stator phase winding, as described in 2.3.3.

The bearing faults considered are the generalized roughness defects. The bearings used are the NSK 6205Z for the healthy condition (healthy baseline), while for the faulty conditions the SKF 1205ETN9 has been used. The NSK bearing is the original bearing mounted on the motor; it is a standard single-crown, with N = 9, d ≅ 7.9 mm, external diameter of 52 mm and internal diameter of 25 mm. The SKF 1205ETN9 has been mounted on the motor to simulate the fault. Only this bearing has been substituted to carry out the faulty tests. The faulty bearing has been inserted, in the various tests, in the drive-end of the motor. The main characteristics of the bearing SKF 1205ETN9 are: outside diameter 52 mm; inside diameter 25 mm; 13 balls for each race, for a total of N = 26; D = 39.06 mm; d = 7.45 mm, $\alpha = 0$.

While the former bearing is a single row deep-groove sealed ball bearing, the latter is a not sealed double row ball bearing. This bearing has been chosen for the experiment because of its ~~the~~ ease of opening and disassembling. In fact, all the balls have been extracted from the SKF 1205ETN9, degreased and put into an acid solution. The acid solution is composed of 5 ml of concentrated sulphuric acid (96%) diluted in 50 ml of water. Two severity levels ("steps") are considered in this experiment:

- Step 1: represents an early wear stage of the bearing. The balls were immersed for 30 minutes in the acid solution;
- Step 2: represents an advanced wear stage of the bearing. The balls were immersed for 70 minutes in the acid solution;

It has to be noted that this kind of fault is considered in the literature as particularly hard to detect, especially in early severity stages and without the measurement of the vibration. An image of the balls of the bearing that have been put into the acid solution compared with a new ball is visible in Figure 51.

Figure 51: A new bearing ball compared with step 1 and step 2 worn balls (respectively from left to right).

The motor has been tested in total 9 times in condition of healthy machine, single fault i.e. bearings faults (BF) or double faults (BF and SSCs). The next Table 13 resumes the combinations of faults considered, the nomenclature used and the number of the acquisitions taken each case (recordings) on which more details will be given in the following of this paragraph.

The experimental tests have been carried out in a condition close to the no-load: the magnetic powder brake PB115 is coupled to the motor with the lamellar joint, but it is de-energized. Only the drag torque of about 2 Nm or less is so applied to the motor.

Table 13: List and characteristics of the cases analysed.

Case	Level of BF	% of SSC	Recordings
Healthy	without fault	without short circuit	40
Step 1	Step 1	without short circuit	40
Step 2	Step 2	without short circuit	40
Step 1_SC5%	Step 1	5% inter-turns	40
Step 2_SC5%	Step 2	5% inter-turns	40
Step 1_SC10%	Step 1	10% inter-turns	40
Step 2_SC10%	Step 2	10% inter-turns	40
Step 1_SC15%	Step 1	15% inter-turns	40
Step 2_SC15%	Step 2	15% inter-turns	40

For each experimental test, three variables have been measured in a synchronous way through the DAQ board:

i) the current of one phase, by means of the Hall effect commercial probe (Tektronix TCP305), with the hardware filtering stage and a TCP305A amplifier. The phase which is measured is different from the phase in which the short circuit is applied; in fact, as stated in 2.2.1 the phase on which the measurement occur can be any of

the three phase since the asymmetry induced by the fault in the rotating magnetic field will link all the three phases.

ii) the axial stray flux, by means of a commercial probe (Emerson M-343F-1204), in frontal position, on the fan side of the motor; this signal will be called in the following “Emerson flux” or axial flux.

iii) the radial stray flux, by means of a custom probe, positioned on the body of the motor in a longitudinal direction and close to the fan-end of the motor; this flux signal, though it contains both radial and axial stray flux (because of the probe orientation and vicinity to the end-winding of the machine) will be called “radial flux” or “custom flux”.

The position of both the flux probes can be seen in Figure 33.

Both the signals of stray flux were adequately hardware filtered (low pass filter at cut-frequency of 2000 Hz) and amplified as described in 3.3.6. In each test the fundamental frequency is fixed on the inverter command to 50 Hz. The acquisition parameters are: number of samples = 2^{20} = 1048576, acquisition frequency = 120 kHz, acquisition time = 8.73 s, number of acquisitions = 40. The acquisition time of the whole set is 40·8.73 = 349 s ≃ 6 minutes. Note that a number of samples equal to a power of 2 is chosen (2^{20}), in order to optimize the FFT results. The sets are divided into 40 acquisitions to not generate very big data files, difficult to treat.

4.5 Analysis of the experimental results

While the recordings are gathered by means of a LabVIEW program connected with the acquisition board NI USB-6212, the analysis of the data is achieved with MATLAB.

The data were stored in .lvm format by the acquisition program; each acquisition has a different file, with a total of 40 files for each set of acquisition regarding each of the 9 cases analysed (see Table 13). The main steps of the MATLAB programs, after importing the data, are the comparison analyses in the frequency domain between different cases:

i) the healthy baseline has been compared by itself;

ii) the faulty acquisitions are compared to the baseline;

iii) the faulty acquisitions are compared to a different faulty case (denominated “faulty baseline”).

The baseline of the motor is generally given by the spectra of its signals in healthy condition. In this work, the healthy baseline is collected at no-load, without any fault on the stator

winding and on the bearings. The healthy baseline has been acquired using the healthy bearings NSK 6205Z on the non-drive end and the SKF 1205ETN9 on the drive end of the motor. Successively also faulty baseline will be used in this work to study the progression of the fault as it will be explained in the following.

The digital processing of each signal is realized in the following main steps (note that the signal has been low-pass filtered before the acquisition, to avoid the aliasing phenomenon):

i) multiplication of a windowing function (e.g. the Hann function) by the signal in the time domain;
ii) application of the Butterworth low-pass filter to the signal;
iii) computation of the FFT transformation;
iv) subdivision of the spectrum of the signal into discrete windows. Capture of the maximum value (peaks) of the spectrum for each window;
v) comparison of the magnitudes of the excited harmonics of the faulty cases with the baselines.

The windowing of a signal as explained in 2.2.1 is used to reduce the leakage effect in the spectra. A Hann window has been chosen for this purpose.

For the digital filtering, a IIR Butterworth filter is chosen, with cut-off frequency fc = 2000 Hz and order 10. This filter is selected to have the maximum flatness of the response in the pass band region. The phase of the signal could vary in the pass band region but in this work the phase has not been considered. An example of the digitally low-pass filtered signal (radial stray flux in time domain) is reported Figure 52.

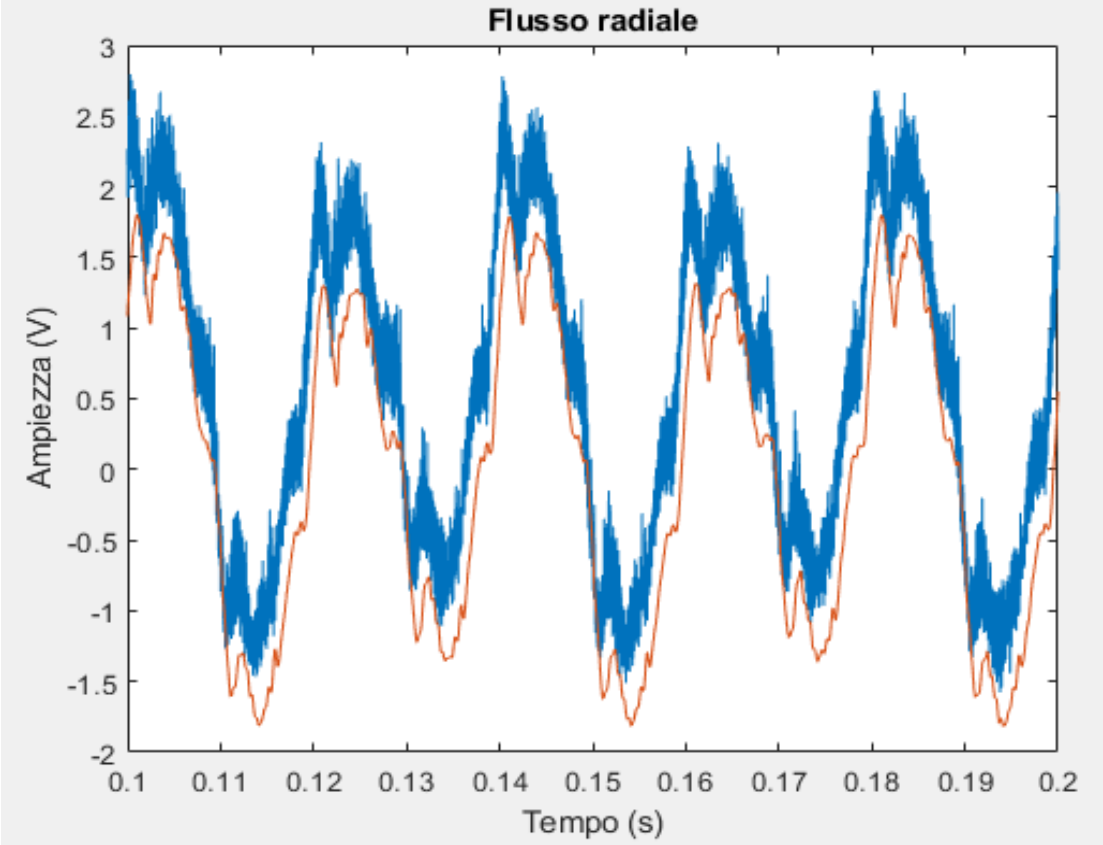

Figure 52: Radial stray flux signal, non- filtered (in blue) and filtered with the IIR Butterworth (in red).

The FFT is performed and the results are converted in dB values. The resolution in the frequency domain is 0.1144 Hz. The spectra can reproduce harmonics till 60 kHz (the Nyquist frequency), though the range that will be considered for searching the characteristic harmonics is 0-2000 Hz. After the computation of the FFT for each acquisition, the mean of the spectra of the 40 acquisitions is calculated for each condition considered.

Then, the resulting averaged spectrum is compared to the baseline spectrum, obtained by following the same steps. To compare the spectra of the faulty cases with the baseline, a windows subdivision in the frequency domain is used: the abscissa is subdivided in windows, each one 18 times wider than the FFT resolution, i.e. 2.06 Hz. In each window of the faulty spectra, the maximum value is compared to the maximum value of the respective window in the baseline spectrum, in order to correctly match the peaks of the harmonics which can appear at short distance of frequency among them. In fact, slight change in load or in the supply frequency can change the fault characteristic harmonics. The subdivision of the spectra into windows can be seen in Figure 53, from a work carried out previously in the laboratory [80].

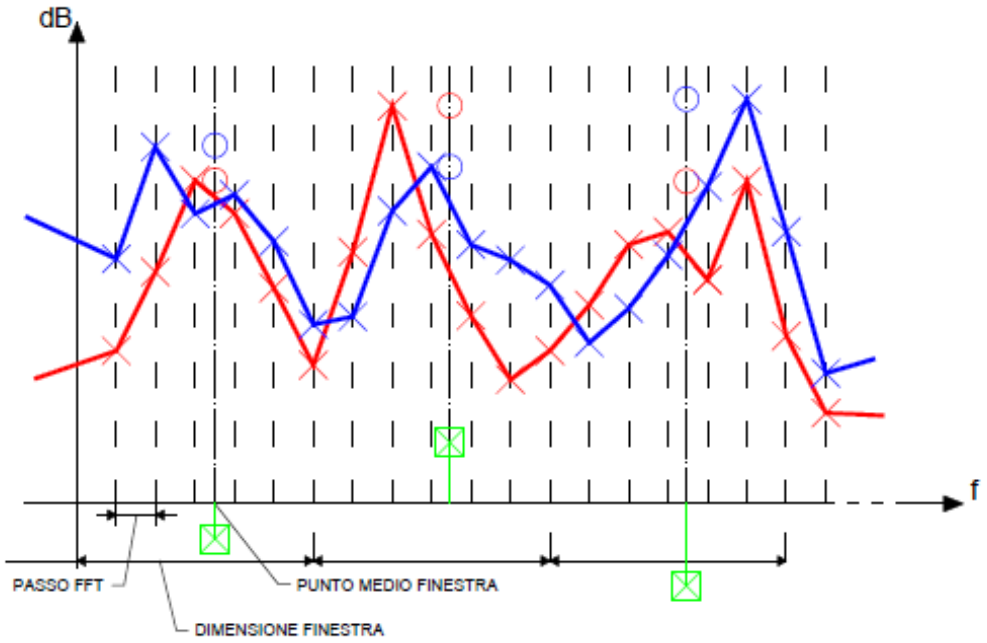

Figure 53: Subdivision of the spectrum into windows for the matching of the fault harmonics [80].

The statistical test used for the comparison is based on a previous work performed in the laboratory [81]. The distribution of the peaks on the 40 acquisitions has been assumed as a Student's t-distribution. The sample standard deviation S of the sample mean of each harmonic divided by the square root of the number of samples (i.e. 40) gives the theoretical standard deviation of the mean of the spectra. To lighten up the program, instead of calculating the standard deviation over each harmonic, it is preferable to calculate the sample standard deviation over the whole spectrum, and then multiply it by the corrective factor given by tables of Student's t-distribution: $2.2467/\sqrt{40} = 0.384$ (for a test validity >99%). Unlike the choice taken in [81], here only the harmonics of the faulty cases that exceeds the corresponding harmonics of the baseline at least of the corrected standard deviation are considered as excited harmonics. This choice is based on the fact that the faulty harmonics should have bigger magnitude than the healthy ones.

Finally, the excited harmonics are compared to characteristic harmonics obtained by 13 formulas; many of these characteristic frequencies are the same as presented in 2.3 while others were taken from other sources in literature and will not be reported for the sake of simplicity.

The tolerance chosen for confronting the harmonics found in the faulty and in the baseline spectra is of ± 2.5 Hz. The number and the amplitude of the harmonics corresponding to a characteristic fault frequency will give an indication about the healthy or faulty status of the machine. Note that in the selected formulas all the multiplicative coefficients needed to calculate all the possible characteristic harmonics in the range between 0 and 2000 Hz are used. Two images of the spectra in the 0-2000 Hz range of the current signal and axial stray flux signal are presented

in Figure 54 and Figure 55, [82]. It could be noted a major presence of harmonics in the axial stray flux signal with respect to the current signal. This characteristic of the stray flux signals (also radial flux presents similar spectra) that are “rich in harmonics” is interesting, since potentially more harmonics can be checked for diagnostic purposes.

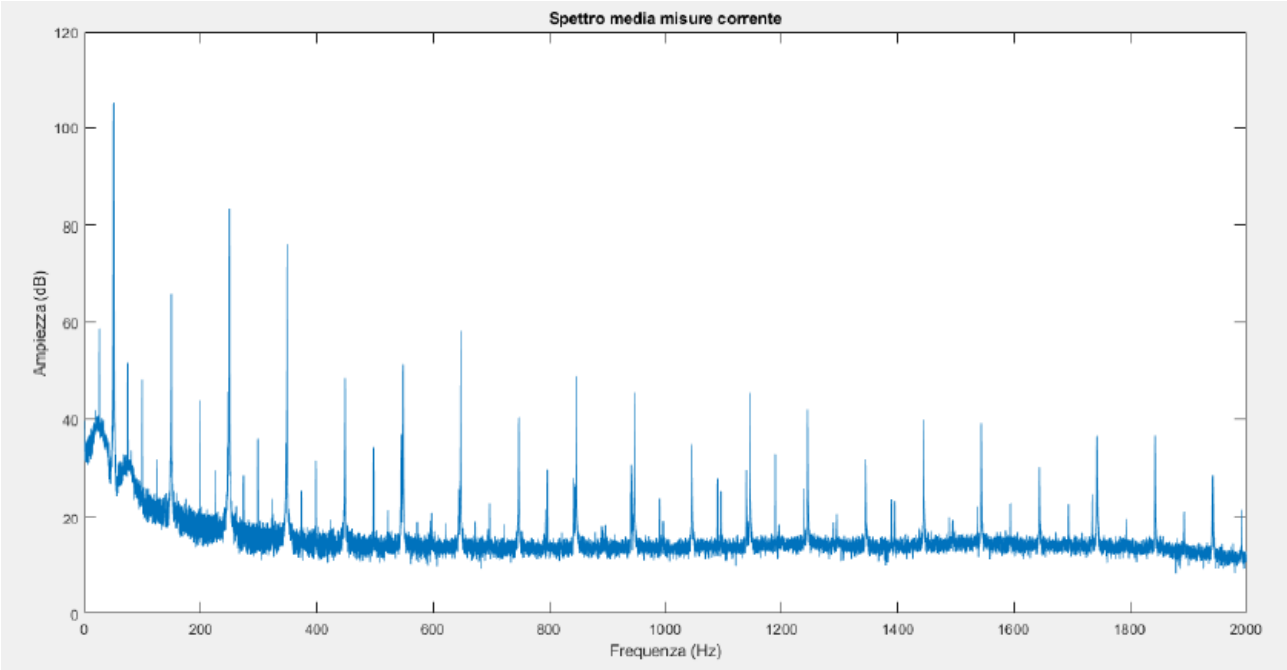

Figure 54: Current signal spectra in the 0-2000 Hz range [82].

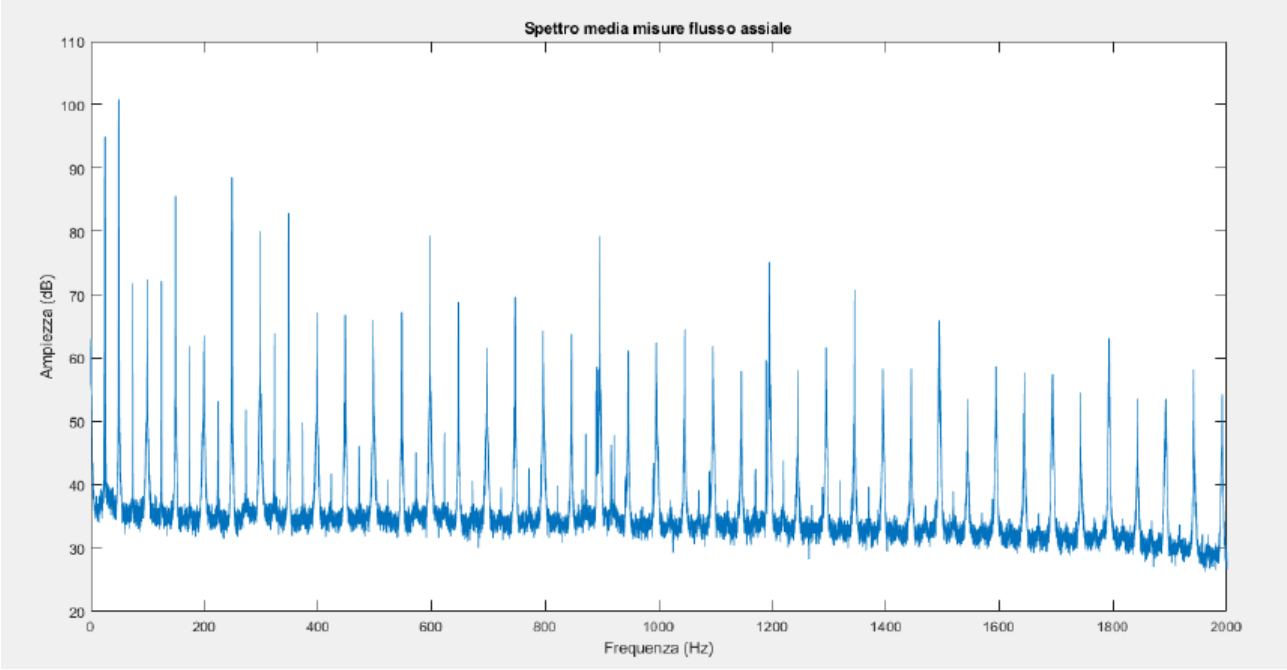

Figure 55: Axial flux signal spectra in the 0-2000 Hz range [82].

4.5.1 Baseline analysis

A preliminary check of the baseline spectrum has been carried out by considering the first 20 acquisitions as reference for the last 20 ones. The two groups of spectra are compared between them following the method of the maximum peak in the windows described above. The standard deviation in this case is corrected by the factor $2.5395/\sqrt{20} = 0.568$ because the considered acquisitions are 20. The results are shown in Table 14. The value in brackets in the column of the total of number of excited harmonics is the maximum amplitude difference between the harmonics at the same frequency of the two groups of spectra, for each type of sensor. As expected, the number of excited harmonics for this case is very low, with only one correspondence with a characteristic harmonic in the axial flux signal. The aim of this test was to validate the baseline as a stable signal without false positives, i.e. the signal of the first 20 acquisitions is very similar to the signal of the last 20 ones. This can be used also to verify a possible change in the signature spectra due to a temperature variation. In fact, with sets of acquisition that last minutes, if the machine is not already in a thermal regime, the temperature can vary, possibly changing the signature spectra.

On the contrary, as it will be shown in the following, the comparison of the harmonics of a faulty case with the baseline will produce a higher number of excited harmonics corresponding to characteristic frequencies.

Note that in the following tables also the eccentricity harmonics are considered. Though no artifice is used to control the eccentricity in the motor, the presence of its specific harmonics has been counted to check how much the eccentricity can increase with bearing faults or how much the presence of the SSC can give false positives in the detection of eccentricity.

Table 14: Number and magnitude of the excited harmonics for the healthy baseline.

Signal	No. excited harmonics	SSC harmonics	BF harmonics	Eccentricity harmonics
Current	1 (6.3 dB)	0	0	0
Emerson flux	2 (7.4 dB)	1	0	0
Custom flux	2 (6.7 dB)	0	0	0

4.5.2 Faulty cases analysis with the healthy baseline

In this section the comparisons of the frequency spectra of the faulty cases with the healthy baseline will be shown. All the 40 acquisitions will be analysed for each case, so the theoretical

standard deviation will be corrected with the factor $2.2467/\sqrt{40} = 0.384$, assuming the Student's t-distribution hypothesis.

The comparisons are reported from Table 15 to Table 22. Except for the first two cases, which are realized with a single fault, i.e. the Bearing Fault (BF) Step 1 and Step 2, the other cases consider a combination of BF and SSC, in a multiple fault configuration.

For the single fault cases, Table 15 and Table 16 resume the fault characteristic harmonics that exceed the statistical threshold. Table 15 shows a relatively small number of correspondences with the characteristic frequencies, with low maximum peak amplitudes (5.9 dB for the current and 8.9 dB for the custom flux). By observing Table 16, it is possible to note a general increase in the number of harmonics at the bearing characteristic frequencies, compared to the case represented in Table 15. The total number of bearing characteristic frequencies on all three sensors is 16, compared to 8 in Table 15. This was expected, because there is a progression of the fault between these two cases. By observing only the current, usually considered as the most reliable signal, there is an increase from 4 to 5 correspondences in the bearing characteristic frequencies. As regards the SSCs and the eccentricity harmonics, it can be noted that there is a slight increase in the number of harmonics of the custom flux signal (8 SSCs and 4 eccentricity harmonics in step 2 BF condition versus 6 SSCs and 3 eccentricity harmonics in step 1 BF condition). However, the overall harmonics for all the three signals decrease (10 SSCs and 6 eccentricity harmonics for step 2 BF versus 11 SSCs and 8 eccentricity harmonics for step 1 BF). This confirms that the method interprets the fault as a BF, since only the BF overall harmonics increase from step1 BF to step 2 BF.

Table 15: Excited harmonics for step 1 BF.

Signal	No. excited harmonics	SSC harmonics	BF harmonics	Eccentricity harmonics
Current	10 (5.9 dB)	3	4	3
Emerson flux	5 (6 dB)	2	0	2
Custom flux	19 (8.9 dB)	6	4	3

Table 16: Excited harmonics for step 2 BF.

Signal	No. excited harmonics	SSC harmonics	BF harmonics	Eccentricity harmonics
Current	13 (4.7 dB)	1	5	1
Emerson flux	3 (9.2 dB)	1	1	1
Custom flux	38 (11 dB)	8	10	4

The cases of double fault condition are presented from Table 17 and successive. The comparison between Table 17 and Table 18, i.e. representation of the cases BF step 1 with 5% SSC and BF step 2 with 5% SSC, shows an increase in the bearing characteristic frequencies for the most severe case; in fact, an increment from 7 to 16 characteristic frequencies is recorded in all three sensors and from 2 to 4 frequencies in the current signal for the two cases analysed. In these tables, with a SSC of 5%, there is a general increase in the stator characteristic frequencies compared to the cases without SSC, represented in Table 15 and Table 16 (except for one case with the custom probe). In addition, in the cases with SSC, the magnitude of the harmonics tends to increase, with values reaching 11-17 dB.

Table 17: Excited harmonics for step 1 BF and 5% SSC.

Signal	No. excited harmonics	SSC harmonics	BF harmonics	Eccentricity harmonics
Current	17 (14 dB)	4	2	4
Emerson flux	38 (13 dB)	4	3	4
Custom flux	19 (15 dB)	1	2	1

Table 18: Excited harmonics for step 2 BF and 5% SSC.

Signal	No. excited harmonics	SSC harmonics	BF harmonics	Eccentricity harmonics
Current	22 (17 dB)	4	4	4
Emerson flux	29 (11 dB)	4	3	4
Custom flux	41 (11 dB)	10	9	3

In Table 19 and Table 20, with the BF at step 1 and step 2 respectively and a SSC level of 10%, there is a general increase of the magnitudes of the harmonics (12-22 dB), compared to the 5% SSC cases. The number of stator characteristic frequencies increase as well, with 13 and 21 total correspondences compared to 9 and 18 total correspondences in Table 17 and Table 18. Considering only the current signal, the number of correspondences remains constant. The number of bearing characteristic frequencies also increases from step 1 to step 2 (from 13 to 22 total bearing harmonics). There is a decrement in this number only in the current signal (from 4 to 2 correspondences), but with an increment in the amplitude (from 19 to 22 dB).

Table 19: Excited harmonics for step 1 BF and 10% SSC.

Signal	No. excited harmonics	SSC harmonics	BF harmonics	Eccentricity harmonics
Current	28 (19 dB)	4	4	4
Emerson flux	44 (14 dB)	6	4	6
Custom flux	30 (12 dB)	3	5	3

Table 20: Excited harmonics for step 2 BF and 10% SSC.

Signal	No. excited harmonics	SSC harmonics	BF harmonics	Eccentricity harmonics
Current	20 (22 dB)	4	2	4
Emerson flux	33 (12 dB)	5	6	5
Custom flux	56 (14 dB)	12	14	5

In Table 21 and Table 22, with a SSC level of 15%, the number of stator characteristic frequencies does not substantially increase compared to the 10% SSC cases. In fact, 16 and 22 total correspondences are found compared to the previous 13 and 21, but the amplitudes of the harmonics increase considerably, with peaks of 15-24 dB. Considering only the current signal, there are 4 and 6 stator characteristic frequencies for the case with BF step 1 and step 2 respectively. The bearing characteristic frequencies increase for the current from 3 to 8 (one of them shows the higher peak amplitude recorded) and for the radial flux sensor (from 5 to 11), but decrease for the Emerson probe (from 8 to 6).

Table 21: Excited harmonics for step 1 BF and 15% SSC.

Signal	No. excited harmonics	SSC harmonics	BF harmonics	Eccentricity harmonics
Current	38 (23 dB)	4	3	4
Emerson flux	56 (16 dB)	10	8	9
Custom flux	43 (15 dB)	2	5	2

Table 22: Excited harmonics for step 2 BF and 15% SSC.

Signal	No. excited harmonics	SSC harmonics	BF harmonics	Eccentricity harmonics
Current	40 (24 dB)	6	8	6
Emerson flux	37 (15 dB)	5	6	5
Custom flux	66 (17 dB)	11	11	6

The cases in Table 21 and Table 22 show that, over a certain severity level of the fault and in presence of simultaneous faults, the number of characteristic harmonics does not increase considerably, whereas the magnitude of these harmonics increases.

Eventually, it should be noted that, in general, the eccentricity characteristic frequencies tend to increase with the progression of the fault: this could be correlated to the larger movement of the shaft in radial direction with a worn bearing and to the superimposition of the harmonics due to the other fault of SSC.

4.5.3 Faulty cases analysis using the faulty baseline

In this section, the case with BF step 1 is chosen as baseline (representing a faulty baseline) and three cases with more advanced faulty conditions were compared. In Table 23 the comparisons with the case with BF step 1 and 5% SSC are visible; it can be seen that a total number of 13 stator characteristic frequencies and 12 bearing characteristic frequencies are found. The maximum magnitude of the harmonics is 15 dB for the current and 18 dB for the custom flux. The number of characteristic frequencies counted for the eccentricity fault is 13. Table 24 includes the results obtained by increasing SSC to 15% while maintaining the BF step 1; there is an increment to 17 stator characteristic frequencies, 23 bearing characteristic frequencies and 18 eccentricity characteristic frequencies. The magnitude of the harmonics also increases to 22-24 dB. By considering only the current signal, there is just an increase in the number of the bearing characteristic frequencies, while the number of eccentricity and stator characteristic frequencies remains constant, compared to the case in Table 23. Anyway, the maximum peak increases of 7 dB compared to the previous case: this shows the more advanced status of the fault.

Table 23: Excited harmonics for step 1 BF - 5% SSC compared to step 1 BF baseline.

Signal	No. excited harmonics	SSC harmonics	BF harmonics	Eccentricity harmonics
Current	20 (15 dB)	5	2	6
Emerson flux	64 (16 dB)	5	6	4
Custom flux	42 (18 dB)	3	4	3

Table 24: Excited harmonics for step 1 BF - 15% SSC compared to step 1 BF baseline

Signal	No. excited harmonics	SSC harmonics	BF harmonics	Eccentricity harmonics
Current	39 (22 dB)	5	3	6
Emerson flux	92 (22 dB)	5	8	6
Custom flux	92 (24 dB)	7	12	6

In Table 25, which reports the comparison of the case BF step 2 with the BF step 1 baseline, the total number of correspondences are only 2 for the SSC, 16 for the BF and 3 for the eccentricity. The increase of the bearing frequencies correctly identifies the higher severity of the fault. The maximum magnitude of the harmonics varies from 9 dB (Emerson flux) to 14 dB (custom flux). In the current signal, there are only one correspondence to the bearing harmonics and one to the eccentricity harmonics. This should appear as a weak fault recognition, but it is anyway a good result, due to the difficulty in identifying the bearing wear by means of electromagnetic signals without any particular processing of the signal.

Table 25: Excited harmonics for step 2 BF compared to step 1 BF baseline.

Signal	No. excited harmonics	SSC harmonics	BF harmonics	Eccentricity harmonics
Current	7 (12 dB)	0	1	1
Emerson flux	14 (9 dB)	0	5	0
Custom flux	31 (14 dB)	2	10	2

It is interesting to note also that the total bearing characteristic frequencies are less in Table 25 than in Table 24: this is probably due to the fact that some stator characteristic frequencies coincide with the bearing frequencies, and therefore there is a decrease in both columns, due to the absence of SSC.

4.6 Discussion

In this chapter the multiple fault detection issue in diagnostics has been treated. In paragraph 4.2 a brief review on the techniques found in literature is presented. Successively, a method implemented by the candidate and his research group has been presented.

The work presented is a novel procedure to diagnose different levels of SSCs and BFs in inverter-fed induction motors, in case of single or multiple faults, by means of the analysis of the electromagnetic signals, i.e. one-phase stator current signal and axial and radial stray fluxes.

The diagnostic method is based on the comparison of the actual spectra of one-phase stator current and external stray flux with the analogous spectra collected on the same motor in a known condition ("baseline").

Firstly, the baseline is referred to a healthy status: the results of the comparisons show that the characteristic harmonics of SSCs and BFs are excited, with increasing amplitude and number of correspondences, as the fault becomes more prominent.

Successively, a baseline related to a faulty status is used as reference for comparison to cases with more serious faults: even with this baseline, the method has been proven as able to distinguish different types of fault and their simultaneous presence, and provides a correct detection of the progression of the fault.

The new methodology proposed is based on a high sampling frequency for the acquisition of the signals, which permits an easier detectability of the faults compared to other methods evaluated by the authors, avoiding advanced filtering techniques to process the experimental data. Moreover, the comparison with a faulty baseline is a novelty to the knowledge of the author. Though a high number of sidebands and fault harmonics are considered for the bearing fault diagnostics in other works, such as [83], the use of all of the coefficients for the checking of all the fault harmonics in the 0-2000 Hz is also an important feature of the method. This increase the variability of the data and improve the detectability of the fault.

Future works can be focused on the implementation of an automatic fault classifier, e.g. with machine learning techniques, able to recognize which fault is prominent with respect to the others. In fact, since some characteristic harmonics of different faults coincide, this makes difficult to distinguish the faults among them.

Moreover, an in deep investigation could explain why certain characteristic harmonics are more or less sensitive to the faults in different sensors, in order to identify which sensor provides the best performance for each fault and to minimize the measurements.

5 Multi-sensor technique for bearings fault detection

5.1 Introduction

In this chapter the multi-sensor approach for the diagnostics of induction motors and other electrical machines will be discussed.

At first a brief literature review focalized on the theme will be introduced. Successively a method proposed by the author and his research group will be presented.

The method uses vibration and electromagnetic signals (current and stray fluxes) to diagnose cyclic bearing faults. Two vibration signals from different sensors, located in different positions, are analysed and compared. Then, the information from the vibration has been used to better identify the fault on electromagnetic signals. More tests are carried out with the introduction of the Low Frequency Torque Oscillations (LFTO); these oscillations, in simultaneous presence with the bearing fault, introduce a double anomaly condition that makes more difficult the diagnosis. Eventually, some tests are carried out with the supply of the motor from the inverter.

The method used lead to the writing of a scientific paper that has been published and presented at the International Conference on Electrical Machines (ICEM), hold online in August 2020, [84].

5.2 Literature review

This review will include two main parts.

The first part is a short summary of the issue with the recall of some of the techniques used for bearings fault detection. This part will focalize especially on the cyclic fault condition as this is the condition that will be presented in the following of the chapter. This part, moreover, will include a brief analysis of the causes that generate failure in bearings. Some references to the previous paragraph 2.3.4, in which the issue is already treated in a more general way, will be present.

The second part of the survey is relative to the multisensor approach for diagnostics of electrical machines.

5.2.1 Bearing cyclic faults diagnosis

As stated in 2.3.4, in which a more general review on bearing fault is presented, the bearing fault is one of the most diffused in electrical machines, in particular small machines. The fault can reach 50-69% of the total faults in induction machines [13], [85], or even more for small machine (75%) according to [67], see Figure 47.

An analysis on the most common causes of failure in bearings is conducted in [86]. From the survey it comes out that the most frequent cause of bearing failure is due to an inappropriate lubrication. This can include inadequate lubrication, lubricant contamination and deterioration of the lubricant due to long time running without renewing. The share of the causes of fault can be seen in Figure 56.

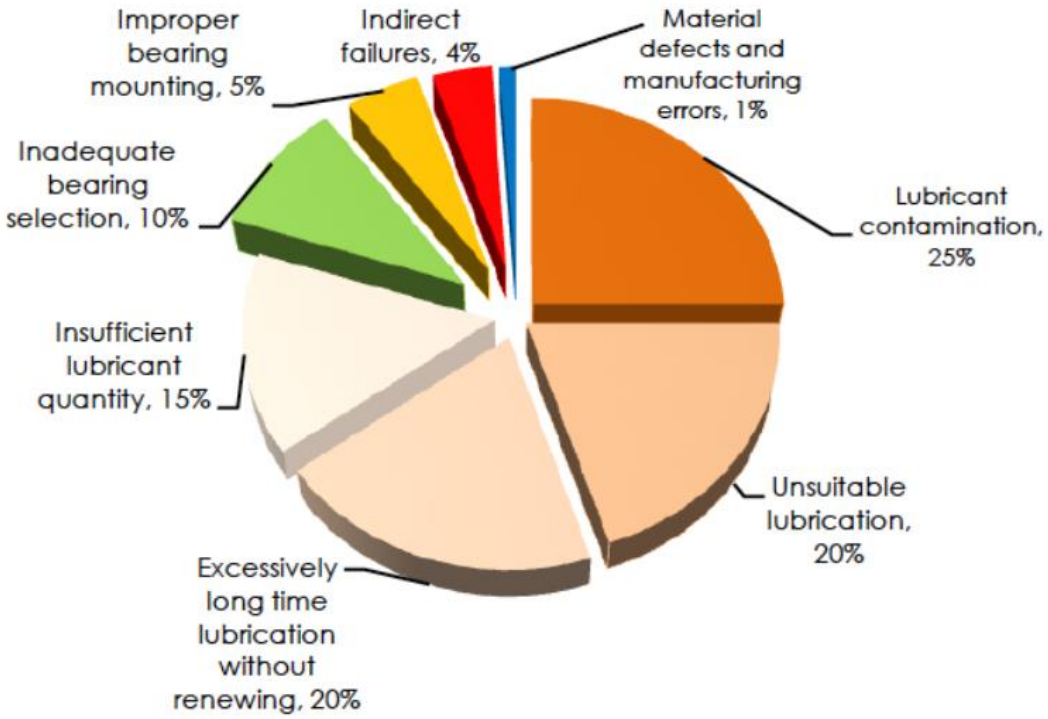

Figure 56: Most common causes of bearing failures [86].

The improper lubrication can cause in a first instance faults correlated to the generalized roughness, for example abrasive wear of the ring race, and in general wear of the parts of the bearing. After the wear has begun, some kinds of localized fault could appear due to the increase of the temperature and so due to the increased fatigue condition of the material.

For example, spalling is a condition in which a crack is formed on the race and, because of the continuous fatigue due to the roller elements passage on it, develops into a bigger material defect as the material breaks away [87]. The spalling occurs at the end of the fatigue life of the material. Since this fault generates a local defect in the bearing race, it is classified as “cyclic” or

"localized". This fault generates the characteristics harmonics that can be calculated with (2.15) in the vibration spectra and with (2.16) and (2.17) in the electromagnetic signal spectra.

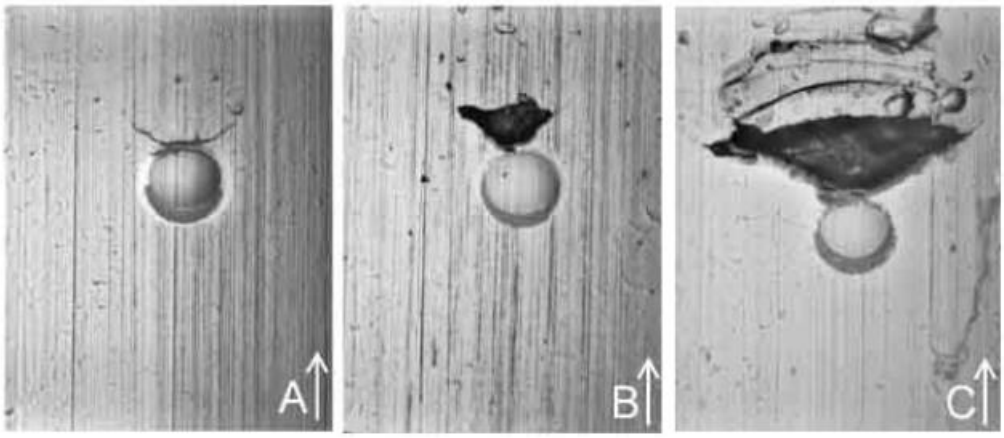

Figure 57: Evolution of the spalling defect [87]

Moreover, about 10% of the causes reported in [86] can lead to localized faults. In fact, according to [86], the cause of improper bearing mounting (which weighs about 5% of the total) includes axes misalignment that generate mechanical stress and fatigue in some parts of the bearing which can again lead to a spalling process.

In the causes denominated "indirect failures" (4% of the total), [86] includes causes of unacceptable operating conditions, transport, storage and handling. Other indirect causes are due to the worst operating conditions, i.e. overloading, excessive vibrations, over-speeding, high temperature and electrical discharges.

A static load or shock on a stationary bearing can lead to an overloading condition that generates a plastic deformation of the balls/raceway contact. This produces shallow depressions or flutes on the raceways spaced by the balls' pitch. This fault is called brinelling and it is cyclic. In contrast to brinelling, called also "true brinelling", the false brinelling produce on the raceways lighter depressions (distanced by the balls' pitch of the cage) generated by excessive vibrations on a stationary bearing, e.g. during inaccurate transportations. This also leads to a cyclic fault, though of low severity with respect to true brinelling.

Another important cause of deterioration of the bearings is due to electrical discharges inside the bearings. This can be due to electrostatic charges generated in V-belts systems [86]. The charges are dissipated through the bearing to ground. This causes the formation of pits or fluting on the bearing surfaces. This happens also with relatively low current discharges. Initially, the damage due to electrical discharge consists in the formation of only small craters or pits, but after some time these defects evolve into flutes. In addition to electrostatic discharges due to V-belt systems, stray magnetic fields generated by the electrical machines (especially in those fed by an

electronic converter) can produce high currents to pass through the bearings. To eliminate the problem is necessary to keep the shaft at ground potential through ground brushes.

All of these defects (pitting, fluting, etc.) produced by electric discharges, are generated on the bearing raceways and balls; they are more than one and in random position and so they can be assumed to be a generalized roughness defect as usually none of the pits will prevail in severity levels with respect to the others. This will not produce only one characteristic frequency but more likely it will produce the increase of the magnitude of a broadband high-frequency (in vibration spectra) [89]. Anyway, if one of the defects produced prevails over the others, e.g. after the spalling process has occurred, it can be diagnosed by monitoring the characteristic frequencies discussed in 2.3.4.

So, it is important to check the harmonics of the cyclic faults, though often the fault will not visible in raw spectra, but more advanced techniques, such as envelope techniques, must be used, as said for example in [29].

The other main works consulted for the writing of the author's paper [84] are [50], [25], [60] and [88].

5.2.2 The multisensor approach

An interesting survey of multi-sensor systems for condition monitoring and diagnosis of electric motors is carried out in [90]. In the work, some definitions are given to understand and classify multi-sensor systems especially for online condition monitoring.

First of all, the online diagnosis process has been analysed in a generic way and it is subdivided into four main steps. The first step is the sensor refinement to acquire more signals that contain valuable information. Choices of sensors and their position are to be evaluated to have better results in this stage.

The second step is the feature optimization. It concerns how effectively extract the most important features to be used from the signals. In this step various features from different domains (time, frequency or other domains) and application of advanced digital signal processing techniques are investigated.

The third step is the classification refinement. Researchers investigated this step to improve the pattern recognition problem. The choice of the classifier which directly influences the accuracy of the system is the main concern in this phase.

The fourth and last step is the decision refinement. At this stage, the researchers investigated how to give a complete and better inference to the motor condition and eventually conclude the health state of the machine. A prediction of remaining useful lifetime in this step can

be an additional benefit that gives a lot of surplus value to the diagnostic system; in fact, this prediction (prognosis of the fault) can be used to apply predictive maintenance programs. Usually, machine learning techniques or anyway Artificial Intelligence (AI) are used to reach this target.

The scheme of the four steps for the diagnosis process of electrical machines is shown in Figure 58.

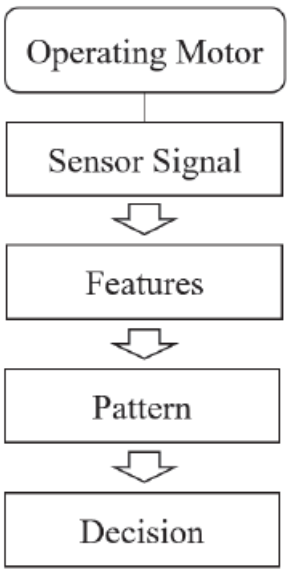

Figure 58: Fault diagnosis for electrical machines [90].

In [90], it is pointed out the importance of the first step of the process (acquisition of the signals) as this first step influences all the successive steps. To have more information on all the physic phenomena that happen in the motor, more than one sensor is necessary. Vibration and current are the most used signals for diagnosing the electrical machines. Stray flux analysis has gained acceptance in the last years because of the simplicity of installation of the probes and of the good results obtained.

The multi-sensor fusion terminology refers to the process of association, correlation, combination and estimation of the data collected from multiple sensors or information sources. This permits to achieve higher quantity estimation accuracy than a single sensor system.

As stated in 2.2, some sensors (and signals) are better than others in recognizing some faults. For example, stator current signal is the most effective for diagnosing Broken Rotor Bars (BRBs) in IM. Vibration signal is more effective in bearings diagnostics. In general, vibration is better to analyse mechanical faults such as unbalanced load, bearings faults, bent shafts, misalignment. On the other hand, current signal performed better for electrical faults detection such as SSC or broken rotor bars but also airgap eccentricity. Stray flux signals (radial or axial) have intermediate characteristics between current and vibration signals: for some aspects, the stray

flux is more sensitive than the current (e.g. bearing faults are more easily detected with the flux than the current) but it has a higher variability on the location and type of the probe used.

The multisensor systems, according to [90], can be classified in two main groups according to the number of sensors used and physical quantities collected: homogeneous sensors systems collect only one physical quantity (e.g. vibration) but with more sensors, while heterogeneous sensors systems give outputs in different physical aspects, e.g. vibration and stator current.

The information collected can be either redundant or complementary.

The information is redundant when it is acquired in a repetitive way, i.e. through repeated measurements or with measurements of the same quantity taken in different conditions (e.g. with sensors in different locations). The redundant information is typical of the homogeneous sensor systems. This type of information helps to reduce noise in the measurements through a signal fusion process and improve measurement accuracy. In the online fault diagnosis systems, the redundancy is only partial, in fact the information from the different sensors is anyway somewhat different; by analysing the non-repetitive part, additional features can be extracted. An example of this kind of measurement is the one used for obtaining the Park's vector, which is a combination of the three-phase current instantaneous values. In this kind of systems, the sensors must be commensurate between them: to fuse the information between the sensors, all of them must have the same parameters (ranges of measurement, accuracy, bandwidth, etc.).

Complementary information systems are generally the heterogeneous sensors systems. In this case, the use of different physical measurement sensors improves the fault specific inference for the classification and extends the coverage of fault types to be recognized also in different operating conditions. In this case the sensors can be non-commensurate between them as the information is collected from different physical aspects and usually the systems are based on the monitoring of relative variations of certain quantities. The most common type of these systems in literature is formed by the sensor combination of the current and vibration signals. For example, in [91], a fusion system is used to combine vibration and three-phase current signals to isolate and distinguish the fault of misalignment and unbalance. These two faults produce the same sideband characteristic harmonics in current spectra. Nevertheless, using the radial vibration signal, it was possible to distinguish between the two faults. In [92], a multisensor heterogeneous system has been used to measure two currents and two voltages signals to calculate airgap torque in the motor; with the analysis of the airgap torque it was possible to recognize stator unbalanced windings or rotor broken bars.

Another important definition given by [90] is about fusion models. Three different types of fusion models are possible. The process flow can be considered divided into three levels: data level, feature level, and decision level. The information fusion process can be applied in any of these three levels. A scheme with the level-fusion model is presented in Figure 59.

The first is data-level fusion. This option is generally used in other applications than diagnostics; this process is used to eliminate the measurement error because of the noise and sensor inaccuracies. This technique largely reduces the online data transmission load. In this case, anyway, a clear relationship between the sensor signals is required. Moreover, the absolute accuracy of the measurements is not required in online monitoring as normally a comparative analysis between data in different lapse of time is used. Data-level fusion is so rarely used in online diagnostics of electrical machines. The only exception is the observation of the Park's vector, electric torque and instantaneous power. The data acquirement for this kind of fusion must be simultaneous and synchronized, in both the measurement and digitizing process.

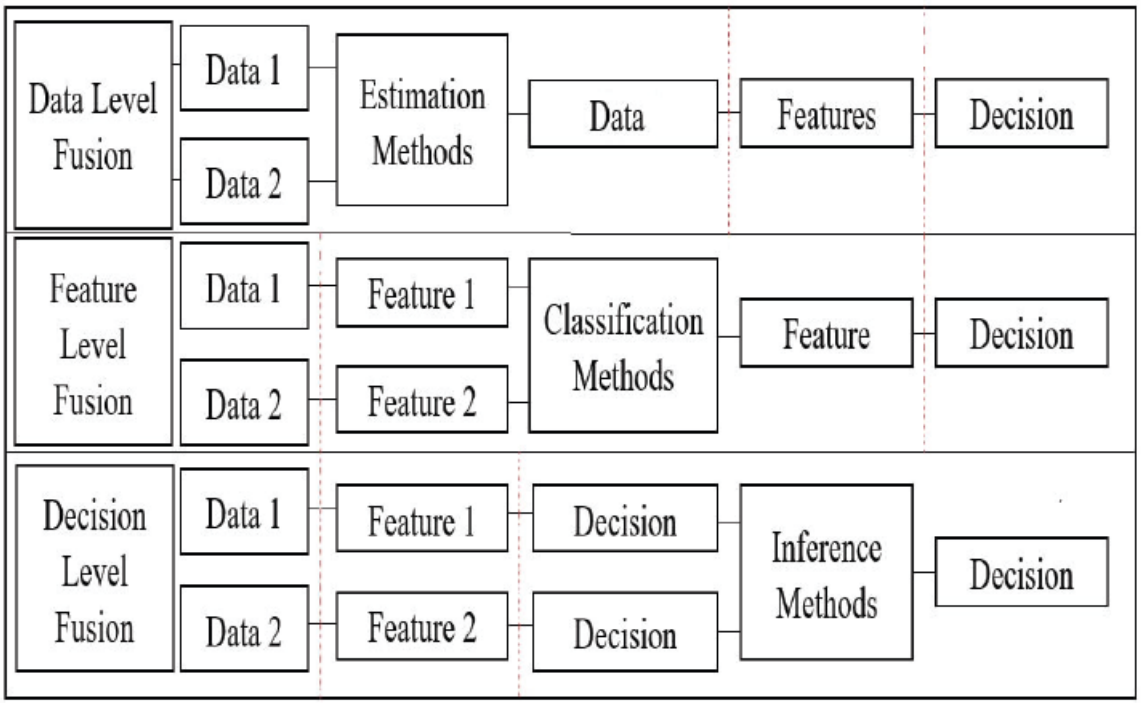

Figure 59: The three-level fusion model [90].

The second possibility is the feature-level fusion. This fusion is applied in most of the works in the area of condition monitoring of electrical machines. With this option, more flexibility is possible for information sources. As opposite to data-level fusion, in this case the exact relation among different information sources is no longer necessary. Moreover, in this case non-commensurate (heterogeneous) sensors can be used as the fault related information are not fused directly at data-level. The fusion process is integrated directly into the classification process. The classification can be made with automatic process like Artificial Neural Network (ANNs); in particular, the Support Vector Machines (SVMs) are very popular in this field.

Decision-level fusion has fewer prerequisites on the system and is used to make the final decision as comprehensive as possible. The information of each sensor in this case is not mixed and handled independently till the final process of the decision-making. Inference methods for the final step are used; some of the most important are majority voting, fuzzy integral and Dempster-

Shafer theory. This level fusion suffers from a greater loss of information than data and feature level fusion systems. The technique in fact is unable to do a comprehensive inference from weak evidences from each sensor. The weak fault information from each sensor, instead of getting summed in the feature process to form a stronger information, is lost in this way. The decision-level fusion is therefore used only in systems which do not require a very specific inference.

An interesting work on multi-sensor techniques used for diagnosing IMs is presented in [93]. The paper presents a method in which 5 tri-axial accelerometers and three current sensors (each on one phase of the machine) are used to diagnose broken rotor bars and eccentricity faults. In the processing scheme of the signals a SVM is used as classifier and Random Forests (RFs) ensemble learning method are used to reduce the dimensionality of the input.

In particular, this work can classify 6 different faults of dynamic eccentricity, one broken bar, two consecutive broken bars, three consecutive broken bars, two non-consecutive broken bars, eccentricity combined with two BRBs. Moreover, three different load conditions are considered: full-load, half-load and no-load.

The data from the accelerometers and current signals are processed and statistical features in both frequency and time domains are extracted in the number of 12 for the frequency-domain and 20 for the time-domain for a total of 32. The already high number of features extracted have to be multiplied by the number of signals that are 15 of vibration (5 accelerometers with 3 axes each) and 3 of current, for a total of 18. The total number of features considering each signal is so 576 (it is given by the multiplication of the number of features, i.e. 32, by the number of signal, i.e. 18). To check which of these 576 features are most correlated with the fault diagnosis, the RF ensemble learning model has been trained and results are extracted. The first 50 fault-correlated features are first considered but using only the top 35 for the training of the SVM. The most important features are from vibration signal (the top 6 selected) in both time and frequency domain. Current signal has only 4 extracted features in the top 35 rank. The scheme of the processing is shown in Figure 60.

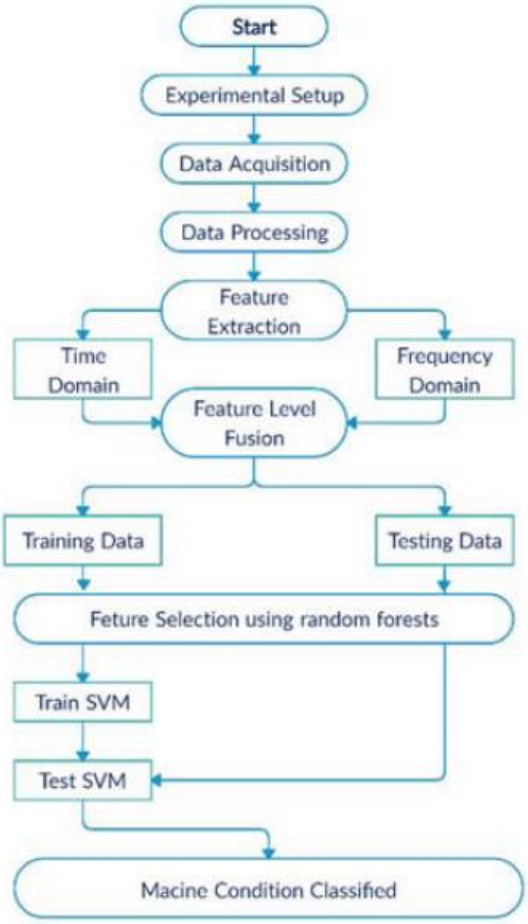

Figure 60: Procedure for fault detection and features selection [93].

Training the SVM with these selected features has brought to high accuracy results with high stability. In fact, two main test scenarios are conducted: one in which all the load-levels are used in the training of the SVM and one in which only full-load and no-load data are used for training, while half-load data are used for testing the network. The tests are conducted with different input signal choices for the feeding of the SVM to compare multi-sensor with one-sensor classification process: some are conducted with only one-phase current, some with the three-phase currents, some with only vibration, others with only vibration in z-axis and the last with all the vibration and current signals available. It turns out that though for the first scenario not many accuracy differences are noted for the single and multi-sensor signals, for the second scenario the multi-sensor classification has kept high accuracy (over 98% for all the 6 faults except one) while the single-sensor classification has lost much of its accuracy in many of the fault cases. It is concluded in the work that, even though one of the signals, i.e. current, has given much less significant features for the training process, using a multi-sensor technique improves the classification accuracy and keep it stable even for data from different load-condition, i.e. totally new data for the SVM-based network.

In [94], a homogeneous multi-sensor technique is used to detect stator fault in synchronous machines. In particular, two stray flux sensors are used in diametrical opposition (180° from each other); the sensors are then rotated (of 60° each time) in three different positions around the body of the machine. The work is based on a previous paper [95], in which the sensors used are two but kept in fixed position.

The physical principle on which [94] and [95] are based is the symmetry of transversal (i.e. radial) stray flux of the machine. In the model proposed, when no fault is present, the airgap flux and the corresponding transversal flux, that can be considered a prosecution of the internal flux, are symmetric around the axis on which the flux is maximum. This corresponds to a three-phase ideal winding with no asymmetries. When a fault occurs it can be though that a second magnetic field is formed by a single-phase winding: this does not generate a rotating field but an alternating field. The two probes can individuate this kind of alternating field generated due to the fault. An interesting fact, stated by the authors, is that this kind of alternating field is generated by any of the faults that can happen to the machine. Moreover, the main advantage of using two flux probes instead of one is that it is not necessary to have a baseline acquisition on healthy state motor. The method is based on signal comparison but instead of using a baseline, the comparisons are carried out on different loading of the machine, i.e. no-load or load operation. The non-necessity of the healthy baseline is a great advantage in any of the cases in which the load of the machine can be changed easily; nevertheless, change the load is not always possible in actual industrial applications. The method used in [95] has been considered valid for both synchronous and induction machines.

In [94], the process has been refined using the two probes in three different positions. This increases the sensitivity of the system. In this case the work is focused on stator short circuits (SSCs) and not on generic fault of the machine. The information from the sensors is statistically processed through Pearson correlation coefficient successively fused with belief functions. With these improvements the method is able to detect incipient SSC faults in different parts of the windings. The harmonics considered for the detection are the sidebands of the first order rotor slot harmonic; in the examined case the rotor slot harmonic is 800Hz and the sidebands are at 750 and 850 Hz. The work proves that more measurements, though from the same physics-based sensors (homogeneous multi-sensor system), increase the detectability of faults considered in literature very hard to detect.

In [76], already presented in paragraph 4.2, a heterogeneous multi-system is used to diagnose multiple faults in induction machines. In particular, vibration and three-phase current signal (Park's vector) are used to diagnose SSCs, gear faults and bearing faults (BFs) in a power train, that is considered a difficult task since speed and load conditions are changing continuously and there is presence of noise (vibration and electromagnetic disturbs from the electronic converters). Though these difficulties, with a feature-level fusion the scheme gives very good accuracy results for all of the three faults, that is always higher or equal to 98.8%. So, this work is

a proof of the fact that using complementary information, in this case from vibration and current sensors, the detectability becomes higher in sensitivity and wider in the fault to be detected as mentioned before. This is true especially for heterogeneous multi-sensor systems that in this way are more adapt also to diagnose multiple faults condition especially of different physical types, i.e. mechanical or electrical faults.

In the PhD dissertation [89], an in-depth study of multi-sensor technique is explained for the diagnosis of strategic IMs used in nuclear power-plants. The tested IMs are of 3.75 kW rated power, with 4-poles.

In the work numerous novelties are proposed. An in depth study of accelerated aging, based on Arrhenius model, is carried out with specific characteristics for each part considered. In particular, three different aging processes are carried out: thermal aging of the bearings (carried at circa 140°C), thermal and electrical aging for the stator windings (overheated by single-phase current at 205°C), electrical aging of the bearing (27 A injected in the bearing for 30 minutes).

A multisensor technique is used: 30 sensors for measurements of vibration, three-phase currents, three-phase voltages, speed, torque, and temperature sensors (thermocouples already installed by the manufacturer inside the machine). The diagnostic system has been denominated "Intelligent Machinery Monitoring System" (IMMS).

The IMMS sensor fusion technique includes fusion in all of the three levels: data-level, feature-level and decision-level. With the use of the data-level fusion, calculation of instantaneous power and component-sequence analysis of impedance are carried out. This diagnostic system includes the following main characteristics:

- Trends of statistical features such as RMS and mean values of measured variables are carried out;
- A sensitivity matrix, i.e. a matrix which represents several signatures, that are sensitive to specific motor faults, is established. From this matrix, already proven and new methods are tested to extract features from raw and derived measurements;
- Least-squares fitting for the selected features;
- An ANN is used to calculated remaining useful life of the machine;
- Fuzzy logic reasoning has been used to implement the sensitivity matrix. The fuzzy variables do the fusion process at the feature-level;
- The Multi Resolution Analysis (MRA) through wavelet transform has been used for the vibration analysis and successfully identifies a thermal degradation or an electrical degradation of the bearing.

The results of the work [89] are very valuable. With the zero-sequence component analysis of the impedance, winding incipient insulation failure has been diagnosed. The MRA identifies

the bearings thermal and fluting degradation. The efficiency of the machine is studied and was found to be an indicator of failure (though not incipient failure). MCSA is compared with instantaneous power analysis which according to the author gives complementary results. The use of the permanently mounted thermocouples revealed a new technique for detection of incipient fault in bearing (in combination with current signal). The use of fuzzy logic based method for fault detection and classification gave successful results except for few false alarms in winding insulation. ANN based remaining useful life estimation has been successfully implemented.

This shows the potentialities of multi-sensor systems for a more comprehensive diagnosis of the electrical machines.

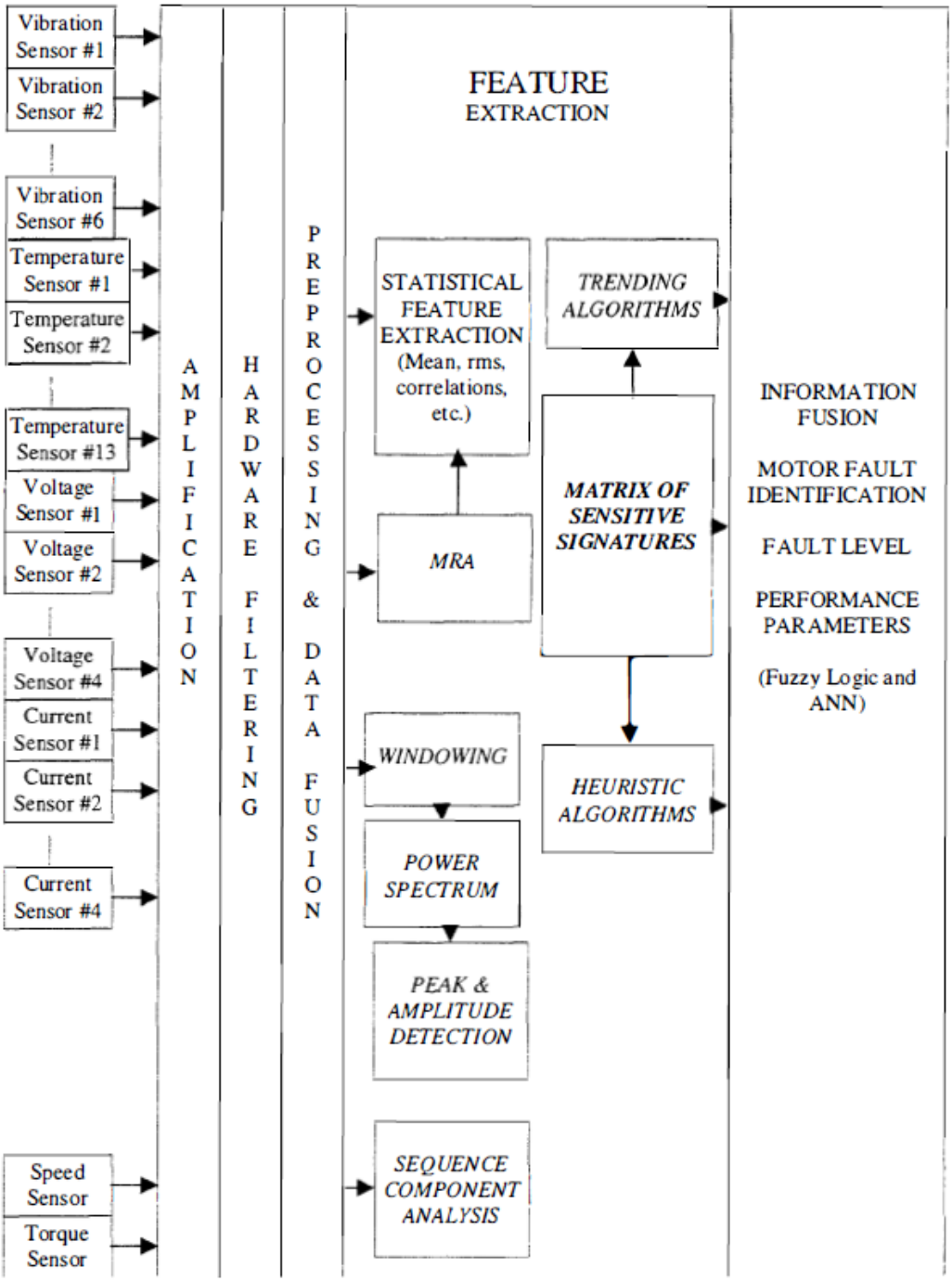

Figure 61: The diagnostic system IMMS [89].

5.3 Proposed method

The work [84], carried out by the author and his research group, at the laboratory of diagnostics and design of electrical machines, will be presented in this paragraph. The work is a multi-sensor based method to detect cyclic bearing faults in induction motors. The sensors used are of current and stray flux signal (electromagnetic signals) and vibration. Different loading conditions are evaluated, among them Low Frequency Torque Oscillations (LFTO) that, in simultaneous presence with the bearing fault, constitute a double anomaly condition of the machine. Tests from mains and inverter supply are carried out and studied.

5.3.1 The approach to the problem

In the work presented, the bearing fault diagnostics is studied through a heterogeneous multi-sensor technique. Five different types of sensors (those presented in 3.3) are used: the Hall effect current sensor, the two coil sensors for detecting the machine's external stray fluxes and the two different types of accelerometers, namely the ADXL 335 MEMS accelerometer and the piezoelectric M608A11 accelerometer.

The bearing used in the experiments for the simulation of the fault, the NSK 6205Z, had a crack in the outer race, resulting in a cyclic bearing fault.

In the work, in a first instance, a brief comparison between the MEMS and Piezoelectric accelerometer's signals was carried out. The two accelerometers have different characteristics and have been positioned in two different parts of the machine. In fact, the piezoelectric one has been positioned on the drive-end bell of the motor, very close to the faulty bearing, while the MEMS has been positioned on the side of the connection box, i.e. approximately on the central part of the body of the machine. More detailed analyses about the different vibration signatures coming from these two different positions are presented in another work of the author, [96], which will be exposed in chapter 6 of this thesis.

A second issue that will be presented is how the acceleration signal can help to identify the fault characteristic frequencies in the current and stray flux spectra. This represents the main advantage of the proposed multi-sensor approach: with the information provided by the vibration signal, it is possible to exactly individuate the harmonic peaks related to the fault in the electromagnetic signals' spectra. This can be explained as in the following.

Some small frequency differences are present between the calculated characteristic frequencies given by the formulas and the actual fault frequencies. In fact, although knowing the exact rotational speed, measured with an optical tachometer, the formulas of the characteristic fault frequencies are approximate due to the slippage phenomenon [29]. The phenomenon is correlated

to a non-perfect rolling of the balls in the bearing, i.e. a mechanical slip of the rolling elements on the inner and outer raceways. According to [29], this slip comes from a variability of the contact angle Φ; this angle varies with the position of each rolling element in the bearing, as the ratio between local radial and axial load changes, and, because of the presence of the retaining cage, all the balls (or rolling elements) must move at the same tangential speed, and so some of them are slipping. This phenomenon introduces an uncertainty of the calculated bearing frequencies of about 1-2%.

On the other hand, in the current and stray flux spectra, the harmonic peaks coming from the bearing cyclic fault are quite weak and often are hidden by noise peaks.

Therefore, the information of the exact bearing peak frequency in the vibration signals gives the possibility to verify if the peaks are also present in the electromagnetic signals' spectra. In fact, the vibration occurs at frequency of which the ball passes over the defect, regardless of whether it is rolling perfectly or there is some slippage. This double detection of the fault confirms the diagnosis revealed only on the vibration signal. This can be considered as a redundant information from heterogeneous signals; though the fault could be in this case recognized with only vibration signals, the visualization on the electromagnetic ones gives stronger inference for the detection and classification. The information redundancy has been used to increase the stability and sensitivity of the detection system as stated in 5.2.2.

Other works in literature highlight the importance of knowing the exact rotational speed, e.g. in [97]. In the work a slip estimation technique is performed to extrapolate the rotational speed. Although the technique presented in [97] can be used even without access to the motor, it requires the knowing of specific construction characteristics such as the number of rotor bars. Moreover, as discussed above, the exact value of the speed (within the small uncertainty of a laboratory estimation) is important but the issue of the slippage random "uncertainty" remains unsolved.

In another work, [98], an interesting technique is used to acquire both vibration and audible noise via commercial smartphones for a preliminary and portable condition monitoring. This suggests that the multi-sensor method proposed in the paper of the author [84] could improve in the future with even cheaper acquisition equipment or based on different physical quantities, e.g. sound measurement.

In the proposed method [84], moreover, a comparison between current and stray fluxes signatures for fault detection is shown. This is another aspect of the multi-sensor technique presented. As it will be reported in the following, in some cases (depending on load condition) the stray flux spectra offer substantially better visibility on the fault characteristic peaks. The current signal instead has kept more stability in detection of the fault with variation of the load.

As announced before, in some of the laboratory tests, the anomaly of the load of the low frequencies torque oscillations (LFTOs) is added. As shown in other works in literature, e.g. [99], when a speed variation appears in the drive, the harmonic peaks dependent on mechanical speed

spread out in the spectra, becoming wider. In fact, with speed variations the signal becomes non-stationary and a frequency transform cannot fix the harmonic frequencies that change with time (a time-frequency domain is more suitable). However, the proposed method for bearing fault detection with frequency domain transformation was used also in this variable-load cases. In fact, though the detectability of fault decreases, with the less severe oscillation conditions some results remain acceptable.

Finally, some acquisition and analysis of data were performed with the motor supplied by the EATON inverter presented in 3.1.

5.3.2 Experimental tests

The experimental tests have been performed on the test bed of the laboratory presented in 3.1. In this work the accelerometers have been added and used in addition to the electromagnetic signals used in the work presented in chapter 4. In this way the systems assume greater variability in the sensor-physics, and so can detect an higher range of faults as discussed in 5.2.2. The location of the sensors is indicated with green arrows for the two accelerometers and in red arrows for the electromagnetic signals (only the stray flux probes are visible) in Figure 62.

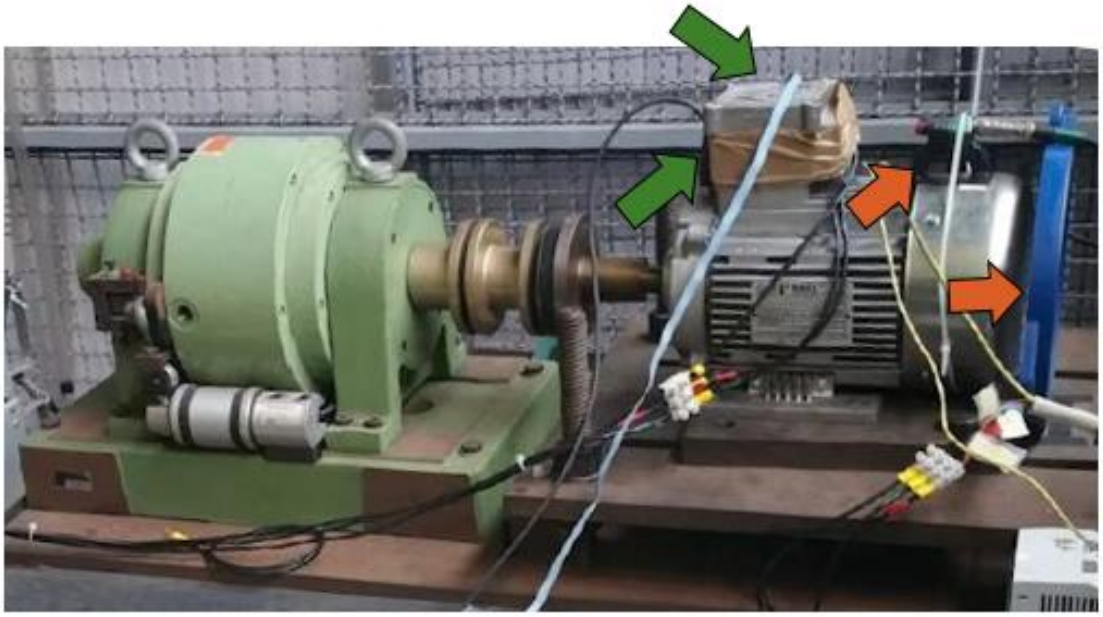

Figure 62: Test bed with positions of the accelerometers (in green arrows) and stray flux probes (in red arrows)

As announced before, the main difference in signatures of the two accelerometers will come from their location. Another important difference between them is given by their different

frequency bandwidth (BW): the piezoelectric accelerometer has 10 kHz BW while the MEMS has a selected BW of 1500 Hz.

The MEMS sensor is a three-axis accelerometer; however, in this work only the Y-axis (parallel to the piezoelectric sensor axis) is considered, i.e. the radial vibration.

The drive-end bearing NSK 6205Z of the motor was replaced for the faulty case experiments by a damaged bearing shown in Figure 63 of the same model. The damage is a structural crack that divides in two the outer ring of the bearing. As stated before, this kind of fault is localized or cyclic, so characteristic harmonics will rise in spectra due to the passage of the rolling elements on the defect. For the series of heathy "baseline" acquisitions, data are acquired with a healthy bearing.

Figure 63: the damaged NSK6205Z bearing.

The NSK bearing is the same used in [66] for the healthy measurements (see paragraph 4.4) and has the following characteristics: standard single-crown, N = 9, d ≅ 7.9 mm, external diameter equal to 52 mm and internal diameter 25 mm.

Three different kinds of load torque are imposed to the motor in the tests:

i) Almost no-load condition. The brake is coupled to the machine but de-energized (there is the drag torque of the brake of about 2 Nm);
ii) Constant load torque. About the 70-80% of the rated torque of the machine is imposed. This correspond to about 7-8 Nm;
iii) Low Frequency Torque Oscillation (LFTO); the torque oscillations correspond to a sum of a constant value and a sinusoidal value (of low frequency compared to the supply fundamental);

The characteristic parameters chosen in the different LFTOs are reported in Table 26.

Table 26: Denomination and characteristics of the LFTO tests.

Denomination LFTO test	Mean load [Nm]	Sinusoidal load (peak) [Nm]	Frequency [Hz]
T1	7	1.5	3.3
T2	7	1.5	2
T3	7	1.5	0.5
T4	7	1.5	0.2
T5	7	1.5	0.1
T6	7	2.5	0.1

The characteristics of the acquisitions are resumed in Table 27. As stated previously, the acquisition set has been carried out dividing each acquisition into smaller measurements to not have to handle with big storage Comma Separated Values (CSV) files. As resumed in Table 27 the number of measurements for each acquisition is 20. For the inverter measurements, a sampling frequency of 120 kHz is used, as in [66]. The Discrete Fourier Transform (DFT) achievable resolution is obtained using (2.1); nonetheless the frequency resolution is set using the "frequencyResolution" parameter of the MATLAB "pspectrum" function, whose values will be exposed in the following.

Table 27: Characteristics of the acquisitions

ACQUISITIONS	Mains supply	Inverter supply
Sampling frequency [kHz]	20	120
# Samples acquired each measurement	2^{19}	2^{20}
# Measurements	20	20
Time of acquisition [s]	≈26·20= 520	≈8.7·20 = 174
DFT achievable resolution [Hz]	0.0381	0.114

All the five signals, i.e. the two vibrations, two stray fluxes and current signals, are collected simultaneously by the DAQ board. In the cases with the inverter supply, fluxes are not measured since with the high sampling frequency (120 kHz) no more than 4 channels can be recorded simultaneously.

5.4 Analysis of the results

The results will be exposed in the next subsections. Firstly, a brief comparison between the two accelerometers will be presented. Secondly, results of the electromagnetic signals will be analysed with the aggregated information coming from vibration signals. Finally, the results with the inverter-fed machines will be discussed.

5.4.1 Analysis of the accelerometers' signals

This subsection will present the vibration signal processing of the two sensors.

Advanced techniques can be used to have a better visualization of the cyclic bearing fault; for example, using a kurtogram, the frequency bands with higher kurtosis parameter can be visible. The parameter is an indication of the impulsiveness of the signal: the higher is the parameter the higher is its impulsiveness (the property to have impulse shapes in the signal). Band-pass filtering the signal around the frequency with higher kurtosis (that corresponds to high frequencies related to resonance frequencies of the bearing) and then performing the frequency transformation of the envelope of the signal lead to a visualization of the BPFO spectra that in other way remain buried in noise (see 4.2, and for example [29]).

In our case, advanced techniques are not implemented because the fault characteristic frequencies were clearly visible on the spectrum of the signal on the first frequency transformation process. This can be due to the quite pronounced bearing crack failure.

In this first comparison between the piezoelectric and MEMS accelerometers, the acquisitions of the signals are carried out under constant load conditions. In Figure 64 the acceleration signals in time domain for the healthy bearings (baseline) are represented. Looking with attention at the picture it is possible to note a slower response of the MEMS sensor, i.e. a smoother waveform, with respect to the piezoelectric sensor. This is due to the limited bandwidth of the MEMS accelerometer with respect to the piezoelectric one. The acceleration signal in this case does not show particular impulsiveness (only a slight magnitude oscillation) and this is characteristic of healthy signals. However, for a more in-depth analysis the signal in time-domain has to be transformed in frequency-domain or statistical parameters of the time domain have to be calculated to have a more precise information. The values of acceleration measured are in the range of ± 0.3 g.

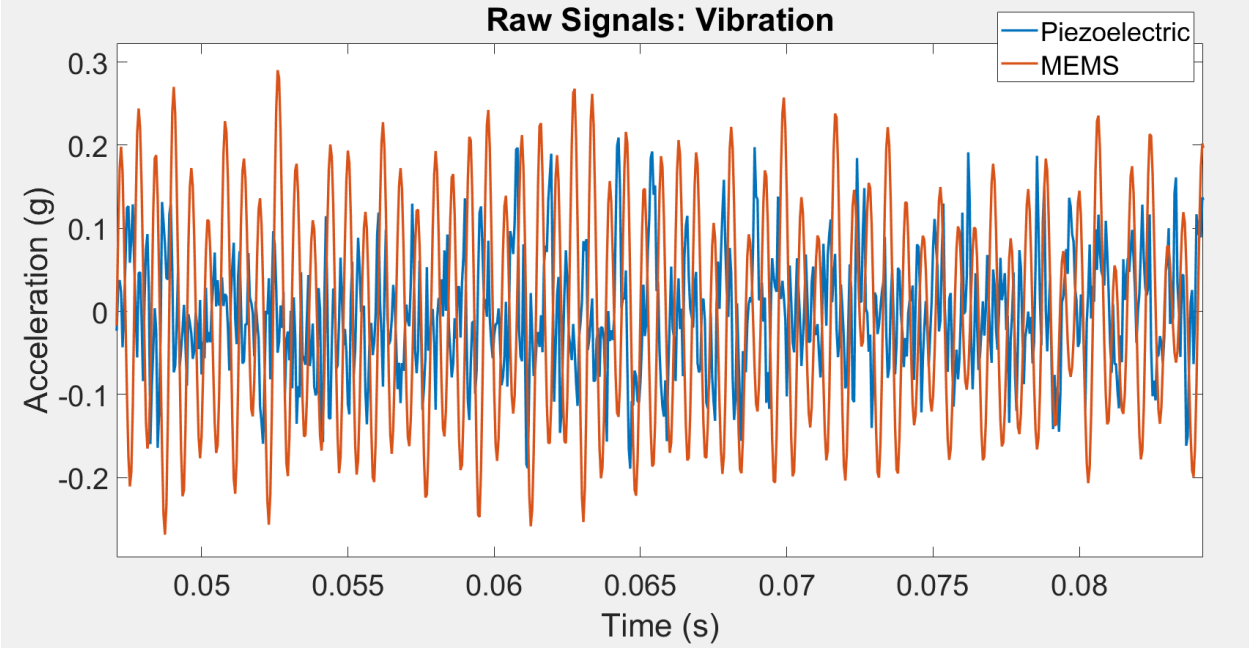

Figure 64: Healthy bearing acceleration signals with constant load.

The waveform of the vibration signal in the time domain of a faulty bearing, as in Figure 65, shows the repetitive impulses generated when one ball of the bearing passes over the crack i.e. every 1/BPFO seconds. As announced before, in this case a very severe fault has been analysed. In other signal representations in time-domain it can be much more difficult to see directly the impulses related to the cyclic fault and advanced signal processing techniques have to be implemented to diagnose the fault.

However, in the vibration waveform analysed the impulses are visible already in the raw signal, indicating that it is important even to check the time-domain signals, since sometimes they can give a first alert of fault presence. The level of vibration has increased with respect to the healthy case. Here, peaks of approximately ± 2 g are present in the waveform.

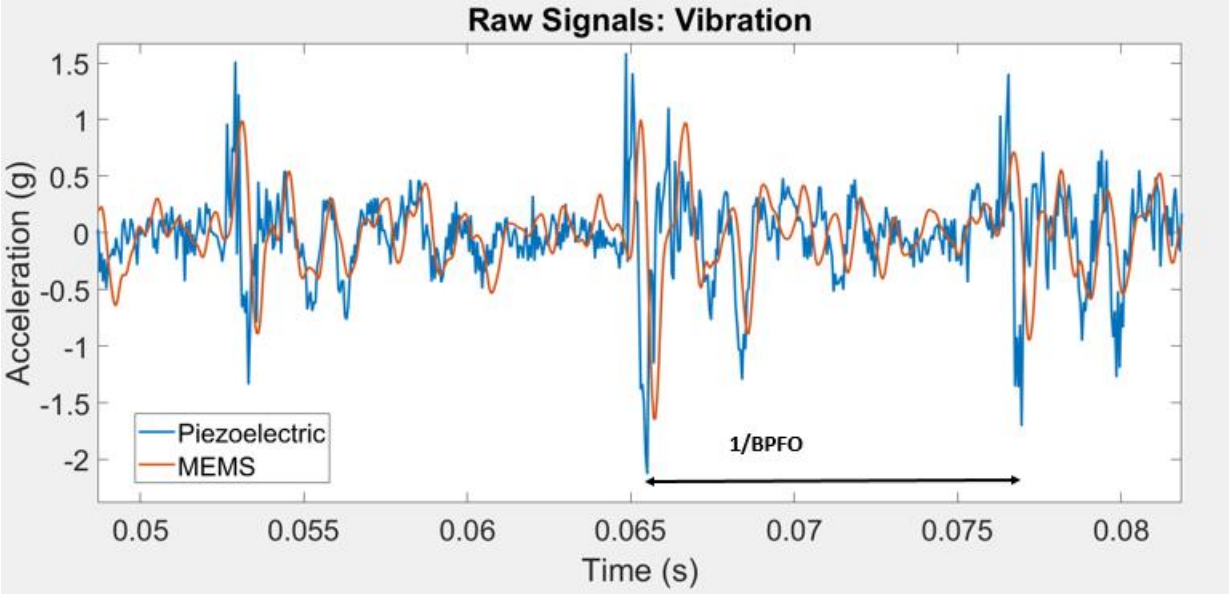

Figure 65: Faulty bearing acceleration signals with constant load.

The time-domain signal can be defined as an infinite sum of sine harmonics according to the Fourier transform theory. By doing the FFT-based frequency transformation of the time domain signal, it is much easier to interpret the signal as the harmonics will be highlighted in the spectra as peaks with a certain magnitude and a corresponding frequency value.

In the case of the cyclic fault introduced, it is possible to see repetitive peaks on the $m \cdot BPFO$ harmonics. This is because the Fourier transform of a pulse train gives a "train" of harmonics in frequency domain distanced by the frequency of repetition of the pulses in time domain (in this case the *BPFO).*

The FFT-based power spectrum is calculated with the *pspectrum* MATLAB function, with the "frequencyResolution" parameter set to 2 Hz, for a first visualization (higher resolutions are possible though 2 Hz was found to be sufficient).

In Figure 66 the presence of the fault is visible: the faulty signals (from piezoelectric and MEMS sensors) have the repetitive peaks on $m \cdot BPFO$, while the healthy one does not (for simplicity, only the piezoelectric signal is represented). The figure shows that good results can also be obtained with a cheap MEMS sensor in case of a pronounced bearing defect. In fact, in this instance the envelope analysis, that implies the study of higher frequency band of the signal, is not necessary. The frequency range in which the analysis occurs for the bearing defect in raw spectra (without envelope analysis) is about 0-1000 Hz, so a sensor with 1500 Hz bandwidth is deemed to be appropriate.

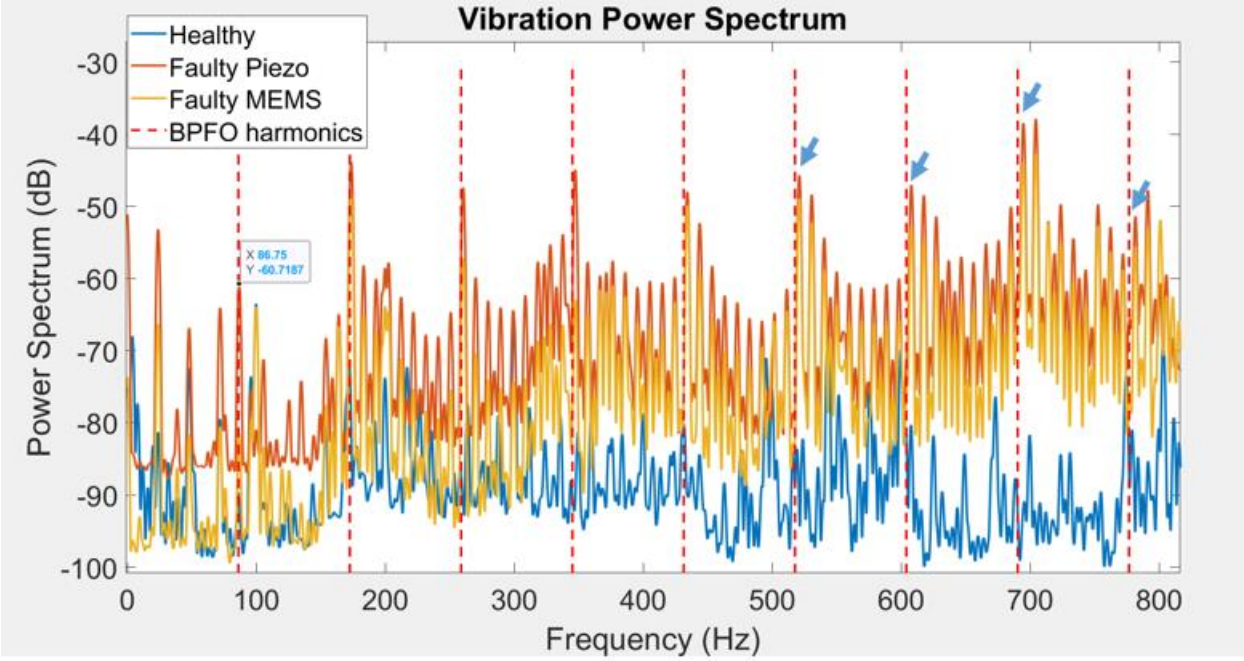

Figure 66 Vibration signals power spectrum with BPFO harmonics.

In Figure 66, the calculated BPFO harmonics are reported in dashed lines. It is possible to see that there is a correspondence with repetitive peaks on the markers of the BPFO. It is important to notice that to affirm that a fault is present, it is necessary that about ten peaks correspond to the characteristic frequencies [29]. If just few peaks (for example four) correspond to the calculated frequencies $m \cdot BPFO$, it cannot be said that a fault is present but further analysis has to be performed to understand if the correspondent peaks are noise or related to the bearing defect.

It can be seen from Figure 66 that the correspondence of the fault peaks with the markers is not exact; especially for the higher frequency peaks (in which the integer coefficient m is higher) there is some "displacement" between the peaks and the calculated $m \cdot BPFO$ frequencies. This is due to the slippage phenomenon as announced in the above paragraph. In Figure 66 these displacements between the calculated frequencies and actual fault harmonics are marked with blue arrow. The value of BPFO calculated for the considered bearing is about 86 Hz for the load condition and 89 Hz for the no-load condition. The more precise derived values will be presented in paragraph 5.4.2.1, in Table 28.

Taking the exact frequency of the fault peak from the graph, visible closer to the calculated BPFO harmonic, and calculating the $m \cdot BPFO$ frequencies with this base frequency leads to a much more accurate correspondence between the peaks and the $m \cdot BPFO$ markers. The method used for extracting these exact-as-possible BPFO frequencies consists in dividing the frequency of a high frequency characteristic peak, recognisable as being near to a $m \cdot BPFO$ marker, by the integer coefficient m. In fact, the difference between the calculated and actual characteristic frequencies become higher at high frequency (because also this difference is multiplied by m) and so with a

given frequency resolution of the spectra it is better to take a high frequency harmonic and then divide it by *m* to obtain the actual *BPFO*.

The difference found between the calculated fundamental *BPFO* (the one with *m*=1) and the value derived from graph is about 0.6 Hz (see Table 28 for more precise values). This difference of frequency will duplicate, triple, etc. with the duplication, tripling, etc. of the coefficient *m*.

Figure 67 shows the spectra of the acceleration signals and the precise correspondences with the adjusted *m·BPFO*. As will be shown in section 5.4.2, this expedient will be useful to improve the matches with the fault harmonics also in the spectra of electromagnetic signals, which have a lower signal-to-noise ratio.

With this method, the chance of detecting false positives and false negatives will be reduced for the entire diagnostic system.

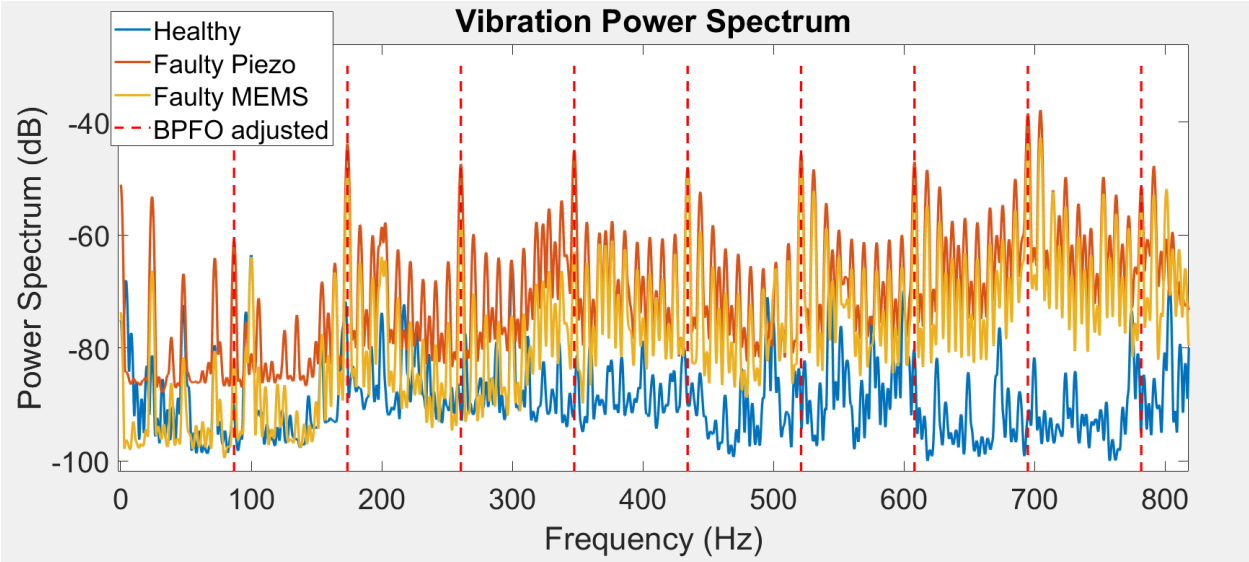

Figure 67: Vibration signals power spectrum with adjusted m·BPFO markers.

5.4.2 Analysis of all signals

In this section, the spectra of the electromagnetic signals are compared with the fault characteristic frequencies f_{bear} derived from (2.16). To obtain the f_{bear} frequencies, both the BPFO frequencies derived from (2.15) and the "adjusted" frequencies coming from the graphs as described in the previous section will be used. The results are shown in the next sub-sections, each one distinguished by a different load condition or supply mode. The two formulas described in 2.3.4 are rewritten here for ease of reading.

For the calculation of the vibration characteristic harmonics, only the BPFO frequency is considered for the work presented in this chapter:

$$BPFO = \frac{n \cdot f_r}{2}\left\{1 - \frac{d}{D}\cos\Phi\right\} \quad (2.15B)$$

with the reference of the variables used explained in (2.15).

For the calculation of the electromagnetic signal fault characteristic harmonics is used:

$$f_{bear} = |f_s \pm k \cdot f_v| \quad (2.16)$$

In which the f_v considered is the BPFO.

5.4.2.1 No load and Constant Load Conditions

The characteristic frequencies BPFO, calculated with (2.15) and derived from the measurements in the vibration spectra, are shown in Table 28, for the two load conditions considered in this subsection. The characteristic frequencies f_{bear} for the electromagnetic signals, calculated from (2.16), are presented in Table 29. Note that relation (2.16) with k = 1, 2, 3, 4 gives eight frequency values (two values for each k, depending on the sign).

Table 28: The characteristic BPFO frequencies for vibration signals

Load condition	Freq. calculated from (2.15) [Hz]	Freq. from graph [Hz]	Difference [Hz]	Measured speed [rpm]
no load	89.17	89.81	0.64	1492
constant load	86.24	86.88	0.64	1443

Table 29: The characteristic frequencies for electromagnetic signals [Hz]

	k = 1		k = 2		k = 3		k = 4	
sign	Calculated with (2.16)	Derived from graphs	Calculated with (2.16)	Derived from graphs	Calculated with (2.16)	Derived from graphs	Calculated with (2.16)	Derived from graphs
	NO LOAD CONDITION [Hz]							
-	39.2	39.8	128.3	129.6	217.5	219.4	306.7	309.2
+	139.2	139.8	228.3	229.6	317.5	319.4	406.7	409.2
	CONSTANT LOAD CONDITION [Hz]							
-	36.2	36.9	122.5	123.8	208.7	210.6	295.0	297.5
+	136.2	136.9	222.5	223.8	308.7	310.6	395.0	397.5

To obtain a better signal-to-noise ratio in the electromagnetic spectra, the "frequencyResolution" parameter is set to 0.5 Hz and the average of the magnitude of the spectra harmonics of the 20 acquisitions is calculated.

Figure 68 and Figure 69 show some examples of peaks detected in the current spectra with the "adjusted" frequencies (those calculated with the information from the vibration spectra). As can be seen, the adjusted frequency markers correspond better to the peaks of the fault, which could otherwise be confused with noise peaks with the calculated frequencies. Figure 70 and Figure 71 show instead some zooms from the average of the 20 measurements of the stray flux spectra.

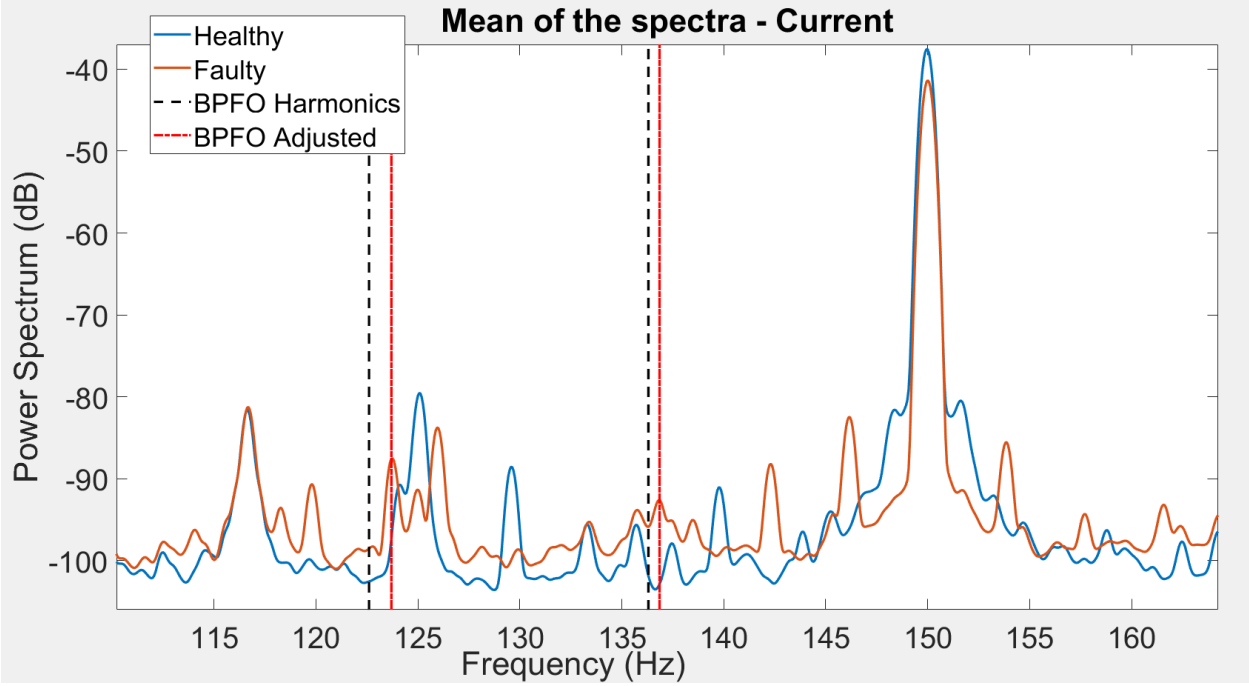

Figure 68: Mean of the current spectra at a constant load.

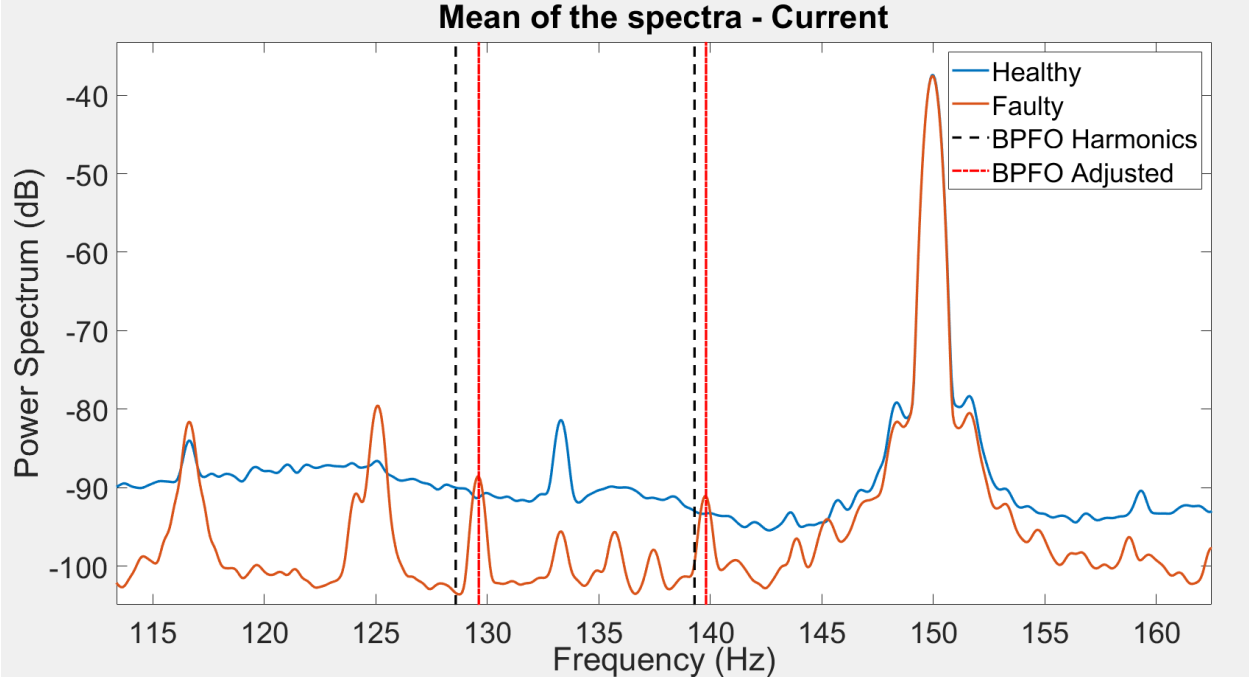

Figure 69: Mean of the current spectra at no-load.

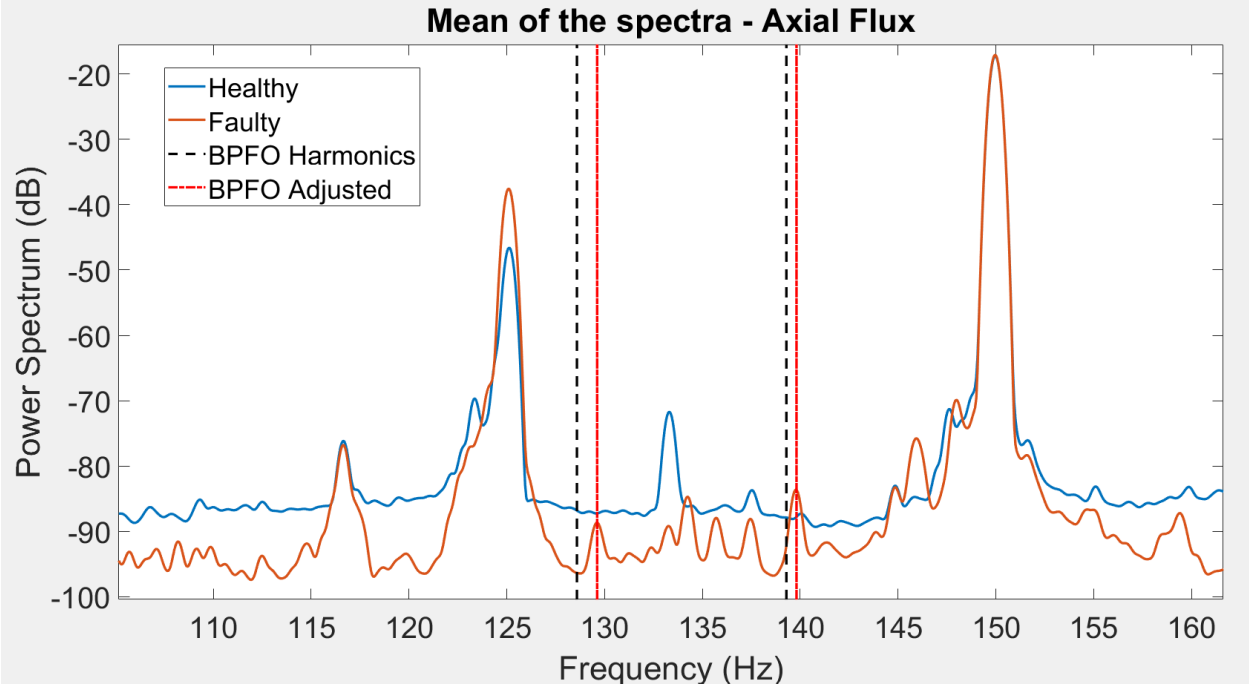

Figure 70: Mean of the stray axial flux spectra at no-load.

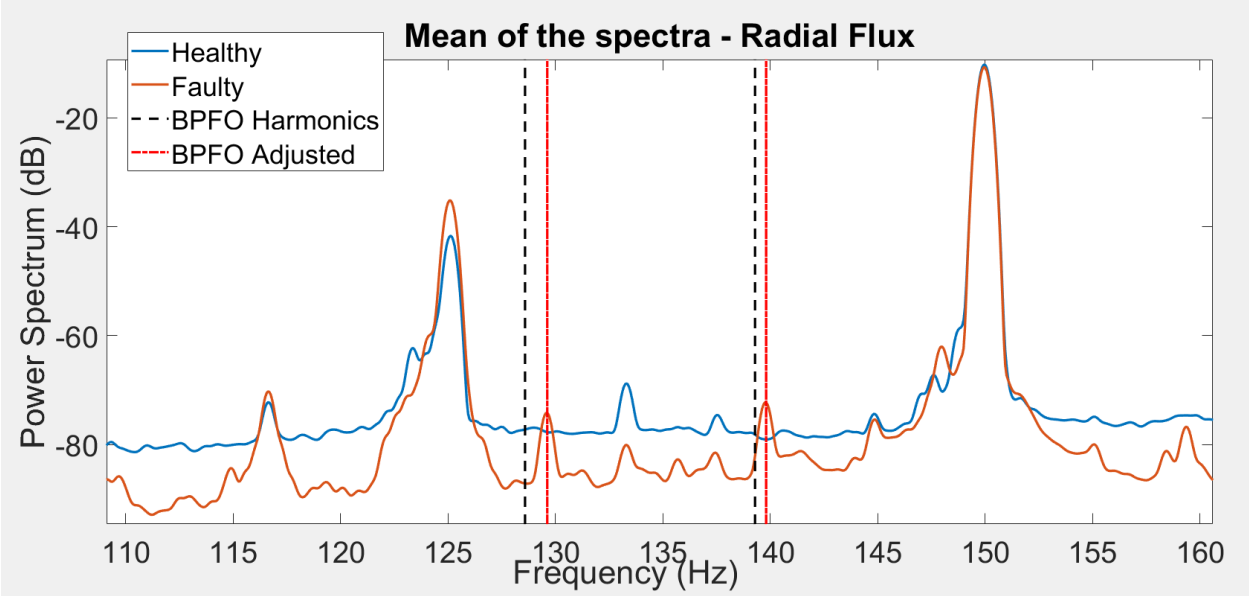

Figure 71: Mean of the radial leakage flux spectra at no-load.

Table 30 and Table 31 summarise the harmonics detected under the two load conditions in the three electromagnetic spectra. The criteria used in Table 30 and Table 31 for checking harmonics are: i) peaks more than 0.5 Hz away from the marked frequency are not counted; ii) peaks of very low amplitude and peaks close to the highest amplitude are signed with the symbol "≈". The detection efficiency is calculated from the number of peak correspondences detected as "successes" divided by the total of the eight frequencies considered. The symbol '≈' is not considered as a success in the efficiency calculation.

Table 30: Characteristic fault harmonics detected with the adjusted frequencies at no-load

Harmonic #	Freq. [Hz]	Current	Axial flux	Radial flux
1	39.81	✓	✓	✓
2	129.62	✓	✓	✓
3	139.81	✓	✓	✓
4	219.43	≈	✓	✓
5	229.62	✓	✓	✓
6	309.24	✓	✓	✓
7	319.43	×	✓	✓
8	409.24	✓	✓	✓
Detection efficiency		75%	100%	100%

Table 31: Characteristic fault harmonics detected with the adjusted frequencies at constant-load

Harmonic #	Freq. [Hz]	Current	Axial flux	Radial flux
1	36.88	×	≈	≈
2	123.76	✓	≈	≈
3	136.88	✓	✓	✓
4	210.64	✓	✓	✓
5	223.76	✓	✓	≈
6	297.52	≈	×	×
7	310.64	✓	✓	✓
8	397.52	≈	≈	≈
Detection efficiency		62.5%	50%	37.5%

The author wishes to point out that, to avoid false positives, the method requires the evaluation of a group of peaks, based on the k coefficient, and not the simple identification of single peaks. Similarly to the vibration spectra analysis, in which about ten fault harmonics have to be detected to state that there is a fault, in the proposed method, on electromagnetic signals spectra, 8 harmonics are considered and the detection efficiency has been calculated on the correspondences with these frequencies.

5.4.2.2 Low-frequency torque oscillations (LFTO)

The variable load applied with the magnetic powder brake provokes a different shape of the peaks in the vibration and current spectra. In fact, the oscillation of the torque will induce an oscillation of the rotational speed of the motor in an open-loop system.

The angular speed variation will spread the rotational frequency dependent peaks in the spectrum, as discussed also in [7]. Fig. 11 shows the vibration spectra with the spread of the peaks due to a torque oscillation of 0.5 Hz (case T3); the spread is more pronounced in the peaks around the frequencies with the highest $m \cdot BPFO$, due to the multiplicative effect of the m coefficient.

The variable load applied with the magnetic powder brake causes the formation of a different shape of the peaks in the vibration and current spectra. In fact, the torque oscillation will induce an oscillation of the motor rotational speed in an open-loop system.

The variation of the rotational speed will spread the mechanical-rotation dependent peaks in the spectrum, as announced before and also discussed in [99]. These peaks are for example visible at the f_r (rotational frequency) and its multiple harmonics. The harmonics dependent on electromagnetic generated vibration, e.g. at $2 \cdot f_s$ (100 Hz for the case considered), do not spread

as the supply frequency do not change (the variation of speed comes from the variation of the load, not from the supply frequency). Figure 72 shows the vibration spectra with peak scattering due to a torque oscillation of 0.5 Hz (the T3 case is considered, see Table 26); the scattering is more pronounced in the peaks around the frequencies with the higher *m* factor, due to the multiplicative effect of the *m* coefficient.

According to the zoom selected, in Figure 72, two BPFO harmonics are visible, the fundamental (for m=1) and the second BPFO harmonic (m=2).

Looking at these BPFO harmonics, a new characteristic signature shape of the peaks can be identified. The harmonics in fact spread in the frequency axis (become wider, especially for higher order harmonics) and usually have two lateral "horns". This shape of the peaks could be identified as a characteristic of this kind of anomaly, guaranteeing a distinguishable signature from other faults.

In this situation, the exact BPFO frequencies are more difficult to identify in the spectrum due to the spread of the peaks; they could be identified with acceptable accuracy in less extreme cases of LFTO, i.e. those with not very low oscillation frequency (the cases T1, T2, T3 in Table 26).

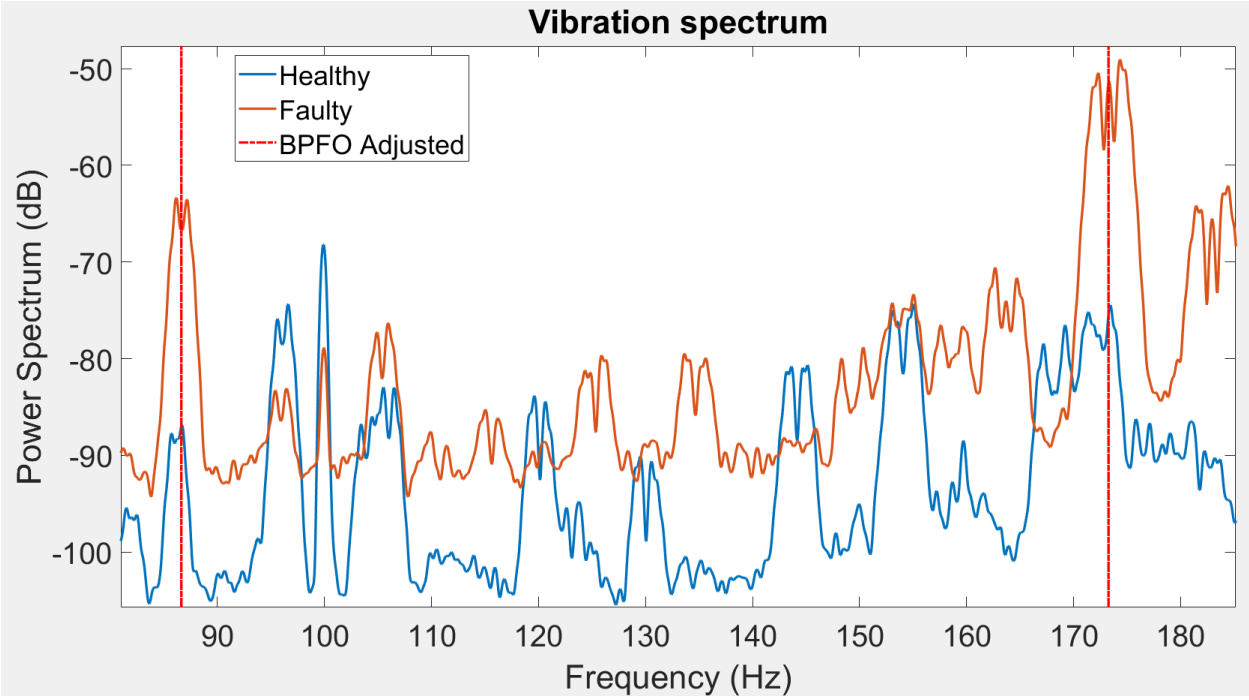

Figure 72: Vibration spectra with T3 oscillating load torque.

Figure 73 and Figure 74 show the signatures detected in the current and radial flux spectra with a torque oscillation of 0.5 Hz (T3 case). Also in these spectra, as in the vibration ones, it is possible to recognise the rotational frequency (or also slip frequency) dependent harmonics as they

spread with double “horns” around the electromagnetic characteristic frequency (f_{bear}) markers or around a central frequency (for the non-fault characteristic harmonics).

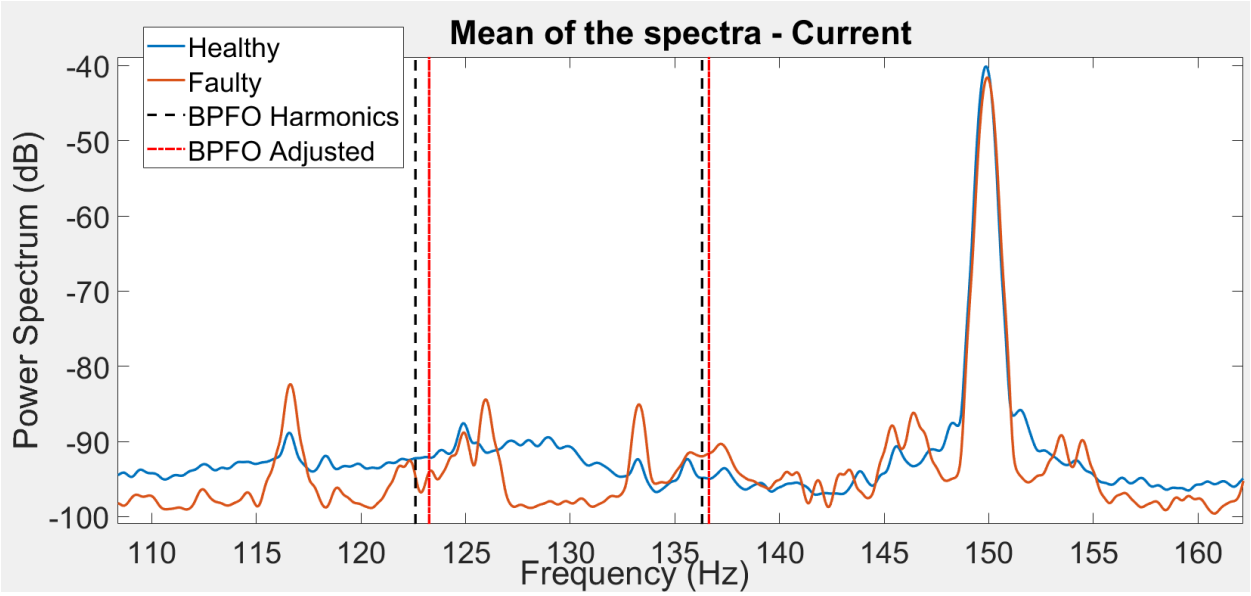

Figure 73: Mean of the current spectra with T3 oscillating load torque.

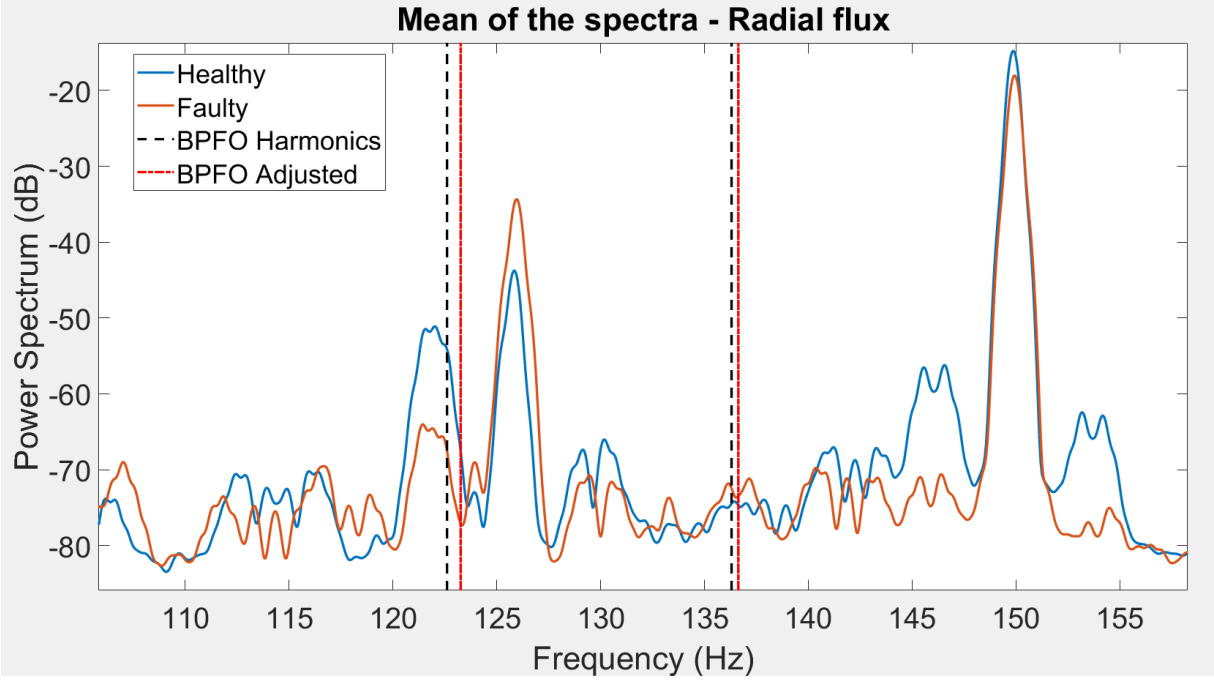

Figure 74: Mean of the radial flux spectra with T3 oscillating load torque.

The BPFO frequencies extracted from the vibration spectra for the various torque loads are given in Table 32. Based on these BPFO values, the corresponding electromagnetic characteristic frequencies f_{bear} are calculated with (2.16), but are not shown for the sake of brevity. Table 33 shows the harmonics detected under these load conditions on the average of the current spectra. The numbers in the first column represent the harmonics in ascending order calculated in each

case with (2.16), using the BPFO in Table 32. Table 34 and Table 35 show the detected fault harmonics in the axial and radial leakage flux, respectively.

Table 32: BPFO detected in vibration spectra for LFTO conditions [Hz]

T1	T2	T3	T4	T5	T6
86.85	86.83	86.63	87.09	87.21	87.21

Table 33: Harmonics detected in current spectra for LFTO conditions

Harmonic #	T1	T2	T3	T4	T5	T6
1	✓	×	×	×	✓	≈
2	✓	✓	✓	≈	✓	×
3	✓	✓	✓	✓	✓	≈
4	≈	×	✓	×	×	≈
5	✓	✓	✓	≈	×	×
6	×	≈	×	✓	≈	✓
7	✓	×	✓	×	≈	×
8	≈	✓	≈	✓	×	✓
Detection efficiency	62.5%	50%	62.5%	37.5%	37.5%	25%

Table 34: Harmonics detected in axial flux spectra for LFTO conditions

Harmonic #	T1	T2	T3	T4	T5	T6
1	≈	✓	×	≈	≈	≈
2	✓	✓	×	≈	≈	×
3	≈	≈	≈	≈	✓	×
4	✓	≈	×	≈	×	×
5	✓	✓	≈	✓	✓	×
6	×	×	×	✓	×	≈
7	✓	≈	×	✓	✓	≈
8	×	×	≈	≈	×	×
Detection efficiency	50%	37.5%	0%	37.5%	37.5%	0%

Table 35: Harmonics detected in radial flux spectra for LFTO conditions

Harmonic #	T1	T2	T3	T4	T5	T6
1	≈	✓	×	≈	≈	≈
2	✓	≈	×	≈	≈	≈
3	✓	✓	✓	✓	✓	≈
4	✓	✓	✓	≈	≈	×
5	✓	✓	×	✓	≈	×
6	×	≈	≈	≈	×	✓
7	✓	✓	✓	≈	✓	×
8	≈	≈	≈	✓	×	≈
Detection efficiency	62.5%	62.5%	37.5%	37.5%	25%	12.5%

From the tables above, it is evident that the fault can still be identified even with an oscillating load, but with some challenges, especially for the most extreme conditions (T4, T5, T6), with very low oscillating frequency, and in the flux signals.

The expedient used previously, to derive the exact fault frequency by dividing the frequency of the *m*-th peak on the vibration spectrum by *m*, has been used also for these LFTO conditions. Anyway, even with this calculation is not easy to identify the exact frequency under oscillating torque conditions, because the peaks for high *m* values become very wide and it is difficult to centre them perfectly. Furthermore, comparing the healthy signal with the faulty one, it is evident that harmonics due to other causes are also present in both signals, as shown in Figure 75; this means that, without the availability of a healthy baseline, it is very easy to misidentify the faulty peaks.

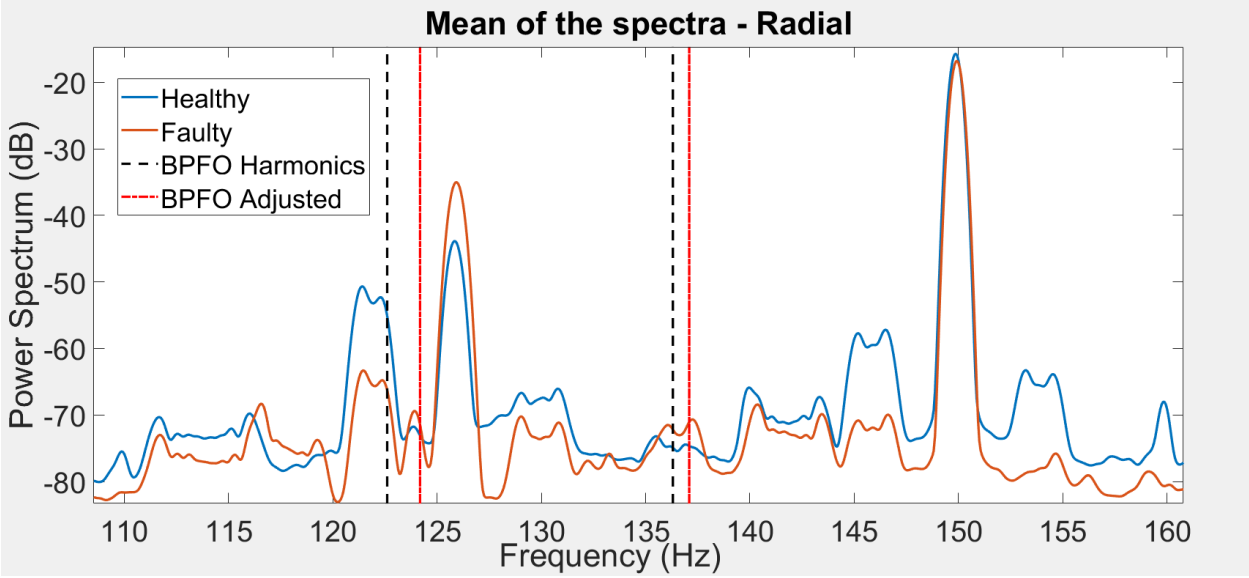

Figure 75: Mean of the radial flux spectra with T4 oscillating load torque condition

5.4.2.3 Inverter supply

With this type of power supply, the acquisition parameters are changed, as shown in Table 27, in order to mitigate the electromagnetic noise coming from the inverter. In particular, for this purpose the sampling frequency has been increased to 120 kHz as discussed in 4.3. Flux signals are not measured in these cases, due to the limitation of the DAQ board inputs to high sampling rates.

Figure 76 shows the vibration spectrum of the piezoelectric signal in this supply condition at no-load. The vibration spectrum clearly shows the fault. Equivalent results are obtained under constant load and oscillating load conditions.

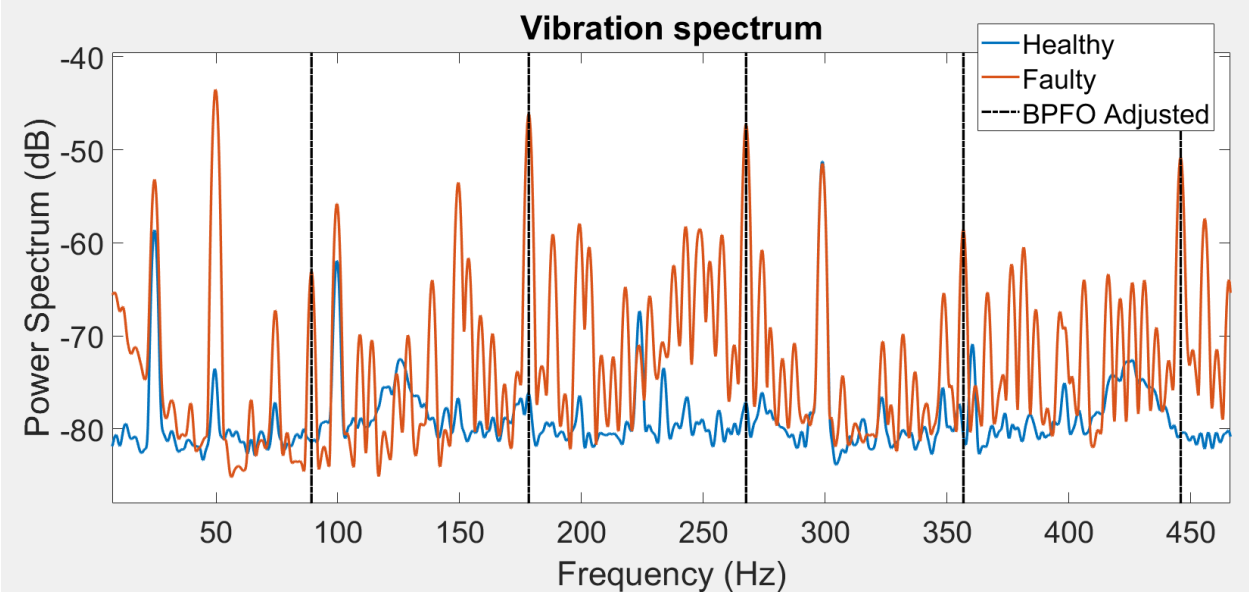

Figure 76: Piezoelectric acceleration spectra with inverter supply at no-load.

Figure 77 shows a zoom of the average of the no-load current spectra and Figure 78 of the constant-load ones. As can be seen, in both healthy and faulty signals, the ground noise level is of the same order of magnitude of the characteristic harmonics due to the fault. This means that this method without any improvement cannot be applied to inverter-powered machines, as pointed out in many previous works, e.g. [66], [100].

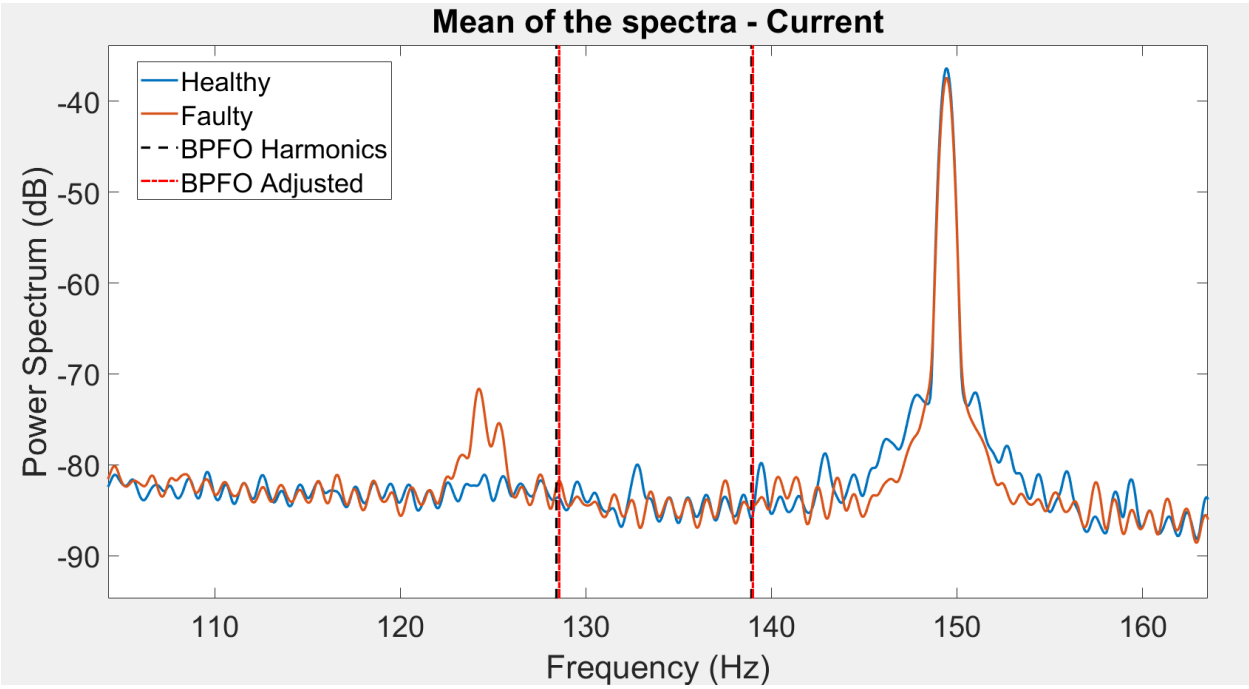

Figure 77: Mean of the current spectra with inverter supply at no-load.

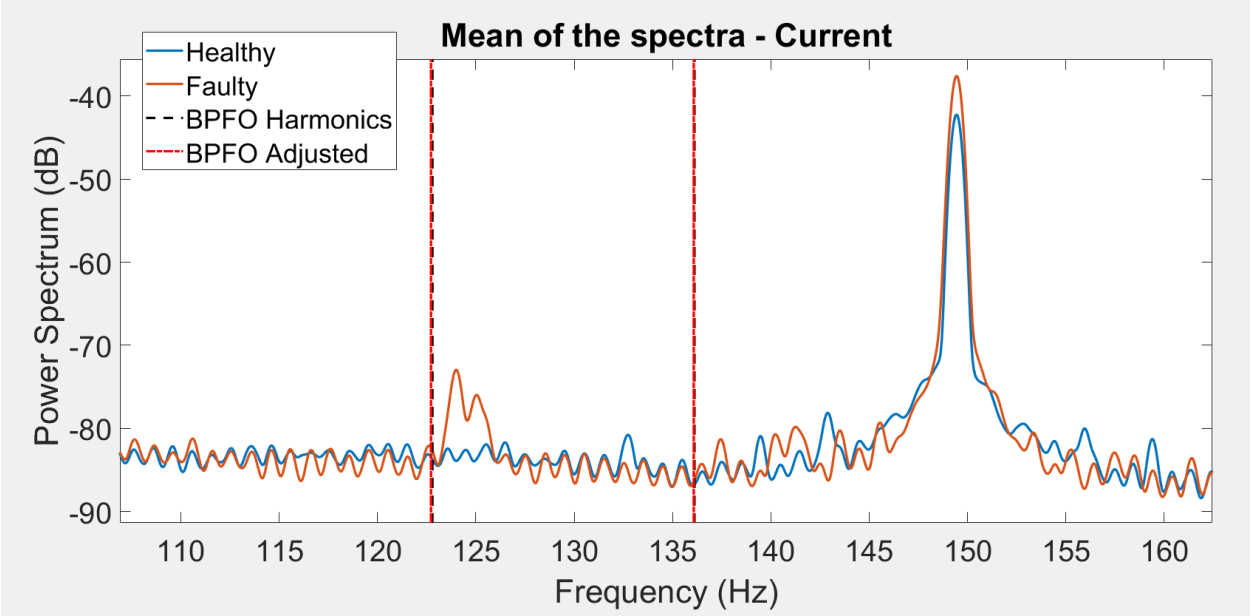

Figure 78 Mean of the current spectra with inverter supply at constant-load.

5.5 Discussion

In this chapter, the theme of the multi-sensor techniques for diagnostics of electrical machines is treated.

In a first instance, a brief literature review is carried out. The first argument treated is about the bearing fault diagnosis, with particular attention to the cyclic bearing faults, derived from localized defects. This kind of fault can be individuated by the monitoring of some characteristic frequencies in the spectra, derivable with formulas and dependent on the bearing geometries and rotational speed of the shaft. The second argument treated in the literature review is about the multi-sensor diagnostic methods. The multi-sensor techniques are interesting because they increase the detectability of a single fault or increase the range and type of fault detectable, for a more complete diagnostic system. However, the cost of the sensors, the complexity of the system, and the maintenance required (batteries and sensors can have shorter life than the motor itself in harsh environments) are to take into account [90].

After the literature review, the work of the author [84] has been presented, in which a multi-sensor approach has been proposed for the detection of bearing cyclic faults in a Squirrel Cage Induction Motor (SCIM).

First of all, a comparison between two type of accelerometers (one of piezoelectric technology and one MEMS) is carried out. Both the MEMS and the piezoelectric accelerometers have provided good diagnostic results. The defect is quite pronounced, but always visible in vibration without the use of any advanced technique. In this condition, an inexpensive MEMS

sensor (with low frequency bandwidth) has proven to be as functional as the wider bandwidth piezoelectric sensor.

Secondly, information from the accelerometer spectrum signatures has been used to extrapolate the correct BPFO frequencies. In fact, the frequencies calculated with the formulas suffer from an uncertainty given by the slippage phenomenon which accounts for 1-2% of the real harmonic value.

With these "adjusted" frequencies, taken from the vibration physics-domain, the fault is also quite clearly visible in the spectra of the electromagnetic signals, confirming its presence. Comparing the signatures of the electromagnetic spectra, it can be concluded that the current signal gives good results under both load and no-load conditions, while the stray flux signals provide excellent fault detection at no-load, but deteriorate their performance under load. This aspect is important in a multi-sensor method: the sensors based on the same physical phenomenon (electromagnetic) can interact between them to improve the detectability of the same fault under different conditions (in this case load-conditions). The fault so can be diagnosed quite well in a range of load conditions with the current signal; at lower load condition, however, the stray flux signal is more sensitive, confirming the presence of the fault for that operating condition.

As a further contribution, a double anomaly condition has been tested by introducing Low-Frequency Torque Oscillations (LFTO) in coexistence with the bearing fault. The LFTO conditions introduce a speed oscillation, because the motor is not speed-controlled. The speed oscillations modify the signals coming from both the vibration and electromagnetic signals. The signal becomes non-stationary as many harmonic frequencies are directly correlated to the rotational frequency or to the slip of the machine, which directly changes with the torque oscillation.

New spectra signatures are revealed and the diagnostic method shows acceptable results in the less extreme cases, i.e. those with the higher oscillation frequency (from 0.5 to 3.3 Hz).

It is stated that the method is effective by monitoring the whole group of peaks calculated with the m and k coefficients in the various signals and not by looking for individual peaks. This is a fundamental aspect of the method, since few harmonics can coincide with the characteristic frequencies, even in healthy spectra, but, when a *series* of harmonics coincides with the characteristic frequencies, it is very likely that the fault is present.

Finally, tests are carried out with an inverter supply of the machine. An improvement in the measurement chain has been executed to reduce the electromagnetic noise coming from the inverter. In particular, the sampling frequency has been increased, as described in the work of the author [66].

On the vibration spectra the fault is still visible with its characteristic harmonics that coincide with the derived BPFO frequencies. As regards the electromagnetic signal spectra, only the current signal has been considered due to limitations of the DAQ board with multiple channels

at high sampling rates. On this signal, however, though the higher sampling frequency used, the characteristic harmonics has not been detected. This can be due to the fact that this method is different from that presented in [66]. In [66] the method was more probabilistic, with a very high number of harmonics to check (the whole range 0-2000 Hz has been considered, with a frequency tolerance of detection of ±2.5 Hz), while the present method is more deterministic, with the monitoring of few harmonics (from 8 to 10 in electromagnetic and vibration signals) but with less tolerance of correspondence (± 0.5 Hz around the derived frequency). Moreover, the type of fault to detect was different as the method has been thought to detect cyclic bearing faults and not generalized roughness defect combined with stator short circuits.

6 Influence of the bearing fault location on signal signatures

6.1 Introduction

The radial force due to the weight of the rotor that acts on the Roller Element Bearing (REB) is of relevant importance to permit the balls or the roller elements to have some adherence on the bearing rings. This fact is important since the roller elements need some adherence to rotate instead of slipping on the rings.

In this chapter the different signatures in vibration and electromagnetic signals due to the variation of the location of the localized fault in the outer ring in a roller element bearing with respect to the load zone will be discussed. This chapter will be mainly based on the work [96], carried out by the author and his research team. The work has been presented at the IEEE 13th International Symposium on Diagnostics for Electrical Machines, Power Electronics and Drives (SDEMPED) conference, held online in August 2021.

In this chapter, firstly, a brief literature review on the theme will be exposed. In particular, the two main aspects treated in [96] will be exposed: the importance of the location of the accelerometers for faults detection and the influence of the angular position of a localized fault in the outer ring of the bearing.

Secondly, the analysis and results of the scientific work [96] will be presented in details.

6.2 Literature review

As announced in the introduction of this chapter, a localized fault in the outer ring has been studied by the author taking into account its different position with respect to the load zone. In the work [96], moreover, the author has carried out some studies on the different signatures presented by two different accelerometers located in different parts of the electrical machine. This review will be focalized on these two main aspects.

6.2.1 Location of the accelerometer sensors

The location of the accelerometer sensors on a machine is very important for the detection of different types of faults. In [101] some indications are given for a correct positioning of the

accelerometer to measure bearing vibration. In particular, for mono-axial sensors, it is recommended that the desired direction of measurement coincides with their main sensitivity axis. The accelerometers are sensitive also to the transverse directions but the signal generated from vibration in these directions is usually ignored as the transverse sensitivity is typically less than 1 - 4% of the main axis sensitivity.

Usually, the position of the measuring point of the vibration is defined according to the fault to look for. For example, in diagnosis of REB the main vibration axis chosen is the radial axis, that can be in horizontal or vertical direction. Usually the radial direction with the lowest stiffness for the measurements is chosen. Also the axial direction can give some information, and can be measured. The most important thing is to locate the sensor in a way to detect the vibration with a direct path from the source to the measuring point. In Figure 79, it is possible to see different locations for the accelerometers for a REB diagnosis. The preferred positions for measuring the vibration of the REB are the position "A" for the radial direction and the position "C" for the axial one. In fact, these positions represent the minimum path length from the bearing to the measuring point. In position "B" and "D" the vibration measured is an overall vibration coming from various sources in the machine. Moreover, the longer paths from the bearing source to the measuring points, in these latter configurations, can bring to more modulation or attenuation to the signal due to mechanical resonances or dampening effect due to the assembled parts of the machine.

Also in [29] the importance of the path of the vibration from the source to the measuring point is highlighted. The vibrations propagate mainly through solid bodies, in contrast to sound that propagates through gases, liquids and solids, and suffer from modulations in the matter they are passing through. These modulations depend on the path crossed by the vibration, mainly due to mechanical resonance of the medium. It is said that the transmission path has a transfer function that modulates the frequency response of the vibration signals. The series of the broadband impulses excited by the shocks in a faulty bearing is modulated in amplitude by two factors:

- The intensity of the bursts depends on the load endured by the roller elements in the load zone; this is usually modulated by the speed at which the fault moves through the load zone
- When the fault is in motion, as in the case of a defected inner ring, the transfer function of the transmission path varies with respect to the fixed positions of the vibration transducers.

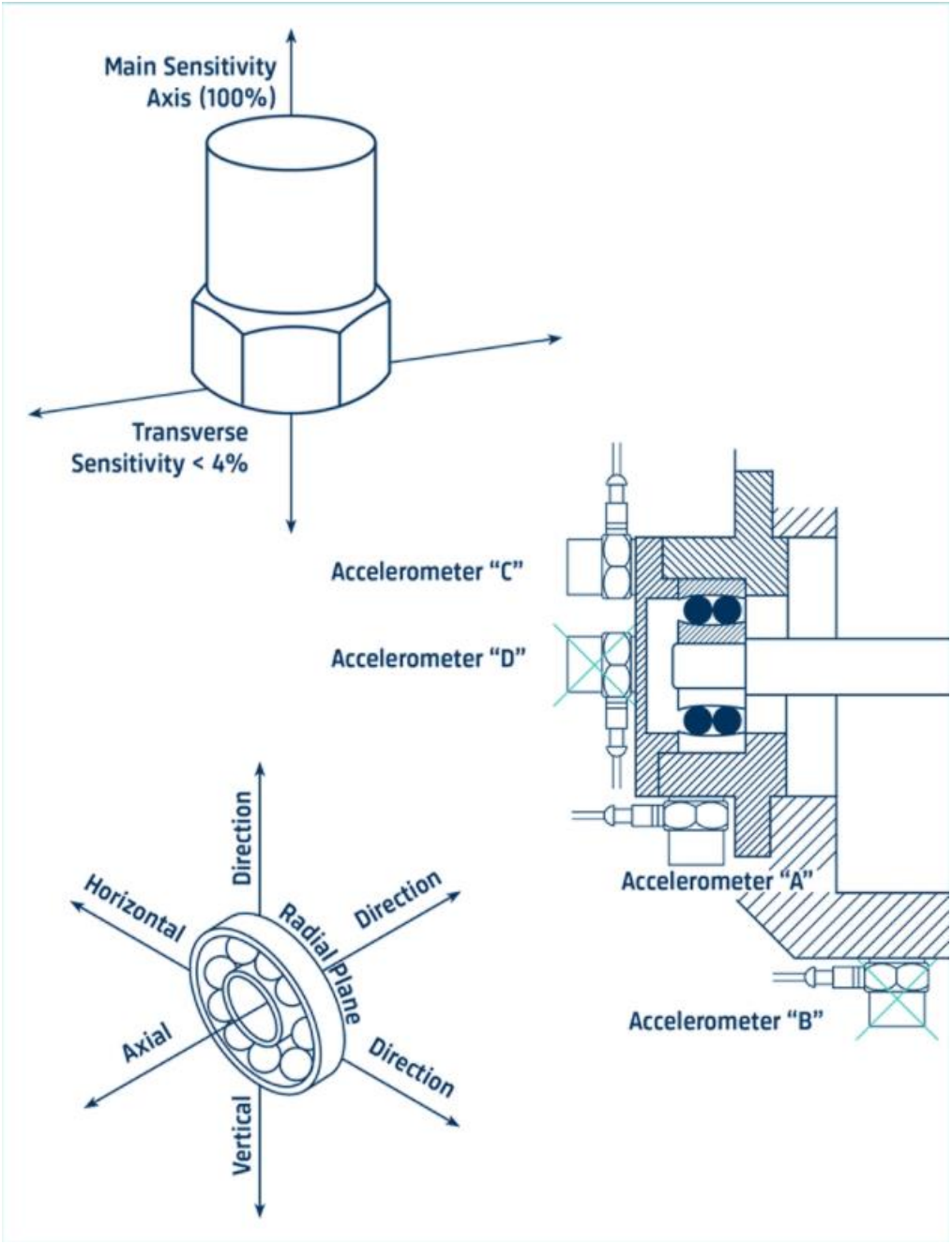

Figure 79: positioning of accelerometers for REB diagnosis [101].

So, it is important to choose an appropriate position to locate the accelerometer so that the transmission path is as shorter as possible and near the part to be diagnosed.

In the bearing datacentre, a database of the Case Western Reserve University (CWRU), [102], measurements for bearing diagnostic systems are carried out and publicly released on the Internet database. In the work, two accelerometers have been located both near the drive-end and the fan-end bearing of a small induction motor, with a magnetic mount. It has been chosen to locate these accelerometers on the upper side of the machine flanges, namely "at hour 12". Moreover, another accelerometer in some measurements is located on the foundation plate of the machine,

far from the bearings under test. These different measurements can be used to compare the different signatures of the vibration for the two bearings and the signature of the vibration on the basement (that include the vibrations from both bearings and other sources) that corresponds to the vibration transmitted to the foundations.

In [35] and [103], the authors use a multivariable analysis to assess the induction motors rotor conditions. Vibrations, current and stray flux signals are monitored to pursue the target. In the works the rotor bars condition is studied taking into account the inter-bar current: when a bar is broken, especially in the section near the end-rings, and not in the central part of the rotor, some current can flow through the rotor core lamination to reach the adjacent bars. With the inter-bar current, the asymmetry of the magnetic field caused by the fault decreases, making the diagnosis more difficult with only current analysis (MCSA). However, the fault is present and can bring to an overheating of the rotor core and other parts of the machine.

To improve the detectability of this fault with the presence of the inter-bar currents, the authors have used a multivariable analysis as stated before. In particular, two vibration signals are used in the work, the radial and the axial vibration of the motor. In fact, since the inter-bar currents flow in a perpendicular direction with respect to the machine axis, the interaction of them with the radial air-gap flux will generate an axial vibration. In particular, characteristic harmonics, related to the slip frequency due to the load, will occur in the axial vibration spectra.

To measure the radial and the axial vibration of the machine, two MEMS accelerometers are installed on the body of the machine in perpendicular position between each other. The position chosen is on the central part of the body of the machine.

So, as stated previously, the positions of the vibration measurements have to be chosen with regards of the fault to be monitored: for a bearing condition monitoring, it is better a measurement point near the bearing, while for other machine parts to be monitored it is better to locate the accelerometer near these parts. In the works [35] and [103], for the monitoring of a rotor condition, a location on the machine-body has been chosen, because the vibrations due to electric faults are transmitted also through the air-gap to the stator and so are measured with better accuracy in these zones of the machine.

6.2.2 Location of the bearing fault with respect to the load zone

The load zone of a bearing is the zone in which the mechanical load is transmitted from the rotating part of the bearing to its stationary part. The mechanical load is usually composed by the weight of the rotating part of the machine (the rotor) and by the weight of part of the equipment connected to the rotating shaft (usually there are more bearings to sustain the equipment and the weight has to be subdivided on these different elements).

The mechanical load distribution changes for radial bearings (i.e. bearings suitable for radial load only), axial bearings or bearings that can support both of these stresses. In the radial bearings, in the case of fixed outer ring and rotating inner ring, considered in the work that will be presented in this chapter, the load zone is distributed at the bottom of the outer ring, where the weight of the rotor acts. A schematic representation of the load zone of this kind of bearing is visible in Figure 80.

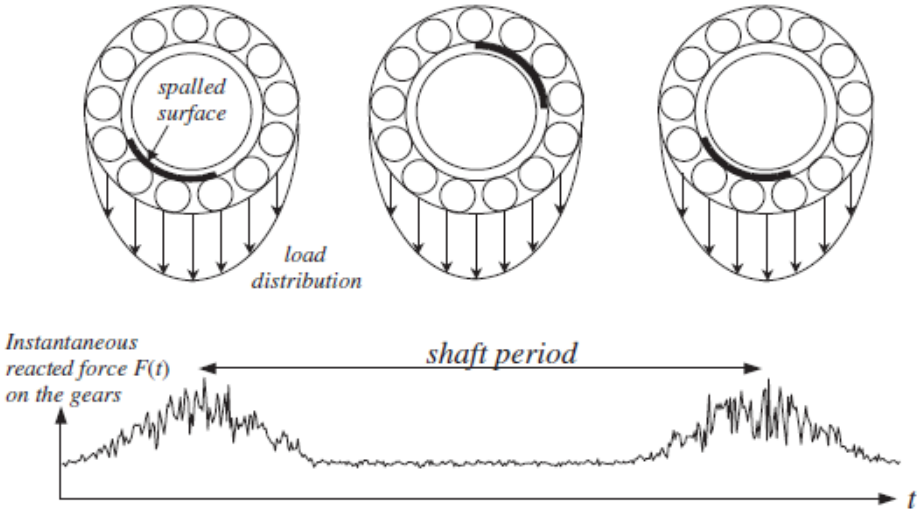

Figure 80: Radial load distribution for a bearing with rotating inner ring and fixed outer ring [29]

In Figure 80 it is also visible how the force on the shaft is modulated by a rotating spalled surface on the inner ring. It is evident that it is important to consider the effects of the load zone in the analysis of the vibration or other signals for the bearing diagnostics (in the case of a rotating defect, the load zone introduce a modulation of the vibration signal).

It has to be said that the load does not reach high values in case of radial rolling bearing, especially for bearings used in small electric motors; the bearings are so lightly loaded in these cases [104]. For very high values of load, or for axial thrust bearing, the journal type bearings are generally preferred. Anyway, as stated before, some level of load is important for the correct operation of the bearing: a too light load does not permit the roller elements to rotate correctly. Skidding of the balls can so occur, leading to an increase in the bearing temperature and deterioration [104]. An abnormal high load instead brings the bearing material to fatigue and spalling and other defects can occur after some time.

An abnormal load on the radial bearing surfaces can occur in case of imbalanced or eccentric load, axial or mixed axial and radial load for radial bearings, outer ring deformation, misalignment [105]. Moreover, the clearance in a bearing, i.e. the average radial distance between the roller elements and the rings, may decrease with respect to its rated value if the fit with the machine shaft is too tight or if too big temperatures differences are present between the outer and

the inner ring. In all of these cases, the fatigue effect increases inducing a more rapid deterioration of the bearing [105].

In normal operation, however, in an electrical machine with horizontal axis, i.e. the case considered in the author's work [96], the only radial load acting on the bearing is due to the rotor weight. If the fault is localized on the rotating inner ring or in a roller element, a modulation in the vibration signal will occur as explained in paragraph 2.3.4. Alternatively, if the fault occurs in the fixed outer ring, no modulation of the fault occurs, as all the rolling elements pass over the defect with the same radial load. This is the fault case considered in [96].

To the knowledge of the author, not many works in literature report a direct comparison between signatures coming from cyclic fault in the outer ring at different angular positions. The few works that the author has found in the literature and considers of most interest are reported in the following.

In [106], a study on early fault detection for localized bearing faults in the outer ring at three different positions is exposed. In the work, the data from the CWRU, freely available from the net [102], are used. The dataset of the CWRU contains data from two accelerometers (on the drive and fan end), at three different positions: looking from the outside the bearing, as it was an analogic clock, the faults considered in the outer ring are at hour 12 (opposite to the load zone), hour 3 (perpendicular to the load zone) and at hour 6 (centred with the load zone). The localized fault was generated through Electro-Discharge Machining (EDM) of three different diameters to simulate three different severity levels of the defect. The data of [102] are presented for four different loading conditions. The induction motor under test has a rated power of 1.5 kW and it was supplied directly from the mains. The load conditions are imposed through the use of a dynamometer. The measured conditions are for no-load, 0.75 kW, 1.5 kW and 2.25 kW load. As the machine is not speed-controlled, there are variations in slip and speed for each load-condition.

In the work [106], time-domain statistical parameters are evaluated for the detection of the fault in different positions and severity levels. In particular, mean, median, standard deviation, variance, max value, min value, skewness, kurtosis value, RMS value, crest factor, impulse factor and shape factor of the vibration in the time-domain are analysed. Comparisons are carried out between data of the different severity levels and fault positions.

The features of standard deviation, RMS, skewness and shape factor of the vibration signals resulted to be the most representative for the fault recognition according to the authors. In almost all the cases analysed the level of the parameters reaches higher values for higher severity of the fault (defect diameter), with some exceptions. Though the RMS value, i.e. the most representative feature of the vibration level, is not higher for all the cases considered at hour 6 with respect to hour 3, that is less radially loaded, in general it is higher in both hour 6 and hour 3 with respect to the less loaded case of the fault localized at hour 12. In general, the diagnostic analyses achieve the detection of the fault with higher values for higher severity and are more or less stable with the

change of the operating condition, i.e. the dynamometer load that corresponds to a change in the motor-speed.

It is interesting to note as the smallest defect (the outer ring hole of diameter of 0.007 inches) generates in some cases higher levels of vibrations than the biggest defects. This fact can be explained as an extended fault but with smoothed edges can generate lower levels of vibration than a smaller one with sharper edges (as in the case of extended spalls discussed in [29]).

As conclusion of the work [106], it is stated that the statistical parameters selected are good indicators of the faults in all the load-speed conditions considered, except for the skewness parameter that in the case with the fault at hour 12 does not give a relation to distinguish the healthy from the faulty cases. Moreover, with the fault at hour 12, the variability of the parameters with the motor speed is higher than in the other cases. This is a confirm to the fact that the angular location of the fault in the outer ring impacts the detectability of the fault. More difficulties to detect the fault are present when the defect is located in less radially loaded zones.

In [107], a study for the detection of defects at different locations in ball bearings, on the outer race, is carried out through vibration analysis and shock pulse method. In the work, measurements are carried out on healthy bearings, on bearing with one defect and on bearings with two defects on the outer ring separated by 180°, 90° or 45° angles between them. The position of the outer ring has been changed for the faulty cases at intervals of 30°, leading to a depth study of the influence of the angular location of the defects to the signal signatures. In Figure 81, the case of the two defects spaced by 45° in various positions is shown.

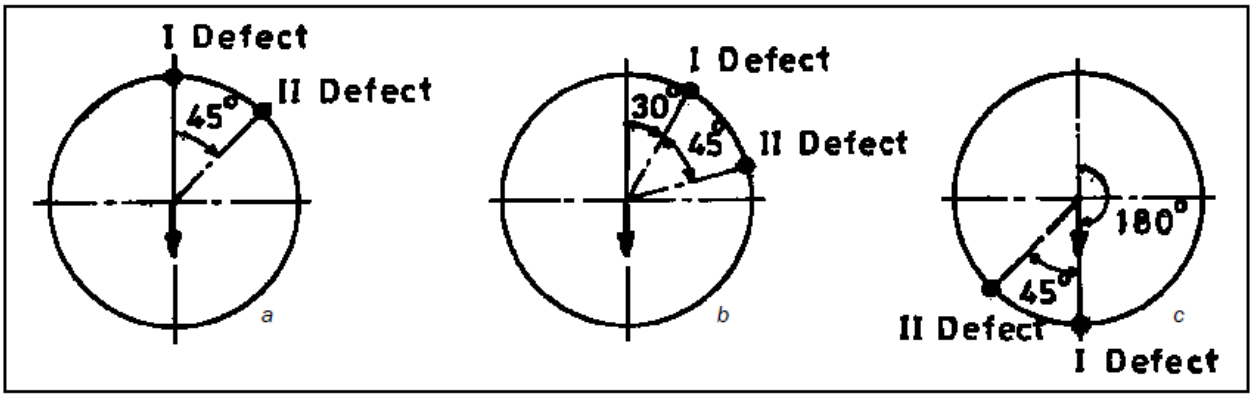

Figure 81: Outer race with two defects 45° apart with I defect at (a) max load position (b) 30° from max load position (c) 180° from max load position [107].

In the motivation of the work, the authors point out that though fatigue pits and cracks will almost always develop in the zone of maximum load, corrosion cracks or manufacturing defects can be at any other angular locations on the races of the bearing. Moreover, the signatures study of the fault in different location reflects the effect of mounting transducers at different angles from the defect location. So the study can have a twofold value as it evaluates both the influence of the

distance between the sensor and the defect and the effect of the angular position of the defect with respect to the load zone.

The shock pulse method is a diagnostic method developed in the late ’60 in which ultrasonic mechanical shock waves, which are provoked by the impacts of rolling elements with the flaws, are analysed. The method uses only high frequency signal (around the accelerometer resonant frequency of circa 32 kHz) and filters out all the other components. The shock pulse due to impacts produces dampened oscillations in the transducer at its resonant frequency. Measuring the maximum value of the damped transient signal provides an indication of the condition of the rolling bearings. The values of the shock pulses generated by healthy bearings have been found empirically as a function of bearing speed and bore diameter. This value is called the initial shock pulse value and, in [107], is subtracted from the shock pulse value of the bearing to be tested to obtain a normalised shock pulse value that is indicative of the condition of a bearing.

In the work, deep groove ball bearings of type SKF 6205 with normal clearance were used. The defects introduced have diameter of 1.5 mm in all cases and are generated by spark erosion technique. Moreover, in [107], a variable radial load is applied to the bearing ranging from 0 to 60 kg and tests are carried out with speed ranging from 500 to 2000 rpm.

Results shown that the location of the fault has a direct influence on the levels of the vibrations and shock pulses. The vibration level, measured as velocity (in mm/s), has reached higher values respectively for the two defects spaced 45°, the two defects 90° apart, the two defect 180° apart and the single defect. Some of the main important results of [107] are reported in the following.

The speed of the machine increases in about a linear way the vibration levels for both the healthy or faulty bearings as shown in Figure 82.

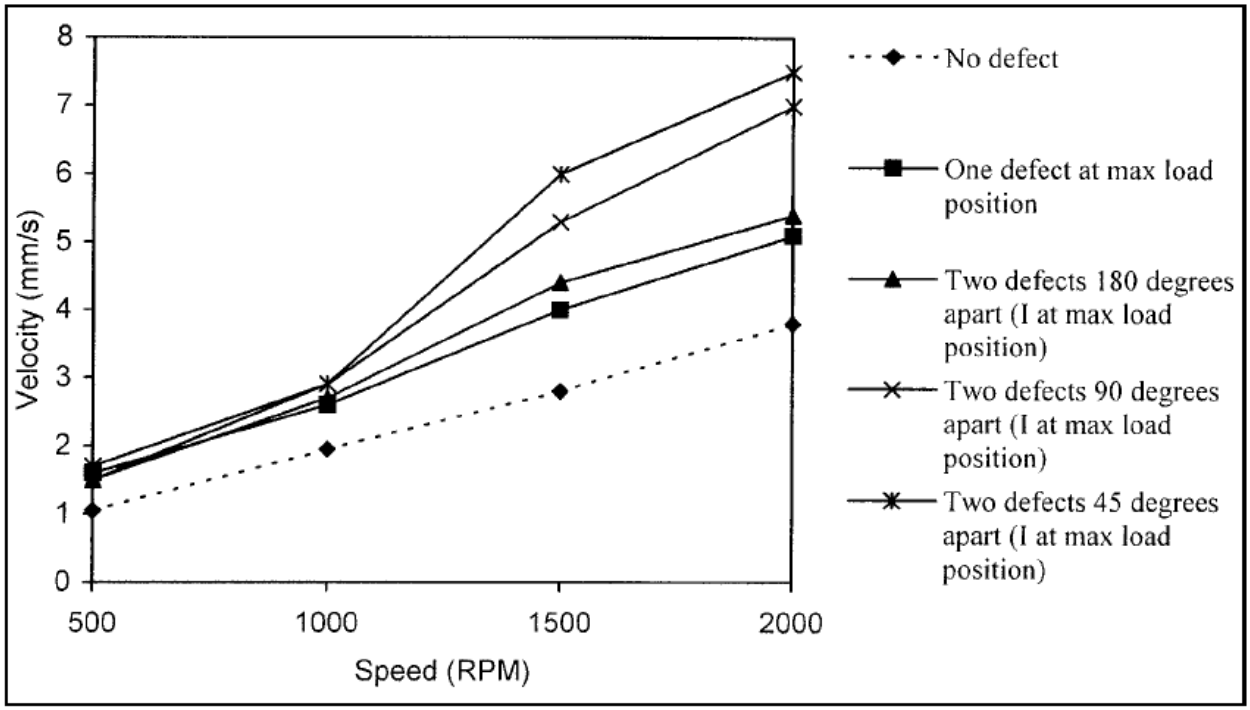

Figure 82: Overall vibrations of the bearings at different speeds [107].

The graphs in Figure 83 demonstrate that the overall vibration velocity levels of a good bearing are almost constant with changing of radial load, but for faulty bearings the levels increase with increasing load.

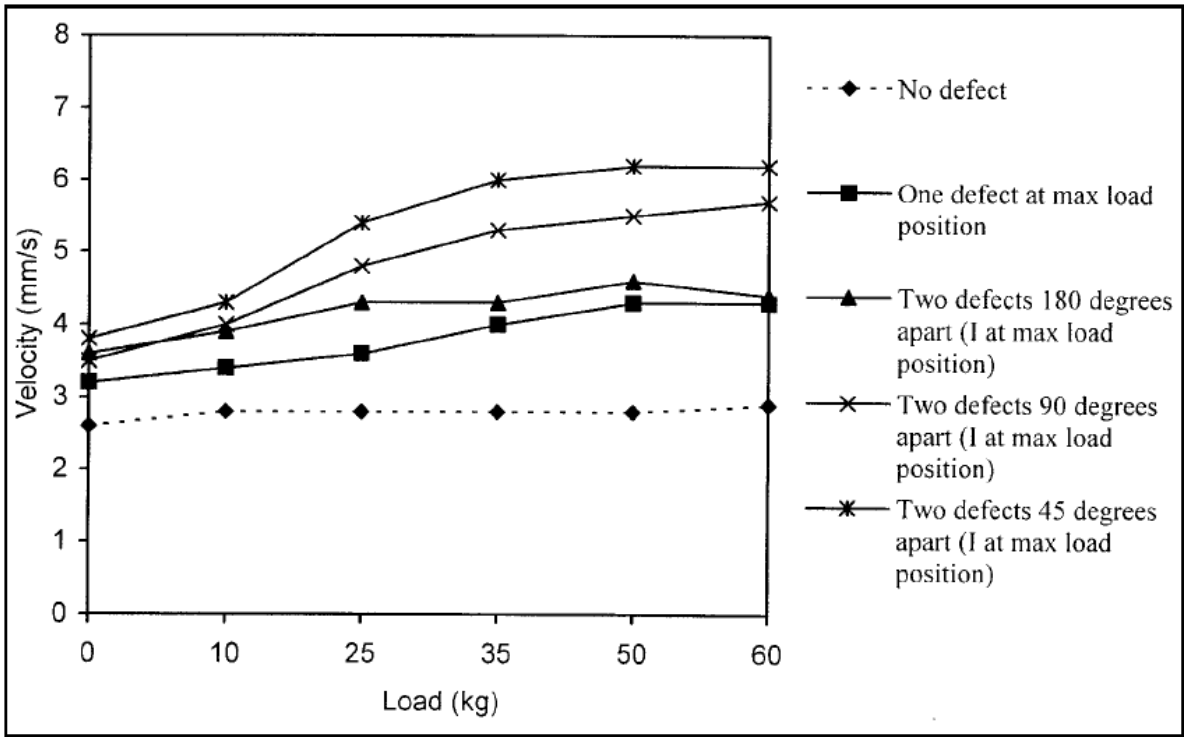

Figure 83: Overall vibrations of bearings at different radial loads [107].

Figure 84 shows diagrams of the overall vibration velocity of all bearings at 35 kg load and 1500 rpm with different defect positions relative to the maximum load axis.

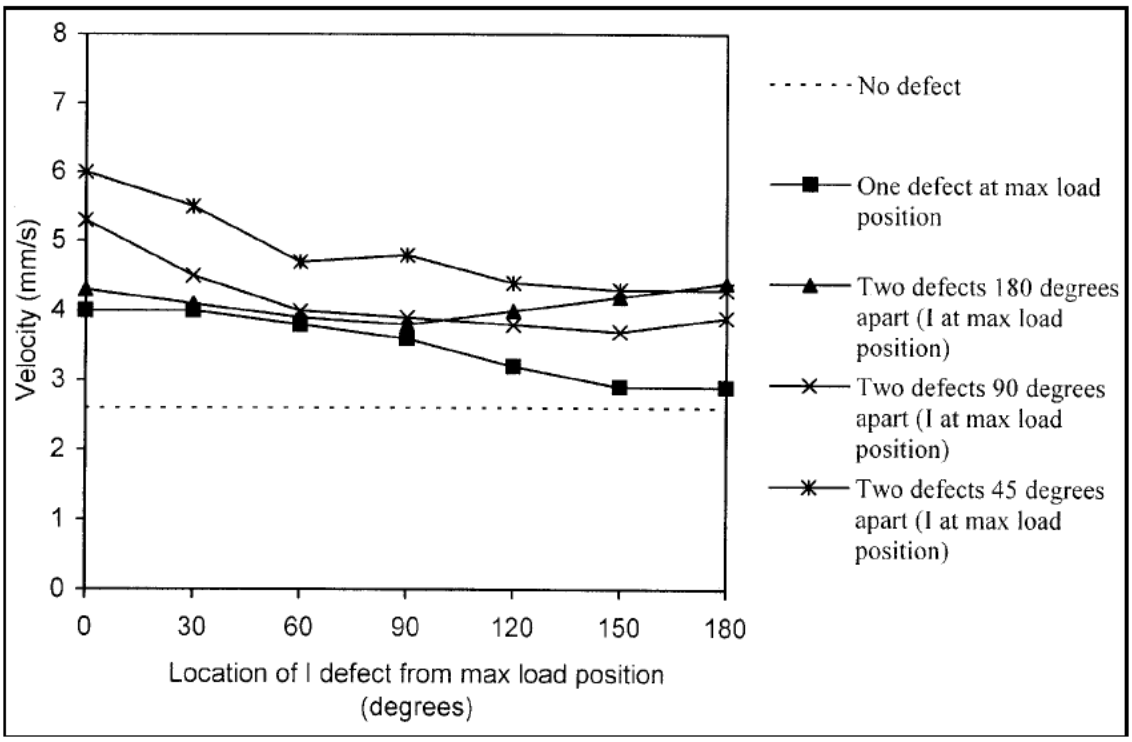

Figure 84: Velocity vibrations of bearings at 35kg of radial load and 1500 rpm with defects at different positions [107].

Figure 84 shows that there is a continuous diminution in the vibration levels of bearings with one defect and with two defects at 45° when the defect position is changed from 0° to 180° because in both cases the defects move away from the maximum load position. Bearings with two defects 180° apart show similar vibration levels at 0° and 180° because the defects only exchange their position relative to the axis of maximum load.

Similar results to that of vibration analysis are obtained with the shock pulse method with the exception that in a low speed (500 rpm) condition it results less effective than vibration analysis. In any case, the study gives an insight of the importance of the issue, with all its facets.

In the next paragraphs, the work [96], proposed by the author of this thesis, will be presented. In the work comparisons of the various signatures are performed for the different hour cases, considering also the electromagnetic signals, which, to the author's knowledge, is not performed in any of the works presented in the literature.

6.3 Proposed method

In the work [96], a new multi-sensor investigation is presented to evaluate the influence of the bearing fault angular location in the outer ring for an induction motor diagnostics.

The motor has been tested in three different load condition: at no-load, with the dynamometer connected but de-energised (only a drag torque is present), at constant-load, at about 60-70% of the rated torque of the machine, and with Low Frequency Torque Oscillation (LFTO).

As in the work presented in 5.3, five signals are acquired and elaborated: two vibration signals and three electromagnetic signals (the stator current and the axial and radial stray fluxes). The tests are conducted for the healthy machine and for the various cases in which the angular position of the localized defect in the outer ring of the bearing is shifted at various "hours": hour 6 (centred with the radial load), hour 3 (orthogonal to the load), hour 12 (opposite to the load), and hour 4.5 (in the intermediate position between centred load and orthogonal load).

A frequency analysis of the signals is carried out, checking the harmonics in vibration and electromagnetic quantities at the frequencies given by (2.15) and (2.16).

The detection efficiency, defined as in 5.3, and the comparisons with the faulty harmonic magnitude are calculated. Moreover, new insights from the two different-located accelerometers are exposed. The majority of the tests are conducted with mains-fed of the motor, but some inverter-fed data are also analysed (especially for the vibration signal).

6.3.1 Experimental tests

The experimental set-up is the same as in the work presented in 5.3. Only some of the main important aspects will be reported here for clarity.

The motor used is the RAEL squirrel cage induction motor, rated 1.5 kW, 4 poles connected to the VIBROTEK magnetic powder dynamometer through a lamellar joint. The bearing tested in the faulty case is the NSK 6205Z, a nine balls deep groove bearing with a crack in the outer ring, mounted on the drive-end of the machine. For the healthy measurements (baselines) a bearing of the same type has been used.

The accelerometers used are the MEMS ADXL335Z, with 1500 Hz bandwidth, mounted on the connection box of the machine, i.e. on the central part of the body of the machine, and the piezoelectric IMI SENSORS M608A11, with 10 kHz of bandwidth, mounted on the drive-end bell of the motor, in the upper position, very close to the bearing to be tested. The stray flux probes are in the same position as in [84]. The sensors' positions are visible in Figure 62.

As stated before, the main issue treated in the work [96] is the influence of the angular position of the fault with respect to the load zone. The positions are indicated by an hour-needle in a 12-hour analogic clock. The positions analysed are visible in Figure 85.

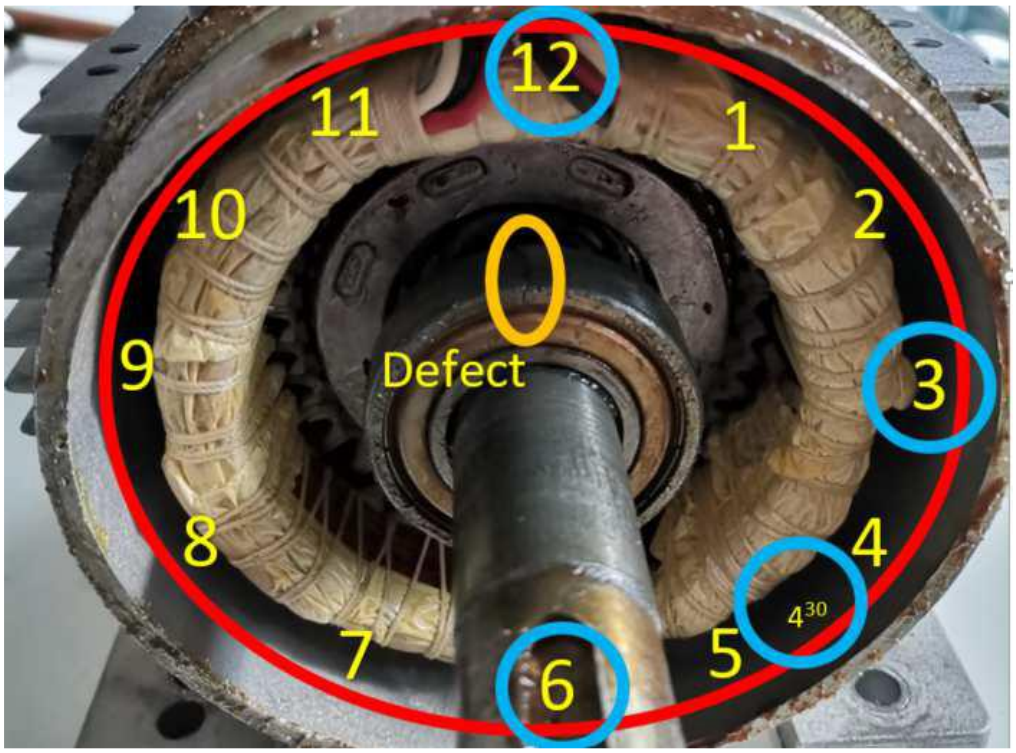

Figure 85: Hour positions of the outer ring defect [96].

To transform the signals into the frequency domain, the MATLAB function "pspectrum", with the setting of the parameter "FrequencyResolution" kept to 0.5 Hz, has been used. The average of the 20 spectra of each condition-case is computed to reduce noise.

The tests with the Low Frequency Torque Oscillation (LFTO) are reduced to five, with respect to [84] in which six LFTO conditions were considered. For each hour-case, the LFTO conditions considered have the characteristics shown in Table 36. As stated in [84], the introducing of the LFTOs makes the detection of the fault more difficult as it is a double anomaly condition of the machine.

Table 36: Characteristics of the tests with LFTO used in [96].

Denomination	Mean load [Nm]	Sinusoidal load (peak) [Nm]	Frequency [Hz]
T1	7	1.5	3.33
T2	7	1.5	2
T3	7	1.5	0.5
T4	7	1.5	0.2
T5	7	2.5	0.1

Some tests are carried-out with the EATON inverter presented in 3.1. Different sampling frequencies have been used for the mains and inverter tests, as explained in 5.3.2, with the details of each acquisition, available in Table 27.

6.3.2 Analysis of the vibrations

6.3.2.1 Piezoelectric signal at no-load and constant-load

In this subsection, the piezoelectric sensor data are presented for the purpose of comparing the signals at different fault positions. This transducer is more accurate than the MEMS one and is placed close to the bearing under test. Figure 86 presents the spectrum of the vibration signal at no load, for the healthy bearing and the defective bearing at hour 6 (with an offset of +20 dB for the healthy signal for a better visualisation).

The BPFO frequencies are determined using the formula reported in (2.15). The frequencies are marked with dashed-lines on the graphs. These calculated frequencies are adjusted in value using the method explained in [84] to avoid the uncertainty caused by the slippage phenomenon. As it can be seen in Figure 86, there are peaks of considerable magnitude in the faulty signal at characteristic frequencies, but there are also small peaks at the same frequencies in the healthy signal. This indicates that even the healthy bearing may have a small defect in the outer ring, perhaps due to the continuous mounting and dismounting of the bearing for laboratory testing. However, the magnitude of the peaks is about 30-40 dB for the defective condition and 10-25 dB for the healthy one, indicating that in the latter case the defect is much less severe.

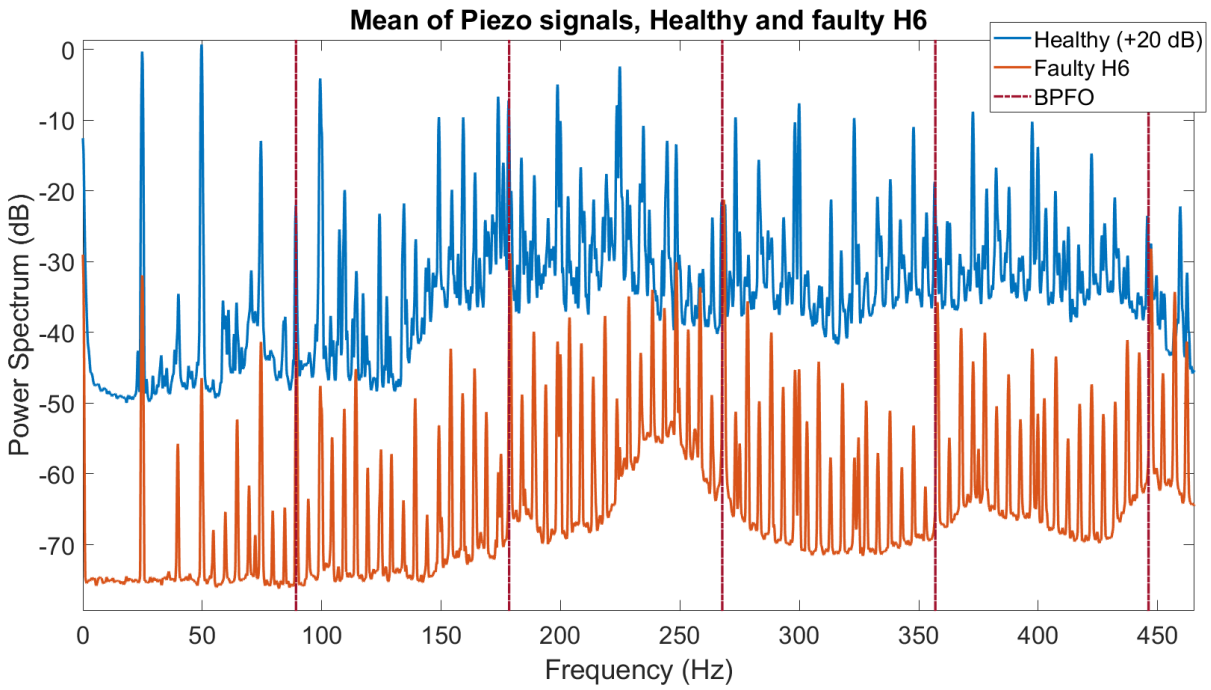

Figure 86: Piezoelectric signal spectra for healthy and faulty bearing at hour 6, with no load.

The first seven peak magnitudes at BPFO frequencies are registered and comparisons between the faulty case and the baseline are carried out. The differences between the peak magnitudes of the faulty cases and the baseline, at no-load and constant load, are listed in Table 37 and Table 38.

Table 37: Differences in amplitude for the first 7 BPFO harmonics of the no-load piezoelectric signal [dB].

CASE	1	2	3	4	5	6	7
12 vs Healthy	12.6	15.9	24.6	12.6	32.0	25.5	33.1
3 vs Healthy	19.6	25.8	34.8	25.3	34.7	34.1	38.0
6 vs Healthy	20.7	17.9	40.7	23.3	36.0	34.0	39.2
4.5 vs Healthy	22.0	13.7	48.4	24.7	21.3	30.9	33.9

Table 38: Differences in amplitude for the first 7 BPFO harmonics of the constant-load piezoelectric signal [dB].

CASE	1	2	3	4	5	6	7
12 vs Healthy	17.2	16.8	37.9	19.5	33.4	29.3	30.5
3 vs Healthy	22.2	24.4	31.6	35.7	41.4	40.1	35.3
6 vs Healthy	17.9	14.5	39.7	23.8	26.4	35.5	33.9
4.5 vs Healthy	24.0	12.5	34.5	30.7	21.4	37.6	29.5

In Figure 87 and Figure 88 the amplitudes of the harmonic differences are plotted: it can be seen that the deviations of the harmonic values of the 12 o'clock fault are of lower amplitude, especially at no load. This corroborates the argument that the vibration intensity is related to the position of the fault in relation to the load zone.

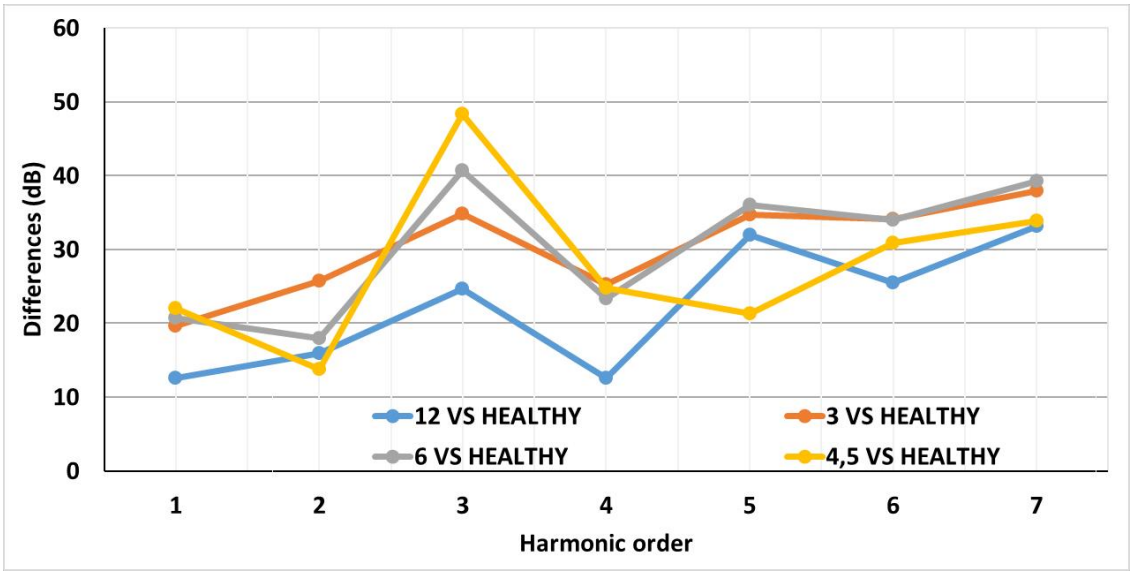

Figure 87: Differences in amplitude between faulty and healthy cases for the first 7 BPFO harmonics of the piezoelectric signal, at no-load.

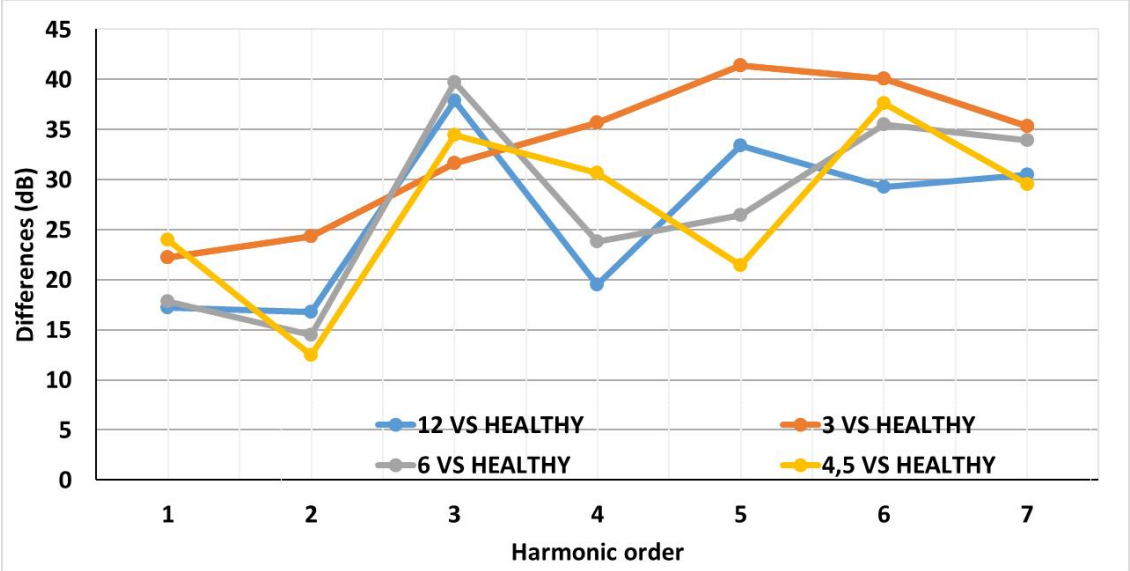

Figure 88: Differences in amplitude between faulty and healthy cases for the first 7 BPFO harmonics of the piezoelectric signal, at constant-load.

The BPFO harmonics frequencies are calculated using (2.15), but, as stated before, they are corrected in values through cursor measurements on the spectra as in [84] (see paragraph 5.4.1). The frequency values are shown in Table 39 and Table 40 for the no-load and constant-load cases

respectively. The differences among the calculated and measured BPFO values are shown as well in Table 39 and Table 40; they are determined using the following formula:

$$\Delta f = BPFO_{\text{calc}} - BPFO_{\text{detected}} \tag{6. 1}$$

Table 39: BPFO frequencies calculated using the formula and measured on the spectra, with their differences values. No-load cases.

Hour-case	BPFO calculated (Hz)	BPFO detected (Hz)	Δf (Hz)
12	89.23	89.30	-0.07
3	89.29	89.80	-0.51
6	89.23	89.45	-0.22
4.5	89.18	89.85	-0.67
HEALTHY	89.18	89.17	0.00

Table 40: BPFO frequencies calculated using the formula and measured on the spectra, with their differences values. Constant-load cases.

Hour-case	BPFO calculated (Hz)	BPFO detected (Hz)	Δf (Hz)
12	86.30	86.51	-0.21
3	86.30	86.85	-0.55
6	86.42	86.72	-0.30
4.5	86.30	86.88	-0.57
HEALTHY	86.30	86.04	0.26

The frequency differences Δf are represented in Figure 89. It is evident, from Figure 89, that the values of Δf change with the position of the fault and this is due to the phenomenon of slippage, i.e. a random slip of the balls on the ring raceways; this slip assumes different values in the different cases analysed. It is worth noting that the calculated frequencies are always lower than those measured: since slippage can only reduce the speed of the cage train, this fact seems to be due to the contact angle α, which can vary from 0° during slippage, as explained in [29], while in the calculation it is kept constant at 0°. Furthermore, from Figure 89 it can be observed that the phenomenon of slippage seems to be almost unaffected by the load conditions of the machine, as the two trends are very similar.

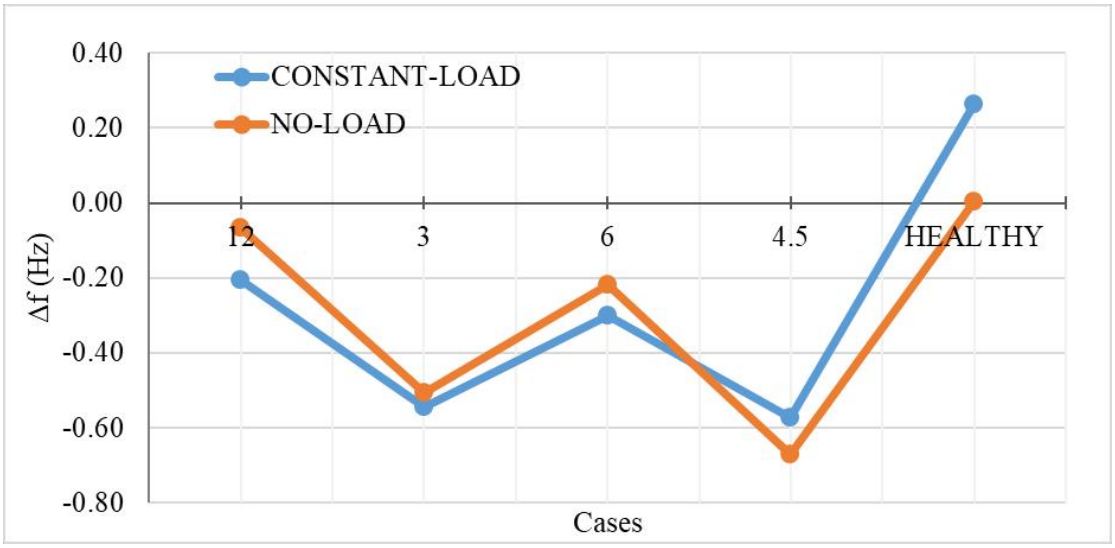

Figure 89: Differences between calculated and measured BPFO frequencies.

6.3.2.2 MEMS vibration analysis

It has been noticed that at load, the accelerometers shown different signature's spectra. This is attributed, by the author, to their different locations on the body of the machine.

In a first instance it can be noticed that the MEMS signal, particularly for the healthy case, is rich in low-frequency harmonics, especially at 4.06 Hz and multiples, as can be observed in Figure 90. The fact can be explained in this way: since the Lorentz force produces vibrations at a frequency equal to twice the frequency of the current that generates them, it is easy to see that the harmonic component at 4.06 Hz is originated from twice the rotor current frequency f_{slip}, where $f_{slip} = s \cdot f_s$. In fact, in the constant-load case analysed, the slip was 4% (the measured speed was f_r = 1439 rpm), f_s is 50 Hz and thus f_{slip} results in approximately 2 Hz.

These harmonics are much more noticeable in the MEMS signal than in the piezoelectric one, presumably because they originate from the rotor and therefore from the central part of the machine; since the MEMS is placed in the centre of the machine, while the piezoelectric is placed at one end of it (above the bearing), the former transducer will be more inclined to pick up these harmonics. Harmonics multiple of 4.06 Hz are also evident at higher frequency parts of the spectrum in both piezoelectric and MEMS signals. Some of these high-frequency signatures will be shown in the successive sub-section dedicated to LFTO conditions 6.3.2.3.

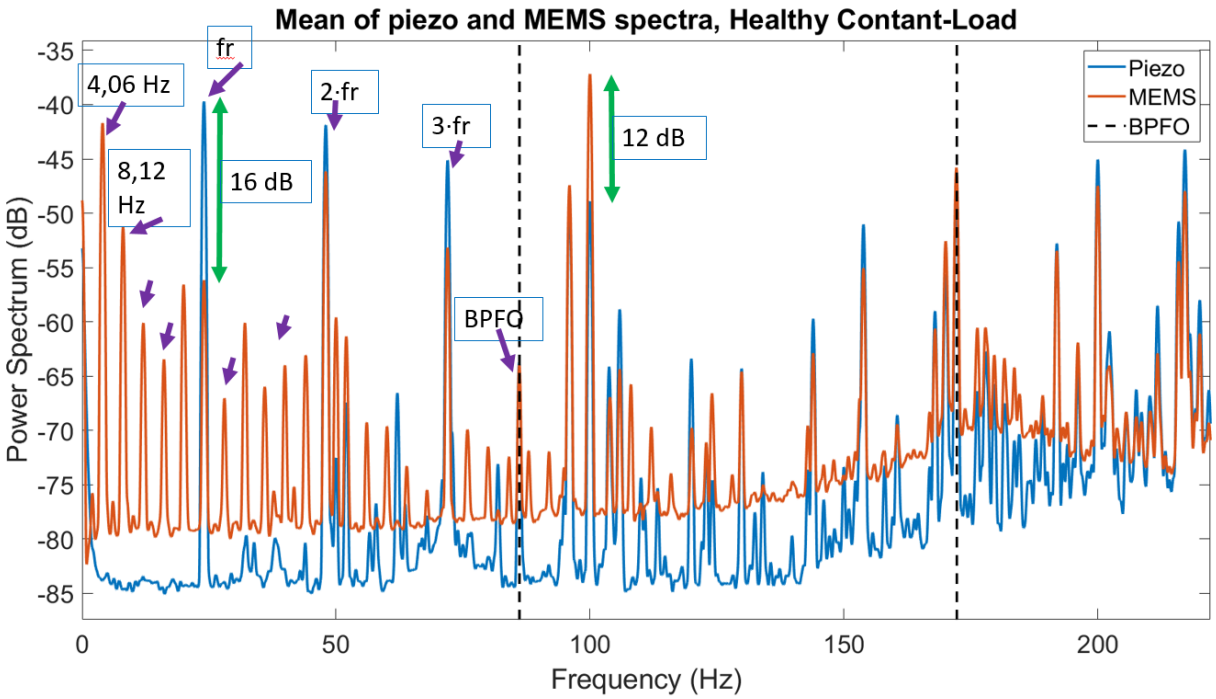

Figure 90: Motor's constant-load MEMS and piezoelectric spectra, with healthy bearing.

The importance of sensor position is also highlighted by the fact that the harmonic content of the rotational frequency f_r is more prominent in the piezoelectric signal (16 dB higher) than in the MEMS one. Similar results are noticeable for the multiple of f_r. Conversely, the components due to the Lorentz and Maxwell forces resulting from the excitation generated by the stator currents at twice the supply frequency f_s, i.e. at 100 Hz, are more strong in the MEMS signal (12 dB higher) than in the piezoelectric one. The author wishes to point out that the power spectra are not normalized in the work, but the voltage signals coming out from the accelerometers have been converted into g values, to make comparisons meaningful, since the two accelerometers have different sensitivities.

These remarks are found to be valid for faulty spectra as well, although in these cases the slip frequency harmonics are more hidden by the faulty and noise harmonics.

Although a modal analysis of the machine might give more precise findings, the above consideration means that the placement of the sensor can be crucial in the effectiveness of the diagnosis, depending on the fault to be detected: for a bearing defect diagnostics, it is preferable to measure vibrations in the adjacent area (as stated in many works in literature), but for broken bars, rotor related faults or in general electrical fault, it might be better to place the accelerometer on the machine's central body.

6.3.2.3 LFTO conditions

Data were also collected in cases with LFTO conditions; the features of these experimental tests are shown in Table 36. In the work [96], due to space constraints, it is not reported an in-depth study of LFTO tests. However, some general but remarkable observations are presented, and so they will be reported in this thesis.

Torque oscillations generate sidebands in the spectra signature of vibrations and electromagnetic signals. Most notably in vibration spectra, these sidebands are visible for T1 and T2 conditions, while for lower oscillation frequencies these lateral bands "merge" with the central one because of the fundamental harmonic changing frequency due to rotational speed variations (with very low frequency torque oscillation the machine has more time to adapt its speed to the load, in other words, the inertia of the machine can be neglected and then the signal is no more stationary). The lateral bands are noticeable around the rotational harmonics, i.e. $k \cdot f_r$, or, in the case of a presence of a localised fault, for example on the outer ring, around the characteristic frequency of this fault and its multiples, i.e. $m \cdot BPFO$, with special reference to $m \geq 2$.

These sidebands may also appear around certain higher frequency harmonics, e.g. around the slot pass harmonics. The slot pass harmonics are vibration harmonics due to the effect of the rotor or stator slots that introduce a deformation of the magnetic field in the machine as showed in Figure 7. This is called also slotting effect. The slot pass harmonic f_{sp} is defined by the formula (6.2) (for the definition, see for example [108]):

$$f_{sp} = Q_{rot} \cdot f_r \tag{6.2}$$

where Q_{rot} is the number of rotor slots, and f_r is the rotational frequency in hertz.

This harmonic is usually recognizable in the high frequency part (around 1000 Hz depending on the parameters of (6.2)), as it is high in amplitude.

In [96], it has been noticed that around the slot pass harmonic and other high-frequency harmonics, the lateral bands due to LFTOs sometimes appear more distinctly than in the low-frequency range. Moreover, this phenomenon has been found to be more evident in the healthy motor's cases than in the faulty ones.

In Figure 91 it is possible to see the LFTO sidebands in the low-frequency area around the rotational harmonic f_r. It is clear from the figure that in the healthy case it is easier to identify the LFTO in vibration spectra. This confirms the fact that the double fault condition increases the difficulty in the detectability of the faults, as the harmonics can smear to each other and in general the signal spectrum is noisier. Note that two BPFOs has been used as the rotational frequencies of the healthy and faulty tests were slightly different.

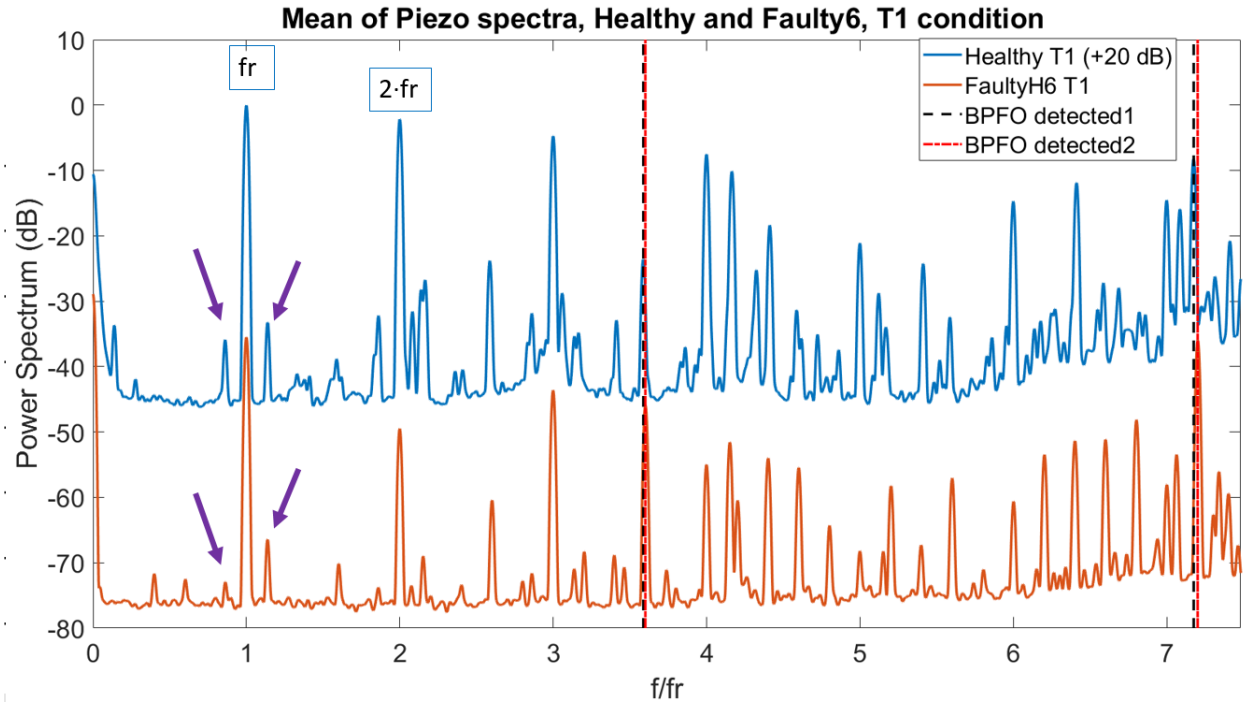

Figure 91: Sidebands due to T1 LFTO in piezoelectric spectra around the rotational harmonics, for healthy and hour 6 faulty bearings.

In Figure 92, the LFTO sidebands (with their multiples) are visible around the slot pass frequency for the healthy and faulty cases. Also in this zone of the spectra, the LFTO sidebands are much better viewable in the healthy signal indicating that the bearing fault generates harmonics that disturb the detection of the torque oscillation bands.

Note that, as in Figure 86, a 20 dB offset has been used in the healthy signal for a better visualization in both Figure 91 and Figure 92. Moreover, a normalization of the x-axis frequency (ratio of the read frequency over the rotational frequency) has been carried out for the sake of clarity. The slot pass harmonic is centred over the ratio $\frac{f}{f_r} = 46$ that corresponds exactly to the number of the rotor slots.

However, the LFTOs sidebands can be seen with more ease on the electromagnetic spectra as shown for example in the work [109]. This is another instance of the increased sensitivity on different fault detection of a multi-sensor system with respect to a single-sensor system, especially for double-fault diagnosis.

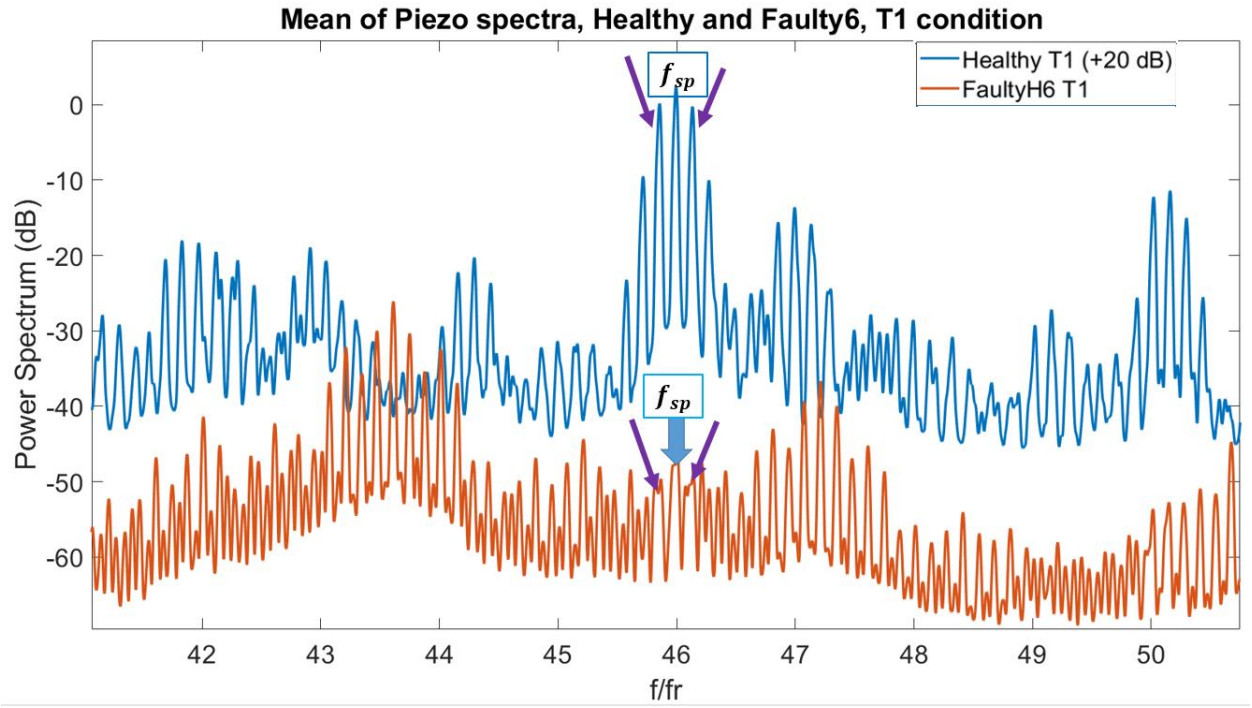

Figure 92: Sidebands due to LFTO in piezoelectric spectra around the slot-pass harmonic, for healthy and hour-6 faulty bearings.

6.3.3 Analysis of the electromagnetic signals

As in [84], for the detection of fault characteristic harmonics in electromagnetic spectra, the accurate value of BPFO is obtained from the vibration spectra to overcome the uncertainty caused by the slippage phenomenon. In the work, comparisons among different fault cases are reported: the detection efficiency of each case is computed as in [84], counting the number of detected harmonics and divide it by the overall of eight harmonics considered, i.e. the lowest frequency harmonics computed using (2.16), with k from 1 to 4.

In addition, the magnitudes of the first eight harmonics are confronted with those of the healthy case. In Figure 93 the electromagnetic signals spectra for the faulty case at hour 6 are displayed; for each faulty case, the fault harmonics magnitudes (marked by arrows) are extracted from these spectra and the detection efficiencies are derived.

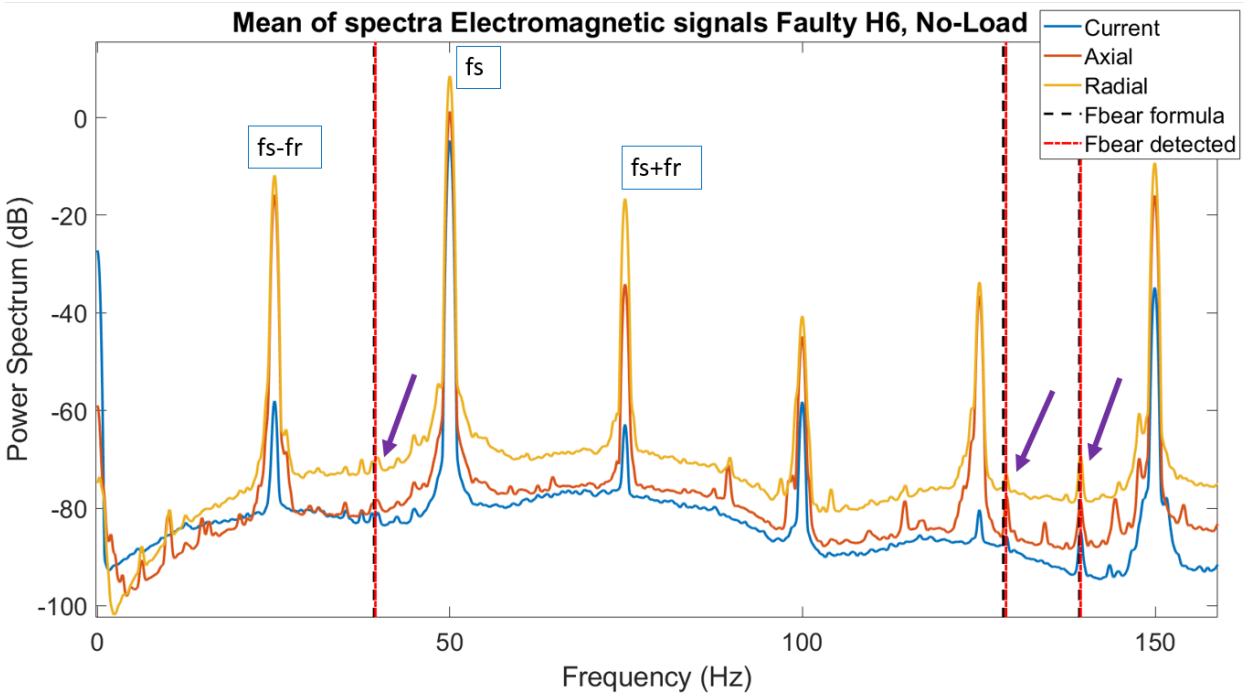

Figure 93: Electromagnetic signals spectra with the fault at hour 6, at no load.

6.3.3.1 Detection efficiency

For every faulty condition, the detection efficiencies are evaluated at no-load and constant load. Table 41 and Table 42 display the count of the fault harmonics detected in the case at hour 6, at no-load and constant load respectively: the magnitudes of the observed harmonics are given in dB, while the undetected harmonics are marked with the symbol "×". Confronting Table 41 with Table 42, a large deterioration in the detection efficiency is evident from no-load to constant load, primarily for axial flux and current. Figure 94 and Figure 95 illustrate the no-load and constant-load detection efficiencies for all faulty cases.

Table 41: Harmonic magnitudes detected in the faulty case at hour 6, no-load condition [dB]

Harmonic #	Freq. [Hz]	Current	Axial flux	Radial flux
1	39.43	×	×	×
2	128.85	-85.76	-77.54	-72.97
3	139.43	-84.83	-78.61	-69.16
4	218.28	×	-71.68	-66.86
5	228.85	-88.74	-77.27	-77.14
6	307.7	×	-82.94	-76.65
7	318.28	×	-84.06	-74.46
8	407.7	-103.39	-84.06	-79.19
Detection efficiency		**50%**	**87.50%**	**87.50%**

Table 42: Harmonic magnitudes detected in the faulty case at hour 6, constant-load condition [dB]

Harmonic #	Freq. [Hz]	Current	Axial flux	Radial flux
1	36.71	×	×	-64.64
2	123.43	×	-65.79	-66.91
3	136.71	-92.18	×	-70.78
4	210.14	×	×	-67.26
5	223.43	-88.37	×	×
6	296.85	×	×	-73.21
7	310.14	×	×	-68.72
8	396.85	×	×	-75.23
Detection efficiency		**25%**	**12.50%**	**87.50%**

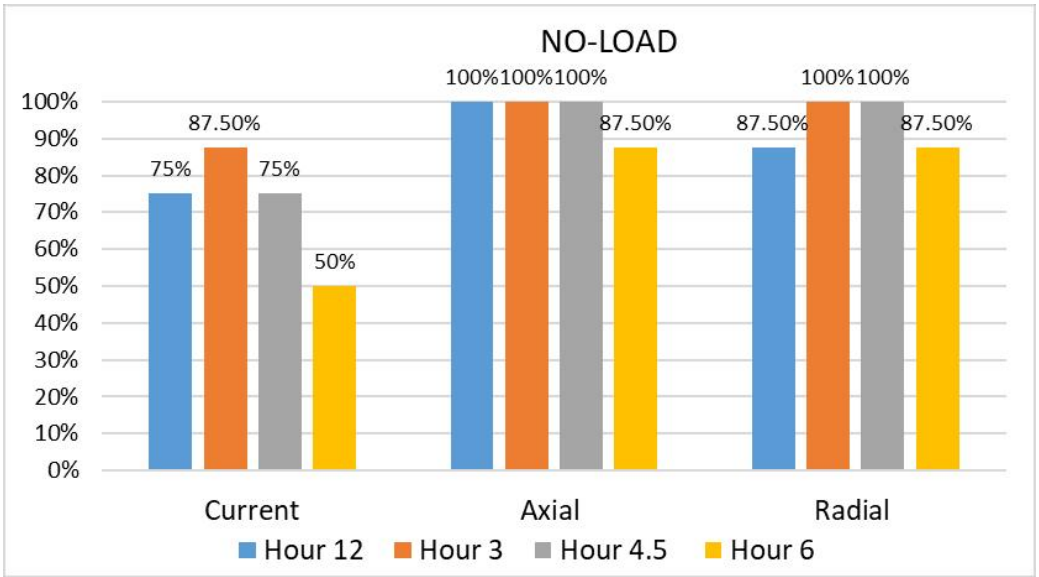

Figure 94: Detection efficiency for electromagnetic signals, with no-load.

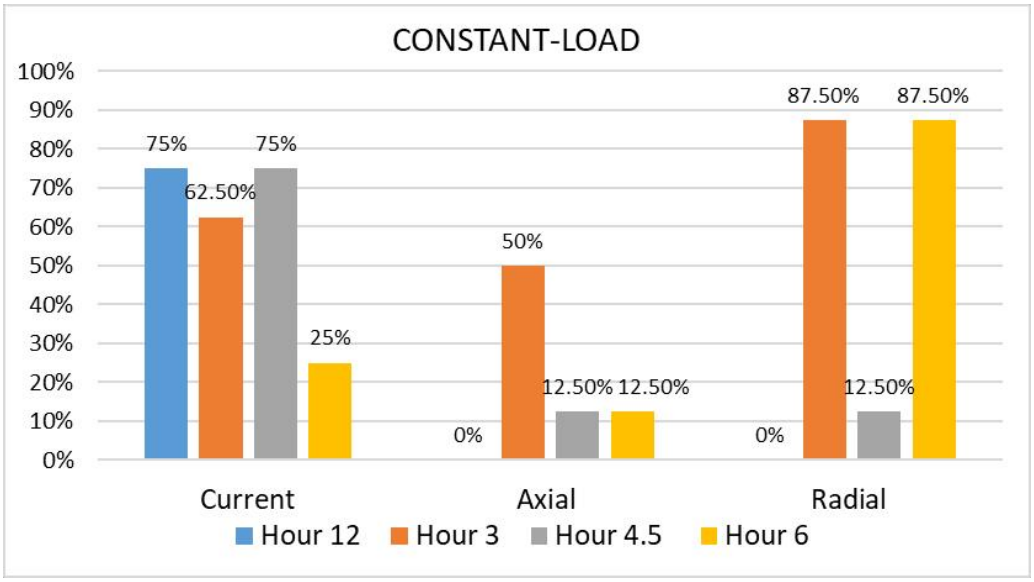

Figure 95: Detection efficiency for electromagnetic signals, with constant-load.

From Figure 94 and Figure 95, it is clear that constant-load cases are more difficult to detect, particularly by axial flux signal. The faulty cases do not always exhibit a straightforward relationship between the detection efficiency and the fault location: in fact, the most loaded fault at hour 6 is sometimes less detectable than the fault at hour 12.

Nevertheless, it is worth pointing out that the less loaded fault at hour 12 is the least detected, at constant load, particularly by the flux signals (0%).

6.3.3.2 Harmonics magnitudes

The magnitudes of the first eight harmonics in the electromagnetic signals have been compared among the faulty cases. To gather the harmonic magnitude at each characteristic frequency of the fault, a margin of ± 0.5 Hz was used around the characteristic frequency f_{bear} (the value is adjusted as in [84]) to find the amplitude of the highest peak in this interval. This approach has been used to compile Table 41 and Table 42.

The mean of the differences of the eight harmonics between the faulty cases and the baseline are shown in Figure 96 and Figure 97 at no-load and constant-load condition. From the figures it is apparent that there is an augmentation of the harmonics average magnitudes in comparison with the baseline for the most heavily loaded cases (at 3, 4.5, 6 hours); this is true primarily at no-load and for the flux signals. Conversely, at constant load, the effect of the bearing load zone on the electromagnetic signals is not very evident. The signals with the maximum degree of variability are the flux signals.

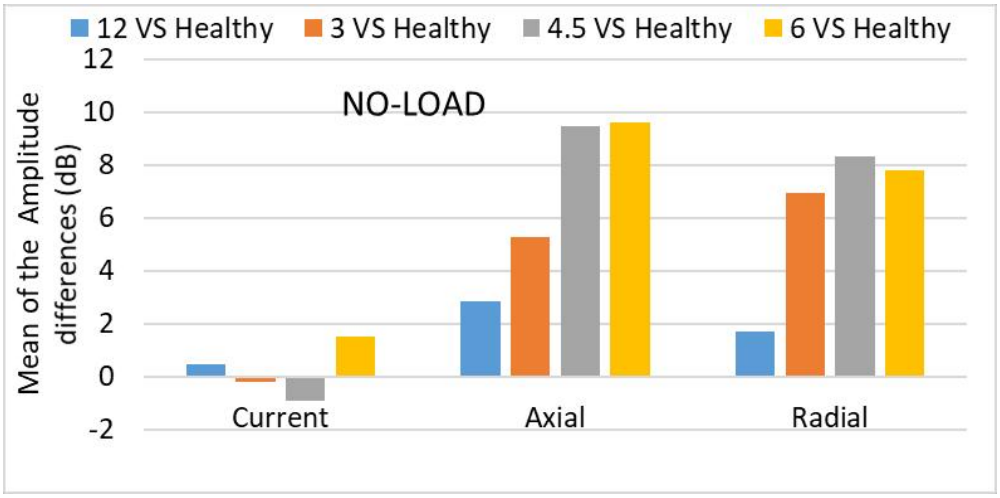

Figure 96: Mean of the differences in magnitude of the first 8 harmonics, at no-load.

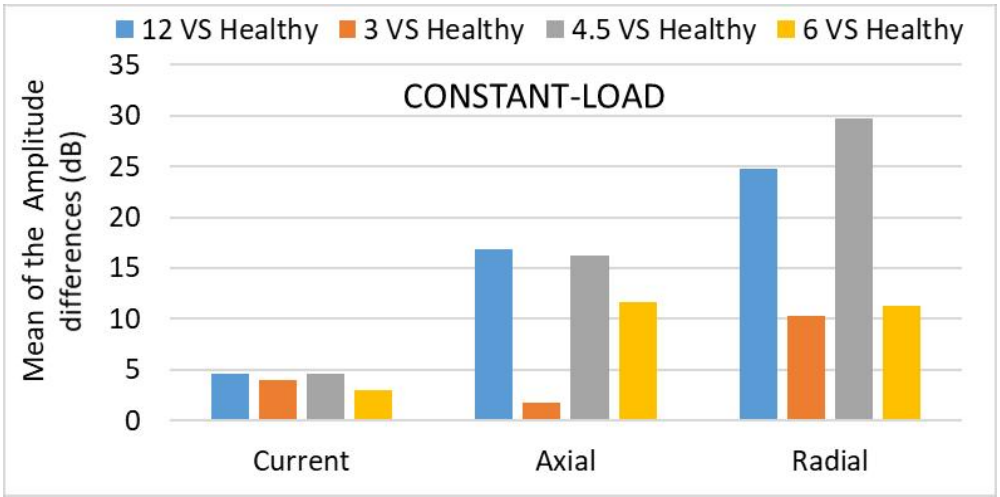

Figure 97: Mean of the differences in magnitude of the first 8 harmonics, at constant-load.

6.3.4 Inverter signal's analysis

As known form the literature and stated in the preceding work of the author [84], it is hard to detect the exact characteristic harmonics in electromagnetic signals with no filtering or advanced techniques in an inverter driven machine. Conversely, vibration analysis with this type of power supply gives more or less the same kind of findings as with the mains-powered machine, with the BPFO harmonics intensity increasing with the severity of the hour-case.

Whereas an in-depth study is not carried out for the sake of conciseness, illustrations of the amplitudes of the no-load and constant-load piezoelectric first seven harmonics are given in Figure 98 and Figure 99 respectively. Though some electromagnetic noise can be present, these figures exhibit the same pattern as the mains-fed test cases, demonstrating more stability of this signal with this type of supply with respect to the electromagnetic signals. In fact, the more radial-loaded cases exhibit higher harmonics amplitudes with respect to the hour 12 case, that is the less radial-loaded case.

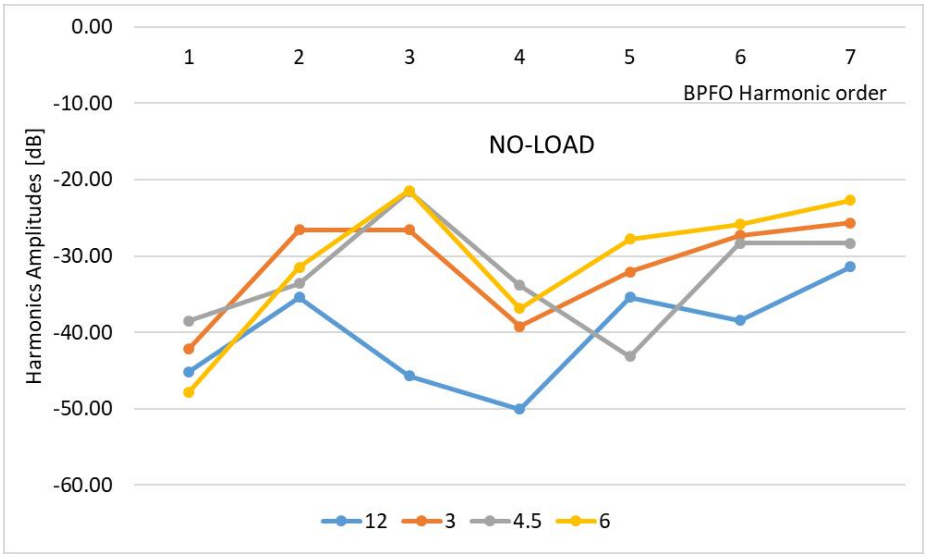

Figure 98: Piezoelectric BPFO harmonics magnitude with supply from the inverter, at no-load.

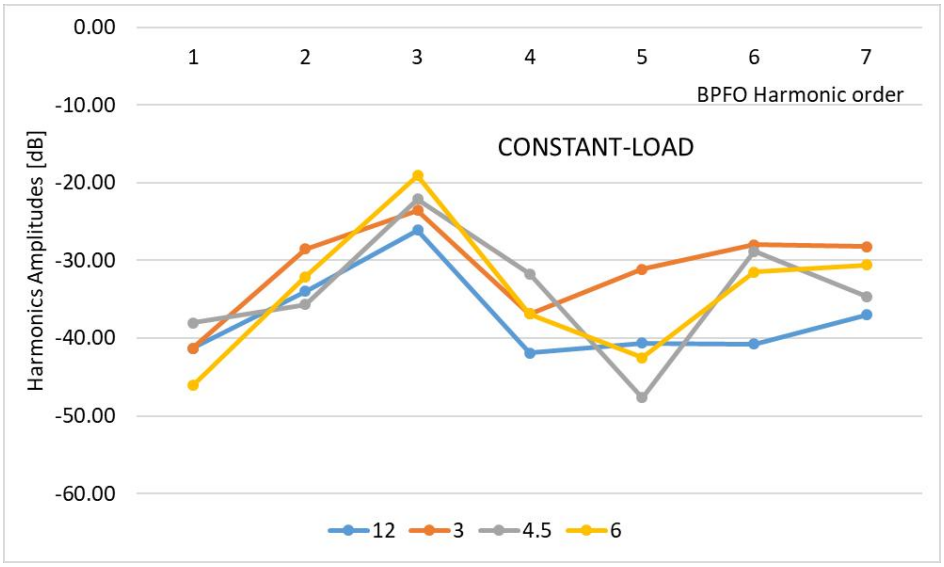

Figure 99: Piezoelectric BPFO harmonics magnitudes with supply from the inverter, at constant-load.

6.4 Discussion

In this chapter, the issue of the influence of the location of an outer ring fault with respect to the load zone of a bearing is treated. In a first instance, a literature review is presented.

The two issues treated in the review are:

- the importance of the sensors position (in particular accelerometers) on the machine to the purpose of the diagnostics;
- the influence of the location of the outer ring bearing fault with respect to the load zone.

It is recognized in the literature as both of these two aspects influence the signals, particularly the vibration ones, in the detection of the bearing or other faults in the machine.

To explore in depth the issue, the author has carried out an investigation that has been published in [96], in which two vibration signals, acquired from different positions of the machine, and electromagnetic signals are studied in a variable location, with respect to the load zone, of an outer ring bearing fault.

The main results of the work are exposed in the chapter and are resumed in the following:

- the vibration of a machine-body located accelerometer can be much more sensible on fault related to the rotor or electrical faults. In the work the vibration harmonics at double the slip frequency and multiples and the electrical-supply harmonic (at the double the supply-frequency) are very visible on the MEMS accelerometer, located on the connection box of the machine.
- The piezoelectric accelerometer, located on the flange of the motor, very close to the bearing under test is more sensible on the rotational frequency and its multiples and on mechanical characteristic harmonics (BPFO are evaluated in the work).
- Studies on the piezoelectric vibration signals for the various angular position of the fault confirm what stated in literature: the most radially loaded fault cases generate higher level of vibration.
- A study on the slippage variability for the various angular locations of the faults is carried out. It turns out that the amount of slippage depends on the angular position of the outer ring bearing fault but it is not clear the relationship between these two quantities. The amount of slippage does not seem to depend on the load of the machine (trends of this quantity for constant and no-load are similar for the various fault cases analysed).
- Low Frequency Torque Oscillations (LFTOs) harmonics are visualized on the vibration spectra. It is noticed in the work as these sidebands are not very easily detected in the low-frequency part of the vibration spectra, e.g. around the rotational harmonic. They can sometimes be better identified in higher frequency parts of the spectra. In the work they are detected around the slot pass frequency (that is a considerable harmonic at frequency given by the rotational frequency multiplied by the number of rotor slots). The double fault condition has been evaluated, considering both the cyclic bearing fault and the LFTO. In this condition, the LFTO sidebands are detectable but with some difficulties: the signal is much more compromised by noise introduced by the fault. A multi-sensor approach can help as the LFTO sidebands are generally detectable with easiness in electromagnetic signal spectra (around central frequency given by the supply frequency or its multiples) with or without bearing fault.

- The electromagnetic signals are analysed in two main aspects: through the detection efficiency and the study of the harmonic magnitudes. The former is calculated dividing the number of fault harmonics found by the number of harmonics considered (in the work 8 harmonics are considered). The detection efficiencies give similar results for all the hour-cases at no-load condition. At constant-load generally the fault is more difficult to recognize. In particular, the fault at hour 12 resulted to be the most difficult to recognize in stray flux signals, with constant load.
- Studying the magnitudes of the electromagnetic signal harmonics, it turns out that the most radially loaded cases generate higher harmonics also in electromagnetic signals and not only in vibration spectra. Nevertheless, at no-load the magnitudes seem more dependent on the load-zone vicinity of the defect (the most loaded defects generate higher electromagnetic characteristic harmonics). Conversely, in constant-load conditions the relationship is not very clear, probably due to interferences given by other harmonics generated by the loaded machine.
- With the inverter-fed machine only studies on vibration signals are presented. The magnitudes of the first seven harmonics present higher values for the most radially-loaded faults. This is true for both no-load and constant load conditions and is very similar to results found in the vibration of the mains-fed machine.

Remembering that the radial load in a bearing of a small electrical machine is not very high – the bearing has to support, in an ideal condition, only the weight of the rotor – further studies could be conducted on bigger machines to have an in-depth interpretation of the data. Moreover, other anomalies, like misalignment or incorrect mounting of the bearing can increase the radial load of the bearing. A dynamic eccentricity, conversely, generates a rotating load zone in the bearing. Studies on these phenomena could be conducted to find the signatures that represent these conditions with or without a bearing fault in the outer ring or in other locations.

7 Machine learning techniques for recognition of machine vibration spectrograms

7.1 Introduction

Machine learning techniques are very used today for the purpose of the electrical machine diagnostics. The machine learning is used in the decision making process of the diagnostics, avoiding the needs of high qualified personnel and increasing the detectability of the faults. In this chapter some of these techniques will be presented.

The topics discussed in the chapter are based on the work of the author [110], published at the 13th IEEE international Symposium on Diagnostics for Electrical Machines, Power Electronics and Drives (SDEMPED), held online in August 2021.

In a first part of the chapter a literature review on the most used machine learning and deep learning techniques for the diagnostics of the electrical machines will be presented. Successively, the work [110] will be described in details. In particular, in the work the transfer learning technique is implemented for the recognition of vibration signal spectrograms. The transfer learning consists in taking Artificial Neural Networks (ANNs) already trained and re-train them substantially in only some of the layers. In [110], two ANNs are taken into considerations, the Convolutional Neural Networks (CNNs) AlexNet and "CommandNet", available in the MATLAB repositories. The two networks are re-trained with the transfer learning technique to the purpose of the classification of the induction machine's vibration spectrograms.

In the final part of the chapter, discussions about the results of [110] will be exposed.

7.2 Literature review

Fault diagnostics has two main development areas: the condition monitoring, which covers the first two stages of diagnostics, i.e. data acquisition and processing, and the fault diagnosis, which covers the last stage, i.e. the decision-making process.

Condition monitoring research is intended to investigate the capability of different sensors and processing techniques to detect characteristic signatures in mechanical and electromagnetic signals that are representative of specific failure. These signatures are generally linked to the machine's parameters, e.g. type of machine, number of poles, number of rotor and stator slots, bearing geometry, etc. Moreover, the operating conditions of the machine, e.g. speed, load percentage, type of power supply, etc., change the signatures, so they have to be taken into account. An in-depth knowledge of the machine is therefore necessary, not only to recognise these

signatures, but also to select the threshold that divides the faulty condition from the healthy condition, which can strongly affect the chances of committing an incorrect evaluation during the decision-making phase. The decision can be taken by an experienced person or by an automatic algorithm and is part of the fault diagnosis process, explained in the following.

Fault diagnosis research focuses primarily on algorithms that can automatically discriminate the presence of a fault, based on the machine's acquired signals. The use of automatic algorithms can prevent the need of highly qualified personnel to do the decision making process and can increase in some cases the detectability of the faults. Such algorithms can be categorised into Machine Learning (ML) and Deep Learning (DL) based techniques; ML techniques involve Artificial Neural Network (ANN), Principal Component Analysis, and other approaches, and have been available for at least three decades, while DL approaches have been developed in recent years [111]. In comparison with traditional ANNs, characteristics of ML architectures, in the DL branch, the principal diversity in network architectures is that they have multiple hidden layers and not just one. Both ML and DL approaches necessitate extensive data collection to be trained; the data can be achieved through datasets available online [112] or through wide laboratory measurement campaigns [113,114]. But while ML methods are trained on features manually selected by the designer or the user of the network, DL algorithms can automatically extract the features and improve classification capabilities [51].

The two algorithm technique branches, ML and DL, will be exposed in the following sections of this review. In particular, the techniques applied to the diagnostics of electrical machines will be reviewed, reporting the main characteristics for some of them. Finally, a third subsection will be reserved for the transfer learning approach, that is, as mentioned before, a way to adapt an already trained network to different tasks with respect to the original task for which it has been designed.

7.2.1 Fault detection with classical ML techniques

Though based only on bearing fault diagnostics and not on all the machine diagnostics, the review [51] can give a solid base for the study of automated techniques for fault identification and recognition, reviewing both ML and DL algorithms. Some of the articles reviewed in [51] will be presented also in this work; in particular, in this section, the works that use classical Machine Learning techniques will be presented, i.e. Neural Networks with one hidden layer or other "shallow" models.

Before the current DL techniques explosion, a number of classical machine learning and "shallow" data mining methods were already in use for many years, e.g. the artificial neural network (ANN). The application of these algorithms demands a lot of domain knowledge and complex feature engineering.

A thorough exploratory data analysis is typically carried out on the dataset, succeeded by dimension reduction techniques such as principal component analysis (PCA) or other, for the feature extraction. Subsequently, the most representative features are transferred to the ML algorithm. The underlying understanding of different domains and applications may be very difficult and often requires wide specialist skills within each field; this makes it challenging to carry out adequate feature extraction or preserve a satisfactory level of transferability of ML models that have been trained in one domain to be generalised or transferred to other tasks.

Following the scheme proposed by [51], a short summary of the main classical ML approaches, and the challenges that these algorithms present, will be listed, with some references of publications.

7.2.1.1 Artificial Neural Networks (ANNs)

All the ANNs in both ML or DL are composed by the same components, that loosely mimic the operation of the animal brain: neurons, synapses (links between the neurons), weights, biases, and activation functions. However, the differences between the various networks are mainly in the architecture on which these components are "mounted" or how they are used.

Classical or "shallow" ANNs are composed by an input layer, a hidden layer and an output layer. Every layer is a set of neurons connected to the next layer through weighted connections (called edges). The weights increase or decrease the strength of the connections. The main concept of the ML is the fact that the machine learns automatically from input data, this means that it learns through experience. This is similar to the learning process experienced by humans or many animals. The artificial intelligence (AI) is a bigger set of methods, including also the subset of ML methods, defined as a technology that permits a machine to simulate the human behaviour.

In the particular case of shallow ANNs, the process in which the machine learns from the experience is the training process. In this method the data are passed through the input layer to the network several times (each complete pass of the data is called "epoch") and the weights of the connections are adjusted. The most efficient process to train the network is usually through supervised learning: the input data are labelled and the output is confronted with the expected output of the network. The weights and biases of the connections are adjusted in a way to increase the probability of obtaining the correct output (target), decreasing the error at each iteration. To evaluate the error of each iteration a cost function is used to compare the output to the target data. The derivative of the cost function is performed with respect to the input of each layer, starting from the outer layers and going backwards, following a computationally optimized algorithm called backpropagation algorithm. Using the Stochastic Gradient Descent (SDG), instead of using the classical Gradient Descent (SD) method, the derivative is computed with respect to the weighted sum just once on each iteration, saving computational cost.

A structure of a shallow neural network, i.e. with only one hidden layer, is shown in Figure 100.

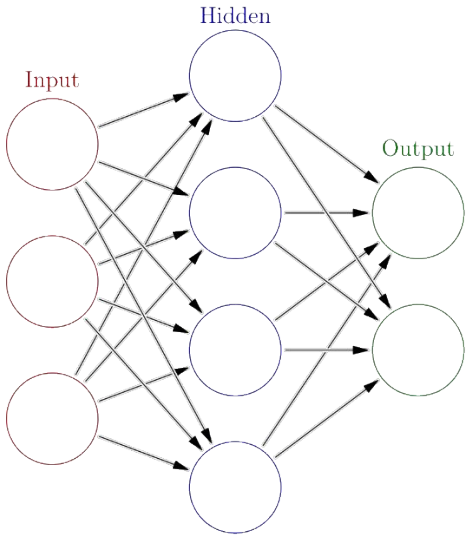

Figure 100: Scheme of a shallow Neural Network [115]

The classical ANNs can be applied to the diagnostics of electrical machines as can be found in literature since almost 30 years [51]. The input data have to be chosen by the designer of the ANN, constituting one of the challenging step of the network design, since the features have to be chosen manually. An example of quantities in input for the network are the steady state current and the rotor speed that reflect the damping coefficient B of the motor [116]. With these inputs the network can achieve almost 95% of accuracy that can be improved adding the square of each input and the multiplication between them.

Other examples of ANNs applied on bearing fault diagnostics are presented in [51]. However, for the implementation of all of them a certain amount of human expertise is required to carried out the feature selection for a more effective training of the networks.

7.2.1.2 Principal Component Analysis (PCA)

The PCA algorithm is used to perform dimensionality reduction of the data to be fed in a ANN. The PCA discloses the intrinsic character of the data in a way that helps to understand the variance of the entries. If a multi-variable set of data is displayed as a set of coordinates in a high dimensional data space (one axis per variable), PCA may provide the user with a low dimensional projection of this data object as seen from its most informative point of view. As the sensitivity of different features that are typical, for example, of a bearing failure or defect can vary significantly under different operating conditions, PCA has been proved to be an efficient and systematic feature

selection tool that provides guidance on the manual selection of the most iconic features for classification tasks [51].

One example of application of the PCA can be found in [117], where the technique is applied for bearing diagnostics purpose. The experimental findings showed that the benefit of the use of only the features identified by PCA rather than the use of the original 13 features is substantial, as the accuracy of diagnosis improved from 88% to 98%. The paper proved that the suggested PCA technique is effective in classifying bearing failures with higher accuracy and fewer input features than using all the original features.

Many other works that use PCA for the purpose of diagnostics can be found in the review [51].

7.2.1.3 Other ML techniques

Other methods different from ANNs used in ML are for example k-nearest neighbours (*k*-NN) and Support Vector Machine (SVM).

The algorithm k-NN is a non-parametric approach applied for both classification and regression problems. According to k-NN categorisation, an object's class is the output, which is determined by a majority vote of its k nearest neighbours.

SVMs are models, trained with supervised learning, that evaluate data used for non-probabilistic classification or regression problems. As stated in [51], results obtained with SVMs in many works are optimal and sometimes outperform ANN in bearing faults diagnostics.

Many others algorithms can be used in classical ML for the purpose of electrical machine diagnostics, besides the common techniques listed above. Some of them are: neural fuzzy networks, self-organizing maps, random forests, linear discriminant analysis, extreme learning machines (ELM), Bayesian networks, transfer learning, etc. [51].

7.2.1.4 Challenges in diagnostics with classical ML techniques

To identify the occurrence of a bearing defect using a classical ML algorithm, characteristic fault frequencies can be computed using the mechanical speed of the rotor and the particular bearing geometry, as described in previous sections of this works. These frequencies will be used as fault features and the process to get them is known as “feature engineering”. The signal strength at such frequencies can be tracked to train different ML algorithms and identify possible anomalies. Nevertheless, this technique can have many challenges that eventually impact the accuracy of the classification. The main challenges are [51]:

- *Sliding*: The frequency of faults is determined on the premise that there is no sliding between the rolling element and the bearing raceway, i.e. that these rolling elements perfectly roll on the raceway. However, this is rare in reality, as the rolling element often undergoes a combination of rolling and sliding motion. As a result, the determined frequency may deviate from the actual frequency of fault and make this feature, that is manually selected, less characteristic of the bearing fault. This phenomenon is also called "slippage" [29].
- *Frequency interaction*: If several types of bearing faults happen at the same time, they will interact. the resulting characteristic frequencies may add or subtract due to a complicated electromechanical process, thus blurring the characteristic frequencies.
- *External vibrations:* The possibility of disturbances from other vibration sources, i.e. bearing looseness and surrounding vibrations, can occur, obscuring the useful characteristics.
- *Observability:* Certain defects, such as improper bearing lubrication and general roughness problems, do not occur either with a characteristic cyclical frequency. This makes very difficult to identify them with classical data-based ML methods or traditional model-based spectral analysis.
- *Sensitivity:* The sensitivity of various features of the bearing defect may differ considerably under different operating conditions. A very in-depth and consistent "learning phase" is usually necessary to test the sensitivity of these harmonics to any working condition before it can be actually used with the traditional approach.

Due to the above challenges, manual feature engineering based on the frequency of characteristic bearing failures can be difficult to interpret and can sometimes lead to inaccurate classification results, especially when applying classical "shallow" ML methods that rely on features built by humans in the formation process. So, an automated feature extraction, typical of DL methods can be desirable, as will be discussed in the next section.

7.2.2 Fault diagnostics with DL techniques

As introduced before, DL is a subset of ML with the main characteristic of having deeper network architecture, i.e. the networks include more hidden layers than that present in shallow NN (that have at maximum one hidden layer). DL algorithms learn to represent the concepts in a hierarchical way, with every notion being defined in connection with simpler concepts, and the more abstract representations calculated from those that are less abstract.

The current transitioning from classical ML algorithms, mainly composed by ANNs with shallow architectures, to deeper architectures typical of DL can be ascribed to the reasons listed in the following [51].

- *Data availability.* With the advent and diffusion of the internet and crowdsourced labelling mechanism e.g. Amazon mTurk, there has been an explosion of data availability essential for the training of deep learning architectures. Datasets in different domains appear and are freely available on the web; for example, ImageNet for image recognition, COCO, a large-scale object detection, segmentation, and captioning dataset, VoxCeleb, an audio-visual dataset consisting of short clips of human speech. DL usually need a large amount of labelled data and these datasets permits the correct training of these architectures. However for some applications, including diagnostics of electrical machines or bearings, although there already exist public datasets, as for example [102], data are not yet in some cases so copious, and are not easy to acquire. In these cases, ML techniques can actually still compete with DL techniques, as the amount of data is sometimes insufficient to train completely a DL network (see Figure 101). However, techniques like transfer learning can help with this issue, as will be explained in the following.

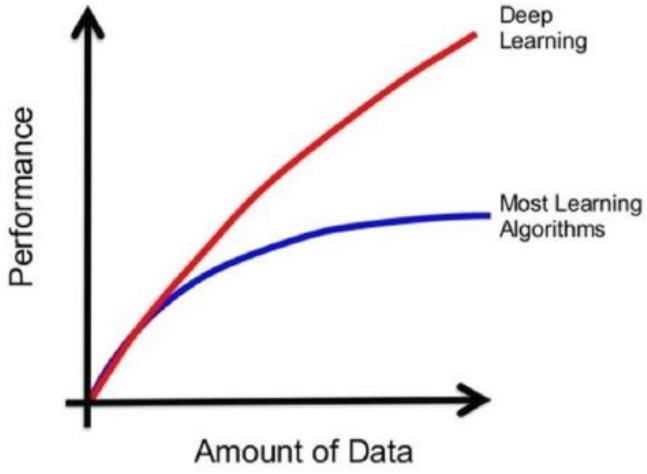

Figure 101: DL and classical ML algorithms performances for certain amount of data [118]

- *Algorithm evolution.* Other techniques have been invented and matured in terms of controlling the process of training the networks of deeper models in order to achieve faster speed, better convergence and better generalisation of the models. For instance, algorithms like ReLU (Rectified Linear Unit) aid speed up convergence time; dropout and pooling techniques help to prevent overfitting of the networks; numerical optimisation, including methods such as mini-batch gradient descent and other optimizers, helps to train deeper models and exploit more the data available.

- *Hardware evolution.* The training of deep networks is very intensive from a computational point of view, but executions on high performance Graphical Processing Units (GPUs) can dramatically speed up the training process. In particular, the GPUs offer parallel computation capabilities and much more compatibility with deep neural networks with respect to CPUs, which makes them favourite for training algorithms based on DL architectures. In the last few years, moreover, in addition to GPUs, hardware like FPGAs (Field Programmable Gate Arrays), ASICs (Application-Specific Integrated Circuits) and TPUs (Tensor Processing Units) have driven the rapid evolution of DL algorithms.

All of the above factors are contributing to the new generation of applying DL algorithms to a variety of data-related applications. In particular, some of the main advantages of using these architectures instead of ML techniques are listed in the following [51].

- *Best performances.* DL algorithms have the best-in-class performances that clearly outperform other solutions in multiple domain problems, e.g. speech recognition, language processing, computer vision, gaming, etc.
- *Feature Extraction*: as announced before, DL remove the necessity of feature engineering. This phase is very decisive in a classical ML algorithm and requires human effort and experience in the domain knowledge. Nevertheless, when a deep neural network is used, there is no need for a manual feature engineering process. It is necessary to just feed the data straight to the network, and it can automatically learn features from the raw data source by auto-adjusting the weights in the network. The challenging phase of feature engineering is so completely removed by the DL architectures.
- *Transferability.* The powerful expression and the high performances of a deep neural network trained in one domain may be readily transferred or generalised to other settings, contexts or domains. Architectures of DL networks can be more readily adapted to new problems than classical ML techniques. For example, issues in various domains such as time series, computer vision, and language processing or synthetizing are solved using the same techniques such as recurrent neural networks, convolutional neural networks, long short-term memory, etc.

Thanks to the reasons expressed in this section the DL techniques have grown and will continue to grow in many applications, including diagnostics of electrical machines and bearings. In the following part of this section a description of the main DL architectures will be presented, with particular regards to the Convolutional Neural Network (CNN) architecture, that is the network used by the author in [110].

7.2.2.1 Convolutional Neural Networks (CNNs)

In the DL contest, CNNs are a class of ANNs commonly used for image analysis or computer vision. CNNs are based on the shared-weight architecture composed by the so called filters or convolution kernels that, sliding along the input multidimensional vector, recognize features and provide the feature maps, i.e. translation-equivariant feature maps.

CNNs are also called Shift Invariant ANNs (SIANNs) because of their property to be translation insensitive as announced above. This architecture is composed of many layers (it is a DL architecture) in which the procedure of convolution is repeated many times to obtain a hierarchical feature recognition: the lower layers recognize low-level features, e.g. edges and corners in an image, while higher levels convolutions recognize more complicated features, e.g. objects composed by many edges and corners. It has to be said, however, that the CNNs are not used only for image recognition and similar applications like video recognition, image classification and segmentation, medical image analysis, but they are also used for recommender systems, natural language processing, financial time series and others [119].

Each filter or kernel used in the convolution operation shifts over the input data involving a small receptive field (e.g. 5x5 pixels) during each movement, as shown in Figure 102.

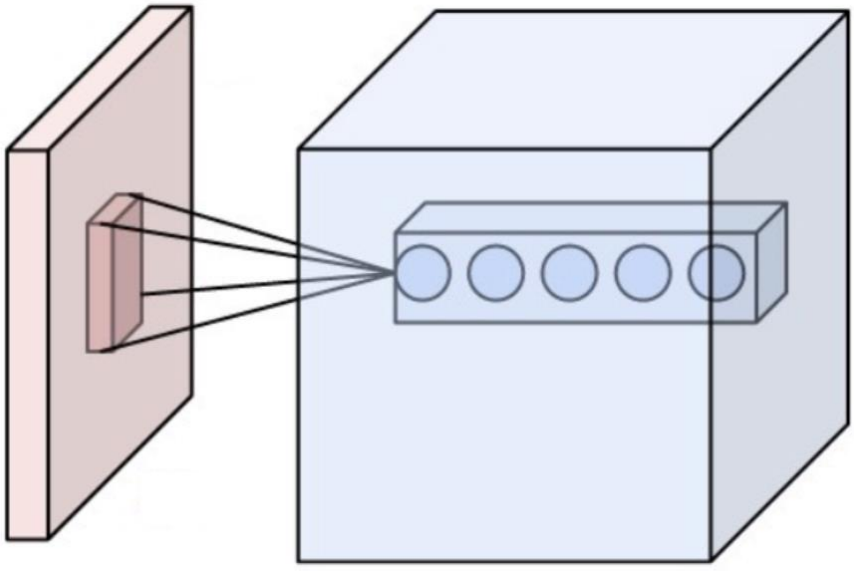

Figure 102: Neurons of a convolutional layer and their receptive field [119]

As announced above, the CNNs are based on the kernels that operate the convolution operation in an image or data vector. However, there are many other kinds of layers in a CNN other than the convolutional ones; some of them are the pooling layers and dropout layers. Usually a pooling layer follows the convolutional layer for the down-sampling process. The pooling layers can be of various type, e.g. average pooling or max pooling. The most used is the max pooling and it is an operation consisting of keeping the maximum value of a neighbourhood (generally a

square) of pixels. The combination of convolution and pooling layers is repeated many times in the architecture to get deeper into the details of the features. It should be noted that with the use of shared weights of the kernels it is possible to have much deeper networks than networks with fully connected layers, i.e. Multilayer Perceptrons (MLPs) or classical shallow ANNs; in fact, sharing the weights means that there are much less weights to train for each layer, giving the possibility to have a much higher number of hidden layers.

Dropout or dilution techniques are regularization techniques implemented for reducing overfitting in the ANN. The dilution technique consists in thinning the weights of the network, while dropout is the random omission (dropping out) of some of the weights in the neurons (both visible or hidden) during the process of the training of the network. These techniques are both carried out for reducing overfitting, as stated before, and sometimes are both referred as dropout technique (also when actually dilution is performed).

In a CNN after the convolution-pooling layer pairs succession and the dropout layers, one or more final fully connected layers are used to perform the classification of the signal (as a classical shallow ANN). Before the final fully connected layers, the data, from a multi-dimensional form, are transformed in a 1-D vector: the data are "flattened" to be fed to the fully connected layers.

A softmax activation function is then generally used in the last fully connected layer to have as classification output the probability of each output class. With this function the sum of the probabilities of all the classes will give 1 (100%) as expected, so it normalizes the output to a probability distribution over the predicted classes. Other activation functions used in the other layers can be for example the sigmoid function, hyperbolic tangent, ReLU, etc. with the latter becoming the most popular for deep learning architectures.

Though CNN were born in the 1980s, for the diagnostic purposes the first paper using this kind of architecture was published in 2016 [120]. After this paper many others were published in a small amount of time using the same DL architecture [51]. A typical scheme of CNN used for a bearing fault detection and classification is presented in [121] and shown in Figure 103.

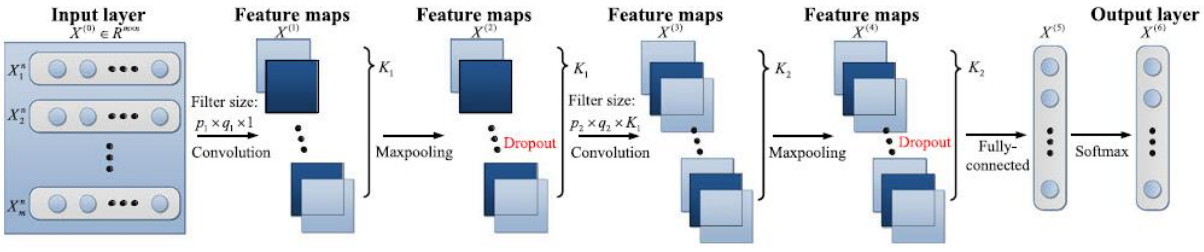

Figure 103: Typical scheme of a CNN for fault detection and identification [121].

Particularly, in the work [121], the vibration signals from different accelerometers are collected as 1-D raw time-data and stacked to form a 2-D vector similar to an image representation.

Then the images are passed through the network in which convolutional and pooling layers are in succession to respectively perform the feature extraction and the down-sampling of the data. As stated before, the succession of these two operations permits to have a deeper network and to extract the features in a hierarchical way. Eventually the output of the hidden convolutional-pooling layers is fed to the final fully connected layer with softmax probability function used as activation function.

Many others CNN based works are presented in the review [51] focused on bearing fault diagnostics. The most important characteristics of this architecture, applied to the diagnostics of electrical machines and bearings are resumed in the following:

- CNN is able to learn from raw data (often vibration data are used).
- If pre-processing of the data is performed, particularly advanced techniques are not required; for example, it can be used a scaled discrete Fourier transform.
- The automatic feature learning of a CNN outperforms the manual feature engineering used in classical ML methods.
- CNN's feature learning approach permits to perform more difficult predictions that are not performed through classical ML methods: bearing health prognostics, early-stage faulty conditions, classifications of faults that do not exhibits characteristics frequencies, e.g. due to lubrication degradation, etc.
- Astonishing classification accuracies can be reached with this architecture, often over 99% on test sets.
- Very deep CNNs can be implemented and can reach and maintain high accuracy in noisy environments and under varying load conditions.
- Some adapted CNNs can reach high accuracies even with large speed variation of the machines due to different supply frequencies imposed by an inverter.
- Sensor fusion used in symbiosis with CNNs increases the fault classification accuracy.
- Though usually 2-D CNNs are used because of their excellent results, with some adaptations also 1-D CNNs can be used simplifying the pre-processing of the time-series signals and reducing the training data required.
- In literature, works are performed with laboratory datasets or public datasets. CNNs show to have high performances with many datasets, with single or multiple signals, and with artificially induced faults or realistic flaws caused by accelerated stress tests.

It has to be said, however, that CNNs and DL algorithms in general can suffer of overfitting (even more than the less complex models used in classical ML). This phenomenon appears when a model attempts to "mechanically" fit all of the training data leading to a memorization of the patterns in the data as well as the noise and random oscillations. Some techniques used to avoid the overfitting phenomenon are [122]:

- The augmentation of the training data, i.e. having more training data by generating slightly different data from the original ones. This is done, for example, in a image recognition task, by flipping the images, translating them of a certain amount of pixels or adding noise to them, etc.
- Early stopping of the training process where a too high number of epochs is set. In other words, if the model achieves a good classification accuracy before reaching the set final epoch, stopping the training can avoid overfitting.
- Features selection. By choosing the best features or data to train the model, removing the useless or unnecessary data and features, the overfitting phenomenon is reduced.
- Reducing as possible the complexity of the model. Starting with a less complex model and then gradually adding complexity to it to increase the performaces, can produce a better neural network model, more immune to overfitting.
- Introducing dropout layers in the model. Dropout layers, placed between other layers in the network, permits to randomly ignore some of the outputs of the previous layer. This helps to reduce the complexity of the model and so to reduce the overfitting phenomenon.

7.2.2.2 Other DL approaches used in bearing diagnostics

Other DL methods, used in diagnostics are reported in this section, though without a detailed explanation since they are not implemented in the work of the author presented in this chapter [110]. The review [51] is used as guideline of this section. Though in [51] only techniques for bearing fault diagnostics are reviewed, these techniques can be used for general diagnostics of electrical machines, carrying some modifications in the input data or in the networks.

7.2.2.2.1 Auto-encoders

Auto-encoders (AEs) were introduced in the 1980s for an unsupervised pre-training of ANNs. After years of development, the auto-encoder has been widely employed as an unsupervised feature learning approach and a pre-training method for multi-layer neural networks. The process of training an auto-encoder with one hidden layer is depicted in Figure 104, [123].

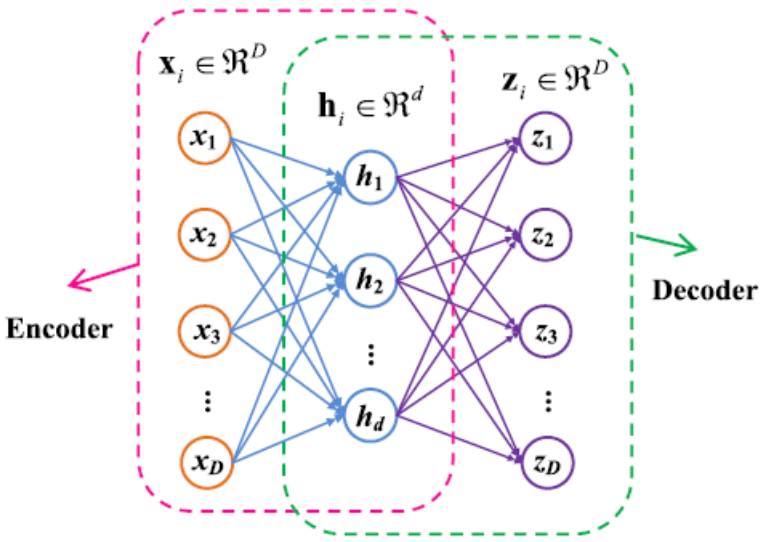

Figure 104: Training process of one hidden layer auto-encoder

In particular, an autoencoder is trained from an ANN, consisting of two components: the encoder and the decoder. The encoder output is supplied to the decoder as input. The ANN uses the mean square error between the native input and output as the loss function, which aims essentially to generate the final output by mimicking the input data. Once this ANN has been trained, the decoder component is dropped and only the decoder component is retained. Thus, the output of the encoder is the feature representation that can be used in the next classifier step.

Many works can be found in literature that apply autoencoders to the bearing fault classification as stated in the review [51]. The main characteristics of ANNs including AEs or modified autoencoders are:

- Higher classification accuracy with respect to normal Back Propagation Neural Networks (BPNNs).
- Stacked Denoising Autoencoders (SDAs) permit to have robust feature extraction in noisy ambients and under different loading conditions. With this classical ML methods architecture can be outperformed, such as SVM and Random Forest (RF), and also DL architectures, such as Deep Belief Networks (DBNs).
- Deep autoencoders can be built also with different activation function for each stacked component for having a better unsupervised feature engineering (from the acquired vibration signal).
- Some kinds of AEs, such as the Deep Wavelet Auto-encoders (DWAE), can outperform ML methods or other form of deep auto-encoders.
- Deep Neural Networks with stacked sparse auto-encoders can be used to reduce the amount of data for the training of the model to the 30% of the original data.

- To reduce the DL model complexity, a fully-connected, winner-take-all autoencoder can be used. The method handles the higher accuracies in bearing fault diagnostics and showed better behaviour in noisy condition than other deeper architectures such as CNNs.
- As a disadvantage it must be said that auto-encoder methods need 6-10 times higher training times with respect to normal ML methods.

7.2.2.2.2 Deep belief networks

In the Deep Learning contest, a deep belief network (DBN) may be thought of as a combination of simple unsupervised networks like Restricted Boltzmann Machines (RBMs) or autoencoders, in which each hidden layer of each subnetwork acts as a visible layer for the subsequent one. The architecture is visible in Figure 105, in which the coloured boxes indicates the subnetworks blocks [124]. An RBM is an undirected generative model based on the energy with an input layer "visible", a hidden layer and linkages between, but not within, the layers. This arrangement yields to a rapid unsupervised layer-by-layer training process, where contrastive divergence is imposed on every subnetwork in turn, starting with the "lowest" couple of layers in the structure. This layer-by-layer avid process for the training of the network brought to one of the earliest efficient deep learning models [125].

A lot of intriguing actuations of DBNs exist in real-world applications like for example natural language understanding and drug discovery. Its first application on the diagnostics of bearing defects was released in 2017 [124].

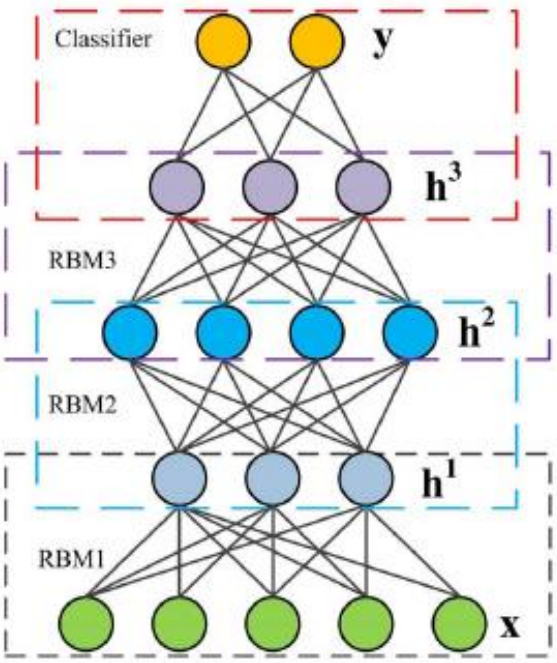

Figure 105: Architecture of a deep belief network [124].

7.2.2.2.3 Recurrent Neural Networks

Unlike a feed-forward neural network, a recurrent neural network (RNN) computes the input information with recurrent patterns. The architecture of a RNN is illustrated in Figure 106.

Having a stream path from the hidden layer to itself, when unwound in series, it may be thought as a feed-forward neural network in the input sequence. Using a sequential pattern, it may catch and model sequential relations in time series or sequential data. Nonetheless, frequently trained by back-propagation through time, RNN suffers from the recognised problem of the gradient vanishing/exploding because of its nature.

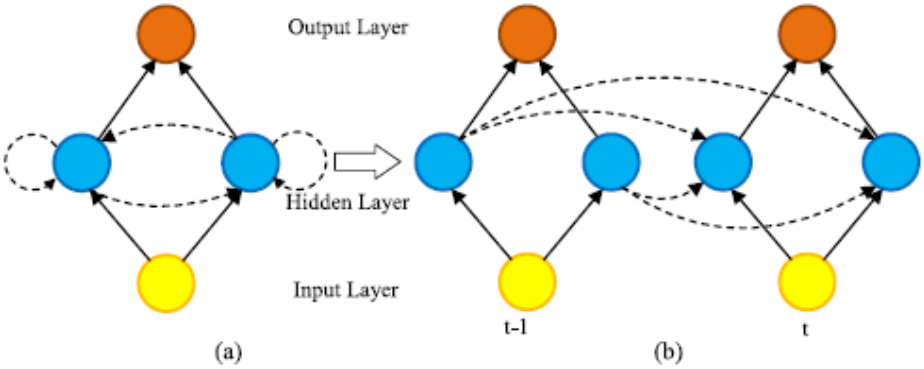

Figure 106: Scheme for a (a) RNN and (b) RNN over time step [126]

The development of long-term short-term memory (LSTM) in 1997, that is part of RNNs, remedied to the above mentioned disadvantage of this kind of architecture and increased the diffusion of RNNs. In particular, LSTMs are enhanced with the addition of recurrent gates (the "forget" gates). LSTMs showed an amazing ability in remembering and modelling long-term dependency in the data, thus taking a dominant role in time series and textual data analysis. Until now, it achieved huge results in the areas of speech recognition, natural language processing, video analysis, handwriting recognition, and other applications.

An early RNN application on bearing faults diagnostics was first reported in 2015 [126]. In the work the fault characteristics are first extrapolated applying the discrete wavelet transform and subsequently selected on the basis of orthogonal fuzzy neighbourhood discriminative analysis. Such features in turn are fed to an RNN in order to accomplish the diagnosis of bearing faults. Experimental results demonstrated that the suggested RNN-based design had the ability to thoroughly detect and classify the faults in the bearing.

Other works with RNN schemes and other architectures such as Generative Adversarial Networks (GANs) are presented in [51] and are not reported here for brevity.

7.2.3 Transfer learning techniques

A successful diagnosis of bearing faults based on ML and DL is founded on a huge quantity of extensively annotated data [51]. Similar are the requirements for general electrical machine diagnostics. However, in most practical uses, the collection of huge mass of data is not reasonable due to: 1) the potentially hazardous and serious effects of running machines in faulty conditions; 2) the potential for a long and tedious degradation process before the desired failure appears; 3) the likelihood of a large number of operating circumstances with various different loads and speeds.

Moreover, when identifying the existence of bearing failure, the classification accuracy of DL techniques trained using either publicly available datasets or self-collected datasets taken in a laboratory setting would inevitably decline in a real-life case. Although, if information from the same machines or bearings is employed, considerable amount of dispersion disagreement between characteristics of the training and test sets is unavoidable if the loads or speeds are different. So performances of the networks are still not optimal in all conditions [51].

Transfer learning, which was created to address this practical and widely existing issue in a variety of applications, has sparked a lot of interest in the machine learning community, and various transfer learning frameworks based on classical ML or, alternatively, DL algorithms have been proposed. Some work and review about transfer learning in classical ML algorithms can be found for example in [127-130].

Domain adaptation is a prominent strategy for all forms of transfer learning methodologies. In fact, domain adaptation establishes knowledge transfer from the source domain to the target domain by examining domain-invariant characteristics [131]. Domain adaptation methods can thereby alleviate the distribution difference between the two domains using labelled data from the source domain and unlabelled data from the target domain.

However, integration of deep learning and transfer learning methodologies has been more and more popular in recent years. To offer the domain-transfer ability while keeping the outstanding automated feature learning ability, specially built domain adaption modules are integrated with deep learning architectures [131-135].

For example, [133] proposes a domain adaption module to help a 1-D CNN to learn the domain-invariant features by optimising the domain recognition error and reducing the distribution distance probability. Three datasets are used to test the efficacy of domain adaptation: the CWRU dataset, the Intelligent Maintenance Systems (IMS) dataset, and the railway locomotive bearing dataset. By training on one dataset and testing on another, a mean accuracy of 86.3% is reached, outperforming the traditional CNN's 53.1% and two current domain adaption frameworks' 75.6% [129] and 78.8% [130].

Other examples of transfer learning applied to DL architectures are presented in [51]. A scheme of the transfer learning technique is reported in Figure 107.

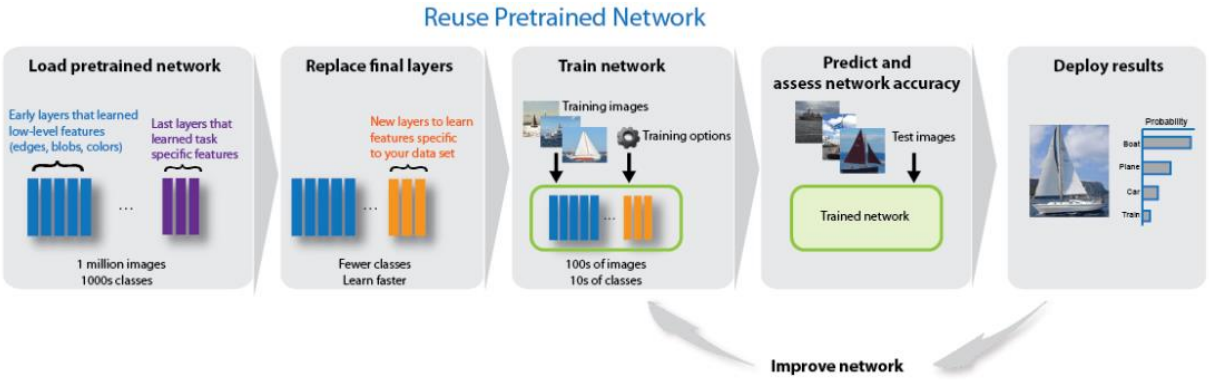

Figure 107: Scheme of the transfer learning technique [136]

7.3 Proposed method

In the work of the author [110], a transfer learning technique is used to train two CNNs for the identification of bearing faults. The two neural networks used, as stated in the introduction, are AlexNet and CommandNet, CNNs originally designed and trained respectively for the image recognition and human speech recognition.

The signal used is the vibration signal that has been transformed into a 2-D time-frequency representation form by the use of the Short Time Fourier Transform (STFT). The vibration signal used is taken from laboratory measurements with the instrumentation described in 3.3.7 and 3.3.8 (MEMS and piezoelectric accelerometers), denominated "Pavia data", and from the publicly available Case Western Reserve University (CWRU) bearing dataset. With the Pavia data, vibrations are collected with healthy bearing, faulty bearing (crack in the outer race), and with Low Frequency Torque Oscillation (LFTO) conditions, with healthy or faulty bearing.

Three different groups of tests are carried out using the two CNNs: a preliminary 3-output classes network test, tests with the two dataset images mixed, and tests with 6-output classes networks.

7.3.1 Experimental setup

The two datasets used for feeding the networks are described in the following.

7.3.1.1 Pavia dataset

The "Pavia" data are collected using the test bench described in Chapter 3. The main characteristics of the acquisitions regarding this work are the following:

- The motor used is mains-fed, 1.5 kW, 4 poles, three-phase squirrel cage. The supply frequency is 50 Hz.
- A magnetic powder dynamometer has been used. Tests are carried out at constant load, or with LFTOs, with different frequencies: very low oscillation and low oscillation frequency.
- Measurements are carried out with a healthy and with an outer-ring fault bearing.
- Two accelerometers with different location on the machine and bandwidth are used. The piezoelectric accelerometer has 10 kHz bandwidth and it is located near the bearing under test. The MEMS accelerometer has 1.5 kHz of bandwidth and it is located on the body of the machine.
- Data are sampled at 20 kS/s and 2^{19} samples are collected for each measurement. A set of 20 consecutive measurements is stored for each machine condition considered.

7.3.1.2 CWRU bearing dataset

The CWRU bearing dataset has the following characteristics:

- The motor used is mains-fed, 1.5 kW, 4 poles, three-phase squirrel cage.
- However, the supply frequency is different, from the motor tested in Pavia, i.e. 60 Hz.
- A DC machine is used as dynamometer. Tests are available in the dataset at three different constant loads. In the work only the cases with constant-load at 1.5 kW have been considered. No LFTO conditions are available in the dataset.
- Three or four different severity of fault are recorded in the dataset. The location of the fault can be in the outer race, inner race or balls. For the outer race, locations at hour 12, 3 or 6 are available. In the work the three severity levels for the outer race fault at hour 6 have been considered.

- Fan-end, drive-end and basement vibration are collected. In the work only drive-end bearing data have been considered to be more coherent with the Pavia data.
- The segments sampled at 12 or 48 kSample/s make up the data from the CWRU dataset. Only one segment of approximately 500000 samples is collected for each machine condition. This corresponds to an amount of data approximately 20 times less rich than the Pavia dataset.

The test bench used for collecting the CWRU dataset is represented in Figure 108. Other information about the dataset can be found in [102].

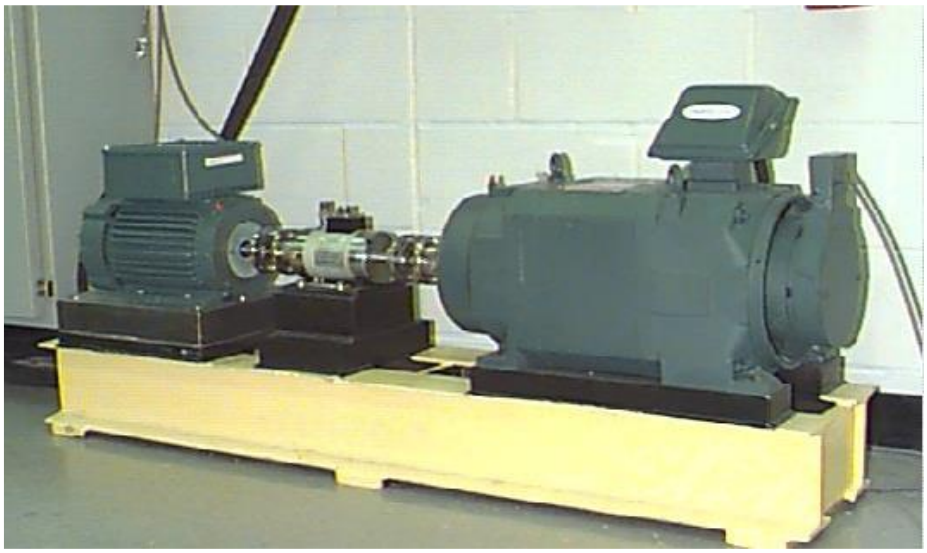

Figure 108: Test bench of the CWRU dataset [102]

7.3.1.3 The AlexNet CNN model

The authentic AlexNet, developed by Alex Krizhevsky and his collaborators in 2012, includes eight layers with learnable weights, the first five of which are convolutional, with some of them that are followed by a max pooling function, and the final three of them are fully connected [136]. The network is built to be trained on two GPUs and includes other essential features, such as the use of Rectified Linear Units (ReLUs) to simulate a neuron's output, that made it particularly novel and efficient at the time.

A model of AlexNet is available in the MATLAB deep learning toolbox and has been used in the work [110]. The model consists of 25 layers in series, of which eight are learnable (as before, five convolutional and three fully connected), as well as layers for normalisation, max pooling, ReLUs, two drop-out layers and a last softmax probability layer. The native network gets colour images of 227×227 pixels as input, with three channels, i.e. red, green and blue (RGB). It takes up approximately 300 Mbytes of disk memory.

The transfer learning technique has been implemented by the author to adapt the network to the target data, i.e. bearing vibration data. Specifically, for the fault diagnostic purposes, the first alteration made to the net is the replacement of the final fully connected layer (with 1000 output classes) with one layer consisting in only two, three, or six output classes, according to the group of tests considered. An additional change is the replacement of the first two layers (the input layer and the first convolutional layer) with some that are more suited to receive grayscale pictures. In opposition to pictures in colour, grey-scale images were favoured to ensure that the net perceived the images' intensity as the signal's intensity (not dependent on the arbitrary colour map chosen in the spectrograms generation).

7.3.1.4 The CommandNet CNN

The commandNet network is a convolutional network with 24 layers that is provided in the MATLAB Audio toolbox. Five convolutional layers, each followed by a batch normalisation layer and a ReLU, four max pooling layers, one dropout layer, one fully connected layer, and a softmax layer make up the network. The network receives grey scale pictures, i.e. vibration spectrograms, with a size of 98x50 pixels, in which the abscissa is representing the time axis and the ordinate represents the frequency axis. The network is considerably less heavy than the AlexNex, weighing only 230 kbytes. The lightness of the network is given from the smaller input layer size, that is composed of only one channel for the recognition of only the grey scale values instead of the three RGB values. Moreover, the network has only one fully connected layer instead of the three present in AlexNet and the size of it is much reduced as it has originally only 12 output classes (it can recognize 12 voice commands), instead of the 1000 of AlexNet.

To the purpose of the transfer learning, the sole change made to the CommandNet network is the replacement of the final fully connected layer (including the connected softmax layer and the output classification layer) with ones that are appropriate for the number of output classes we are interested in. It was not necessary to change the input layer since the network was already set to receive grey scale images.

In the next sections of this chapter the parameters and hyper-parameters employed in the retraining process will be presented.

7.3.1.5 Transformation in time-frequency domain

The vibration data are acquired in time domain, and stored as a series of time-sequence segments. The Short time Fourier Transform (STFT) is used to transform the data in time domain into the time-frequency domain. The generated images, called spectrograms, represent many Fourier transforms in short time intervals with colour intensity representing the signal intensity.

For each motor condition, the processing of the Pavia data begins with 40 main time-segments of 2^{18} samples each. The record-sequences are first decimated: data is decimated with a decimation ratio of 10, so from a sampling frequency of 20 kHz, a decimated sampling frequency of 2 kHz is reached and a size of 26215 samples for each record-segment. For the Shannon-Nyquist theorem, this indicates that the spectrograms will have a frequency range of 0-1000 Hz. This frequency range was chosen because it produced the greatest results in several preliminary experiments. Indeed, while specific fault characteristics can be found and enhanced at higher frequencies [29], the networks appear to see domain invariant characteristics at low frequencies; evidently, the Ball Pass Frequencies Outer Race (BPFOs) [29], [84], while not always markedly prominent, are visible with very similar patterns (dependent only on the rotational frequency and geometrical characteristics of the bearing) in the low-frequency range and are not dependent on natural resonance frequencies of the bearing.

In the case of the CWRU data, the data taken from the dataset had a sample frequency of 48 kHz. To get a decimated frequency of 2400 Hz, the data was decimated using a decimation factor of 20. This value was used because the motor's mains frequency in the dataset is 60 Hz, thus 6/5 of the Pavia data's decimated frequency was utilised to maintain the same spectrogram's harmonic order range (50 Hz mains supply has been used in the Pavia dataset).

The length of the segments extracted from the CWRU dataset for each scenario is around 500000 samples; after decimation, the segment is reduced to 24254 samples. For the production of the images, this segment is separated into 20 overlapping parts. Each overlapping segment has a total of 2425 samples. The overlapping ratio is 2/3 of the segment length.

The vibration signals are normalised after decimation: the mean value is removed and the set of data is divided by its standard deviation; this is done in many works in literature, see for example [138], to make it easier to compare signals from different sources.

The function to perform the STFT is the *spectrogram* function of MATLAB. The spectrograms have to be created using subdivision windows on which the Fourier transform is carried out (short-term). Table 43 summarises the length of the windows and other factors selected for the STFT transformation. A Hamming function is applied to each window.

Although the spectrograms are resized after the generation with the *imresize* MATLAB function (included in the *ImageDataAugmenter* set of options for the training of the networks) to match the precise dimension of the network's input layer, the spectrogram parameters are chosen as shown in Table 43 to generate an image with a size very close to AlexNet's input layer size (227x227 pixels), and to avoid possible information loss during the resizing of the image. Conversely, for the image generation for the feeding of CommandNet, the spectrograms generated with the parameters of Table 43 are resized with *imresize* to a 98x50 pixel format images, to match the network input layer.

Table 43: Parameters of the spectrogram transformations

DATA	Window length	Overlapping samples	FFT bins	Frequency resolution [Hz]	Window time [ms]
Pavia	157	42	452	4.4	78.5
CWRU	452	433	452	5.3	188

7.3.1.6 Image generation

Following the formation of the spectrograms, the values are transformed into dB values in order to compress the dynamic range; the value is then renormalized to the range of values 0-1 in order to provide an intensity signal for picture generation.

The picture is created by utilising the "*imwrite*" function to create grey-scale images in jpg format for network feeding. To avoid any information loss, the transformation mode is set to "lossless."

In certain tests, a threshold filter is employed to increase the network accuracy: all signals below a certain dB threshold are set to zero. This means that only harmonics with an intensity greater than the threshold are visualised in the spectrogram picture, allowing the networks to detect the patterns of the fault characteristic harmonics in a better way. The choosing of the threshold value, however, may be challenging since the strength of the fault harmonics varies with the intensity of the fault.

The amount of pictures used for each motor state varies depending on the test, but in general, 20 to 60 frames are utilised for each condition. Typically, 70% of each of these sets of photos is set aside for training and 30% is set aside for validation. In other experiments, the image groups are separated into three categories: 65% training, 25% validation, and 10% network testing.

The ImageDataAugmenter MATLAB training option is used to augment all training pictures: the images are mirrored on the X axis and translated on the X and Y axes by a value of up to 30 pixels. With a bilinear pixel value interpolation and an antialiasing filter, the ImageDataAugmenter function also provides a resizing function for pictures.

Figure 109 shows some examples of pictures generated from Pavia data.

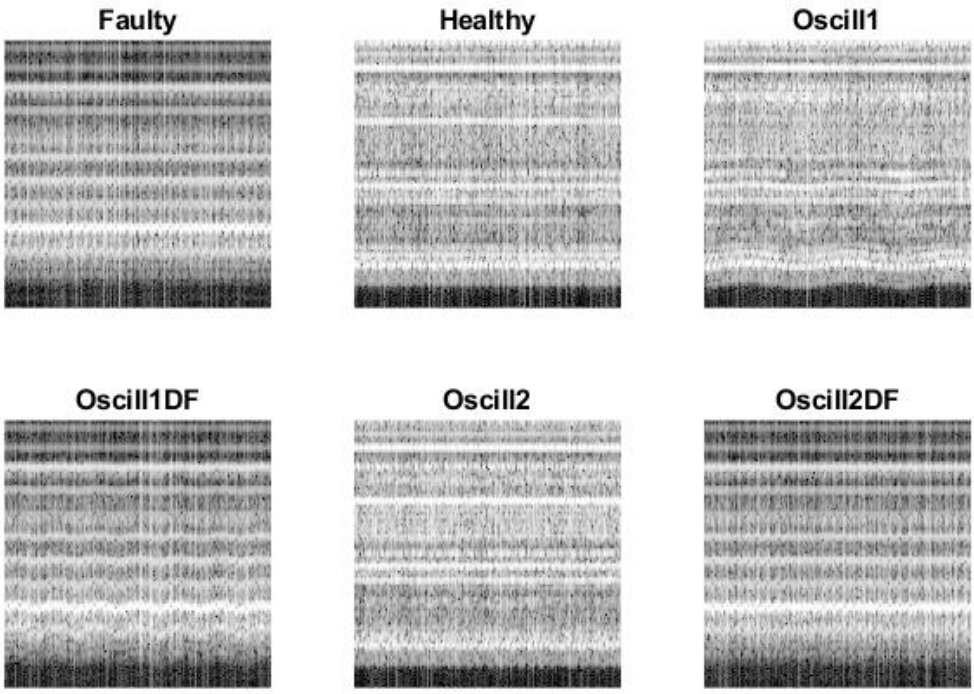

Figure 109: Images of various motor conditions from Pavia data, with 227x227 pixels (6 classes tests).

7.3.2 Tests carried out with the CNN networks

The classification results of the networks will be reported in this section. Variants to the tests include different number of output classes and the use of one or both the datasets combined.

A Stochastic Gradient descent with Momentum (SGDM) optimizer with a cross entropy loss function is utilised to retrain the networks for the Transfer Learning (TL) procedure. The chosen momentum value is 0.9. The momentum can be chosen between 0 and 1 and represents the value of the contribution of the previous iteration step to the optimization function. The SGDM method calculates the loss function gradient and changes the parameters using a mini-batch of training data. In the majority of tests, the mini-batch size is set to 10 images, with each mini-batch is representing the imaged passed in one iteration. As opposed to an iteration, an epoch is a full pass of data to the network; the number of epochs chosen in the process of the networks training in the various tests has been set to a maximum of 16 epochs.

Since the weights of the transferred layers, i.e. the central layers of the original network, do not have to change their values during the retraining phase, the network's learning rate for these connections is maintained low (10^{-4}). Conversely, the replaced last fully connected layer is the layer that must learn fast; as a result, the weight and bias learn factor ratio for this layer is set at values ranging from 3 to 40. This means that the final fully connected layer will learn three to forty times faster than the other layers of the network. The validation frequency, in contrast, is a

coefficient that specifies how many times the validation procedure is done after each iteration. The value for this parameter has been set to 3.

A laptop of the year 2019, ASUS "VivoBook S15 X530FN", with intel i7 processor, 16 Gb of RAM and dedicated NVIDIA "GEFORCE MX150" GPU has been utilised for the calculations. The MATLAB Parallel Computing Toolbox is used to run the computations using GPU resources.

7.3.2.1 Preliminary tests on three-output classes networks

To get preliminary results on their functioning, networks with three output classes are employed in these first tests. Solely Pavia data are utilised, with 40 images per class including just the vibration from the piezoelectric accelerometer. The three classes to be identified by the networks are "Healthy" state, "Faulty", i.e. bearing with localised fault in the outer raceway ring, and "Oscill", i.e. the bearing in healthy condition but with LFTO at 0.5 Hz.

The training/validation subset ratio, weight, and bias learning rate are all hyper-parameters that are evaluated with the AlexNet network model. In addition, in certain experiments, the threshold approach in spectrograms is used for image pre-processing. Figure 110 depicts some of the images created using this approach showing more contrast with respect to the images generated without threshold (see Figure 109).

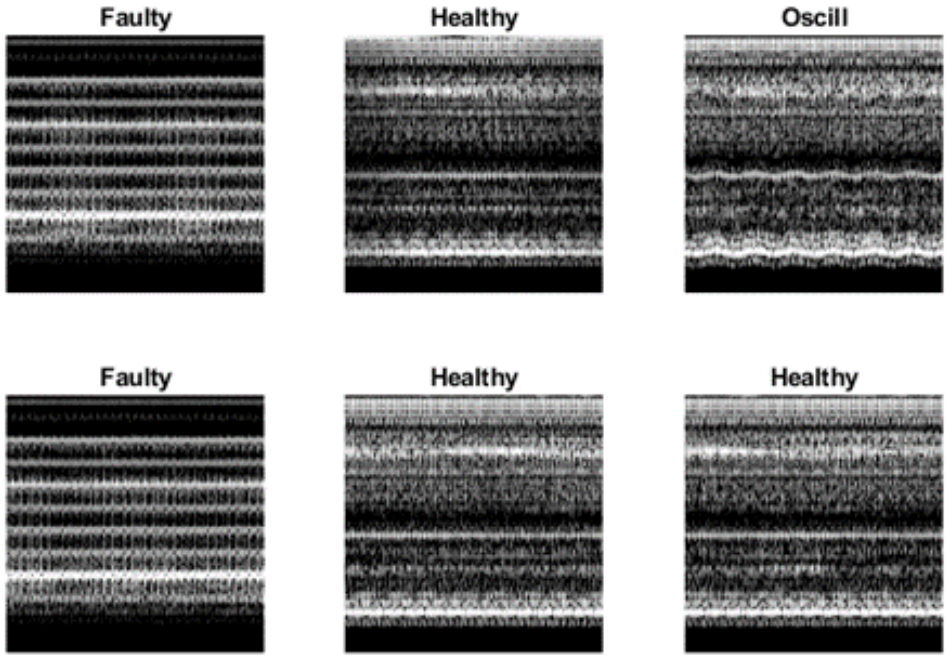

Figure 110: Images generated with Pavia data, magnitude threshold set to -45 dB.

The validation accuracy is calculated using the MATLAB training-progress interface, which plots the training and validation accuracy, as well as the loss function, as the training progresses. The steady-state value attained in the graph is the recorded value of the validation accuracy for the various tests; an example of a validation accuracy plot is shown in the next subsection, in Figure 112.

Table 44 illustrates the hyper-parameters and pre-processing technique utilised in the AlexNet-based network validation tests, as well as the validation accuracy achieved. Table 44 shows that the optimal weight and bias learning rate variables have a value equal to 5 (in the case of 80/20% train/validation ratio), and that the threshold strategy enhances accuracy in Test B when compared to Test A, but not in Tests D when compared with test C.

Table 44: 3-output classes preliminary tests with the network based on AlexNet

Test	Train/Val ratio %	Weight and Bias rate	Threshold technique	Validation accuracy
A	70/30	20	NO	66.7 %
B	70/30	20	-45 dB	85 %
C	80/20	5	NO	91.7 %
D	80/20	5	-45 dB	79 %

In the training process of the networks 16 epochs and 10 pictures for each mini-batch were used. Table 45 summarises the number of pictures, iterations, and execution time of the process used in the AlexNet based network.

Table 45: Training parameters for the AlexNet based network

Train/Val ratio %	Train images	Validation images	Process iterations	Time for training [s]
70/30 %	28	12	128	57
80/20 %	32	8	144	103

Table 46 summarises the hyper-parameters used for the commandNet network, as well as the characteristics and validation accuracy outcomes. The results of threshold pre-processing are not presented in this scenario since they are completely equivalent to those without threshold.

As can be seen confronting Table 45 with Table 46, in the majority of the tests, this network outperforms the AlexNet-based network in terms of validation accuracy.

Table 46: Training characteristics and accuracy results of the commandNet based network

Test	Train/Val ratio %	Weight and Bias rate	Time for training [s]	Validation accuracy
A	70/30	20	16	90%
B	70/30	5	16	95.6%
C	80/20	5	16	95.1%

Even though the validation accuracy differs significantly across different tests, it is preferred to use learning rate variables with a low weight and bias (a value of 5) since they provide better outcomes and the training process is more reliable.

Because this network is substantially lighter, each computation takes just roughly 16 seconds to complete the training compared with 57 or 103 seconds necessary for training the AlexNet based network.

7.3.2.2 Tests on the networks with two mixed dataset

The more varied the data utilised to train an ANN, the more reliable the classification results. The outcomes of the models trained with both the datasets used in this study (the CWRU and the Pavia data) will be provided in this section.

In the datastore of the images, the data are mixed together before being split into validation and training images. In this test scenario, there are just two output classes: Healthy and Faulty. In fact, since no data with LFTO conditions are available in the CWRU dataset, the class "Oscill" has been eliminated to have an equivalent number of classes between the two datasets.

The data from three distinct severities of the defect, given from the CWRU dataset, are combined with Pavia data for the training process in the Faulty class. In the healthy case scenario, part of the CWRU images are reused to achieve the same number of the faulty and healthy pictures. Because of the large collection of pictures already existing owing to the CWRU dataset, only 20 images per class are utilised with the Pavia data, all of them from the piezoelectric accelerometer. Table 47 summarises the current scenario.

Table 47: Subdivision of the images from the two datasets used for the training and validation process

Dataset	Fault diameter (inches)	#images	Data store	Tot images
CWRU	0.007	20	"Faulty"	80
CWRU	0.014	20		
CWRU	0.021	20		
Pavia	Crack	20		
CWRU	Healthy	60	"Healthy"	80
Pavia	Healthy	20		

Moreover, in Figure 111 several images created through STFT transformation from the mixed datastore are shown.

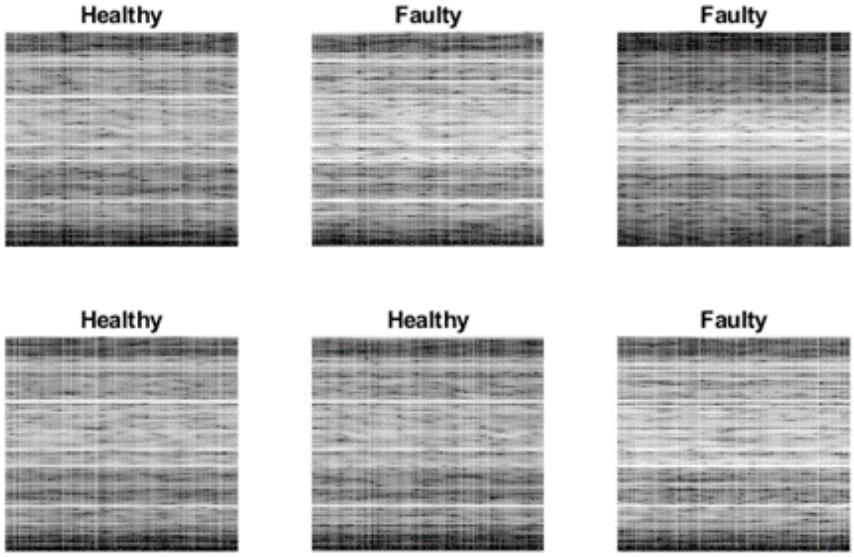

Figure 111: Spectrogram images from the Pavia and CWRU mixed data-store

As can be noticed confronting Figure 111 with Figure 109, the quality of the spectrogram pictures is degraded due to the shorter length of the segments of the CWRU data with respect to the Pavia data. Furthermore, it is possible to see in Figure 111 that two images of class "faulty" might appear highly different due to the fact that the harmonic patterns characteristics of the fault alter with the severity of the fault. This means that appropriately classifying the input data will be more challenging than in the previous group of tests, in which only one fault severity was considered.

The train/validation ratio in these experiments is kept at 75/25 %. As a result, there are 60 images for each output class in the training process and 20 validation images for each class. The maximum number of epochs is set at 16, and the procedure takes 192 iterations with a mini-batch

size of 10. After the 12th epoch, the AlexNet-based network reaches a stable validation accuracy of 97.5%, as shown in Figure 112. To achieve the optimum outcome, the weight and bias rate factor were set to 3 and 5, respectively.

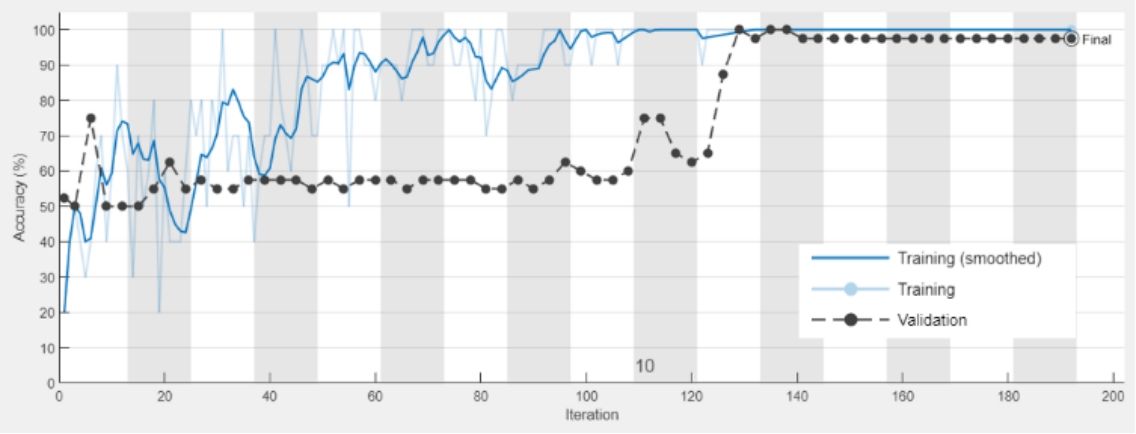

Figure 112: Training and validation accuracies for the AlexNet based network trained with the mixed dataset

In this scenario of a mixed dataset, the accuracy results achieved with the commandNet-based network are worse to those obtained with the AlexNet model. With a weight and bias rate factor of 2 and 5, respectively, maximum validation accuracy is around 90%. Figure 113 depicts the validation and training accuracy procedure.

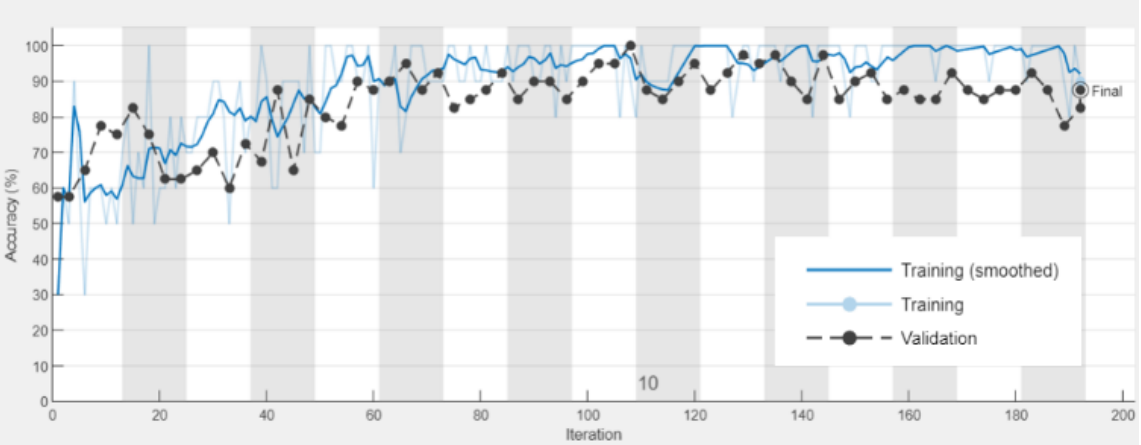

Figure 113: Training and validation accuracies for the CommandNet based network trained with the mixed dataset

7.3.2.3 Networks with six output classes

Three additional output classes are introduced into the networks in these final tests. Pavia data are used to train and validate, and in addition some data are kept apart so that a test accuracy and confusion matrix plot may be produced. Both piezoelectric and MEMS accelerometer data are used in this group of tests.

Two torque oscillation types and two double anomaly situations, corresponding to a simultaneous bearing fault and torque oscillation condition, are among the new output classes. Torque oscillations of 0.2 and 0.5 Hz are included in the "Oscill1" condition, while those of 2 and 3.33 Hz are included in "Oscill2". The torque oscillation condition denominations "Oscill1DF" and "Oscill2DF" indicate that the torque oscillation condition is in simultaneous presence of the bearing defect.

Table 48 lists the number of images generated for each sensor and oscillation condition. A total of 80 pictures for each condition, corresponding to an output class of the network, are generated.

Table 48: Quantity of spectrogram images generated for each sensor and oscillation condition

Class	**Piezo**	**MEMS**
"Healthy"	40	40
"Faulty"	40	40
"Oscill1"	20 @ 0.2 Hz & 20 @0.5 Hz	20 @ 0.2 Hz & 20 @0.5 Hz
"Oscill2"	20 @ 2 Hz & 20 @ 3.33 Hz	20 @ 2 Hz & 20 @ 3.33 Hz
"Oscill1DF"	Oscill1 + Fault	Oscill1 + Fault
"Oscill2DF"	Oscill2 + Fault	Oscill2 + Fault

The proportions 65%, 25%, and 10% are used in the datastore for subdividing the train, the validation, and the test data respectively. This means that, with 80 pictures for each class, the training, validation, and test datasets employ 52, 20, and 8 images, respectively. The maximum number of epochs is set to 16 and the mini-batch is set to 10. The number of iterations required to finish the training process is 496.

To choose the hyper-parameters, various experiments are conducted; it was discovered that, for the AlexNet model, the weight and bias learning factors set to a high value of 40 result in the highest validation accuracy achieved, i.e. 80.8%.

Conversely, with the weight and bias learn factors set to 20 and a mini-batch value of 5, the commandNet model achieves a good and steady validation accuracy of 95%, as shown in Figure 114.

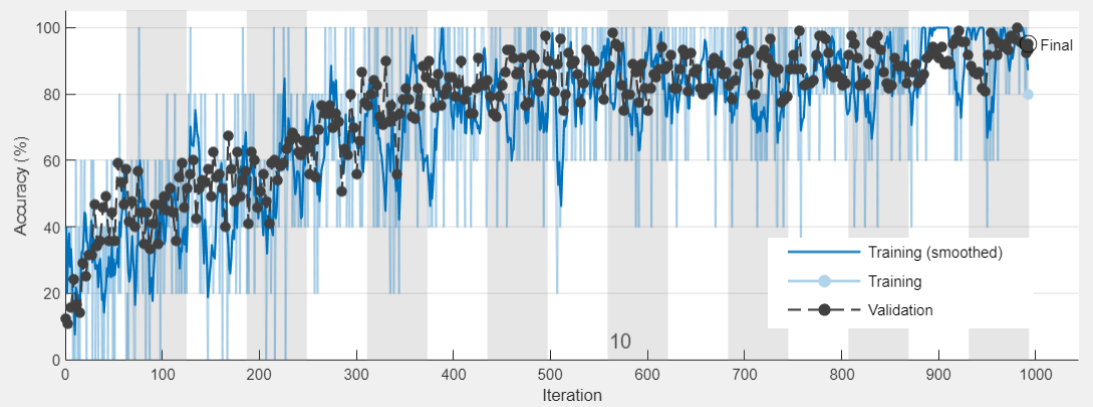

Figure 114: The training and validation accuracy evolution during the training process for the 6-output classes CommandNet model

The confusion matrices are useful for evaluating the target classes misclassified with the output classes. The confusion matrices are assessed using the test dataset, in this group of experiments with 6-output classes. The matrices are reported in Figure 115.

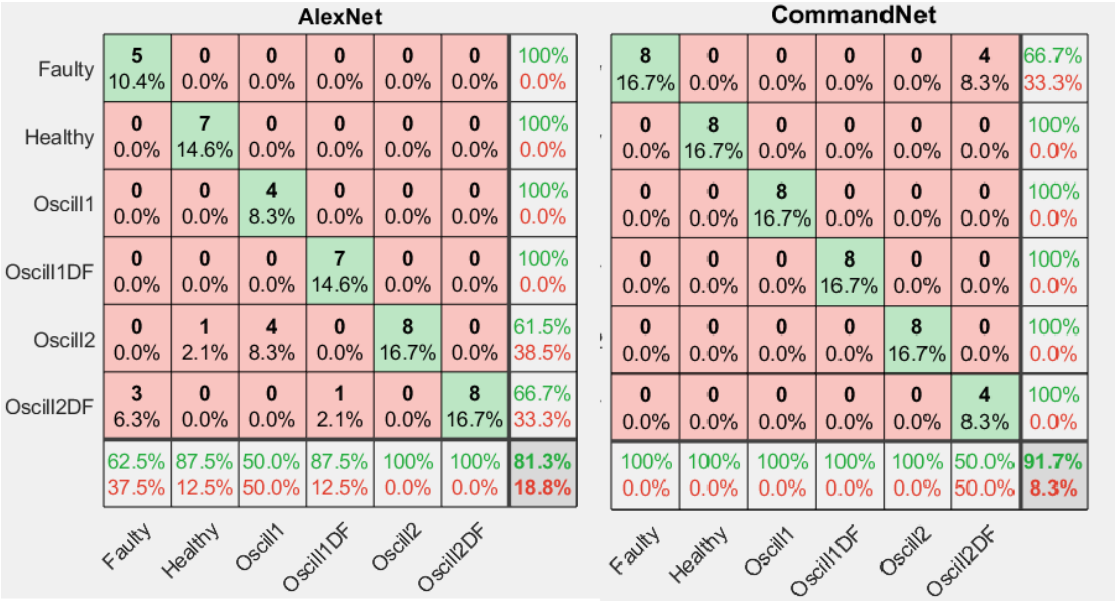

Figure 115: Confusion matrices of the two networks for the 6-output classes tests

As can be noticed looking at the spectrogram pictures in the previous Figure 109, some classes are difficult to discern at first sight. For example, "Oscill2" and "Oscill2DF" are quite similar to "Healthy" and "Faulty", as confirmed by the confusion matrices' results. These classifications are, in fact, among the most misclassified. In any case, both the AlexNet and CommandNet models achieve acceptable test accuracy of 81.3% and 91.7%, respectively. These values are similar to the validation accuracies evaluated with the training progress plots for the two networks (80.8% and 95%): this confirm the validity of the models.

The computation time for the training processes was around 2-3.5 minutes for the networks.

7.4 Discussion

Machine Learning and Deep Learning are more and more used in the field of diagnostics of electrical machines. DL models can be more accurate than classical ML ones, however they need more data to be correctly trained. The Transfer Learning technique can be used in both ML and DL contests: it permits to use a network already trained with abundant "source" data to be adapted to another task using much less "target" data for the training.

A Deep Learning-based approach for diagnosing bearing faults in an induction machine is provided in the work of the author [110]. In the work, through the TL technique, two pre-trained networks, AlexNet and CommandNet, accessible in the MATLAB archive, have been modified to the aim of bearing fault identification and classification. Both of the networks are CNN networks that were originally created respectively for image recognition and speech commands recognition. However, both the AlexNet and CommandNet models recognize images, but while the former directly processes images as input, the latter takes as input auditory spectrograms, that are images as well, but more similar to the images that will be used in the specific application, i.e. spectrograms of the vibration signals.

With the two modified networks, diverse tests are carried out: initially, a preliminary training and validation process with three output classes is performed, using only data from the Pavia University laboratory dataset; secondly, both data from the laboratory and CWRU are used in the training for a two classes output tests; eventually, a six output classes arrangement is tested with the laboratory data. The network's aptitude to distinguish LFTO of various frequencies, as well as the simultaneous existence of the fault and the torque oscillation condition, i.e. a double anomaly situation, is also examined in this final assessment.

For both of the networks, the research results support the validity of the method. The AlexNet and CommandNet models achieved validation accuracy of 91.7% and 95.6%, respectively, in the preliminary test. Conversely, the accuracy in the second test was 97.5% and 90%, respectively. Lastly, the validation accuracy for the two networks in the third group of experiment tests is of 80.8% and 95%, respectively, while the test accuracy is 81.3% and 91.7%. In this final performance, confusion matrices are used to indicate which classes are more difficult to detect, such as some with the torque oscillations and the double anomaly classes.

With the outcomes of the experiments of the work, it can be stated that a Transfer Learning approach may produce good results with limited data for training and with reduced computational time. Although AlexNet's image recognition has occasionally outperformed the CommandNet, i.e. in the second group of tests, however, CommandNet, can be considered more appropriate, since it gives better classification and test results in the first preliminary tests and in the third group of tests.

8 CNN based electromagnetic signals analysis for bearing diagnostics

8.1 Introduction

In this chapter the work of the author [139], published on the "MDPI" peer reviewed journal "Applied Sciences", will be presented.

The work presents a method for diagnosing bearing defects in induction motors by analysing the machine's electromagnetic signals, specifically radial stray flux and stator current signals. The work considers different locations of the defect on the outer raceway of the bearing (different hour positions as in [96]) and load oscillations (LFTO) that form a double anomaly condition when considered together. The machine has been supplied by an inverter, condition that makes difficult the analysis of the signals. In addition to the localized defect, another type of bearing defect has been investigated: the generalized roughness.

The data are converted into a 2-D representation through the Continuous Wavelet Transform (CWT) and the Short time Fourier Transform (STFT). The data are collected in experimental tests in laboratory and a neural network model based on the CNN "GoogLeNet" and trained though transfer learning technique has been used for the classification of the machine conditions.

The most important originality of the work is the use of the CWT on radial stray flux signal for the bearing fault recognition, that, to the knowledge of the author, is a method that has no similar works already published in literature.

8.2 Motivation and literature review

The wavelet transform was chosen to be implemented in the work because it has lately been employed in a number of studies for electrical machine diagnostics, such as [12]. Interesting discoveries on bearing defects can be found in [140, 141], where a Discrete Wavelet Transform (DWT) and a CWT were employed on vibration data for bearing diagnostics. For bearing defect identification, a wavelet packet decomposition and a Hilbert envelope have been applied to the motor current signal in [142]. Two further papers that use Wavelet Transforms to diagnose induction devices are [143-145]. Finally, a CWT analysis of the motor current signal is presented in [147]. However, as stated in the introduction, there are currently no articles available that use wavelet analysis of machines' stray flux for bearing defect identification, to the best of the authors' knowledge.

The signals investigated in the work of the author [139] are coming from an induction motor supplied by an inverter. This implies that categorization of faults will be more challenging, as indicated in numerous publications across the literature, such as [148,149]. One of the current challenges is that the frequency of the current waveform may be changeable for machine speed control, resulting in transient conditions wherein the characteristic harmonics of the desired defects cannot be reliably recognised using a standard frequency-domain analysis. Another significant challenge is that the electrical commutations used in the inverter to generate the waveform result in the development of Electromagnetic Interference (EMI), which may readily mask the fault frequency components. Lastly, the existence of a closed-loop controller, particularly in Field Oriented Control (FOC) drives, is a major challenge in searching for machine faults in electronic-fed drives. In reality, as noted in [53], while fault harmonics may still be seen with a V/f open-loop drive, standard voltage and current acquisitions are insufficient to identify bearing failures with a FOC closed-loop (without certain FOC structure changes). Many strategies were used in different studies to mitigate these issues on the diagnostic system, particularly for the identification of bearing defects with extremely low characteristic harmonic magnitudes, i.e. incipient faults.

Since the mechanical defects in bearings create a change in the characteristics of the vibrations signatures as a primary consequence, it is frequently mentioned in the literature that the examination of vibration signals may be the best alternative for bearing diagnostics. Secondary effects of the fault, such as changes in the air-gap length (air-gap eccentricity) and the establishment of torque fluctuations owing to the fault in the bearing, cause harmonics in the electromagnetic signals such as current or stray flux spectra [25], [50]. Aside from that, vibration measurements may be problematic in some circumstances since the machine may not be easily accessible, and sensor purchase and maintenance costs may be considerable, increasing the system's complexity. Furthermore, the vibration signature may differ from one physical location of the machine to another; for example, multiple accelerometers may be required to inspect both the fan-end and drive-end bearings.

The current signal is frequently considered not sufficient for a complete bearing diagnosis and therefore it is recommended to be used together with vibration data [25]. However, many works attempt to extrapolate diagnosis information solely from this signal due to the ease of sensor installation or the cost-effectiveness of using a transducer already embedded in the converter for machine's control purposes.

The machine was monitored using both stator current and exterior radial stray flux signals in the study of the author [139]. The stray flux signature study has been shown to be as successful as current signature analysis and, in some situations, can even provide superior diagnostic results as reported also in [36]. As previously stated, the analysis of the signals was carried out in the article using the GoogLeNet CNN with transfer learning training approach for the classification and identification of the machine faulty or healthy conditions.

It has to be said that CWT is sometimes not recommended for fault diagnosis as explained in [146]. This is due to the fact that the CWT is a multiresolution technique: at low frequencies the frequency resolution is much better but the time resolution worsens and viceversa at high frequencies. For this reason, the authors state that the CWT does not give any advantage with respect to STFT and so they do not recommend the use of it in fault diagnosis. However, in the presented work [139] the CWT is used on stationary signals (the frequency of the fundamental component is not changing during the measurements) and not in transient signal (inverter-fed machines start-up) as in [146]. Moreover, in [139] a comparison between CWT and STFT is performed, giving new insights on both the transformation techniques applied to the current and stray flux signals for the purpose of diagnostics of bearing faults.

8.3 Procedure and methods

8.3.1 The transformation in time-frequency domain: spectrograms and scalograms

Spectrograms are graphical representations of signals' spectrum component frequencies as they change over time. A spectrogram may be produced in a variety of methods. The STFT and CWT were utilised to create spectrograms in the study presented. The pictures produced by the wavelet transform are generally known as scalograms. In the work of the author [139] and in this chapter, the nomenclature "spectrograms" is referred solely to the STFT pictures whereas "scalograms" is referred to the CWT images.

The STFT of a signal is calculated by applying the Fast Fourier Transform (FFT) method repeatedly. In specific, digitally sampled time-domain data are partitioned into window frames, which generally overlap, and thereafter they are Fourier transformed to determine the frequency spectrum of every window. Each window spectrum is then represented by a vertical line in the graph, with the intensity of the colour proportional to the relative amplitude of the signal at the frequency in question. The complete spectrogram image is then created by laying these window spectra "side by side".

The main disadvantage of the STFT is that the resolution is fixed. The width of the recovered windows influences whether there is strong frequency resolution, which allows two close harmonics to be discriminated on the spectra, or good time resolution, which allows one to discern quick changes in the time-axis of the frequency harmonics. The Gabor limit summarises the concept: it stipulates that a signal may not be precisely localised in the time and frequency domain simultaneously.

The signal to be converted is multiplied by a function that is always zero except for a short time interval (a window function), in the continuous-time representation of the short-time Fourier

transform. As the window shifts along the time axis, the signal's Fourier transform is constructed, yielding a two-dimensional representation [150]:

$$STFT\{x(t)\}(\tau,\omega) \equiv X(\tau,\omega) = \int_{-\infty}^{\infty} x(t)\omega(t-\tau)e^{-i\omega t}dt \tag{8.1}$$

In which $x(t)$ is the signal to be modified, and $\omega(\tau)$ is the window function that might be a Hann window or a Gaussian window function.

Conversely, discrete time transformations divide the data to be changed into time-frames that, to reduce artefacts, generally overlap. The amplitude and phase of the complex value at each point in time and frequency are retained for each frame after Fourier transformation:

$$STFT\{x[n]\}(m,\omega) \equiv X(m,\omega) = \sum_{n=-\infty}^{\infty} x[n]\omega(n-m)e^{-i\omega n} \tag{8.2}$$

in which the signal to be converted is $x[n]$ and the window is $\omega(n-m)$, with m and ω being discrete and continuous values, respectively. In practical, both variables are discrete.

Lastly, the Power Spectral Density (PSD) is a measure of the signal's power as a function of frequency per unit frequency. The spectrogram representation of the function's Power Spectral Density is given by the STFT's squared magnitude:

$$spectrogram\{x(t)\}(\tau,\omega) \equiv |X(\tau,\omega)|^2 \tag{8.3}$$

In opposition to the STFT, a wavelet transform is produced by the operation of convolution over a signal with wavelet functions. A wavelet is a wave-like oscillation with zero amplitude at its beginning and end. A wavelet could be constructed with a specific characteristic frequency; when this wavelet is convolved with a signal, the output waveform can be used to evaluate if the specified frequency was contained in the signal. To completely examine the data, sets of complementary wavelets are usually required.

Opposed to the STFT, the wavelet analysis uses a windowing method with variable-size windows. This allows for the use of lengthy time intervals when low-frequency harmonic components must be seen, and narrower windows when high-frequency components changing with time have to be interpreted. Wavelet analysis is moreover better suited not just for the analysis of transient signals, but also for the reduction of noise in the operation.

CWT was used in the study. Unlike the DWT, the CWT allows the wavelet parameters called translation and scale to fluctuate continuously, resulting in a comprehensive representation of the input. Compared to a periodic signal, the scale parameter is similar to the period parameter (reciprocal of frequency); it can expand or shrink the wavelet in relation to its value. Slow changes in the signal can be identified using a reduced scale, while quick transients in the studied signal can be identified using a stretched scale.

The CWT is a mathematical technique that provides a comprehensive representation of a signal by varying the translation and scale parameters of wavelets. The following integral expresses the CWT of a function $x(t)$ at a scale $(a > 0)$ with $a \in \mathbb{R}^{+*}$and a translational value $b \in \mathbb{R}$ [151]:

$$X_{\omega}(a,b) = \frac{1}{|a|^{1/2}} \int_{-\infty}^{\infty} x(t)\, \bar{\psi}\left(\frac{t-b}{a}\right) dt \tag{8.4}$$

in which $\psi(t)$ is the so-called "mother wavelet", a continuous complex function in both time and frequency domains; as denoted by the over-line symbol, in (8.4), the $\psi(t)$ function is complex conjugated. The mother wavelet's main function is to provide a source function for the daughter wavelets, that are the scaled and translated variants of the mother wavelet.

The CWT was processed in the work using a filter-bank with 12 voices per octave, resulting in 12 intermediary scale values in every octave. This discretization of the scale is not very high, but it was deemed adequate due to the CCN network's satisfactory classification results. The analytic Morse (3,60) wavelet is employed in the filter bank. This wavelet function has a symmetric parameter (gamma value) equal to 3, indicating that it is symmetrical in thefrequency domain. The time-bandwidth product of the wavelet is 60. This value may not be bigger than 40 times the gamma value; a larger value corresponds to larger time domain dispersion of the wavelet but also to an improved frequency resolution.

The width of the input signal frames and the frequencies for the sampling process utilised for the specific situations investigated have been changed for different tests and are given in the following sections of the chapter.

More information on scalogram synthesis is provided in paragraph 8.5.1, where the first findings are revealed; however, identical settings were used in all parts where a CWT was done. Similarly, paragraph 8.5.4 contains more information on the production of the spectrograms with the STFT process.

8.3.2 The GoogLeNet Convolutional Neural Network

GoogLeNet, the convolutional neural network utilised in the publication, is a variation of the Inception Network, a Deep Convolutional Neural Network built by Google researchers. It is constructed of 22 layers, with portions of these levels incorporated in a total of 9 inception modules. Inception units are commonly employed in CNNs to achieve more efficient processing and deeper networks by reducing dimensionality. The modules were created to address difficulties such as computational costs and overfitting. In summary, the idea is to use various kernel filter sizes inside the CNN and order them to function on the same level instead of stacking them consecutively. This sort of adaptation causes the network to get wider instead of deeper. Figure

116 depicts the net structure employed in the work, with the layout of the inception module emphasised.

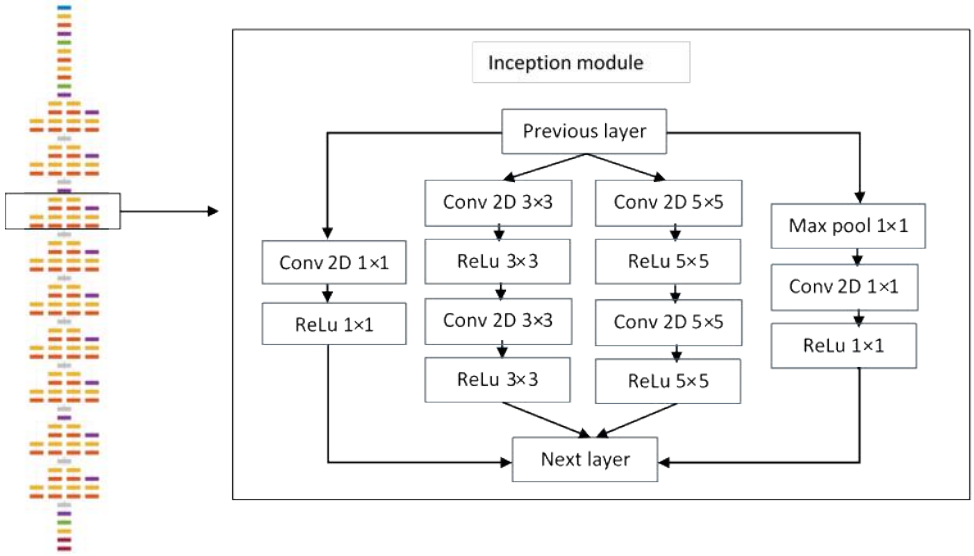

Figure 116: structure of GoogLeNet, with an inception module highlighted [139]

According to the designers of GoogLeNet's [152], the inception units are implemented with 3 distinct size of the convolutional filters: 1x1, 3x3, and 5x5. Furthermore, max pooling is employed in parallel since, according to the published literature, this enhances the network performances. The parallel routes of the inception blocks provide a feature extraction with diverse sizes of the filters (the scales), that are then combined before being recovered by the following stage, allowing it to abstract features coming from various scales at the same time. If no dimensionality reduction approach were utilised, the usage of numerous convolution layers and inception blocks would lead in an unnatural number of parameters to train. Thus, in the inception blocks, the basic approach is a 1x1 convolution filter inserted before any of the computationally more costly 3x3 or 5x5 filters.

According to [152], it may be more convenient to start the series of inception blocks after some traditional old-style convolutional layers, as implemented in GoogLeNet. To have more details on the network, [153] has a complete example of the exact network utilised in the study, which is provided from the MATLAB repository. The pre-trained network was updated in the study by changing several of the last layers, as is discussed below.

The dataset ImageNet was utilised to train the GoogLeNet variant used in the research [154]. This collection is made up of 1000 various picture categories, such as objects, flowers and animals. The net received a 224x224 pixel picture with three Red Green Blue (RGB) streams as input.

The selection of a 2D CNN instead of a 1-D CNN was decided in order to have a greater availability of pre-trained at state-of-the-art image recognition models. Furthermore, as

demonstrated in [155], even transitory signals may be properly investigated using a 2D representation. The choice of GoogLeNet compared to alternative networks such as VGG (Visual Geometry Group) or ResNet was based on the high accuracy attained by GoogLeNet in comparison to its memory use and processing resources.

The network was supplied with the scalograms and spectrograms mentioned in the preceding section. Because these “pictures” were not among the original classes with which the model was trained, the network had to be altered in order to perform an appropriate classification procedure. This was accomplished using the transfer learning approach, similar to what carried out by the author in [110]. The approach consists in the replacing and re-training of the final fully-connected and classification layers with new ones that have a number of output class categories equal to the number of classes in the new target task. It has to be remembered that the number of the target classes, with respect to the number of the original classes, must be one or two orders of magnitude smaller.

Because the initial layers had previously been trained and properly retrieved the features from the pictures, the network required considerably fewer data to be retrained once these last layers were replaced (particularly for a 2D CNN). High weight and bias learning, i.e learning rate factors, were employed to let the final layer to learn fast, but low learning rate factors were retained for the earlier layers since they do not need to modify their learning parameters. This approach is important since it eliminates the requirement for a whole new network to be designed and trained for this purpose.

The dataset for the training and test of the network has been chosen in this way: the training set had 65% of the database pictures, the validation set contained 25% of the images, and the test set contained the remaining 10%.

More details on the parameters chosen and modified in the original network, such as dropout probability of dropout layers, minibatch size, etc. are reported in the original work [139], and not repeated here for the sake of brevity and easiness of reading.

8.4 Experimental measurements

As cited in the introduction of the chapter, the tests reported in the study are all based on experimental laboratory acquisitions. The experimental setting is the same as in the author’ earlier papers, such as [110], and it is described in chapter 3.

To quickly resume the equipment, the test bed is composed of the 1.5 kW 3-phase induction motor, coupled with a magnetic-powder brake. In the work only tests with inverter supply are considered. The inverter works in open-loop with a space vector control and a Pulse Width Modulation (PWM) of the output voltage.

The brake is controlled to give constant-torque or Low-Frequency Torque Oscillation (LFTO) conditions: in this latter case a sinusoidal torque with low frequency is added to a constant mean load torque.

Among the signals available, presented in chapter 3, in the work only the radial stray flux signal and the stator current of the machine are analysed. The position of the c-shaped flux-probe is near the fan-end of the motor, recognized as the most effective location for diagnostic purposes in a previous work carried out in the laboratory [156].

The multichannel NI-USB6212 Data Acquisition Board was used to sample data from the different sensors. The sampling frequency of 120 kHz was selected because the inverter's switching frequency is 6 kHz and, following the procedure described in [66], a sampling frequency 20 times the converter switching frequency is considered appropriate for correctly evaluating the harmonic distortion added by the inverter. A hardware single-order 2 kHz bandwidth low-pass filter was added to the measurement chain among each probe and the acquisition board for anti-aliasing benefits.

The experiments were conducted using two types of bearings and two distinct defective situations of the bearing: generalised roughness and a localized-point defect (particularly a fracture) on the outer raceway of the bearing. Similarly to the study reported in [102] and the work of the author [96], the condition of localized fault was tested for different angular locations of the crack. The studied fault positions have been at hours 12, 3, 4.5, and 6, and will be indicated as H12, H3, H45, and H6 in the following.

The bearings characteristics are exposed in 3.2.1, and summarised in Table 49.

Table 49: main features of the bearings used for the study of the two defects.

Bearing Model	**Fault Simulated**	**Number of Balls**	**Ball Diameters**
NSK 6205Z	Single-point defect	9 (single row)	d ≅ 7.9 mm
SKF 1205ETN9	Generalized roughness	26 (double row)	d = 7.45 mm

The localized-defect generates characteristic harmonics, the BPFO harmonics in vibration signal and corresponding harmonics in electromagnetic signals, as discussed in 2.3.4.

Conversely, the generalised roughness defect does not display harmonics at specific frequencies, but the vibration spectra and stator current of the machine alter in an unexpected manner, frequently resulting in a broadband harmonic excitation [29].

In combination with the healthy measurements, which served the baseline for the generalised roughness testing, two fault intensity levels were employed: Step 1 and Step 2 roughness-defect were produced using acid corrosion wear, as explained in the previous study of the author on this kind of defect (see paragraph 4.4).

Table 50 shows the acquisition settings for each example. Each instance studied consisted of many acquisitions (from 40 to 80), to collect longer measurements spread over a larger period, for the aim of thermal stability and for computing the average of the spectra to decrease noise, as previously described in [66,84].

Table 50: Characteristics of the acquisitions

N° of Sample for Each Acquisition	**Acquisition Frequency**	**Achievable FFT Resolution**	**Number of Acquisitions**	**Time of The Whole Set**
2^{20} = 1,048,576	120 kHz	0.115 Hz	40 to 80	40·× 8.73 = 349 s 80·× 8.73 = 698 s

Table 51 shows the specific number of images (spectrograms or scalograms) created for each scenario.

Table 51: Number of images generated for each study case and denotation of the conditions

Type of Fault	**Denotation**	**Number of Images Generated**
Baseline	Bas	80
Generalized roughness step 1	BF Step 1	40
Generalized roughness step 2	BF Step 2	40
Crack at hour 12	H12	60
Crack at hour 3	H3	60
Crack at hour 4.5	H45	60
Crack at hour 6	H6	60

During the study, no data pertaining to other kinds of bearing defects (e.g. inner ring defect, ball defect) has been used in the tests. Nevertheless, the research suggests that if the network can distinguish between two specific hour-case localised faults in the outer ring, which may have comparable signatures, the network may also distinguish other kinds of defects.

8.5 Results

The results of the paper [139] will be summarised in the next subsections.

Different situations were investigated in the conversion of raw data into the time-frequency domain: (i) the use of CWT vs STFT approaches, (ii) the use of decimated versus non-decimated data, and (iii) the use of just one sensor signal against the use of two signals. Furthermore, a LFTO

condition current signal was included to evaluate the suggested CNN technique in a more difficult scenario.

The results of the several tests are intended as the classification and test accuracies of the revised deep neural network GoogLeNet. Both stray flux and stator current signal are considered and compared in various tests.

8.5.1 Three Output Classes tests

The first tests on the network only used three categorization classes: healthy (baseline), defective with generalised roughness of severity Step 1 and Step 2.

The baseline had 80 images, and each of the instances Step 1 and Step 2 had 40 images. The CWT with the MATLAB filter bank "cwtfilterbank" was employed in the transformation with 12 voices per octave.

The first 100,000 samples of each acquisition were used as segments for image generation. This resulted in an interval of 833 ms at a sample frequency of 120 kHz. This time span was deemed sufficient because it comprised about 41 fundamental periods, since all the tests were supplied with a 50 Hz waveform generated by the inverter. In the tests in which more than 40 pictures were created for each class, other successive 100,000 sample segments were acquired from the same 2^{20} sample acquisitions in addition to the initial 100,000 sample segments of each acquisition.

Further details are reported in [139].

Figure 117 depicts some random pictures of the current and radial stray flux signal for the three output classes tests. Note that the figure represents the images to be fed to the neural network. The x-axis is the time-axis, going from 0 to 833 ms; the y-axis is the frequency axis, going from 0 to 60 kHz growing from the bottom to the top in a logarithmic way (and from 0 Hz to 6 kHz for the decimated data, see 8.5.1.1). The validation accuracies achieved with the model supplied with the signals are 100% for the radial flux and 50% for the current signal, respectively. Figure 118 depicts an example of training progress. As seen in Figure 118, the network quickly attained convergence (after 4 epochs) and the entire procedure took less than a minute. Figure 119 depicts the confusion matrices in the two scenarios.

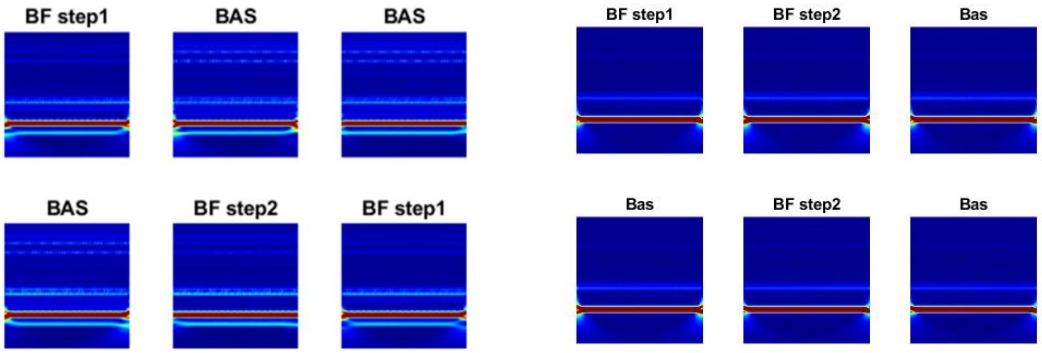

(**a**) (**b**)

Figure 117: Some examples of CWT-generated training images: (a) radial flux and (b) current signal.

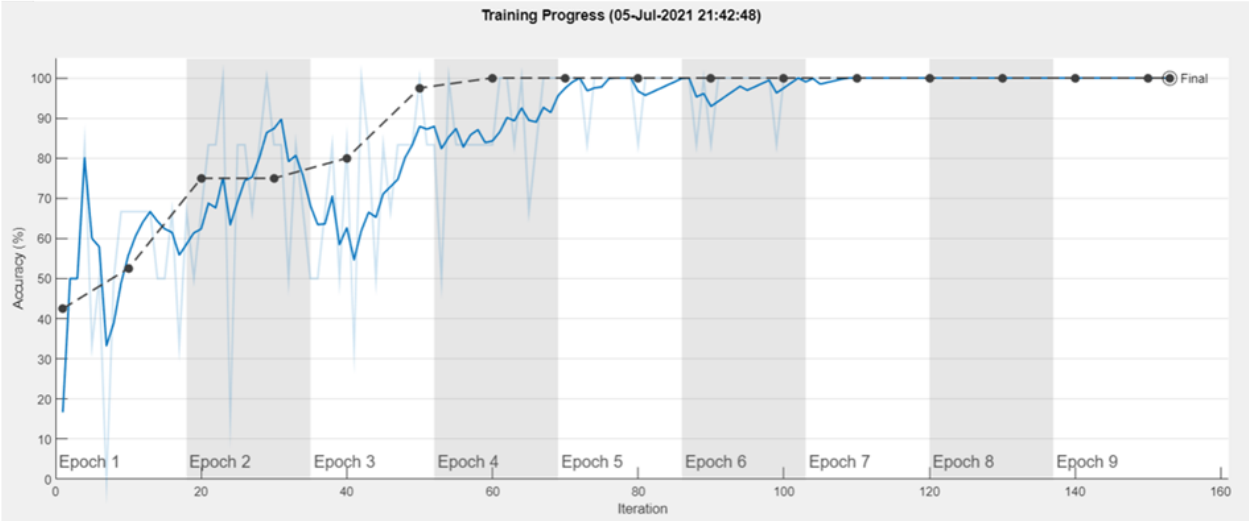

Figure 118: Accuracy progress for training and validation data: training in light blue and blue (smoothed), validation in black dashed.

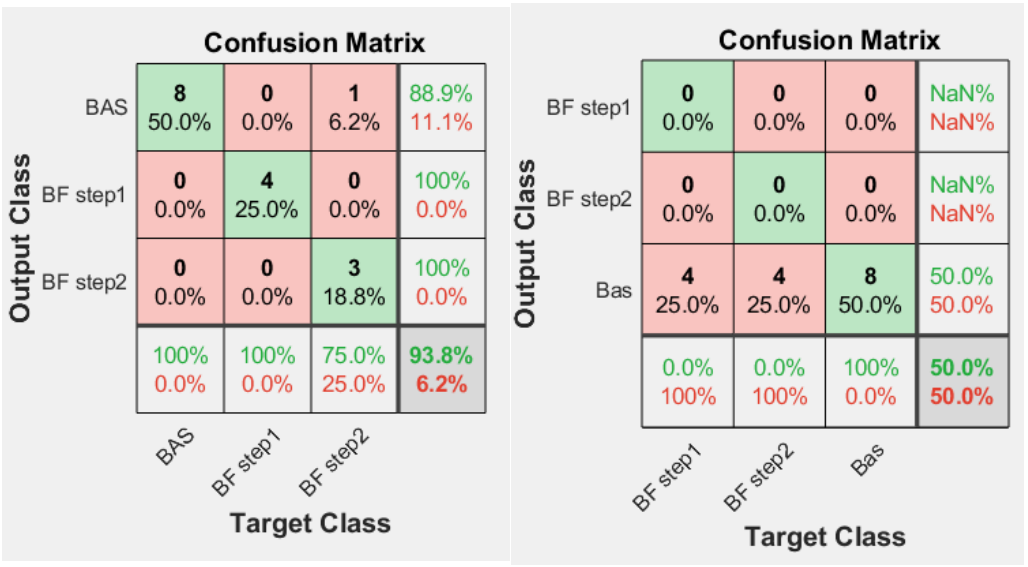

(**a**) (**b**)

Figure 119 Confusion matrices for (a) radial flux and (b) current signal (test set).

The flux signal's test accuracy, i.e. 93.8%, was somewhat lower than the validation accuracy, while the current signal's test accuracy (50%) was the same as the validation accuracy.

These preliminary tests show that the radial flux signal outperforms the current signal with the identical transformation parameters.

8.5.1.1 Three Output Classes Tests with Decimated Data

Identical tests that were performed with a decimated sampling frequency, since the sampling rate typically assumes lower limits and the fault characteristic patterns investigated are at lower frequencies, e.g. from 0 to 2 kHz.

The decimate MATLAB function has been used for the decimation. The reduction parameter chosen was 10, reducing the sampling frequency from 120 kHz to 12 kHz and the segment length from 100000 to 10000 samples.

One non-decimated and one decimated scalogram images are depicted in Figure 120.

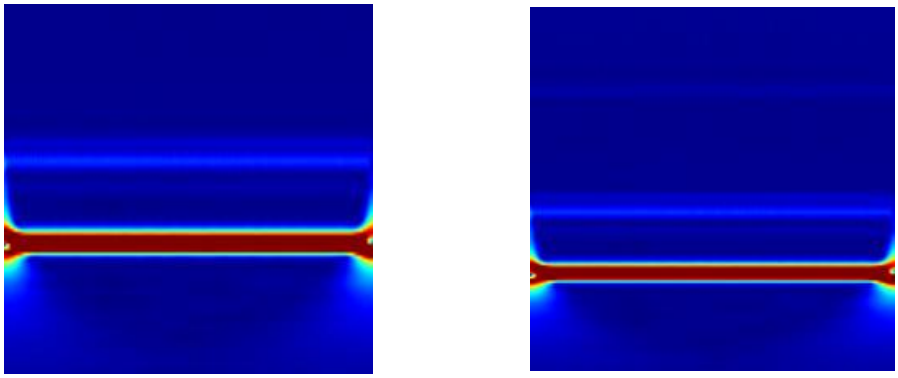

(**a**) (**b**)

Figure 120: Scalogram examples from current signals: (a) with decimated sampling frequency and (b) with non-decimated sampling frequency.

The validation accuracy rates achieved with the decimated data were 97.5% for the radial flux and 40.0% for the current signals. This indicates that the pictures may be identified also with a decimated sample frequency, however the validation accuracy for both flux and current signals would deteriorate: from 100% to 97.5% for the radial flux and from 50% to 40% for the current.

8.5.2 Seven Output Classes tests

Additional tests were performed by including four classes to the network: the bearings faults characterized by a localised crack in the outer ring at four distinct angular positions. The data pre-processing was carried out in the same manner as stated in the paragraph 8.5.1; the network was configured with the same hyper-parameters as the previous tests. The acquired segments utilised were not decimated. The names of the classes and the quantity of scalograms created in each class are summarised in Table 51.

8.5.2.1 Radial Stray Flux Signal Analysis

With the radial stray flux, the network's accuracy remained very good also with seven output classes. As seen in Figure 121, the network obtained convergence quickly, in roughly 4 epochs, yielding a validation accuracy of 100%. Conversely, Figure 122 depicts the confusion matrix, which shows that every class was accurately classified.

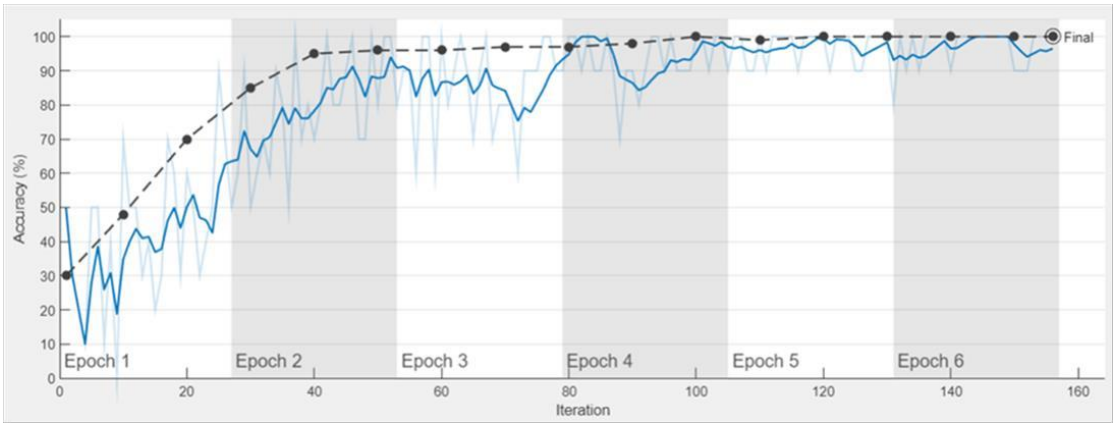

Figure 121: Accuracy progress for training and validation data in the 7-output classes tests with radial flux signal: training in light blue and blue (smoothed), validation in black dashed.

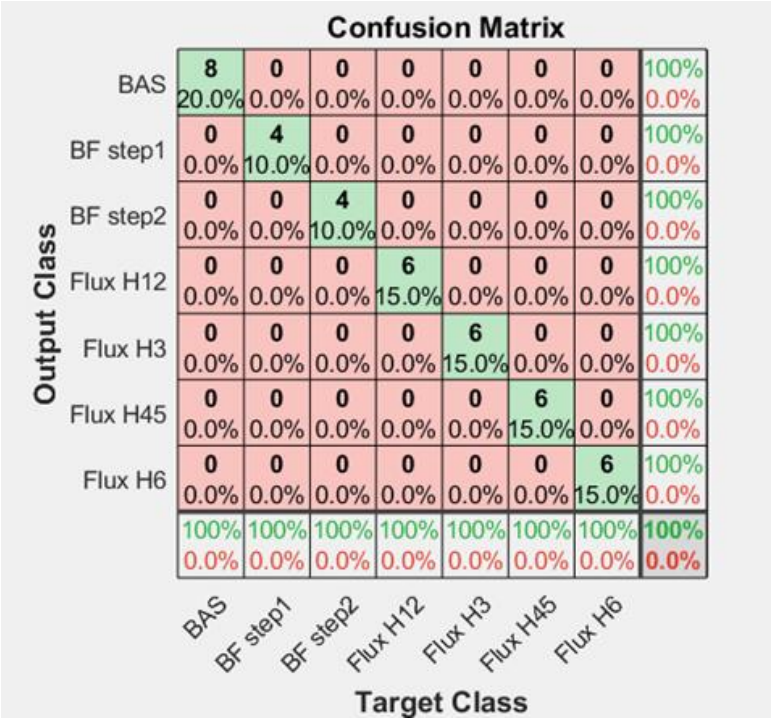

Figure 122: Confusion matrix (using the test set) for the seven classes tests with radial flux signal

8.5.2.2 Current Signal Analysis

In comparison to the previous scenario with three classification classes, the network training with current signals required more iterations to achieve convergence in training accuracy. The stable validation accuracy was around 85%, which was lower than for the radial flux signal but greater than for the current signal in the first test with three output classes.

Figure 123 depicts the training and validation progress of the seven output classes test with current signal. The limit of the number of epochs was set to 24 to reach convergence; the procedure took around 7 minutes. Figure 124 depicts the confusion matrix.

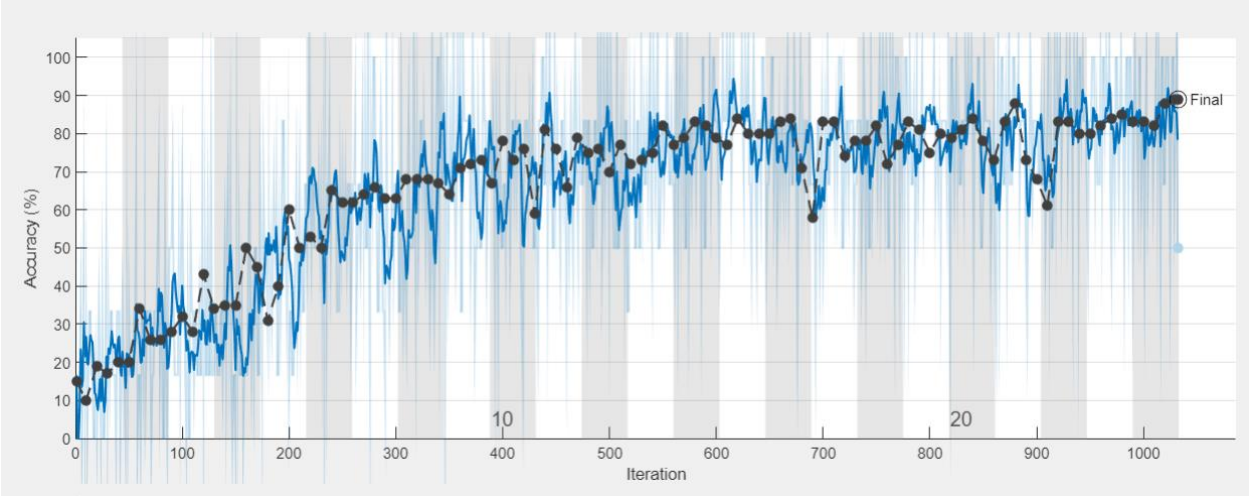

Figure 123: Accuracy progress for training and validation data in the 7-output classes tests with stator current signal: training in light blue and blue (smoothed), validation in black dashed.

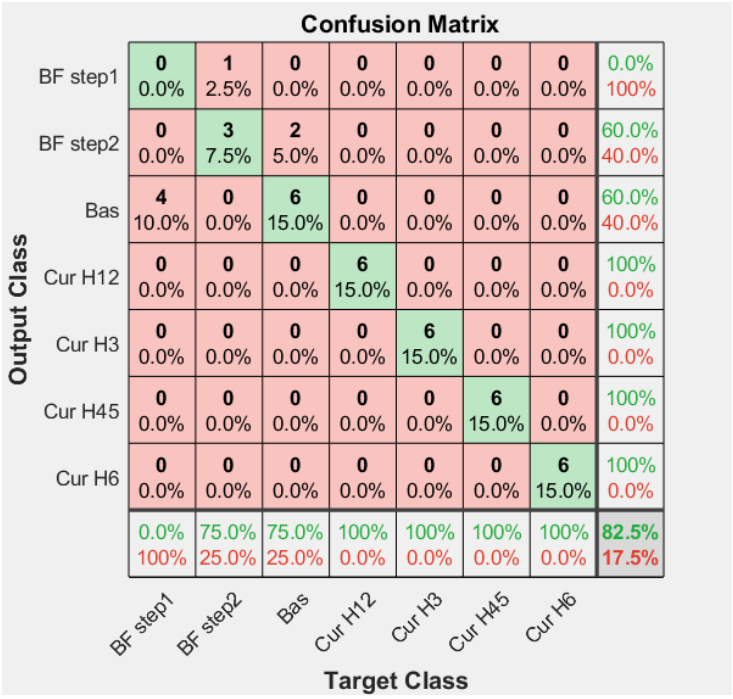

Figure 124: Confusion matrix (using the test set) for the seven classes tests with stator current signal

Figure 124 shows that the most incorrectly classified categories are those with the generalised roughness flaw. Furthermore, the baseline class was occasionally misidentified as the bearing fault step 2 (BF Step 2).

8.5.2.3 Mixed signals analysis

This paragraph presents the network that has been trained utilising both the current and flux signals. The amount of pictures utilised was double compared to the single-signal analysis. The maximum number of epochs was increased to 24, and the weight and bias learning rate was extended from 15 to 25. The validation accuracy was 89%, and convergence went roughly after 18 epochs. The computation took about 13 minutes.

An identical test was performed using decimated data. Validation accuracy was lower than non-decimated data (76%), but a quick convergence is reached in about 10 epochs. Figure 125 depicts the confusion matrices for both non-decimated and decimated data sets.

As shown in Figure 125, the sole misclassification for the non-decimated data was for the class “BF Step 1”, which included 50% misclassified pictures. The overall test accuracy was 95%. Conversely, many classes were misinterpreted in the decimated data, including “Bas”, “BF Step 1”, “H12”, and “H45”. For the decimated data, the overall test accuracy was 81.2%. This can indicate that the network sees feature patterns also at a high frequency in the scalograms, allowing it to achieve greater validation and test accuracies for non-decimated data.

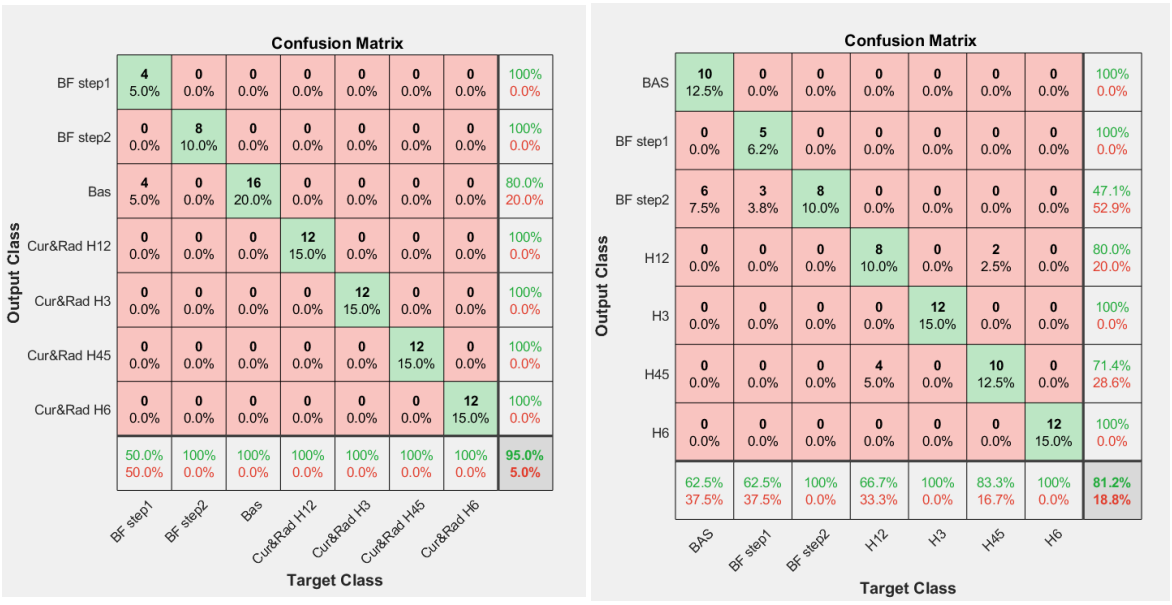

(a) (b)

Figure 125: Confusion matrices for (a) non-decimated and (b) decimated data, analysing both current and flux signals (mixed-signal).

8.5.3 LFTO conditions analysis

LFTOs were introduced in several tests; this condition might emulate a rotor bar defect or a specific sort of mechanical load, as discussed in paragraph 2.3.5. As mentioned in [84], a double fault scenario was simulated using data from a motor with a bearing problem and an oscillating load torque.

Just the stator current data has been used in this scenario. The LFTO condition was created by summing a sinusoidal torque wave of 0.5 Hz over a constant load torque. Due to scarcity of LFTO data, only four classes were employed, in particular the classes of the localised fault, at four distinct angular points, excluding the baseline class.

The analyses present a comparison between decimated and non-decimated data. Furthermore, the neural network was used to classify the same four classes with localised faults without LFTO, enabling direct comparison among the single and double fault scenarios. In a first evaluation, the single and double fault conditions were input into the neural network independently; secondly, all eight classes were supplied into the model together for a 8-class classification objective.

8.5.3.1 Four output Classes tests with LFTO condition

The localized bearing fault data with LFTO (double anomaly condition) and without LFTO are supplied into the network separately. Decimated and non-decimated data are considered. The upper limit for the number of epochs was set to 24 in these tests. The validation and test accuracies are summarised in Table 52.

Table 52: Validation and test accuracy for the LFTO double anomaly condition compared to the single fault condition.

Case	Decimation	Validation Accuracy	Test Accuracy
Bearing fault + LFTO	NO	65%	83.3%
	YES	56.7%	29.2%
Bearing fault	NO	98.33%	95.8%
	YES	75%	75%

As visible in Table 52, the double anomaly condition caused additional challenges in the classification procedure, as predicted. Data having a non-decimated frequency spectrum yields superior categorization results. As demonstrated in Figure 126, distinguishing the H12 class for both single and double fault scenarios and the H6 class in the event of double fault was particularly challenging with the decimated data.

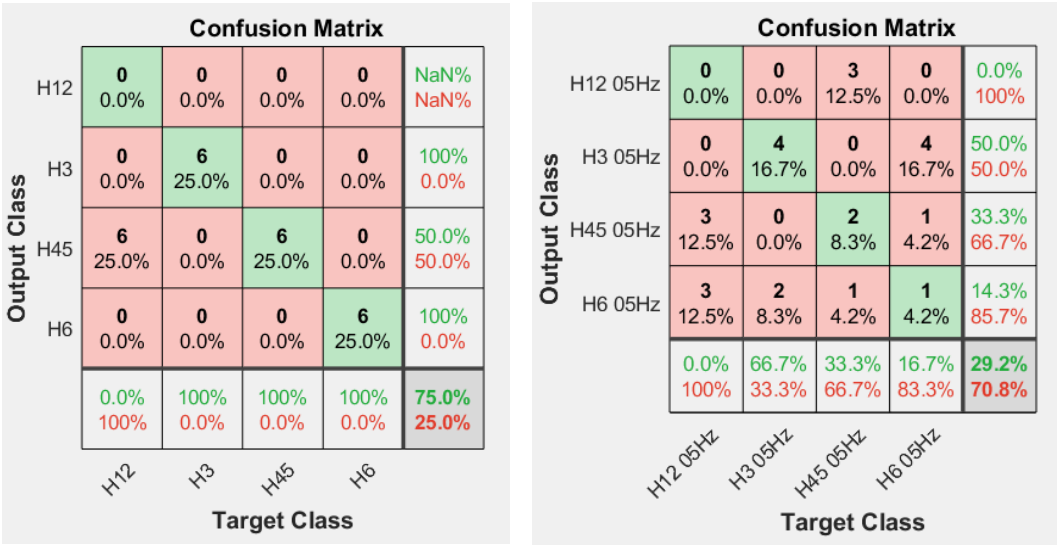

(a) **(b)**

Figure 126: Confusion matrices generated from decimated data in (a) single fault and (b) double anomaly conditions

It may be noted that, in the situation of LFTO, the electromagnetic signal images produced with the CWT do not exhibit characteristics patterns recognizable by the human eye, in opposition to vibration spectrogram images presented in [110], in which torque oscillation are easily recognizable. Figure 127 shows two example pictures from the decimated data showing very similar images in the two conditions.

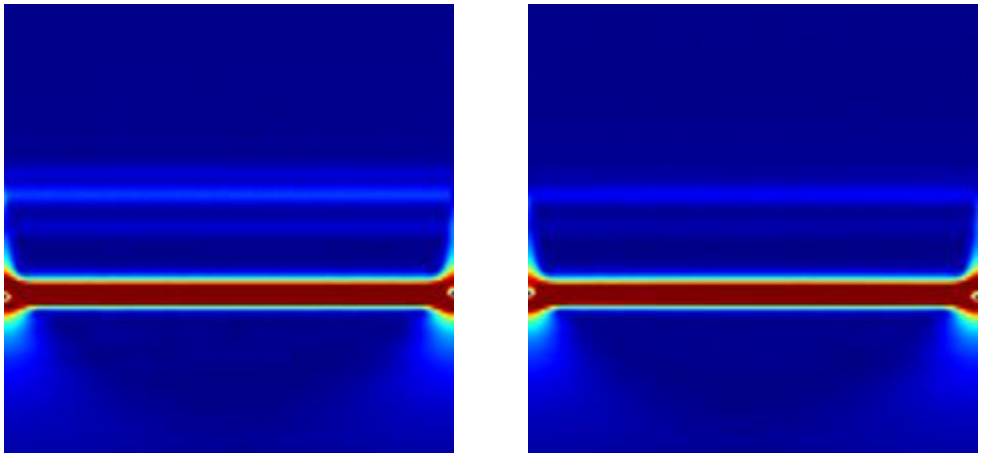

(a) **(b)**

Figure 127: Scalogram pictures of the current signal produced with decimated data: (a) H6 single fault condition and (b) H6 and LFTO double fault condition.

8.5.3.2 Eight-output Classes tests with LFTO condition

In the test of this scenario, non-decimated data are used. This test was carried out by combining the signals of the single defect with the data of the double anomaly. With this eight-class configuration, it was feasible to determine if the network successfully distinguished between single and double failure situation classes. The output confusion matrix will be presented in the next subsection 8.5.4.2 (Figure 131) to a direct comparison with STFT 8-classes tests.

8.5.4 STFT spectrograms tests

In order to compare scalograms and spectrograms output of the network, in this paragraph the images were created through STFT (generating spectrograms).

Data pertaining to the localised bearing fault, with and without the double anomaly state caused by LFTO, were supplied into the network. Only the current signal had been acquired in this situation.

The spectrogram was generated using the same approach as in paragraph 8.5.3, with 4 or 8 output classes tests, but the data were mean-var normalised and decimated with a decimation rate of 20 or 30, which yielded superior categorization results. As in the previous experiments, the number of pictures created for each category was limited to 60, the base sampling rate was set to 120 kS/s, and the base input segment length was set to 100,000 samples. The main characteristics of the decimated data are resumed in Table 53.

Table 53: Main characteristics of the decimated data and spectrogram generation.

Decimation Factor Used	**Decimated Sampling Frequency**	**Number of Samples (Decimated)**	**Window Length**	**Overlapping Samples**	**Number of DFT Points**	**Dimension of The Spectrogram Generated**
Input Segment			**Parameters for The Spectrogram Generation**			
20	6 kHz	5000	750	739	452	227 × 387
30	4 kHz	3333	750	739	452	227 × 235

All the images generated are resized to a 224x224 pixel size images through “imresize” function of MATLAB. While other particulars for the spectrogram generation are reported in [139], Figure 128 shows examples of STFT images of current signal with LFTO condition. The showed images are the ones fed to the neural network. Their axes are the time-axis (x-axis) going from 0 to 833 ms in all of the cases; the frequency-axis (y-axis) going from 0 to half of the sampling frequency employed, starting from the top to the bottom of the image, in linear scale (0 to 3 kHz or 0 to 2 kHz, depending on the decimation factor used).

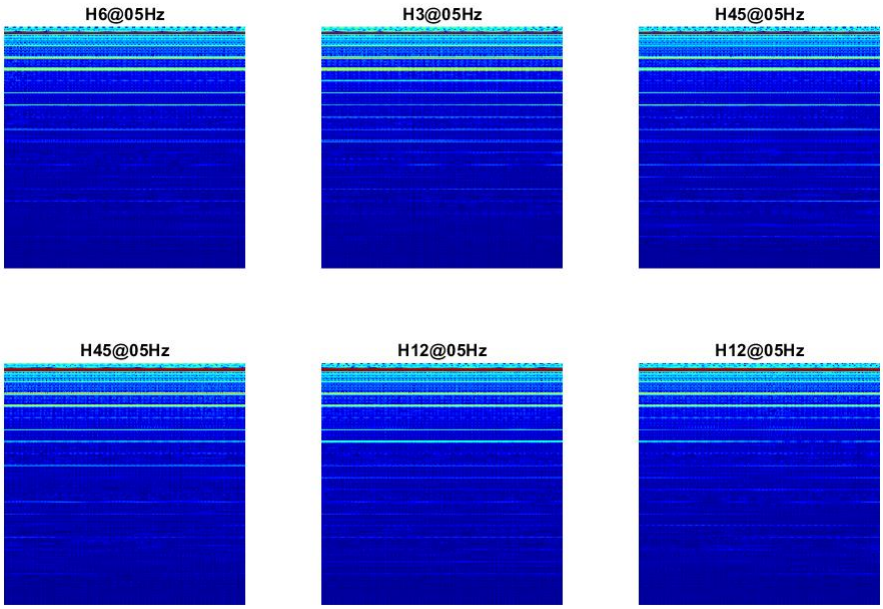

Figure 128: Examples of STFT images of current signal with LFTO condition with decimation factor equal to 30.

8.5.4.1 Four output Classes tests with LFTO condition

Table 54 reports the validation and test accuracies for every arrangement of four classes for the various situations. Figure 129 depicts the confusion matrices for situations with a decimated ratio of 30.

Table 54: Spectrograms in four classes cases, validation and test accuracies.

Case	Decimation Factor	Validation Accuracy	Test Accuracy
Four localized bearing faults + LFTO	20	75%	79.2%
	30	61.7%	62.5%
Four localized bearing faults without LFTO	20	90%	87.5%
	30	91.6%	87.5%

In this case of decimated data, the accuracies acquired with the spectrogram pictures tended to be superior to those obtained with the scalograms, as seen in Table 54 and Figure 129, when compared to the respective Table 52 and Figure 126.

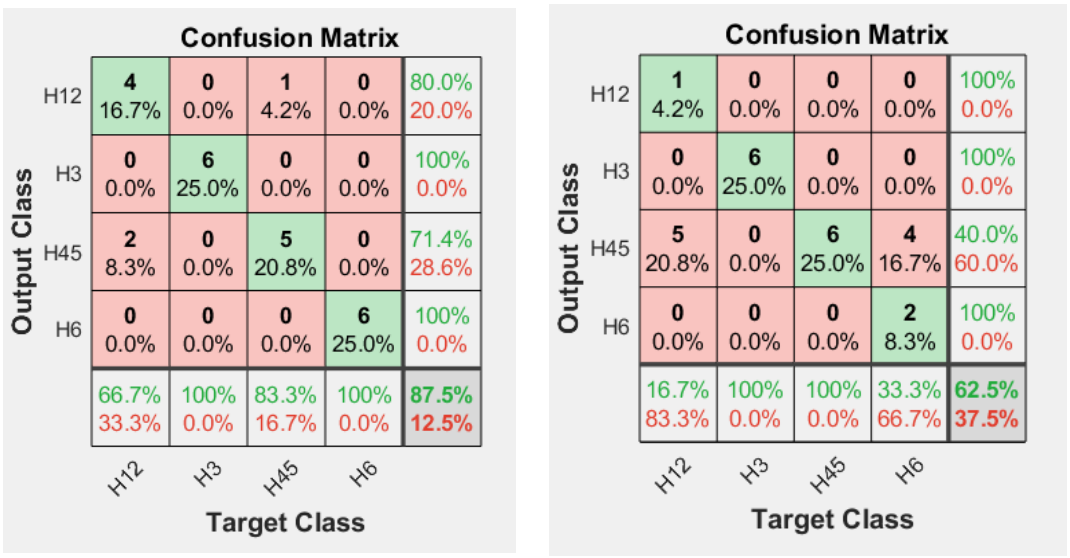

(**a**) (**b**)

Figure 129: Confusion matrices for four-class classifications and spectrograms with decimation factor of 30: (a) four hour single-point bearing faults and (b) four hour single-point bearing faults with LFTO.

8.5.4.2 Eight-output Classes tests with LFTO condition

For brevity just the analysis with decimation factor of 20 are reported. The accuracy of classification process in the eight-class arrangement with spectrograms was 75.8%. Figure 130 depicts the confusion matrix for this scenario.

In this example, the test accuracy was lesser than in the preceding part (see Figure 131); in fact, the test accuracy here was 66.7% rather than 91.7% as in the scalogram classification.

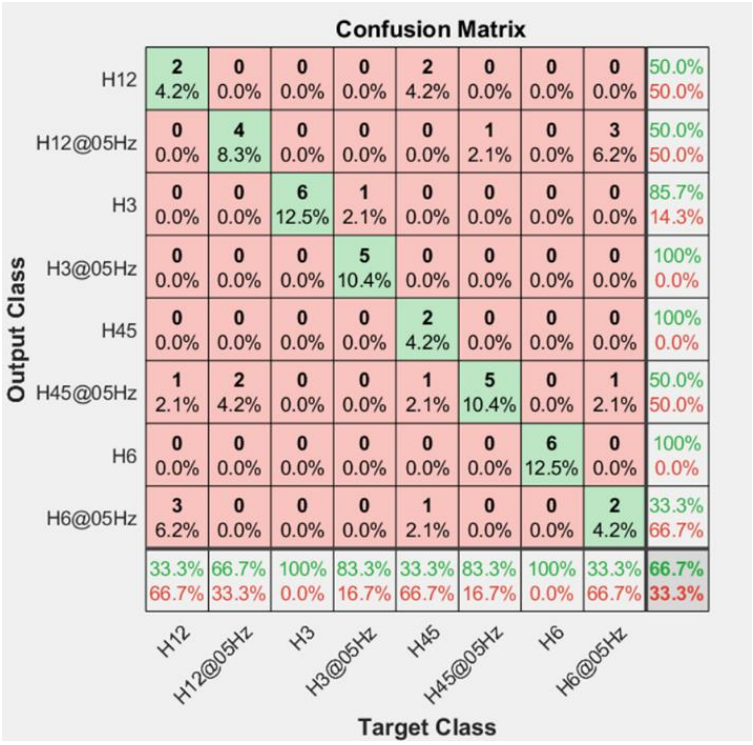

Figure 130: Confusion matrix (using test set) comprising spectrogram pictures for the eight-class arrangement.

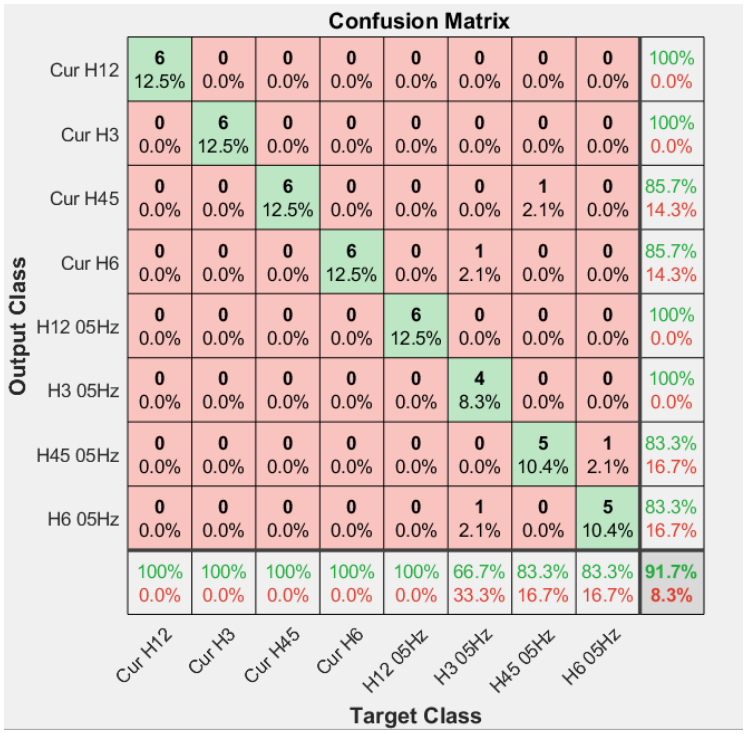

Figure 131: Confusion matrix (using test set) comprising scalogram pictures for the eight-class arrangement.

8.6 Discussion

The work presented in the chapter is a study of stator current and radial stray flux signals for diagnosing an induction machine with bearing defects. Laboratory acquisitions were used throughout the analysis.

The signals were analysed by means of GoogleNet, a deep Convolutional Neural Network (CNN). Using the transfer learning approach, the network was customised for the categorization of various bearing defects. This strategy entails retraining a pre-trained network (GoogleNet), trained for the classification of 1000 classes of object photos, just in the final fully connected layers, with the number of output classes reduced of one or two order of magnitude. Throughout the training process, the network retains the feature extraction abilities learnt in the previous layers, but it may adjust these abilities for the categorization of new classes of input pictures, i.e. the time-frequency domain images of the electromagnetic signals (current and stray flux) acquired on the machine.

Generalized roughness at two severity levels and localised faults in the outer ring in four different hour positions were the bearing defects investigated. Furthermore, tests with a localised fault and LFTO (Low Frequency Torque Oscillation) were performed; this latter condition, represents a double anomaly condition in the machine when the fault and LFTO are considered simultaneously. CWT (continuous Wavelet Transform) and STFT (Short Time Fourier Transform) are the transformation in time-frequency domain performed in the work, and classification accuracy results of the network are compared between these two kinds of input images.

The work discusses many types of evaluations. The first looked at three types of damage, including the baseline (healthy) state and faults with roughness of the bearing balls. The wavelet transform was used to perform these tests on both the current and stray flux sources. In these studies, the stray flux signal outperformed the current signal in terms of classification accuracy.

Additional experiments were performed by combining the bearing's localised defect data with the baseline and generalised roughness data. The stray flux signal achieved a validation and test accuracy of 100% with these tests, while the current signal achieved an accuracy of around 80% with an upper limit in number of epochs of the training procedure increased to 24. The current and stray flux data were then combined, yielding a validation accuracy of roughly 90%. In these studies, both the original sampling frequency of 120 kHz and the decimated frequency data were employed; in the instance the non-decimated segments achieve higher classification accuracy.

Thereafter, classification tests were run on the localised fault data types with and without the LFTO. Due to a lack of stray flux data, these experiments were conducted only with the current signal. The experiments were performed using scalogram and spectrogram pictures generated by the two alternative time-frequency domain transformations: CWT and STFT. Furthermore, the double fault situation, which was defined by the existence of a localised fault in the bearing and

the LFTO, was investigated both jointly and independently to the single fault situation, generating respectively 4 and 8 output classes tests.

In these last experiments, the disparities in accuracy rate of the network with data processed with the CWT, i.e., scalogram pictures, and with the STFT, i.e., spectrogram images, were examined. The results reveal that the test and validation accuracy can differ between the four and eight class settings. The spectrogram images produced better results for the four class configurations, with test accuracies of up to 87.5%, whereas the scalogram images produced better results for the more complicated eight class setups, with test accuracies of up to 91%.

It can be observed that the decimation factor had a play-role in the classification of the images: for the scalogram pictures, a non-decimated signal yields superior classification accuracy, but for spectrogram images, a larger decimation factor leads to a better accuracy.

In conclusion, the work presents results that demonstrate and confirm the capability of electromagnetic signals produced by an induction motor to identify various bearing failures and mechanical load anomalies.

The results accord with numerous recent works in literature. However, some discrepancies can be found: for example, in contrast with [157], the external stray flux in the work showed to be more efficient than the current in identifying bearing problems. This difference could be explained by the fact that in this study, a small motor was used, with the stray flux sensor installed very close to the defected bearing; in contrast, the large size of the motors analysed in [157] does not allow for the setup of an external sensor close enough to the bearings. In any event, it can be affirmed that, as recommended in the literature, measuring both flux and current signals may be effective for increasing diagnostic efficiency for motors of all sizes.

Regarding the Convolutional Neural Networks, the results suggest their capability to automatically discern between different bearing defects, double anomaly conditions and healthy conditions. The comparison between scalograms or spectrograms as network inputs has demonstrated that they can provide different classification accuracies and the optimal choice cannot be determined categorically; hence, an examination of both approaches could be helpful for automatic defect identification.

9 Conclusions

In this work the main activities of the author during his Ph.D. course of study are resumed. Apart of the first two chapters that are related to the state of art of diagnostics of electrical machines and to the description of the laboratory equipment used, every chapter describes a scientific work published in literature by the author. The main methodologies and results obtained in the different chapters are summarised below:

- The third chapter is related to the description of the test bench and laboratory equipment used by the candidate in his research activities. Moreover, the modalities with which the faults and load anomalies are replicated in laboratory are described. The machine used for all the works presented is an induction motor rated 1.5 kW. The main faults and anomalies tested are inter-turn stator short circuits, bearing faults, air-gap eccentricity and load anomalies, i.e. Low Frequency Torque Oscillation (LFTO).
- The fourth chapter describes a method for detecting multiple faults in electrical machines; in particular, the generalised roughness bearing defects, partial stator short circuits and air-gap eccentricity of the machine are taken into account. The analyses of the data (current and stray flux signals) are in the frequency-domain but using a "statistical" approach: the harmonics are counted as fault indicators if they fall in a frequency-gap with a certain tolerance and the trend over time of the various cases with different fault severity and fault combination is considered. Moreover, baseline data are used for the comparison with cases with different severity levels. Baseline data include both healthy and faulty data with a certain severity and are compared with more severe faults or combination of multiple faults. The machine is inverter-supplied and a high sampling frequency is used during the acquisitions showing good results without the need of sophisticated filters or digital manipulation of the data.
- The fifth chapter describes a multi-sensor technique for localized bearing fault detection. The signals analysed are vibrations, from two different accelerometers located in different parts of the machine, stator current and stray magnetic fluxes (axial and radial). The approach is more deterministic than the approach described in the previous chapter: the exact fault characteristic frequencies are identified in vibration spectra and then visualized for comparison in electromagnetic signals spectra. With the use of vibration signal, instead of just calculating the characteristics frequencies with the formulas related to the bearing geometries, it was possible to avoid the uncertainty of 1-2% generated by the slippage phenomenon on the calculation of the characteristic frequencies. Current and stray flux signals are compared between them showing different performances according to the load condition. In particular, stray flux signals give excellent detection efficiency at no load but degraded efficiency at constant load

and with LFTOs. Current signal does not reach a very high detection efficiency at no load, but remains more stable in load conditions. Insights about characteristic signatures in spectra due to LFTO are showed in the chapter.

- The sixth chapter presents a study on the influence of the location of the fault in the outer ring of the bearing, with respect to the axis of the rotor-weight force, on the signal signatures. The experimental measurements include vibrations from two accelerometers as well as electromagnetic signals. An accurate analysis of the two vibration signals, located in different zone of the machine, is performed. It is shown that the piezoelectric sensor, located close to the faulty bearing, is more prone to see the vibrations related to the mechanical rotation and faults (like bearing faults), while the MEMS accelerometer, mounted on the central part of the machine, better intercepts vibration related to electrical quantities and faults, like the double of the slip frequency of the rotor (related to broken rotor bars), or double the supply frequency (relative to airgap eccentricity). The intensity of the vibration harmonics is then compared among the faults at different angular positions in the bearing outer ring. Similar amplitude comparisons are carried out with the electromagnetic signals and the detection efficiency is evaluated, calculated as the ratio of the number of fault harmonics detected over a total of 8 harmonics considered. Results show in general a more difficult detection of the fault with the position at hour 12, as expected, especially in loaded cases. Some tests are carried out with inverter-supplied machine and LFTO conditions. With the inverter supply, the localized fault can be identified only on the vibration signal. The LFTO conditions can be visualized in the vibration spectra, as sidebands of the slot pass harmonic, if no other prominent fault is present in the machine.

- The seventh chapter describes a machine learning technique for automatic recognition of bearing fault in vibration spectrograms. The approach used for the training of the network is the transfer learning technique applied to deep learning architectures. Specifically, in the work, 2-D CNNs (Convolutional Neural Networks) are adapted and used. This technique permits to adapt an already trained network to purposes different from the original ones. In particular, the networks used in the study, AlexNet and CommandNet, were originally designed to classify object images and spectrograms of voice commands. Retraining the networks using high learning rate for the weight and bias parameters just in the final fully connected layer permits to use the features extraction abilities acquired by the original training of the networks for the recognition of new classes (the number of the new classes is one or two order of magnitude less than the original classes). The amount of training data of the new classes can be much lower in quantity with respect to the original training data; this is the main advantage of the implementation of this technique to the diagnostics of electrical machines, in which faulty data are difficult to obtain in large quantities. The work has been based on

two datasets, one from laboratory measurements (denominated “Pavia data”) and one from the online public dataset of the Case Western Reserve University (CWRU). Tests are carried out with three different setups of the networks, including tests with only Pavia data, tests with mixed data, and tests with 6-output classes that include healthy, faulty, two different LFTO conditions and LFTO in simultaneous presence with bearing fault (double anomaly conditions). Results show the feasibility of the transfer learning technique applied to this diagnostic purpose and highlight differences in output between the two networks; in particular, CommandNet, though it is smaller and lighter network, reaches in general higher classification accuracies probably because of its attitude on recognizing spectrograms.

- The eighth chapter presents a CNN based method for recognizing electromagnetic signals time-frequency domain images of an induction machine. Similarly to the work presented in the chapter 7, the approach used is to apply the transfer learning technique to retrain a pre-trained CNN network, i.e. GoogleNet. In contrast to the work presented in chapter 7, the electromagnetic signals (stator current and radial stray flux) are used for the generation of the time-frequency images and the Continuous Wavelet Transform (CWT) is used for the image generation, though also Short Time Fourier Transform (STFT) spectrograms are generated for comparison. All the measurements analysed come from an inverter-supplied machine. Both localized bearing defect in the outer ring at different angular positions and generalised roughness bearing defect are taken into account in the analyses. Moreover, a 0.5 Hz LFTO condition is added in the tests with bearing localised defect to obtain a double anomaly condition. A sampling frequency of 120 kHz has been employed in the measurements; in the analyses both full frequency and decimated sampling frequencies with different decimation factors have been used in scalograms and spectrograms generation. Different types of classification setups are fed into the network: i) three output classes, in which only the two severity levels of the generalised roughness and healthy signal are considered; ii) seven output setup, in which localised, generalised roughness and healthy conditions are fed together; iii) eight output setup in which localised and double anomalies conditions are fed into the network. Classification accuracies of the network show very good results with radial flux signal, which in the cases analysed generally outperforms the current signal. Also the CWT is more effective than STFT in many of the cases analysed. In some instances, however, STFT with appropriate decimation factors gave better results demonstrating that both options can be used for this kind of automatic fault recognition and classification with a convolutional neural network.

As stated in the abstract and in the introduction, the aim of this thesis was to summarize the main research works carried out by the author during his PhD program; other works not yet

published are not presented in the thesis. The author wishes this work can be used as a state of art of diagnostics of electrical machines for other researchers and as starting point and inspiration for future works in this field.

10 Bibliography

1. N. Rosenberg, “The Role of Electricity in Industrial Development.” The Energy Journal, vol. 19, no. 2, International Association for Energy Economics, 1998, pp. 7–24, http://www.jstor.org/stable/41322772.
2. H. A. Toliyat, S. Nandi, S. Choi, and H. Meshgin-Kelk, Electric Machines, Modeling, condition monitoring and Fault diagnosis. CRC Press, 2012.
3. Y. Gritli, “Diagnosis and Fault Detection in Electrical Machines and Drives based on Advanced Signal Processing Techniques”, PhD thesis, 2014.
4. https://www.nextbigfuture.com/2015/04/siemens-and-emrax-claim-best-power-to.html, [accessed on October 2021].
5. https://www.nrcan.gc.ca/energy-efficiency/energy-star-canada/about/energy-star-announcements/publications/electric-motors-energy-efficiency-reference-guide/motor-classification/15146, [accessed on October 2021].
6. R. M. Cuenca, “Simple cost model for EV traction motors”. United States, 1995. https://www.osti.gov/servlets/purl/79757 [accessed October 2021]
7. L. E. Timothy, “The Cost of Manufacturing Electric Vehicle Drivetrains,” Institute of Transportation Studies, UC Davis, 1999.
8. A. T. de Almeida, F. J. T. E. Ferreira and G. Baoming, “Beyond Induction Motors—Technology Trends to Move Up Efficiency,” in IEEE Transactions on Industry Applications, vol. 50, no. 3, pp. 2103-2114, May-June 2014, doi: 10.1109/TIA.2013.2288425.
9. S. Nandi and H. A. Toliyat, “Fault diagnosis of electrical machines-a review,” IEEE International Electric Machines and Drives Conference. IEMDC'99. Proceedings (Cat. No.99EX272), 1999, pp. 219-221, doi: 10.1109/IEMDC.1999.769076.
10. https://uk.mathworks.com/campaigns/offers/predictive-maintenance-with-matlab.html?s_tid=vid_pers_ofr_recs, [accessed on November 2021].
11. A. Muetze, E.G. Strangas, “The useful life of inverter-based drive bearings: Methods and research directions from localized maintenance to prognosis.” IEEE Ind. Appl. Mag. 2016, 22, 63–73.
12. L. Frosini, “Novel Diagnostic Techniques for Rotating Electrical Machines—A Review.” Energies. 2020; 13(19):5066. https://doi.org/10.3390/en13195066
13. W. Zhou, T. G. Habetler and R. G. Harley, “Bearing Condition Monitoring Methods for Electric Machines: A General Review,” 2007 IEEE International Symposium on Diagnostics for Electric Machines, Power Electronics and Drives, 2007, pp. 3-6, doi: 10.1109/DEMPED.2007.4393062.
14. S. B. Lee et al., “Condition Monitoring of Industrial Electric Machines: State of the Art and Future Challenges,” in IEEE Industrial Electronics Magazine, vol. 14, no. 4, pp. 158-167, Dec. 2020.

15. W.T. Thomson, R.J. Gilmore “Motor current signature analysis to detect faults in induction motor drives- fundamentals, data interpretation, and industrial case histories”. Turbomachinery symposium, 2003.
16. W. T. Thomson, I. Culbert, “Current Signature Analysis for Condition Monitoring of Cage Induction Motors-Industrial Application and Case Histories” IEEE Press - Wiley, 2017.
17. P. L. Alger, “The magnetic noise of polyphase induction motors,” in Electrical Engineering, vol. 73, no. 6, pp. 497-497, June 1954, doi: 10.1109/EE.1954.6438808.
18. P. Mancinelli, S. Stagnitta and A. Cavallini, “Lifetime analysis of an automotive electrical motor with hairpin wound stator,” 2016 IEEE Conference on Electrical Insulation and Dielectric Phenomena (CEIDP), 2016.
19. F. Filippetti, G. Franceschini, M. Martelli, and C. Tassoni, “An Approach to a Knowledge Representation about Induction Machine Diagnostics in Expert Systems,” International Conference on Electrical Machines ICEM’88, Pisa, Italy, September 1988.
20. P. Vas, “Steady state and transient performance of induction motors with rotor asymmetry”, IEEE Transactions on Power Apparatus band Systems, vol. PAS-101, no. 9, September 1982, pp. 3246– 3251.
21. G. B. Kliman and J. Stein, Methods of Motor Current Signature Analysis Electric Machines and Power Systems, Hemisphere Publishing, New York vol. 20, 1982.
22. J. R. Cameron, W. T. Thomson, and A. B. Dow, “Vibration and current monitoring for detecting airgap eccentricity in large induction motors”, IEE Proceedings, vol. 133, Part B. no 3, May 1986.
23. M. E. H. Benbouzid, “A review of induction motors signature analysis as a medium for faults detection,” IEEE transactions on industrial electronics 47, no. 5 (2000): 984-993.
24. https://www.slideshare.net/ramagianhendraloka/windowing-signal-processing [accessed December 2021].
25. M. Blodt, P. Granjon, B. Raison and G. Rostaing, “Models for Bearing Damage Detection in Induction Motors Using Stator Current Monitoring,” in IEEE Transactions on Industrial Electronics, vol. 55, no. 4, pp. 1813-1822, April 2008.
26. https://www.imv.co.jp/e/pr/vibration_measuring/chapter03/ [accessed December 2021].
27. Mechanical Vibrations in SI Units, 5th Edition, Singiresu S. Rao, University of Miami, ©2011, Pearson [Chapter 1].
28. https://community.sw.siemens.com/s/article/what-is-a-frequency-response-function-frf [accessed December 2021].
29. R. B. Randall and J. Antoni, “Rolling element bearing diagnostics – A tutorial,” Mechanical Systems and Signal Processing. vol. 25, no. 2, pp. 485-520, Feb. 2011.
30. S. A. Mcinerny, Y. Dai. “Basic vibration signal processing for bearing fault detection.” IEEE Trans. Educ. 46 (2003).

31. L. Frosini “Dispense di diagnostica di machine elettriche” (slide number 4) http://www-9.unipv.it/dmae/diagnostica/materiale_didattico/Diagnostica_4.pdf [accessed January 2022] (in Italian).
32. D.G. Dorrell, W.T. Thomson, “Analysis of airgap flux, current, and vibration signals as a function of the combination of static and dynamic airgap eccentricity in 3-phase induction motors”, IEEE Trans. Ind. Appl., 33(1), 1997, 24-34.
33. Y. Park et al., “Stray Flux Monitoring for Reliable Detection of Rotor Faults Under the Influence of Rotor Axial Air Ducts,” in IEEE Transactions on Industrial Electronics, vol. 66, no. 10, pp. 7561-7570, Oct. 2019.
34. V. Kokko. “Condition monitoring of squirrel-cage motors by axial magnetic flux measurements,” PhD thesis dissertation, Department of Electrical Engineering, Optoelectronics and Measurement Techniques Laboratory, University of Oulu, 2003.
35. A. Bellini, C. Concari, G. Franceschini, C. Tassoni and A. Toscani, “Vibrations, currents and stray flux signals to asses induction motors rotor conditions,” IECON 2006 - 32nd Annual Conference on IEEE Industrial Electronics, 2006.
36. H. Henao, C. Demian and G. A. Capolino, “A frequency-domain detection of stator winding faults in induction machines using an external flux sensor,” in IEEE Transactions on Industry Applications, vol. 39, no. 5, 2003.
37. J. Fulnečck and S. Mišák, “Stator current and axial magnetic flux analysis of induction motor,” 2018 International Conference on Diagnostics in Electrical Engineering (Diagnostika), 2018.
38. P. A. Panagiotou, I. Arvanitakis, N. Lophitis and K. N. Gyftakis, “FEM Study of Induction Machines Suffering from Rotor Electrical Faults Using Stray Flux Signature Analysis,” 2018 XIII International Conference on Electrical Machines (ICEM), 2018.
39. C. Yang, T.-J. Kang, S. B. Lee, J.-Y. Yoo, A. Bellini, L. Zarri, and F. Fiilippetti, “Screening of false induction motor fault alarms produced by axial air ducts based on the space-harmonic-induced current components,” IEEE Transactions on Industrial Electronics, vol. 62, no. 3, March 2015.
40. S. Lee, J. Hong, S. B. Lee, E. J.Wiedenburg, M. Teska, and H. Kim, “Evaluation of the influence of rotor axial air duct on condition monitoring of induction motors,” IEEE Transactions on Industrial Applications, vol. 49, no. 5, September/October 2013.
41. G. M. Joksimović, J. Riger, T. M. Wolbank, N. Perić and M. Vašak, “Stator-Current Spectrum Signature of Healthy Cage Rotor Induction Machines,” in IEEE Transactions on Industrial Electronics, vol. 60, no. 9, pp. 4025-4033, Sept. 2013
42. J. Jung, J. Lee and B. Kwon, “Online Diagnosis of Induction Motors Using MCSA,” in IEEE Transactions on Industrial Electronics, vol. 53, no. 6, pp. 1842-1852, Dec. 2006
43. R. R. Obaid, T. G. Habetler and D. J. Gritter, “A simplified technique for detecting mechanical faults using stator current in small induction motors,” Conference Record of the 2000 IEEE Industry Applications Conference.

44. M. Sahraoui, A. Ghoggal, S. E. Zouzou, and M. E. Benbouzid, “Dynamic eccentricity in squirrel cage induction motors – Simulation and analytical study of its spectral signatures on stator currents,” Simul. Model. Pract. Theory, vol. 16, pp. 1503–1513, 2008.
45. F. Filippetti, M. Martelli, G. Franceschini and C. Tassoni, “Development of expert system knowledge base to on-line diagnosis of rotor electrical faults of induction motors,” Conference Record of the 1992 IEEE Industry Applications Society Annual Meeting, 1992.
46. F. Filippetti, G. Franceschini, C. Tassoni, P. Vas, “Impact of Speed Ripple on Rotor Fault Diagnosis of Induction Machines,” Proc. Intern. Confer. on Electrical Machines ICEM '96, Vigo, Spain, 1996.
47. G. Y. Sizov, A. Sayed-Ahmed, C. Yeh and N. A. O. Demerdash, “Analysis and Diagnostics of Adjacent and Nonadjacent Broken-Rotor-Bar Faults in Squirrel-Cage Induction Machines,” in IEEE Transactions on Industrial Electronics, vol. 56, no. 11, pp. 4627-4641, Nov. 2009
48. J. Shin, Y. Park and S. B. Lee, “Flux-based Detection and Classification of Induction Motor Eccentricity, Rotor Cage, and Load Defects,” 2020 IEEE Energy Conversion Congress and Exposition (ECCE), 2020.
49. A. Ceban, R. Pusca, R. Romary, “Study of Rotor Faults in Induction Motors Using External Magnetic Field Analysis,” IEEE Trans. Ind. Electron., vol. 59, no. 5, pp. 2082-2093, May 2012.
50. R. R. Schoen, T. G. Habetler, F. Kamran and R. G. Bartfield, “Motor bearing damage detection using stator current monitoring,” in IEEE Transactions on Industry Applications, vol. 31, no. 6, pp. 1274-1279, Nov.-Dec. 1995.
51. S. Zhang, S. Zhang, B. Wang and T. G. Habetler, “Deep Learning Algorithms for Bearing Fault Diagnostics—A Comprehensive Review,” in IEEE Access, vol. 8, pp. 29857-29881, 2020.
52. L. Frosini, M. Magnaghi, A. Albini, and G. Magrotti, “A new diagnostic instrument to detect generalized roughness in rolling bearings for induction motors,” in Proc. SDEMPED, 2015.
53. B. Akin, U. Orguner, H.A. Toliyat, and M. Rayner, “Low order PWM inverter harmonics contributions to the inverter-fed induction machine fault diagnosis,” IEEE Trans. Ind. Electron., vol. 55, no. 2, 2008.
54. L. Wu, T. G. Habetler and R. G. Harley, “Separating load torque oscillation and rotor fault effects in stator current-based motor condition monitoring,” IEEE International Conference on Electric Machines and Drives, 2005.
55. L. Wu, T. G. Habetler and R. G. Harley, “A Review of Separating Mechanical Load Effects from Rotor Faults Detection in Induction Motors,” 2007 IEEE International Symposium on Diagnostics for Electric Machines, Power Electronics and Drives, 2007.
56. H. Kim, S. B. Lee, S. B. Park, S. H. Kia and G. Capolino, “Reliable detection of rotor faults under the influence of low frequency load torque oscillations for applications with speed reduction couplings,” 2015 IEEE 10th International Symposium on Diagnostics for Electrical Machines, Power Electronics and Drives (SDEMPED), 2015.

57. M. Minervini “Individuazione delle oscillazioni della coppia di carico nei motori asincroni tramite l’analisi della corrente di statore e del flusso disperso,” M.Sc. Thesis, Università di Pavia, 2018 (in Italian).
58. L. Frosini, M. Magnaghi and A. Albini, “An improved diagnostic system to detect inter-turns short circuits in low voltage stator windings,” 2015 IEEE Workshop on Electrical Machines Design, Control and Diagnosis (WEMDCD), 2015.
59. L. Frosini, A. Borin, A. Albini, and F. Benzi, “New techniques to simulate and diagnose stator winding faults in low voltage induction motors,” in Proc. ICEM 2012, pp. 1781-1787.
60. L. Frosini, C. Harlişca and L. Szabó, “Induction Machine Bearing Fault Detection by Means of Statistical Processing of the Stray Flux Measurement,” in IEEE Transactions on Industrial Electronics, vol. 62, no. 3, pp. 1846-1854, March 2015.
61. L. Frosini, A. Borin, L. Girometta and G. Venchi, “Development of a leakage flux measurement system for condition monitoring of electrical drives,” 8th IEEE Symposium on Diagnostics for Electrical Machines, Power Electronics & Drives, 2011.
62. L. Frosini, A. Borin, L. Girometta and G. Venchi, “A novel approach to detect short circuits in low voltage induction motor by stray flux measurement,” 2012 XXth International Conference on Electrical Machines, 2012.
63. D. López-Pérez, J. Antonino-Daviu, “Application of Infrared Thermography to Failure Detection in Industrial Induction Motors: Case Stories”, IEEE Transactions on Industry Applications, 2017.
64. A.E. Fitzgerald, C. Kingsley, A. Kusko, “Electric Machinery” third edition, McGraw-Hill/Kogakusha, 1971.
65. R. Galluzzi, A. Tonoli and N. Amati, “Magnetic hysteresis machines for next-generation electric turbochargers,” 2017 International Conference of Electrical and Electronic Technologies for Automotive, 2017.
66. L. Frosini, M. Minervini, L. Ciceri and A. Albini, “Multiple faults detection in low voltage inverter-fed induction motors,” 2019 IEEE 12th International Symposium on Diagnostics for Electrical Machines, Power Electronics and Drives (SDEMPED), 2019.
67. K. N. Gyftakis and A. J. M. Cardoso, “Reliable Detection of Stator Interturn Faults of Very Low Severity Level in Induction Motors,” in IEEE Transactions on Industrial Electronics, vol. 68, no. 4, pp. 3475-3484, April 2021.
68. S. Nandi, H. A. Toliyat and X. Li, “Condition Monitoring and Fault Diagnosis of Electrical Motors—A Review,” in IEEE Transactions on Energy Conversion, vol. 20, no. 4, pp. 719-729, Dec. 2005.
69. M. Riera-Guasp, J. A. Antonino-Daviu and G. Capolino, “Advances in Electrical Machine, Power Electronic, and Drive Condition Monitoring and Fault Detection: State of the Art,” in IEEE Transactions on Industrial Electronics, vol. 62, no. 3, pp. 1746-1759, March 2015.
70. S. Cheng, P. Zhang and T. G. Habetler, “An Impedance Identification Approach to Sensitive Detection and Location of Stator Turn-to-Turn Faults in a Closed-Loop Multiple-Motor

Drive," in IEEE Transactions on Industrial Electronics, vol. 58, no. 5, pp. 1545-1554, May 2011.

71. L. Fornasari, A. Caprara, and G. C. Montanari, "Partial discharge measurements in electrical machines controlled by variable speed drives: From design validation to permanent PD monitoring," in Proc. 39th IEEE Int. SDEMPED, Aug. 27–30, 2013.
72. A. Khechekhouche, H. Cherif, A. Benakcha, A. Menacer, S. E. Chehaidia, H. Panchal, "Experimental diagnosis of inter-turns stator fault and unbalanced voltage supply in induction motor using MCSA and DWER," in Periodicals of engineering and natural sciences, Vol 8, No 3 (2020).
73. A. Kabul and A. Ünsal, "A Diagnosis Method of Multiple Faults of Induction Motors Based on Vibration Signal Analysis," 2021 IEEE 13th International Symposium on Diagnostics for Electrical Machines, Power Electronics and Drives (SDEMPED), 2021.
74. M. Messaoudi and L. Sbita, "Multiple faults diagnosis in induction motor using the MCSA method," International Journal of Signal and Image Processing, Vol. 1, No. 3, 2010.
75. E. Cabal-Yepez, R. A. Osornio-Rios, R. J. Romero-Troncoso, J. R. Razo-Hernandez, R. Lopez-Garcia, "FPGA-based online induction motor multiple-fault detection with fused FFT and wavelet analysis," in Proc. Int. Conf. on Reconfigurable Computing and FPGAs, 2009.
76. J. Sri Lal Senanayaka, H. Van Khang, and K. G. Robbersmyr, "Multiple fault diagnosis of electric powertrains under variable speeds using convolutional neural networks," in Proc. ICEM, 2018.
77. E. Smart, D. Brown, L. Axel-Berg, "Comparing one and two class classification methods for multiple fault detection on an induction motor," in Proc. ISIEA, 2013.
78. R. H. C. Palácios, W. F. Godoy, A. Goedtel, I. N. da Silva, D. Moríñigo-Sotelo, and O. Duque-Perez, "Time domain diagnosis of multiple faults in three phase induction motors using intelligent approaches", in Proc. SDEMPED, 2017
79. J. D. Martínez-Morales, E. R. Palacios-Hernández, D. U. Campos-Delgado, "Multiple-fault diagnosis in induction motors through support vector machine classification at variable operating conditions," Electrical Engineering, Vol. 100, No. 1, pp 59-73, 2018.
80. M. Magnaghi. "Strumenti diagnostici per l'individuazione di guasti di statore e dei cuscinetti nei motori asincroni". M.Sc. Thesis. Università degli studi di Pavia, 2015 (in Italian).
81. L. Frosini, S. Zanazzo, and A. Albini, "A wavelet-based technique to detect stator faults in inverter-fed induction motors," in Proc. ICEM, 2016.
82. L. Ciceri. "Diagnosi di guasti multipli in motori asincroni alimentati da inverter". M.Sc. Thesis. Università degli studi di Pavia, 2018 (in Italian).
83. O. Duque-Perez, D. Pozo-Gallego, D. Morinigo-Sotelo and W. Fontes Godoy, "Condition monitoring of bearing faults using the stator current and shrinkage methods", Energies, vol. 12, no. 17, pp. 3392, 2019.

84. M. Minervini, L. Frosini, L. Hasani and A. Albini, “A Multisensor Induction Motors Diagnostics Method for Bearing Cyclic Fault,” 2020 International Conference on Electrical Machines (ICEM), 2020.
85. A. H. Bonnett and C. Yung, “Increased efficiency versus increased reliability,” IEEE Ind. Appl. Mag., vol. 14, no. 1, 2008.
86. C. Radu, “The Most Common Causes of Bearing Failure and the Importance of Bearing Lubrication,” 2020. https://www.bearing-news.com/the-most-common-causes-of-bearing-failure-and-the-importance-of-bearing-lubrication/ [accessed January 2022]
87. D. Collins, “Bearing damage: What’s the difference between brinelling, spalling, and fretting?”, 2019 https://www.linearmotiontips.com/whats-the-difference-between-brinelling-spalling-fretting/, [accessed January 2022].
88. F. Immovilli, C. Bianchini, M. Cocconcelli, A. Bellini, and R. Rubini, “Bearing fault model for induction motor with externally induced vibration,” IEEE Trans. Ind. Electron., Aug. 2013.
89. A. Seyfettin Erbay, “Multi-Sensor Fusion for Induction Motor Aging Analysis and Fault Diagnosis,” PhD thesis dissertation, University of Tennessee – Knoxville, https://trace.tennessee.edu/utk_graddiss/2541, 1999.
90. G. Luo, J. E. D. Hurwitz and T. G. Habetler, “A Survey of Multi-Sensor Systems for Online Fault Detection of Electric Machines,” 2019 IEEE 12th International Symposium on Diagnostics for Electrical Machines, Power Electronics and Drives (SDEMPED), 2019.
91. J. D. Martínez-Morales, E. Palacios, and D. U. Campos-Delgado, “Data fusion for multiple mechanical fault diagnosis in induction motors at variable operating conditions,” in 2010 7th International Conference on Electrical Engineering Computing Science and Automatic Control, 2010.
92. J. S. Hsu, “Monitoring of defects in induction motors through air-gap torque observation,” IEEE Transactions on Industry Applications, vol. 31, no. 5, 1995.
93. A. N. Saberi, S. Sandirasegaram, A. Belahcen, T. Vaimann and J. Sobra, “Multi-Sensor Fault Diagnosis of Induction Motors Using Random Forests and Support Vector Machine,” 2020 International Conference on Electrical Machines (ICEM), 2020.
94. M. Irhoumah, R. Pusca, E. Lefèvre, D. Mercier, R. Romary, “Stray Flux Multi-Sensor for Stator Fault Detection in Synchronous Machines”. “Electronics” journal https://doi.org/10.3390/electronics10182313 , 2021.
95. R. Pusca, R. Romary, A. Ceban, J-F. Brudny. “An Online Universal Diagnosis Procedure Using Two External Flux Sensors Applied to the AC Electrical Rotating Machines”, “Sensors” journal. https://doi.org/10.3390/s101110448 , 2010.
96. M. Minervini, L. Frosini, G. Guri and A. Albini, “Influence of the Location of a Bearing Fault in Induction Motor Multi-Sensor Diagnostics,” 2021 IEEE 13th International Symposium on Diagnostics for Electrical Machines, Power Electronics and Drives (SDEMPED), 2021.

97. L. Sun and B. Xu, “An improvement of stator current based detection of bearing fault in induction motors,” in Proc. IEEE Industry Applications Annual Meeting, pp. 2277-2281, 2007.
98. T. Vaimann, J. Sobra, A. Belahcen, A. Rassõlkin, M. Rolak, and A. Kallaste, “Induction machine fault detection using smartphone recorded audible noise,” IET Science, Measurement & Technology, vol. 12, no. 4, pp. 554–560, 2018.
99. J. H. Jung, J. J. Lee, and B. H. Kwon, “Online diagnosis of induction motors using MCSA,” IEEE Trans. Ind. Electron., vol. 53, no. 6, pp. 1842-1852, Dec. 2006.
100. K. M. Siddiqui, K. Sahay, and V. K. Giri, “Modelling and detection of bearing fault in SPWM inverter fed squirrel cage induction motor drives,” in Proc. ICCPCT 2015.
101. Brüel & Kjær handbook on vibration measurement, available at: https://www.bksv.com/en/knowledge/blog/vibration/measuring-vibration, [accessed February 2022].
102. Case Western Reserve University “bearing data center”, https://engineering.case.edu/bearingdatacenter/apparatus-and-procedures [accessed February 2022].
103. C. Concari, G. Franceschini and C. Tassoni, “Differential Diagnosis Based on Multivariable Monitoring to Assess Induction Machine Rotor Conditions,” in IEEE Transactions on Industrial Electronics, vol. 55, no. 12, pp. 4156-4166, Dec. 2008.
104. https://www.skf.com/binaries/pub12/Images/0901d196802b0348-13459-EN-Rolling-bearings-and-seals-in-electric-motors-and-generators_tcm_12-134586.pdf [accessed February 2022]
105. https://www.skf.com/binaries/pub12/Images/0901d1968064c148-Bearing-failures---14219_2-EN_tcm_12-297619.pdf [accessed February 2022]
106. A. A. Borhana Omran, Y. Hassan Ali, U. Shankar, F. Saeid Ali, S. Gareh, O. Suliman Zaroog, and N. A. Mardhiah, “Early fault detection in bearing with fault seeded on outer raceway at three different position: orthogonal, centered and opposite,” Int. J. Recent Technol. Eng, 2019.
107. N. Tandon and K. S. Kumar, “Detection of defects at different locations in ball bearings by vibration and shock pulse monitoring,” Noise Vib. Worldw., pp. 9-16, 2003.
108. I. Ahmed, M. Ahmed, K. Imran, M. S. Khan, and S. Junaid Akhtar, “Detection of eccentricity faults in machine using frequency spectrum technique,” Int. J. Comput. Electr. Eng., vol. 3, pp. 111-119, 2011.
109. T. Goktas and M. Arkan, “Discriminating of rotor fault and low frequency load torque oscillation using motor square current signature analysis,” in Proc. ICEM 2018, pp. 2365-2370.
110. M. Minervini, S. Hausman and L. Frosini, “Transfer Learning Technique for Automatic Bearing Fault Diagnosis in Induction Motors,” 2021 IEEE 13th International Symposium on Diagnostics for Electrical Machines, Power Electronics and Drives (SDEMPED), 2021.

111. M. He, D. He, “Deep learning based approach for bearing fault diagnosis”. IEEE Trans. Ind. Appl. **2017**, 53, 3057–3065.
112. A. Guedidi, A. Guettaf, A.J.M. Cardoso, W. Laala, A. Arif, “Bearing faults classification based on variational mode decomposition and artificial neural network,” In Proceedings of the 2019 SDEMPED, Toulouse, France, 27–29 August 2019.
113. A. Khlaief et al., “Feature Engineering for Ball Bearing Combined-Fault Detection and Diagnostic,” 2019 IEEE 12th International Symposium on Diagnostics for Electrical Machines, Power Electronics and Drives (SDEMPED), 2019.
114. F. Immovilli, M. Lippi and M. Cocconcelli, “Automated Bearing Fault Detection via Long Short-Term Memory Networks,” 2019 IEEE 12th International Symposium on Diagnostics for Electrical Machines, Power Electronics and Drives (SDEMPED), 2019.
115. https://en.wikipedia.org/wiki/Artificial_neural_network#Learning [online, accessed April 2022]
116. M. Chow, P. M. Mangum and S. O. Yee, “A neural network approach to real-time condition monitoring of induction motors,” in IEEE Transactions on Industrial Electronics, vol. 38, no. 6, Dec. 1991.
117. A. Malhi and R. Gao, “PCA-based feature selection scheme for machine defect classification,” IEEE Trans. Instrum. Meas., vol. 53, no. 6, pp. 1517-1525, Dec. 2004.
118. A. Ng, “CS229 course notes: Deep learning,” Dept. Comput. Sci., Stanford Univ., Stanford, CA, USA, Tech. Rep., 2018.
119. https://en.wikipedia.org/wiki/Convolutional_neural_network#Shift-invariant_neural_network [accessed April 2022]
120. O. Janssens, V. Slavkovikj, B. Vervisch, K. Stockman, M. Loccufier, S. Verstockt, R. Van de Walle, and S. Van Hoecke, “Convolutional neural network based fault detection for rotating machinery,” J. Sound Vib., vol. 377, pp. 331-345, Sep. 2016.
121. L. Wen, X. Li, L. Gao, and Y. Zhang, “A new convolutional neural network-based data-driven fault diagnosis method,” IEEE Trans. Ind. Electron., vol. 65, no. 7, Jul. 2018.
122. https://www.v7labs.com/blog/overfitting [accessed September 2022]
123. H. Shao, H. Jiang, H. Zhao, and F. Wang, “A novel deep autoencoder feature learning method for rotating machinery fault diagnosis,” Mech. Syst. Signal Process., Oct. 2017.
124. Z. Chen andW. Li, “Multisensor feature fusion for bearing fault diagnosis using sparse autoencoder and deep belief network,” IEEE Trans. Instrum. Meas., vol. 66, Jul. 2017.
125. Y. Bengio, “Learning deep architectures for AI,” FNT Mach. Learn., vol. 2, no. 1, pp. 1-127, 2009.
126. W. Abed, S. Sharma, R. Sutton, and A. Motwani, “A robust bearing fault detection and diagnosis technique for brushless DC motors under nonstationary operating conditions,” J. Control Autom. Electr. Syst., vol. 26, no. 3, pp. 241-254, Jun. 2015.
127. S. Pan and Q. Yang, “A survey on transfer learning,” IEEE Trans. Knowl. Data Eng., vol. 22, no. 10, pp. 1345-1359, Oct. 2009.

128. C. Tan, F. Sun, T. Kong, W. Zhang, C. Yang, and C. Liu, "A survey on deep transfer learning," in Proc. Int. Conf. Artif. Neural Netw. Cham, Switzerland: Springer, 2018.
129. E. Tzeng, J. Hoffman, N. Zhang, K. Saenko, and T. Darrell, "Deep domain confusion: Maximizing for domain invariance," arXiv:1412.3474. [Online]. Available: http://arxiv.org/abs/1412.3474 , 2014.
130. Y. Ganin, E. Ustinova, H. Ajakan, P. Germain, H. Larochelle, F. Laviolette, M. Marchand, V. Lempitsky, "Domain-adversarial training of neural networks," J. Mach. Learn. Res., vol. 17, no. 59, pp. 1-35, 2016.
131. W. Lu, B. Liang, Y. Cheng, D. Meng, J. Yang, and T. Zhang, "Deep model based domain adaptation for fault diagnosis," IEEE Trans. Ind. Electron., vol. 64, no. 3, pp. 2296-2305, Mar. 2017.
132. W. Zhang, C. Li, G. Peng, Y. Chen, and Z. Zhang, "A deep convolutional neural network with new training methods for bearing fault diagnosis under noisy environment and different working load," Mech. Syst. Signal Process., vol. 100, pp. 439-453, Feb. 2018.
133. L. Guo, Y. Lei, S. Xing, T. Yan, and N. Li, "Deep convolutional transfer learning network: A new method for intelligent fault diagnosis of machines with unlabeled data," IEEE Trans. Ind. Electron., vol. 66, no. 9, pp. 7316-7325, Sep. 2019.
134. W. Zhang, G. Peng, C. Li, Y. Chen, and Z. Zhang, "A new deep learning model for fault diagnosis with good anti-noise and domain adaptation ability on raw vibration signals," Sensors, vol. 17, no. 2, p. 425, Feb. 2017.
135. X. Li, W. Zhang, and Q. Ding, "Cross-domain fault diagnosis of rolling element bearings using deep generative neural networks," IEEE Trans. Ind. Electron., vol. 66, no. 7, pp. 5525-5534, Jul. 2019.
136. A. Krizhevsky, I. Sutskever, and G. E. Hinton, "ImageNet classification with deep convolutional neural networks," Communications of the ACM 60, pp. 84-90, 2012.
137. https://uk.mathworks.com/help/deeplearning/ug/transfer-learning-using-alexnet.html [accessed April 2022]
138. S. R. Park and J. Lee, "A Fully Convolutional Neural Network for Speech Enhancement," arXiv 1609.07132, 2016.
139. M. Minervini, M. E. Mognaschi, P. Di Barba, and L. Frosini, "Convolutional Neural Networks for Automated Rolling Bearing Diagnostics in Induction Motors Based on Electromagnetic Signals," Applied Sciences, vol. 11, no. 17, p. 7878, Aug. 2021.
140. P.K. Kankar, S.C. Sharma, S.P. Harsha, "Fault diagnosis of ball bearings using continuous wavelet transform," Appl. Soft Comput., doi:10.1016/j.asoc.2010.08.011, 2011.
141. X. Lou, K.A. Loparo, "Bearing fault diagnosis based on wavelet transform and fuzzy inference," Mech. Syst. Signal Process., doi:10.1016/S0888-3270(03)00077-3, 2004.
142. Y. Imaouchen, R. Alkama, M. Thomas, "Bearing fault detection using motor current signal analysis based on wavelet packet decomposition and Hilbert envelope," MATEC Web Conf., 20, 03002, doi:10.1051/matecconf/20152003002, 2015.

143. G. Georgoulas, V. Climente-Alarcon, L. Dritsas, J.A. Antonino-Daviu, G. Nikolakopoulos, “Start-up analysis methods for the diagnosis of rotor asymmetries in induction motors-seeing is believing,” In Proceedings of the 2016 24th Mediterranean Conference on Control and Automation (MED), Athens, Greece, 21–24 June 2016.
144. Y. Merizalde, L. Hernández-Callejo, O. Duque-Perez, R.A. López-Meraz, “Fault detection of wind turbine induction generators through current signals and various signal processing techniques,” Appl. Sci., 10, 7389, doi:10.3390/app10217389, 2020.
145. E.H.E. Bouchikhi, V. Choqueuse, M. Benbouzid, “Induction machine diagnosis using stator current advanced signal processing,” Int. J. Energy Convers., 3, 76–87, 2015.
146. V. Fernandez-Cavero, D. Morinigo-Sotelo, O. Duque-Perez and J. Pons-Llinares, “A Comparison of Techniques for Fault Detection in Inverter-Fed Induction Motors in Transient Regime,” in IEEE Access, vol. 5, pp. 8048-8063, 2017.
147. S. Singh, A. Kumar, N. Kumar, “Motor current signature analysis for bearing fault detection in mechanical systems,” Procedia Mater. Sci., doi:10.1016/j.mspro.2014.07.021, 2014.
148. M.E.A. Khodja, A.F. Aimer, A.H. Boudinar, N. Benouzza, A. Bendiabdellah, “Bearing fault diagnosis of a PWM inverter fed-induction motor using an improved short time fourier transform,” J. Electr. Eng. Technol., doi:10.1007/s42835-019-00096-y, 2019.
149. T.W. Chua, W.W. Tan, Z. Wang, C.S. Chang, “Hybrid time-frequency domain analysis for inverter-fed induction motor fault detection,” In Proceedings of the 2010 IEEE International Symposium on Industrial Electronics, Bari, Italy, 4–7 July 2010.
150. S.K. Mitra, “Digital Signal Processing: A Computer-Based Approach,” 2nd ed.; McGraw-Hill: New York, NY, USA, 2001.
151. E. Sejdic, I. Djurovic, L. Stankovic, “Quantitative performance analysis of scalogram as instantaneous frequency estimator.” IEEE Trans. Signal Process., 56, 3837–3845, 2008.
152. C. Szegedy, W. Liu, Y. Jia, P. Sermanet, S. Reed, D. Anguelov, D. Erhan, V. Vanhoucke, A. Rabinovich, “Going deeper with convolutions,” In Proceedings of the 2015 IEEE Conference on Computer Vision and Pattern Recognition (CVPR), Boston, MA, USA, 7–12 June 2015.
153. Mathworks. Classify Time Series Using Wavelet Analysis and Deep Learning. Available online: https://uk.mathworks.com/help/wavelet/ug/classify-time-series-using-wavelet-analysis-and-deep-learning.html [accessed on 12 August 2021].
154. ImageNet. Available online: https://www.image-net.org/index.php [accessed on 22 June 2021].
155. J. Burriel-Valencia, R. Puche-Panadero, J. Martinez-Roman, A. Sapena-Bano, M. Pineda-Sanchez, “Fault diagnosis of induction machines in a transient regime using current sensors with an optimized slepian window,” Sensors, 18, 146, doi:10.3390/s18010146, 2018.
156. L. Frosini, A. Borin, L. Girometta, G. Venchi, “A novel approach to detect short-circuits in low voltage induction motor by stray flux measurement,” In Proceedings of the 2012 ICEM, Marseille, France, 2–5 September 2012.

157. K.N. Gyftakis, P.A. Panagiotou, D. Spyrakis, “Detection of simultaneous mechanical faults in 6-kV pumping induction motors using combined MCSA and stray flux methods,” IET, https://doi.org/10.1049/elp2.12054, 2021.

Acknoledgements

I would like to acknowledge all the people who made this work possible. First of all, my academic tutor, Prof. Lucia Frosini for her tireless guidance throughout these years. Also, I would like to thank Prof. Sławomir Hausman, from the Technical University of Łódź, for his teaching and guidance during and after my abroad period in Poland. Moreover, I want to thank him for the review of this work together with Prof. Daniel Moríñigo-Sotelo from the University of Valladolid, Spain. I wish to thank all the colleagues, students, and staff from Pavia and other universities or institutions who give me support and/or professional advice during this period. Finally, I want to thank all the friends and family members who supported me during this time of work and personal growth.